

UNIVERSITY of CATANIA

**Department of BIOLOGICAL, GEOLOGICAL AND ENVIRONMENTAL
SCIENCES**

**PhD COURSE IN EARTH AND ENVIRONMENTAL SCIENCE
(XXXV CYCLE)**

Curriculum in GEOSCIENCE

**SEISMIC AND GEODETIC MOMENT-RATES COMPARISON:
SOME APPLICATIONS IN THE MEDITERRANEAN AREAS**



Advisor: Prof. Maria Serafina Barbano

Co-Advisor: Dr. Mimmo Palano

Coordinator: Prof. Agata Di Stefano

PhD Student:
Federica Sparacino

Academic Year 2021-2022

TABLE OF CONTENTS

Page

Table of Contents.....	2
List of Figures.....	5
List of Tables.....	8
Abstract.....	9
1. Introduction and Proposed Research.....	12
1.1 Introduction and state of the art.....	14
1.2 Proposed research.....	15
1.3 Specific goals.....	16
1.4 Impacts.....	16
2. Geodetic and Seismic Moment-rates.....	17
2.1 Geodetic Moment.....	19
2.1.1 Geodetic Strain-rates.....	21
2.1.1.1 The role of the geodetic strain inside of the seismic cycle.....	27
2.1.2 Seismogenic thickness.....	29
2.2 Seismic Moment.....	29
2.2.1 Maximum Magnitude Estimation.....	34
2.2.2 Gutenberg-Richter parameters and magnitude of completeness.....	35
2.3 Seismic Coupling Coefficient (SCC).....	36
3. A workflow to estimate SCC.....	39
3.1 Input and output files.....	41
3.2 <i>Cells_maker.m</i>	47
3.3 <i>Hs_estimation.m</i>	48
3.4 <i>GM_estimation.m</i>	51
3.5 <i>SM_Kostrov.m</i>	52
3.6 <i>MMAX.m</i> software.....	54
3.7 <i>SM_GR.m</i>	55

3.8 Possible improvements.....	59
4. The case study of Italy.....	61
4.1 General background of Italy.....	61
4.2 Data.....	64
4.2.1 Seismological data.....	64
4.2.1.1 Historical Seismicity.....	64
4.2.1.2 Instrumental Seismicity.....	68
4.2.2 GNSS data.....	72
4.2.2.1 Data processing.....	74
4.2.2.2 Analysis of time series parameters.....	76
4.2.2.3 Velocity field computation.....	76
4.2.2.4 Strain-rates computation.....	79
4.3 The application of the workflow: Results.....	81
4.3.1 Seismic source zonation and cell size definition.....	81
4.3.2 M_{max} estimation.....	81
4.3.3 Coefficients of the Gutenberg-Richter recurrence relation.....	83
4.3.4 The seismogenic thickness.....	86
4.3.5 Seismic moment-rates.....	88
4.3.6 Geodetic strain and moment-rates.....	90
4.3.7 Seismic Coupling Coefficient (SCC).....	92
4.3.8 Discussion.....	94
4.3.9 Conclusive remarks.....	97
5. Other Applications of the Method.....	98
5.1 The Ibero-Maghrebian Region.....	99
5.1.1 Seismological Data.....	100
5.1.2 Geodetic Data.....	102
5.1.3 SCC Results and Conclusive Remarks.....	104
5.2 The Sicily Channel.....	106
5.2.1 Seismological Data.....	107
5.2.2 Geodetic Data.....	108
5.2.3 SCC Results and Conclusive Remarks.....	109
5.3 The Aegean-Anatolian Region.....	110
5.3.1 Seismological Data.....	111
5.3.2 Geodetic Data.....	112
5.3.3 SCC Results and Conclusive Remarks.....	114
5.4 Egypt.....	115
5.4.1 Seismological Data.....	117
5.4.2 Geodetic Data.....	119
5.4.3 SCC Results and Conclusive Remarks.....	120

6. General Discussion.....	122
6.1 General Estimation Problems.....	122
6.2 General Uncertainties and Limits.....	124
6.3 Efficiency of the method.....	126
Supplementary Material.....	127
S1 – The Summation Method.....	127
S2 – Moment-rates tests for Sicily Channel.....	132
References.....	135
Acknowledgments.....	161

LIST OF FIGURES

Page

Figure 1.1 Simplified map of the studied Mediterranean areas.....	13
Figure 1.2 Exemplary cartoon of a crustal volume.....	15
Figure 2.1 The scalar seismic moment.....	18
Figure 2.2 The strain.....	23
Figure 2.3 Different methods to derive GPS strain-rates.....	25
Figure 2.4 Voronoi cell.....	25
Figure 2.5 Wessel and Bercovici (1998) method.....	25
Figure 2.6 Spherical wavelet frame functions.....	26
Figure 2.7 Elastic rebound model.....	27
Figure 2.8 Geometry of models of a strike slip faulting.....	28
Figure 2.9 The seismogenic thickness.....	29
Figure 2.10 Moving average of seismic moment.....	31
Figure 2.11 Gutenberg-Richter Law.....	33
Figure 2.12 Regression of surface rupture length on magnitude.....	35
Figure 2.13 The geodetic moment.....	37
Figure 2.14 Estimated SCC for the Zagros collisional belt.....	38
Figure 3.1 The core of the workflow.....	40
Figure 3.2 A summary of the workflow.....	40
Figure 3.3 Input seismic catalog file.....	41
Figure 3.4 Input geodetic file.....	42
Figure 3.5 Output summary <i>file.csv</i>	44
Figure 3.6 Output figure 1 of the workflow.....	45
Figure 3.7 Output figure 2 of the workflow.....	45
Figure 3.8 Output figure 3 of the workflow.....	46
Figure 3.9 Output figure 4 of the workflow.....	46
Figure 3.10 A summary of <i>Cells_maker.m</i> program.....	47
Figure 3.11 A summary of <i>Hs_estimation.m</i> program.....	49

Figure 3.12 Output file from <i>Hs_estimation.m</i> program.....	50
Figure 3.13 Output figure 1 from <i>Hs_estimation.m</i> program.....	51
Figure 3.14 Output figure 2 from <i>Hs_estimation.m</i> program.....	51
Figure 3.15 A summary of <i>GM_estimation.m</i> program.....	51
Figure 3.16 Output figure from <i>GM_estimation.m</i> program.....	52
Figure 3.17 A summary of <i>SM_Kostrov.m</i> program.....	53
Figure 3.18 Output figure from <i>SM_Kostrov.m</i> program.....	54
Figure 3.19 A summary of <i>MMAX.m</i> program.....	55
Figure 3.20 A summary of <i>SM_GR.m</i> program.....	56
Figure 3.21 Output figure 1 from <i>SM_GR.m</i> program.....	58
Figure 3.22 Output figure 2 from <i>SM_GR.m</i> program.....	59
Figure 4.1 Main structural and kinematics features of the Italian orogeny.....	63
Figure 4.2 The historical merged SHARE catalog.....	65
Figure 4.3 The historical CFTI5Med catalog.....	66
Figure 4.4 Some plots for the SHARE catalog.....	67
Figure 4.5 The instrumental seismicity for Italy (http://iside.rm.ingv.it/).....	69
Figure 4.6 The instrumental seismicity for Italy (http://horus.bo.ingv.it/).....	70
Figure 4.7 Some plots for the instrumental catalog.....	71
Figure 4.8 Continuous GNSS stations for the Italian region.....	73
Figure 4.9 Summary of data in daily solutions.....	75
Figure 4.10 The processed sub-networks.....	75
Figure 4.11 Geodetic velocity field for Italy.....	78
Figure 4.12 Geodetic strain-rate field for Italy.....	80
Figure 4.13 Spatial pattern of estimated maximum magnitude.....	82
Figure 4.14 Spatial pattern of <i>a-value</i> for Italy.....	83-84
Figure 4.15 Spatial pattern of <i>b-value</i> for Italy.....	85-86
Figure 4.16 Smoothed seismogenic thickness for Italy.....	87
Figure 4.17 Spatial pattern of seismic moment-rates.....	88-89
Figure 4.18 Spatial pattern of seismic moment-rates (Kostrov).....	90
Figure 4.19 Spatial pattern of geodetic strain and moment-rates for Italy.....	91
Figure 4.20 Spatial pattern of the SCC for Italy.....	92-93

Figure 4.21 Spatial pattern of the SCC for Italy (Kostrov).....	94
Figure 5.1 Simplified map of the studied Mediterranean areas.....	98
Figure 5.2 Simplified tectonic map of Ibero-Maghrebian region.....	99
Figure 5.3 Seismological data for Ibero-Maghrebian region.....	101
Figure 5.4 Geodetic data for Ibero-Maghrebian region.....	103
Figure 5.5 SCC for Ibero-Maghrebian region.....	104
Figure 5.6 Simplified tectonic map of the Sicily Channel.....	106
Figure 5.7 Seismological data for the Sicily Channel.....	108
Figure 5.8 Estimated GPS velocities for the Sicily Channel.....	109
Figure 5.9 Tectonic setting of the Aegean-Anatolia region.....	111
Figure 5.10 Seismological data for the Aegean-Anatolia region.....	112
Figure 5.11 GNSS velocities and strain-rate for the Aegean-Anatolia region..	114
Figure 5.12 SCC for the Aegean-Anatolia region.....	115
Figure 5.13 Compiled global tectonic sketch for Egypt.....	116
Figure 5.14 Historical seismicity for Egypt.....	118
Figure 5.15 Instrumental seismicity for Egypt.....	118
Figure 5.16 Geodetic strain-rate field for Egypt.....	119
Figure 5.17 SCC for Egypt.....	121
Figure S1 Selected cell of Northern Italy.....	128
Figure S2 Selected cell of Central Italy.....	129
Figure S3 Selected cell of Southern Italy.....	130
Figure S4 Selected cell of Southern Italy (Sicily).....	131
Figure S5 Moment-rates tests for Sicily Channel.....	132
Figure S6 Strain-rate tests for Sicily Channel.....	133
Figure S7 Geodetic moment-rate tests for Sicily Channel.....	134

LIST OF TABLES

Page

Table 6.1 Summary of adopted and estimated parameter values.....123

Abstract

Seismic and geodetic moment-rate comparisons can reveal regions with unexpected potential seismic hazards, as well as the presence of asperities along plate zones. Even if the estimations of geodetic and seismic moment-rates are affected by some uncertainties, their ratio, defined as Seismic Coupling Coefficient (hereafter SCC), allows establishing if a region deforms in plastic modality or in a seismic one. This comparison has been performed for five Mediterranean areas: the Ibero-Maghrebian region (Sparacino et al., 2020), Italy (the unpublished element of this PhD Thesis), the Sicily Channel (Palano et al., 2020), the Aegean-Anatolian region (Sparacino et al., 2022) and Egypt (Sawires et al., 2021). For the Ibero-Maghrebian region and Egypt case studies, the calculation of SCC was made adopting the existing seismic zonation. A single area was considered for the Sicily Channel case study, based on the distribution of the GNSS stations. The developed workflow (MATLAB program language; <https://it.mathworks.com>) was used for Italy and Aegean-Anatolian regions.

For what concern the first analysed area, located at the western Mediterranean border along the Eurasia-Nubia plate convergence, the Ibero-Maghrebian region has been subject to a number of large earthquakes ($M \geq 6.5$) in the last millennium. In order to provide a first estimation of SCC values for this area, we divided the study area into twenty-five seismogenic source zones, based on available geological, tectonic, and seismological data. Achieved results highlight that many of these seismogenic source zones, comprising the Western Betics, the Western Rif mountains, and the High, Middle, and Saharan Atlas, are characterized by SCC values lower than 23%, evidencing their prevailing aseismic behavior. Intermediate SCC values (between 35% and 60%) have been observed for some zones belonging to the Eastern Betics, the central Rif, and the Middle Atlas, indicating how crustal seismicity accounts only for a moderate fraction of the total deformation-rate budget. High SCC values ($> 95\%$) have been observed along the Tell Atlas, highlighting a fully seismic deformation.

For what concern Italy case study, the SCC has been calculated by adopting a workflow written in the MATLAB program language (<https://it.mathworks.com>; see Chapter 3) and dividing the area into a $1^\circ \times 1^\circ$ regular grid. Regions with very high to high SCC are located in a small area of Northern Apennines (Friuli), Central and Southern Apennines, and in the Southern part of Sicily. These regions, characterized by active faults, show a prevalent seismic deformation. Regions with intermediate to low SCC are located in Alps, Northern Apennines and part of Central Apennines and this could be partially attributed to the aseismic components of deformation and to catalog incompleteness, or in absence of large earthquakes could be identified as potential seismic gaps.

For what concern the Sicily Channel, based on multidisciplinary data, including seismological and geodetic observations, as well as seismic reflection profiles and gravity maps, the pattern of crustal deformation and active tectonics in the Sicily Channel, has been analysed. Our large dataset allowed us to highlight the presence of an active ~ 220 -km-long complex lithospheric fault system (here named the Lampedusa-Sciaccia Shear Zone), approximately oriented N-S,

crossing the study area with left-lateral strike-slip deformations, active volcanism and high heat flow. We suggest that this shear zone represents the most active tectonic domain in the area, while the NW-SE elongated rifting pattern, considered the first order tectonic feature, appears currently inactive and sealed by undeformed recent (Lower Pleistocene?) deposits. Estimates of seismological and geodetic moment-rates, $6.58 \cdot 10^{15}$ Nm/year and $7.24 \cdot 10^{17}$ Nm/year, respectively, suggest that seismicity accounts only for $\sim 0.9\%$ of crustal deformation, while the anomalous thermal state and the low thickness of the crust would significantly inhibit frictional sliding in favour of creeping and aseismic deformation. We therefore conclude that a significant amount of the estimated crustal deformation-rate occurs aseismically, opening new scenarios for seismic risk assessments in the region.

For what concern the Aegean-Anatolian region, an improved picture of the SCC has been provided by taking advantage of extensive seismic and geodetic datasets. SCC is low ($< 35\%$) or intermediate ($35\% - 70\%$) in most of the area, while the Karliova triple junction, on a N-S-oriented belt along the boundary between western and central Anatolia, and the south-eastern Peloponnese are fully coupled, suggesting a full seismic release of the entire deformation budget. An intermediate value of seismic coupling is observed for the eastern and central segments of the Northern and Eastern Anatolian Fault zones, for part of the Hellenic volcanic arc, the Kefalonia Transform Fault and the Corinth gulf active faults. Considering historical earthquake data, these intermediate coupling values indicate either aseismic deformation or catalog incompleteness. Furthermore, the elapsed time since large magnitude earthquakes clearly raises the possibility of impending earthquakes on the Northern and Eastern Anatolian Fault zones. A broad seismic gap is evidenced along the Hellenic subduction zone, because of the reduced coupling and the absence of $\sim M 8$ earthquakes in the last 700 years, at least. We conclude that in most of the central Aegean Sea aseismic deformation prevails as suggested by the small value of coupling and the modest seismic release over the last millennium.

For what concern the last analysed area, the present-day tectonics and seismicity of Egypt result from the long-lasting interaction between the Nubian, Eurasian, and Arabian plates. The study region was divided into ten (EG-01 to EG-10) crustal seismic sources based mainly on seismicity, focal mechanisms, and geodetic strain characteristics. The delimited seismic sources cover the Gulf of Aqaba-Dead Sea Transform Fault system, the Gulf of Suez-Red Sea Rift, besides some potential seismic active regions along the Nile River and its delta. For each seismic source, the estimation of seismic and geodetic moment-rates has been performed. Although the obtained results cannot be considered to be definitive, among the delimited sources, four of them (EG-05, EG-06, EG-08, and EG-10) are characterized by low seismic-geodetic moment-rate ratios ($< 20\%$), reflecting a prevailing aseismic behaviour. Intermediate moment-rate ratios (from 20% to 60%) have been obtained in four additional zones (EG-01, EG-04, EG-07, and EG-09), evidencing how the seismicity accounts for a minor to a moderate fraction of the total deformational budget. In the other two sources (EG-02 and EG-03), high seismic-geodetic moment-rates ratios ($> 60\%$) have been observed, reflecting a fully seismic deformation.

These different studies have provided new insights into the seismic hazard of large areas of the Mediterranean region, which have been subject to relevant seismic release. Our approach along

with the associated workflow can be easily applied in other tectonic worldwide frameworks, providing new tools to the fundamental understanding of earthquake prediction.

1 – Introduction and Proposed Research

In this chapter, the arguments and the principal goals treated in this PhD Thesis will be briefly exposed.

The identification of reasonable earthquake scenarios involves several scientific fields. Studies on seismicity come together with the analysis of the deformation field. In such a framework, geodetic and seismic moment-rates comparisons would provide crucial insights for understanding fault behaviour (seismic vs aseismic), as well as to highlight regions showing gaps in seismic cycle, with obvious implications on seismic hazard assessment of regions subjected to relevant ongoing tectonic deformation (essentially for time-dependent seismic hazard assessments).

The principal goal of this PhD Thesis is the estimation and the comparison between the geodetic and seismic moment-rates above the Mediterranean regions (Fig. 1.1). At this purpose, several studies conducted in these years will be presented (Chapter 5). Furthermore, the innovative element proposed is the Italian region (Chapter 4), since it has been historically stroked by the occurrence of large earthquakes, with magnitude exceeding 7. A careful study of the quantities involved accompanied by a detailed exposition of the existing formulas will be treated in Chapter 2. The developed workflow (written in MATLAB program language; <https://it.mathworks.com>) for automatize the estimation of seismic and geodetic moment-rates will be shown in details in Chapter 3.

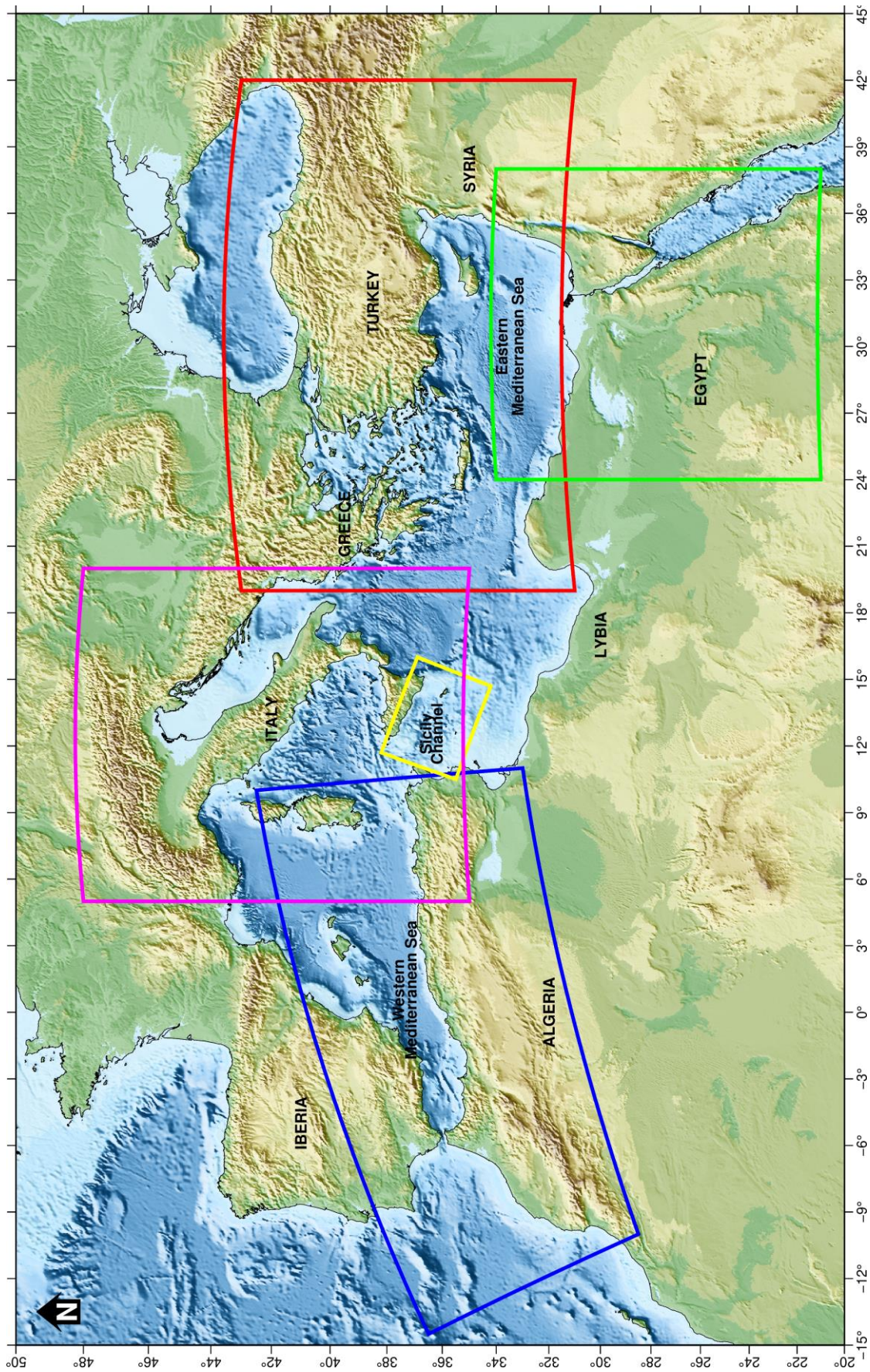


Figure 1.1 - Simplified map of the studied Mediterranean areas. From W to E, the Ibero-Maghrebian region, Italy, the Sicily Channel, the Aegean-Anatolian region and Egypt are delimited with blue, magenta, yellow, red and green boxes, respectively.

1.1 Introduction and state of the art.

The comparison between the geodetic and seismic deformation rates provides significant information on the seismic hazard of a region subject to active tectonics (Mazzotti et al., 2011). Ideally, the geodetically measured moment-rate of a crustal volume affected by seismogenic faults could be compared by the one seismically released in a time interval equals to the seismic cycle of the volume (Fig. 1.2). Relying on this simple concept, several authors started in studying this approach in order to analyse regions with ongoing tectonic deformation. The first who derives some formulations was Kostrov (1974). In the last twenty years several studies have been conducted worldwide, i.e. in Iran (Masson et al., 2005; Palano et al., 2018), western Canada (Mazzotti et al., 2011), western USA (Pancha et al., 2006; Bos and Spakman, 2005), Greece (Rontogianni, 2010; Chousianitis et al., 2015), Southern Italy (Jenny et al., 2006; Palano et al., 2011; D'Agostino, 2014; Ferranti et al., 2014), Himalayas (Bilham and Ambraseys, 2005; Bungum et al., 2017; Stevens and Avouac, 2017), and the East African Rift (Déprez et al., 2013), with satisfying results. Even if the estimations of geodetic and seismic strain-rates are affected by some uncertainties, their ratio, defined as Seismic Coupling Coefficient (hereafter SCC), allows establishing if a region deforms in plastic modality or in a seismic one (Palano et al., 2018 and reference therein). These studies have highlighted that a mismatch over varying spatial and temporal scales may be observed between the two estimates, with the geodetic estimates usually larger than the seismic ones (Pancha et al., 2006; Mazzotti et al., 2011). It is well known that geodetically observed strains include both elastic and anelastic components and that only the elastic strain is responsible for earthquakes; so, it is difficult to differentiate these two contributions without a priori knowledge of the rheology of the crust investigated. Consequently, the comparison between geodetic and seismic strain-rates may not be balanced in regions cut by creeping faults or where significant amounts of deformation take place plastically (Palano et al., 2011; applied geophysics methods may be useful). Generally, geodetic moment-rates greater than seismic ones are observed in:

- regions characterized by faults with aseismic behaviour;
- regions characterized by seismic gaps, in which the excess of the geodetic strain-rate can be released through large impending earthquakes;
- regions in which the seismic catalog is incomplete;
- regions in which the seismic catalog covers a very short time interval if compared to the seismic cycle of the investigated region.

The converse is rare but possible: seismically estimated strain is larger than geodetically measured shortly after a major earthquake if the time covered by the geodetic data is shorter than the seismic cycle, and so it is not sufficient to capture the entire spectrum of seismic and aseismic components of the investigated crustal volume (Fig. 1.2). Another possibility could be a bad geometry of the geodetic network, due to a highly heterogeneous distribution in the territory. Thus, constraining the mismatch between the geodetic and the seismic strain-rates requires a high level of accuracy and spatially (as well as temporally) dense and extensive geodetic observations, coupled with the most complete possible seismic-event catalog covering a long time interval.

In the last two decades, the rapid growth in continuous and episodic GPS networks as well as the seismic ones allowed for the acquisition of temporally and spatially extensive datasets over

large areas worldwide, hence providing useful data for geodetic and seismic strain-rate estimations and comparisons. Italy presents these characteristics and for this reason it may represent an ideal study case.

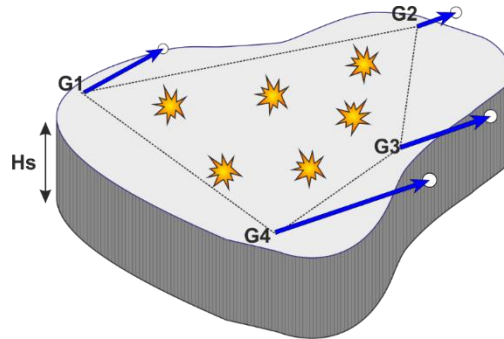


Figure 1.2 – Exemplary cartoon of a crustal volume (with seismogenic thickness, H_s) characterized by the occurrence of seismic events (represented by the yellow polygons) during a seismic cycle. GPS stations able to measure the geodetic moment-rate of the underlying crustal volume are represented with G1, G2, G3, G4.

1.2 Proposed research.

As has been said above, the principal goal of this PhD Thesis is the estimation and the comparison between the geodetic and seismic moment-rates in some Mediterranean regions (Fig. 1.1). The following explanation will be focused on Italy case study, even if the listed steps have been adapted for all the analysed regions.

For this purpose, all the available online permanent and campaign GPS data will be collected and processed (on a global, national and regional scales, etc.). The GPS data will be processed using the GAMIT/GLOBK software (Herring et al., 2018; <http://www-gpsg.mit.edu>). In order to improve the crustal deformation field of the study area, the obtained solution will be merged with the available ones coming from literature, using a unique reference frame. Afterwards, the study area will be divided in regular polygons and for each of them the geodetic moment-rates will be estimated with the formulation proposed by Savage and Simpson (1997). The dimension and delimitation of each polygon will be properly chosen following these important aspects:

- seismicity distribution (explained later);
- number of available GPS stations;
- geologic and seismotectonic local characterization.

In order to investigate the seismic characteristics of the study area, a catalog of instrumental and historical seismicity will be compiled. For each polygon, the seismic moment-rates will be estimated with the formulation proposed by Hyndman and Weichert (1983). This approach estimates the seismic deformation rate considering the cumulative truncated Gutenberg-Richter distribution up to the maximum magnitude value that could occur within each polygon. This approach allows taking into account the probable incompleteness of the existing catalog. In addition, the seismic moment-rates will be calculated even with the formulation proposed by Kostrov (1974), which allows estimating the seismic moment-rates of a specific area adopting the scalar moment

summation of each earthquake. Moreover, the catalog suffers from the possible lack of both large earthquakes (with high recurrence rate compared to the catalog length) and undetected small magnitude events. Estimations coming from both methods can be compared in order to adequately characterize the seismic behaviour of each identified polygon and to highlight any significant discrepancy related to the adopted approach.

In the final step, for each identified polygon, the SCC will be estimated from the ratio between seismic and geodetic moment-rates. The obtained spatial SCC distribution will be compared with the active tectonic structures and with the high magnitude earthquake distribution in order to better evaluate the obtained results and to propose a realistic picture of the crustal deformation modality in the study area.

1.3 Specific goals.

As we told above, the principal goal of this PhD Thesis is to analyse the areal distribution of the SCC over the study area. This goal will be obtained with the following partial steps:

- geodetic velocity field estimation (it will be referred to adequate reference frames);
- seismicity and historical catalogs collection; seismicity distribution maps of the study area;
- geodetic strain-rates field of the study area;
- seismic strain-rates field of the study area.

1.4 Impacts.

The proposed PhD Thesis will have a strong scientific and socio-economic impact since it provides significant insights into the seismic hazard of Italy, which has been affected by the occurrence of large earthquakes in the last millennium as has been said above. In addition, it will improve the knowledge about the elastic and anelastic behaviour of this region. Moreover, it is important to emphasize that at this moment, a complete analysis of Italy region was missing, and together with the other studies presented, this PhD Thesis provides an improved picture of the seismic hazard of the whole Mediterranean area.

2 – Geodetic and Seismic Moment-rates

In this chapter, the principal quantities involved in the calculation of the Seismic Coupling Coefficient (SCC) will be introduced in detail, i.e., the geodetic and seismic moment-rates, as well as the by-products required for their computation.

The most reliable measure able to provide a “size” of an earthquake with an empirical connection with the amount of slip is the seismic moment (M_{seis}). It is a fundamental parameter relating to the source area of the earthquake and deducible information contained in the seismograms. In physics, the moment is defined as the product between the force, F , and the distance from the center of rotation of a system, δ :

$$M = F \times \delta \quad (2.1)$$

The force is determined by the elasticity of the crust, in fact it is defined as the product between the aforesaid elasticity, k , and the displacement, u :

$$F = k \cdot u \quad (2.2)$$

The distance is given by the width of the deforming zone. The “spring constant” is determined by material and geometry, and substituting eq. (2.2) in eq. (2.1) the following equation is obtained:

$$M = k \cdot u \times \delta \quad (2.3)$$

where

$$k = A \frac{K}{\delta} \quad (2.4)$$

- K is the bulk modulus (incompressibility) in homogeneous media. The spring constant increase with the area, A , decrease with length, δ , and increase with modulus, K .

$$k = A \frac{\mu}{\delta} \quad (2.5)$$

- μ is the shear modulus (rigidity) in homogeneous media. The spring constant increase with the area, A , decrease with length, δ , and increase with modulus, μ .

Returning to the moment, and remembering that the spring constant increases with cross-sectional area and rigidity, while it decreases with length eq. (2.5) and that the moment is given by the product of force with distance eq. (2.3), substituting k in the definition of the moment, in the field of seismology the following relation is obtained:

$$M_{seis} = \mu \cdot \Delta u \cdot A \quad (2.6)$$

So the seismic moment is defined in terms of rigidity, μ , slip vector, Δu , and fault area, A , in eq. (2.6) (see Fig. 2.1).

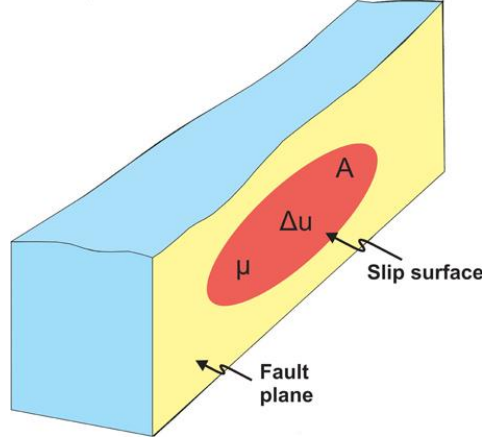


Figure 2.1 - The scalar seismic moment defined as the product between the shear modulus, μ , the average displacement on the fault, Δu , and the fault area that slipped, A (Aki, 1966).

The width of deformation perpendicular to the fault, δ , is deleted:

$$M_{seis} = \mu \cdot \left(\frac{\Delta u}{\delta}\right) \cdot \delta A \quad (2.7)$$

It is important to point out that the elastic strain released is given by $(\Delta u / \delta)$, and that its product with the rigidity, μ , gives the stress. This particular stress is called the co-seismic stress drop, $\Delta\sigma$. The product of the area and the width normal to it is the volume of the fault zone, δA . The slip and the stress drop are not uniform across the area; hence, the moment is an integral:

$$M_{seis} = \int_V \Delta\sigma dV \quad (2.8)$$

The stress drop evolves during the event, as do the displacement and the area of rupture. Therefore, it is useful to define the rate of moment release:

$$M(t) = \mu D(t) S(t) \quad (2.9)$$

The time integral of eq. (2.9) is the total scalar seismic moment per event, defined as (Aki, 1966):

$$M_{seis} = \mu \bar{D} S \quad (2.10)$$

where, considering two different blocks of a fault in contact and in relative motion:

- μ (N m^{-2}) is the shear modulus defined in eq. (2.5);

- \bar{D} (m) is the average displacement on the fault;
- S (m²) is the fault area that slipped.

The seismic moment-rate, if compared with the geodetic one, can provide crucial insights for understanding fault behavior (seismic vs aseismic), with obvious implications on seismic hazard assessment.

2.1 Geodetic Moment.

Although the scalar moment accumulation rate within the seismogenic zone, beneath an investigated area, is sometimes deduced from the observed average surface strain accumulation rate over the same area, the correspondence between the two quantities reported by [Kostrov \(1974\)](#) is very uncertain. In fact, only in exceptional cases the moment-rate tensor will correspond to a double-couple mechanism that can be represented by a scalar moment accumulation rate. More generally, the moment tensor must be resolved into the superposition of two or more double-couple moment-rate and so the resolution is not unique. Moreover, earthquake potential is measured by accumulated seismic moment, whereas geodetic surveys measure surface strain accumulation that presumably could be released by earthquakes.

In light of this, several attempts have been made by scholars to establish an equivalence between the two measurements. Regarding the geodetic moment-rate, different formulations relating the surface strain-rates to moment-rates have been proposed in literature ([Pancha et al., 2006](#)). Strain accumulation is conventionally attributed to steady slip on the downdip extension of the fault below the seismogenic layer, while the portion of the fault within the seismogenic layer remains locked ([Savage and Burford, 1973](#); [Savage, 1983](#)). In the previous generic formulation by [Kostrov \(1974\)](#) it was defined as follow:

$$M_{geod}^{\dot{}} = 2 \mu V \varepsilon_{ij} \quad (2.11)$$

where:

- μ (N m⁻²) is the shear modulus of the crust. It usually varies between $3.0 \cdot 10^{10}$ Pa and $3.3 \cdot 10^{10}$ Pa, for depth less and greater than 20 km, respectively (e.g., $3.0 \cdot 10^{10}$ Pa is the typical value of average crustal rocks; [Turcotte and Schubert, 2002](#));
- $V = H_s \cdot A$ (km³) is the deforming volume;
- H_s (km) is the seismogenic thickness over which strains accumulate and its elastic part release in earthquakes, i.e., the depth above which a given percentage (e.g., 90%, [Miller and Furlong 1988](#); 95%, [Williams, 1996](#); [Chiarabba and De Gori, 2016](#)) of the hypocenters or the moment release within a depth column occurs (see [Par. 2.1.2](#));
- A (km²) is the surface area of the volume;
- ε_{ij} is the strain-rate measured geodetically at the Earth's surface (see [Par. 2.1.1](#)).

Subsequently, several formulations were proposed. [Anderson \(1979\)](#) proposed a best estimate, by modelling a volume extending or contracting in one direction:

$$M_{geod}^{\dot{}} = 2 \mu H_s A \frac{\varepsilon_{hmin}^{\dot{}}}{k} \quad (2.12)$$

where:

- μ , H_s and A are defined as above;
- $\varepsilon_{hmin}^{\dot{}}$ is the strain-rate referred to the relative extension or convergence velocity of the opposite sides of the region;
- k is a dimensionless constant that adjusts for the inefficiency of randomly oriented faults to accommodate strain.

[Ward \(1994, 1998a, 1998b\)](#) proposed a minimum rate that incorporates the maximum eigenvalue, that is the principle horizontal extension and contraction rates:

$$M_{geod}^{\dot{}} = 2 \mu H_s A [Max(|\varepsilon_{Hmax}^{\dot{}}|, |\varepsilon_{hmin}^{\dot{}}|)] \quad (2.13)$$

where:

- μ , H_s and A are defined as above;
- Max is a function returning the largest of the arguments;
- $\varepsilon_{Hmax}^{\dot{}}$ is the principle horizontal extension rate;
- $\varepsilon_{hmin}^{\dot{}}$ is the principle horizontal contraction rate.

The [Working Group on California Earthquake Probabilities \(1995\)](#) proposed a minimal approach to represent the moment-rate tensor, using the difference between the principal strain-rates:

$$M_{geod}^{\dot{}} = 2 \mu H_s A (\varepsilon_{Hmax}^{\dot{}} - \varepsilon_{hmin}^{\dot{}}) \quad (2.14)$$

where μ , H_s , A , ε_{Hmax} and ε_{hmin} are defined as above.

In this thesis the [Savage and Simpson \(1997\)](#) formulation is adopted, which derives from [eq. \(2.11\)](#) and allows to consider strains in multiple directions. They suggest that the scalar moment-rate equivalent to a given surface strain accumulation is at least as large as:

$$M_{geod}^{\dot{}} = 2 \mu H_s A [Max(|\varepsilon_{Hmax}^{\dot{}}|, |\varepsilon_{hmin}^{\dot{}}|, |\varepsilon_{Hmax}^{\dot{}} + \varepsilon_{hmin}^{\dot{}}|)] \quad (2.15)$$

where

- μ , H_s , A and Max are defined as above;
- ε_{Hmax} and ε_{hmin} are the principal horizontal strain-rates.

The [eq. \(2.15\)](#) is generally equal to the approximate scalar moment used by [Ward \(1994\)](#), [eq. \(2.14\)](#), but is greater than the scalar moment-rate used by the [Working Group on California Earthquake Probabilities \(1995\)](#), [eq. \(2.14\)](#). It is important to point out that the moment-rate estimation from geodetic strain-rates is proportional to the chosen seismogenic thickness, H_s , and therefore this last parameter plays a fundamental role. For simplicity, the constant, k , was set to 2 according to [Ward \(1994\)](#), even if [Carafa et al. \(2017\)](#) have shown that a different value needs to be considered if the

active-fault planes in the modelled volume of lithosphere are not angles of 45° from the largest value of the strain-rates. In order to connect the recent tectonic activity to seismicity, [Carafa et al. \(2017\)](#) predicted long-term-average seismic moment-rates for deforming volumes of the lithosphere using long-term tectonic moment-rate with the following equation:

$$M_{tect}^{\dot{}} = k \mu H_s A [\text{Max}(|\varepsilon_{Hmax}|, |\varepsilon_{hmin}|, |\varepsilon_{Hmax} + \varepsilon_{hmin}|)] \quad (2.16)$$

where:

$$k = \left(\frac{\varepsilon_{hmean}}{\cos(\theta_1)\sin(\theta_1)} + \frac{\varepsilon_{hmin}}{\cos(\theta_2)\sin(\theta_2)} \right) = 2.31 \quad (2.17)$$

and

- $\theta_1 = \theta_2 = 60^\circ$ for extensional horizontal strain-rates;
- $\theta_1 = \theta_2 = 30^\circ$ for compressional horizontal strain-rates.

In this way, there will be a net increase of moment-rate estimation of 15 per cent just due to a different friction value assigned to active fault sets ([Carafa et al., 2017](#)).

It is important to underline that if strain is only in the x_2 direction, the strain-rate terms are identical for all formulations ([Pancha et al., 2006](#)).

2.1.1 Geodetic strain-rates.

Modern GPS networks are, at a regional scale at least, much more spatially complete than earlier networks, thus allowing us to calculate the 2D velocity gradient tensor ([Allmendinger et al., 2007](#)). Deformation is the gradient of the displacement field ([Cardozo and Allmendinger, 2009](#)). As could be seen in [Fig. \(2.2\)](#), three points in an initial coordinate system, \mathbf{X} , which are displaced along three non-parallel vectors, \mathbf{u} , to their final coordinates, \mathbf{x} . If the deformation is homogeneous (i.e., parallel lines in the initial state remain parallel in the final state), the relation between the displacement vectors and the initial positions is expressed by the following equation:

$$u_i = t_i + \frac{\partial u_i}{\partial x_j} x_j = t_i + e_{ij} x_j \quad (2.18)$$

where

- u_i is the GPS measured velocity of the station;
- t_i is a constant of integration that corresponds to the displacement at the origin of the coordinate system;
- x_j is the position of the station;
- e_{ij} is the displacement rate (velocity) gradient tensor.

From [eq. \(2.18\)](#) it is clear that there are six unknowns in 2D: the two components of the translation vector and the four components of the Lagrangian or Eulerian displacement gradient tensor. In 3D dimension, there are twelve unknowns: the three components of the translation vector

and the nine components of the Lagrangian or Eulerian displacement gradient tensor. Each point with displacement/velocity data furnishes two (2D) or three (3D) equations. Therefore, in 2D a minimum of three non-colinear stations, and in 3D a minimum of four non-planar stations, are required to compute strain.

To solve this system of linear equations using linear algebra methods, eq. (2.18) should be recast into three matrices, two of which contain known quantities and one that contains unknown quantities. Therefore, we have:

$$\begin{bmatrix} {}^1u_1 \\ {}^1u_2 \\ {}^2u_1 \\ {}^2u_2 \\ \dots \\ \dots \\ {}^nu_1 \\ {}^nu_2 \end{bmatrix} = \begin{bmatrix} 1 & 0 & {}^1x_1 & {}^1x_2 & 0 & 0 \\ 0 & 1 & 0 & 0 & {}^1x_1 & {}^1x_2 \\ 1 & 0 & {}^2x_1 & {}^2x_1 & 0 & 0 \\ 0 & 1 & 0 & 0 & {}^2x_1 & {}^2x_2 \\ \dots & \dots & \dots & \dots & \dots & \dots \\ \dots & \dots & \dots & \dots & \dots & \dots \\ 1 & 0 & {}^nx_1 & {}^nx_1 & 0 & 0 \\ 0 & 1 & 0 & 0 & {}^nx_1 & {}^nx_2 \end{bmatrix} \begin{bmatrix} t_1 \\ t_2 \\ e_{11} \\ e_{12} \\ \dots \\ e_{21} \\ e_{22} \end{bmatrix} \quad (2.19)$$

Eq. (2.19) is not only written for three stations in 2D, but for n stations. If there are more than three stations in 2D, the system is overdetermined (number of equations greater than number of model parameters). In this case, the extra information can be used to assess the uncertainties of the fitted parameters. The solution to eq. (2.19) is a classical application of inverse theory (Menke, 1989), specifically the solution of the linear least-squares problem, which has the following formulation:

$$\mathbf{b} = \mathbf{M} \mathbf{a} \quad (2.20)$$

where

- \mathbf{b} is the vector with known displacements/velocities;
- \mathbf{M} is the matrix with initial positions of the stations (the design matrix);
- \mathbf{a} is the vector with the unknown model parameters.

To solve for \mathbf{a} , \mathbf{b} is multiplied by the inverse of matrix \mathbf{M} and we have

$$\mathbf{a} = \mathbf{M}^{-1} \mathbf{b} \quad (2.21)$$

Once the parameters \mathbf{a} and the displacement gradient (the last four elements in 2D of the vector \mathbf{a}) are estimated, the Eulerian strain tensor is obtained. For infinitesimal strains, the displacement tensor, e_{ij} , can be decomposed into a symmetric part, ε_{ij} , and into an antisymmetric one, Ω_{ij} , as follows:

$$e_{ij} = \frac{1}{2} \left(\frac{\partial u_i}{\partial x_j} + \frac{\partial u_j}{\partial x_i} \right) + \frac{1}{2} \left(\frac{\partial u_i}{\partial x_j} - \frac{\partial u_j}{\partial x_i} \right) = \varepsilon_{ij} + \Omega_{ij} \quad (2.22)$$

where

- ε_{ij} is the infinitesimal strain-rate tensor;

- Ω_{ij} is the local rotation rate (vorticity) tensor.

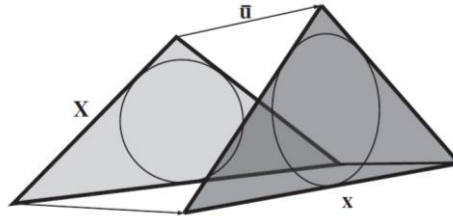


Figure 2.2 – Three points in an initial configuration, \mathbf{X} , move along non-parallel vectors, \mathbf{u} , to a final configuration, \mathbf{x} , resulting in strain. Modified from [Cardozo and Allmendinger \(2009\)](#).

Three possible relations exist between the principal strains, e_1 and e_2 . In the first case we have

$$(e_1 + e_2) < 0 \quad (2.23)$$

when there is an excess of horizontal compression which should be balanced by vertical extension; in the second case we have

$$(e_1 + e_2) = 0 \quad (2.24)$$

when neither thinning nor thickening occurs in the vertical dimension; finally, we have

$$(e_1 + e_2) > 0 \quad (2.25)$$

when the excess of horizontal extension should be balanced by vertical compression. In this case, the maximum shear strain-rate $(e_1 - e_2)$, and the second strain-rate invariant $\sqrt{e_1^2 + e_2^2}$, are then computed ([Farolfi and Del Ventisette, 2017](#); [Haines and Holt, 1993](#)).

The principal goal is the determination of the deformation field, which has a spatially continuous distribution, using a discrete number of sites. However, several complications must be kept in mind. The geographic distribution of GPS stations is non-uniform, and the study area may involve a complex velocity field. The geodetic strain-rates are the result of averages over distances that, in many cases, cross geologic structures and non-homogeneous geologic settings and fault patterns. For these reasons, the choice of the interpolation method and the geometric approach to the problem play fundamental roles in the strain-rate field determination ([Farolfi and Del Ventisette, 2017](#)).

Several methods can be used to derive GPS strain-rates, ranging from simple Delaunay triangulations, in which GPS stations coincide with the vertices of the triangles ([Fig. 2.3](#)) to more complex parametric inversions ([Haines and Holt, 1993](#)), where the observed GPS velocity fields interlock over regular/irregular grids, with significant variations in their results. Indeed, a high variety of methods and approaches has been developed over the years for the estimation of the strain

tensor in order to emphasize the deformation patterns of the study area, starting from the geodetic velocity fields (Frank, 1966; Prescott and Savage, 1976; Haines and Holt, 1993; El-Fiky et al., 1997; Shen et al., 1996). Fitting scattered data on a sphere is a long-standing problem that has been approached using local regression, kernel-based methods, statistics-based methods such as kriging, spline-based methods or by estimating a smooth field using an expansion of radial basis functions (such as spherical harmonics), with a smoothing constraint applied to stabilize the inversion. The use of one approach over another requires parameterizations and basic assumptions, with significant variations in the obtained results. Therefore, in order to optimize the calculation procedures and evaluate the variability of the results (strictly dependent on the approach in use), the methods mostly used by the geodetic community were examined. These methods allow estimating the continuous gradient of the horizontal velocity field starting from discrete measurements and with non-homogeneous spatial distribution by using different interpolation techniques, without the assumption that the medium is homogeneous and isotropic. The examined approaches are the following:

- in the first, the interpolation of the velocity field (in plane geometry) occurs through the use of different spatial “weighting” functions (for example, Gaussian or quadratic function), where the velocity value at each station is “weighted” as a function of the values measured at the nearest stations (Shen et al., 2015). If a Gaussian function is used, the “weighting” value depends on the distance between the individual stations and on the spatial coverage of the stations: it decreases as the distance between the stations increases. The Gaussian function offers a fine resolution of the interpolation result if the data are clean and homogeneous, while if the data are heterogeneous, the use of the quadratic function provides a more “smoothed” solution, especially in those regions where the data is poorly distributed. An alternative way to assign the spatial “weighting” value is based on the Voronoi decomposition method, where the study region is divided into polygons (or Voronoi tiles, Fig. 2.4) based on the distribution of the stations and the “weighting” values are based on the azimuth coverage among the various stations.
- in the second one, the velocity field is interpolated on a regular grid, in plane geometry, by using a “spline in tension” function (Wessel and Bercovici, 1998). The “tension” value is generally set by the user and can vary between 0 and 1. In the case of values equal to or close to 0, the velocity field is very “smoothed”, while for values equal to or close to 1, the local effects of the individual stations are accentuated. The “tension” value to be used is usually chosen by the user through a series of preliminary tests where, as the tension varies, the goodness of the fit between the observed and interpolated velocity field is evaluated (Fig. 2.5).
- in the third one, *surfacevel2strain.m*, written in *Matlab* programming language, the velocity field is interpolated adopting a spherical geometry, through the use of spherical “wavelets”, a particular type of spherical harmonics (Tape et al., 2009). The basic assumption is that any velocity field on a sphere can be represented as the linear combination of several spherical “wavelets” (Fig. 2.6). This approach allows the decomposition of the velocity field in different spatial scales, as a function of the spatial distribution of the stations. It allows the identification of different physical phenomena or noise sources operating at different spatial

scales. Wavelets provide a natural representation for such multiscale signals (Tape et al., 2009).

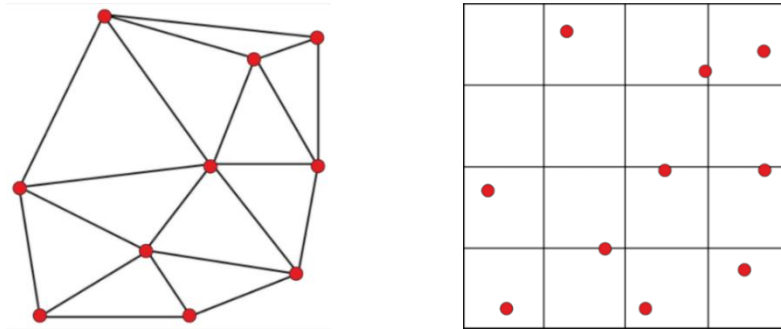


Figure 2.3 – Different methods to derive GPS strain-rates. GPS stations are represented with red circles. On the left panel, the simple Delaunay triangulations; in this case, the GPS stations coincide with the vertices of the triangles. On the right panel, an example in which the calculation is made by interpolating the velocity field on a square mesh grid. The strain is referred to the center of each cell, or to its edges; in this case, the GPS stations do not coincide with the vertices of the squares but they could be located inside them or at their edges.

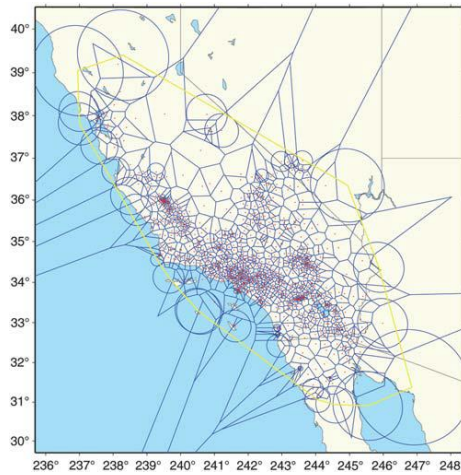


Figure 2.4 - Voronoi cell meshing based on Crustal Motion Map version 4.0 (CMM4) network station distribution. For sites located at the vertices of the network exterior, circular areal weightings replace their Voronoi cell areal weightings. Modified from Shen et al. (2015).

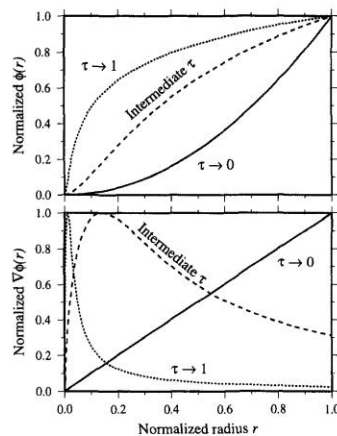


Figure 2.5 – On the top panel, radial cross section of Green’s function, $\phi(r)$, for 2D spline in tension. On the bottom panel, radial cross section of gradient, $\nabla\phi(r)$, in radial direction for several values of tension. Modified from Wessel and Bercovici (1998).

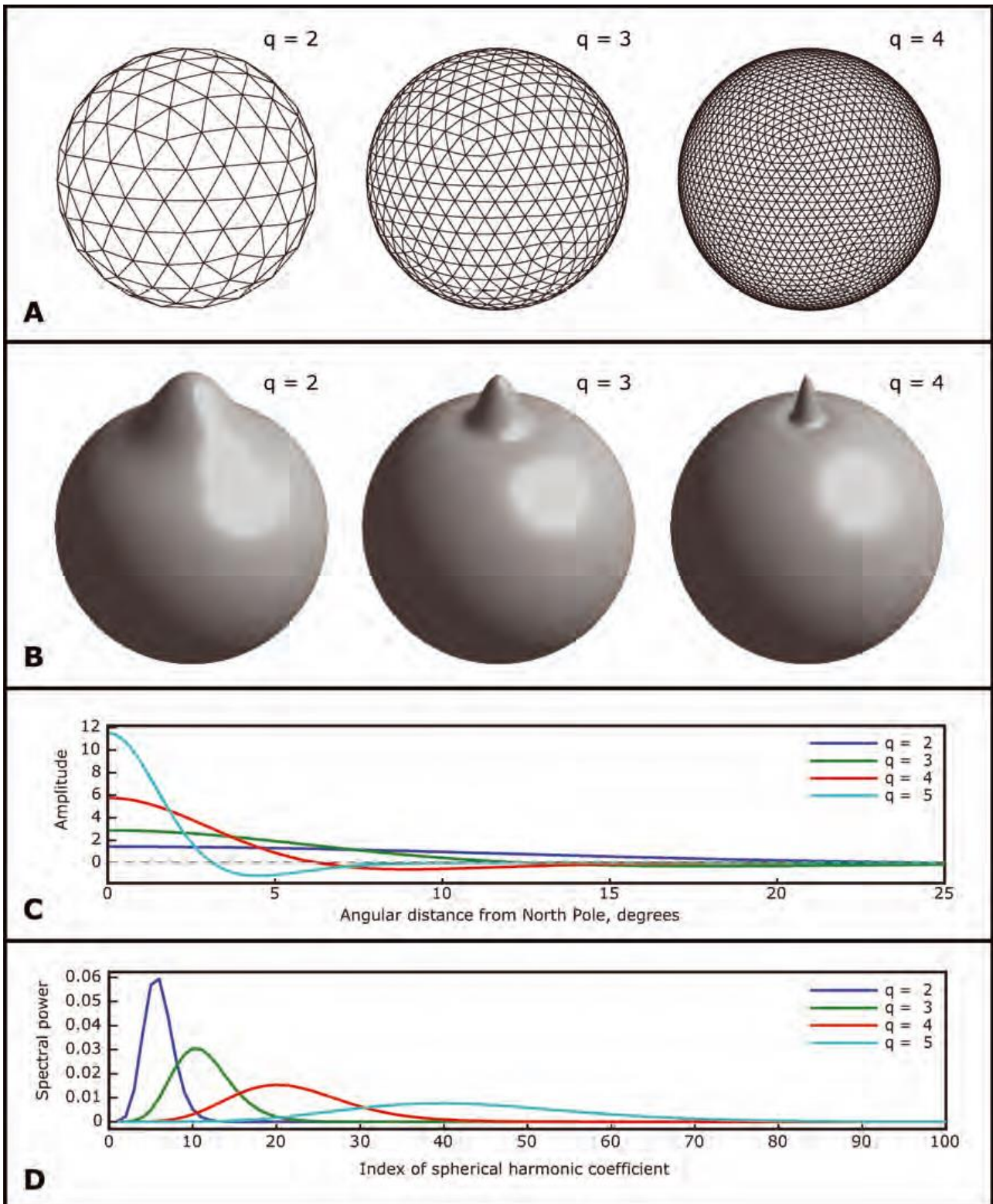


Figure 2.6 – Spherical wavelet frame functions. (a) Triangulated spherical grids used for determining the locations for the centres of the spherical wavelet frame functions. From left- to right-hand side are grids for orders $q = 2$ (162 vertices), $q = 3$ (642 vertices) and $q = 4$ (2562 vertices). (b) Three different scales of a DOG (Difference Of Gaussian) spherical wavelet centred at the North Pole. (c) Corresponding profiles of wavelets in (b), for a fixed longitude φ . (d) Corresponding spectra of wavelets in (b). Modified from [Tape et al. \(2009\)](#).

2.1.1.1 The role of the geodetic strain inside of the seismic cycle.

Oscillatory stress loading and relaxation at plate boundaries is known as the earthquake loading, or seismic, cycle (Scholz, 1990). In its simplest form, the seismic cycle can be thought of as a linear elastic system (Fig. 2.7) in which strain accumulation exactly counters the periodic seismic release so that the result of one complete cycle is no net-strain (Reid, 1910). Under this assumption, strain release in the form of earthquakes is periodic and predictable. The crustal deformation phases associated with the steady strain build up and occasional instantaneous ruptures on the simple elastic rebound theory are termed inter-seismic and co-seismic, respectively.

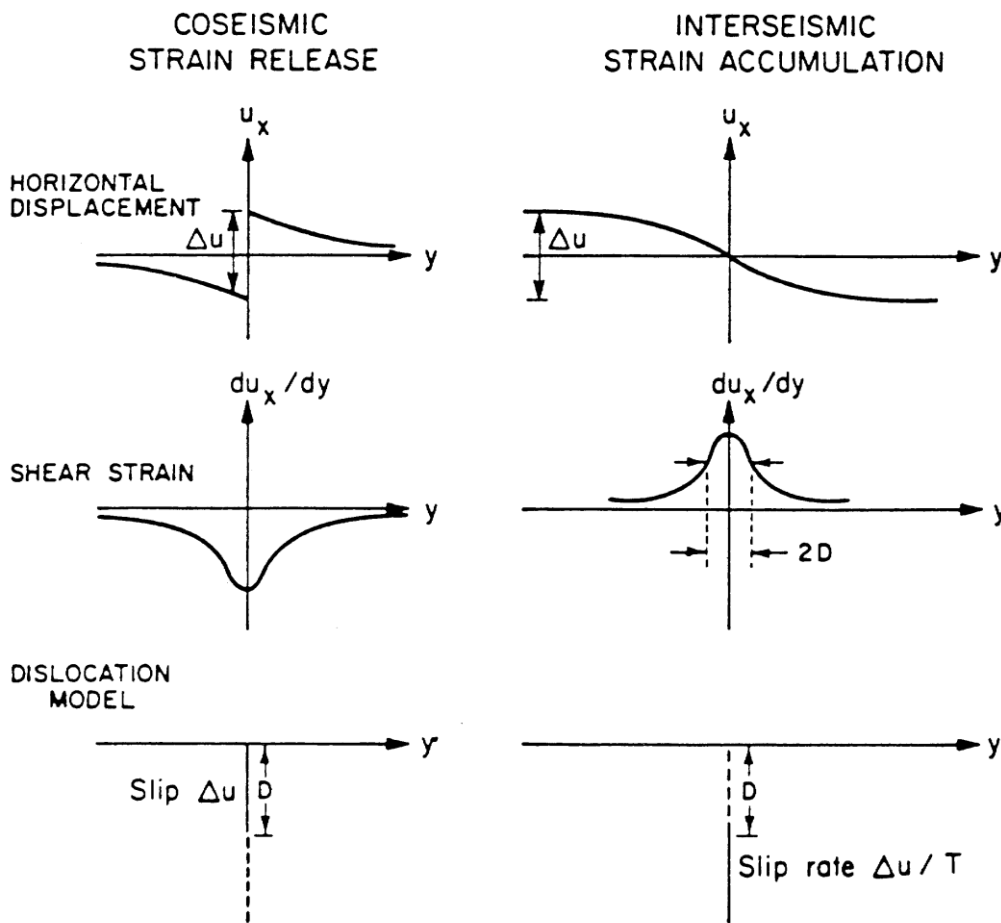


Figure 2.7 – Elastic rebound model. Co-seismic displacements and strain fields are modelled with a slip on a vertical fault with depth, D (left panel). Inter-seismic strain accumulation is modelled with a steady slip rate on the fault below D (right panel). Modified from Thatcher (1986).

The loading cycle is complicated by a post-seismic crustal deformation phase, in which the crust exhibits a transient relaxation back to the steady inter-seismic rate (Scholz, 1990).

Two different types of models have been used to explain the post-seismic rebound that results from co-seismic stress concentration (Fig. 2.8): elastic after slip below seismogenic depth on

the fault plane, and viscoelastic relaxation in the lower crust and/or upper mantle (Molnar, 1992). Both types of models predict deformation patterns at the free surface similar to those observed geodetically, so that the underlying process is still poorly understood.

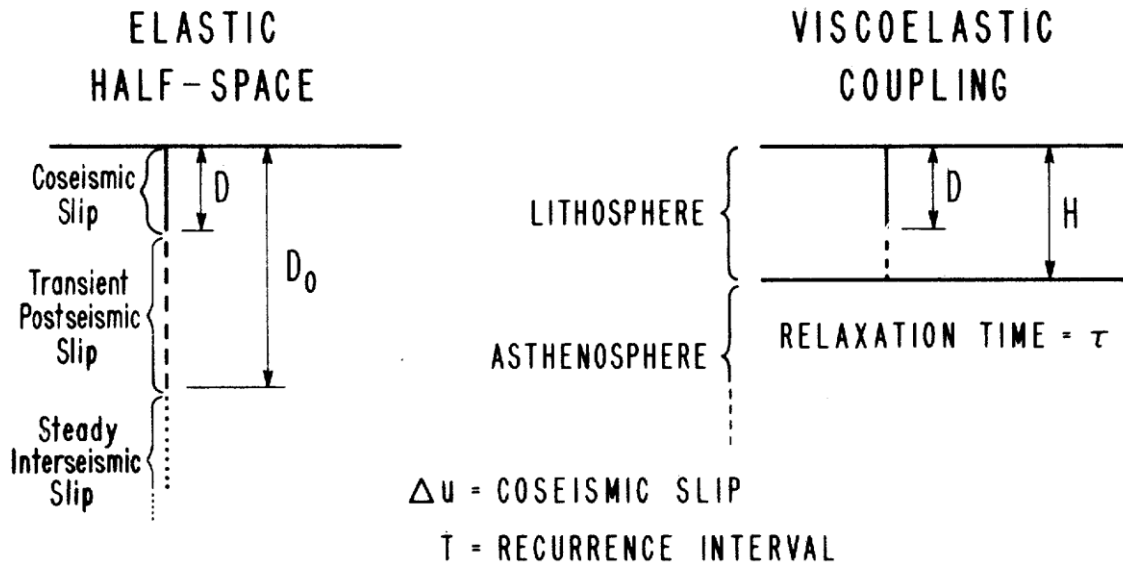


Figure 2.8 – Geometry of elastic half-space (left panel) and viscoelastic coupling (right panel) models of a strike slip faulting. Modified from Thatcher (1983).

Savage (1990) showed that a slip distribution on a long, vertical strike-slip fault embedded in an elastic half-space could produce the same surface deformation as that from a layered Earth model with an elastic plate (lithosphere) over a viscoelastic half-space (asthenosphere). For this simple case, geodetic observation of the surface deformation cannot distinguish between the after slip and viscoelastic earth models. The equivalent slip distribution for this hypothetical fault includes a segment, just below the co-seismic rupture, of rapid post-seismic slip that decays exponentially with time (Savage et al., 1990). The equivalent slip gradually becomes linear with depth on the fault plane.

For real earthquakes, the fault-perpendicular and vertical components of surface displacements predicted by an after slip model differ from those of a viscoelastic earth model. Consequently, geodetic observation should be sufficient to distinguish between the two models.

Models of the earthquake loading cycle based on experimentally derived constitutive relations describing the frictional sliding of rocks suggest that there might also be a pre-seismic deformation phase leading up to the co-seismic phase (Tse and Rice, 1986). While there are a few accounts of unusual localized occurrences prior to certain earthquakes, there has been no geodetic observation of a regional-scale change in crustal deformation associated with the pre-seismic phase of an earthquake cycle.

While many have described one or more of the various crustal deformation phases using different types of geodetic data, there are no accounts of observation of a complete seismic cycle at any one location.

2.1.2 Seismogenic thickness.

In all formulations of the geodetic moment-rate previously exposed (eqs. 2.11-2.15), an important role is played by the seismogenic thickness, since it is proportional to the moment. The thickness of the seismogenic layer limits the depth of faulting and the magnitude of potential large earthquakes. It is a key parameter for seismic hazard since it helps constrain the maximum depth of faulting and the potential earthquake magnitude, and it can predict the timing of the next failure (Nazareth and Hauksson, 2004). To achieve robust depth estimates, most studies have assigned a cut-off depth of seismicity or seismic moment, i.e., the depth above which a given percentage, which has ranged from 90% to 99% (e.g., 90%, Miller and Furlong, 1988; 95%, Williams, 1996; Chiarabba and De Gori, 2016), of the hypocenters or the moment release within a depth column occurs (Fig. 2.9). A different approach takes into account the 99% limit in total seismic moment. Although the choice of this percentage is related to the amount and quality of locations, the 90% value is widely used in seismic hazard (e.g., Nazareth and Hauksson, 2004; Pancha et al., 2006; Stein, 2008; Smith-Konter et al., 2011).

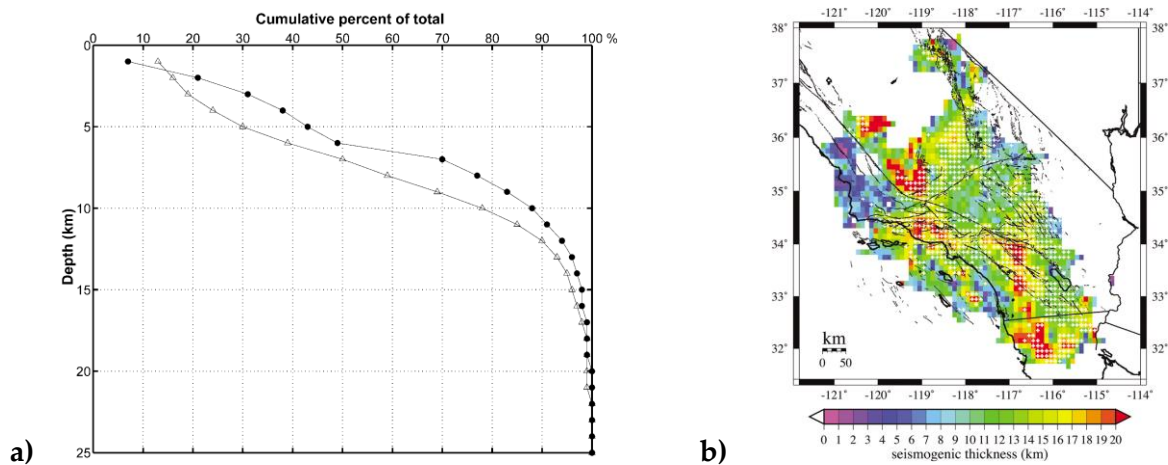


Figure 2.9 - a) Depth distribution of earthquakes within Nevada (white triangles) and Utah (black circles) from Pancha et al. (2006). b) Smoothed seismogenic thickness for all regional bins from Nazareth and Hauksson (2004).

2.2 Seismic Moment.

The seismic moment tensor is the characteristic contribution from an earthquake to seismic rock flow. The rate of seismic deformation is defined to be the sum of the tensors of the seismic moments of earthquakes per unit time in a unit volume of a seismic zone (Kostrov, 1974). So, according to Kostrov (1974), the scalar seismic moment-rate can be estimated by adopting the moment summation approach of:

$$M_{seis}^{\dot{}} = \frac{1}{\Delta T} \sum_{n=1}^N M_{seis}^{(n)} \quad (2.26)$$

where

- N is the number of events occurring during a given time interval ΔT (yr) in the volume $A \cdot H_s$ (with A , the surface area and H_s , the seismogenic thickness);
- M_{seis} (N m) is the scalar seismic moment of the n^{th} earthquake from the N total earthquakes.

Looking at [eq. \(2.26\)](#), it is clear that the more temporally homogeneous is the distribution of the magnitudes falling into the investigated area, the more the Kostrov seismic moment-rate estimation will be accurate. So, chosen a time interval in which each investigated area (with a certain associated value of geodetic moment-rate) is subdivided, it can be useful to calculate the moving average of the seismic moment-rate of Kostrov at several time windows in a timeline ([Middleton et al., 2018](#)), in order to study its distribution over time within each specific source zone. This timeline allows also identifying span times (within each source zone) where there is a mismatch between the seismic and the previously estimated geodetic moment-rates ([Fig. 2.10](#)).

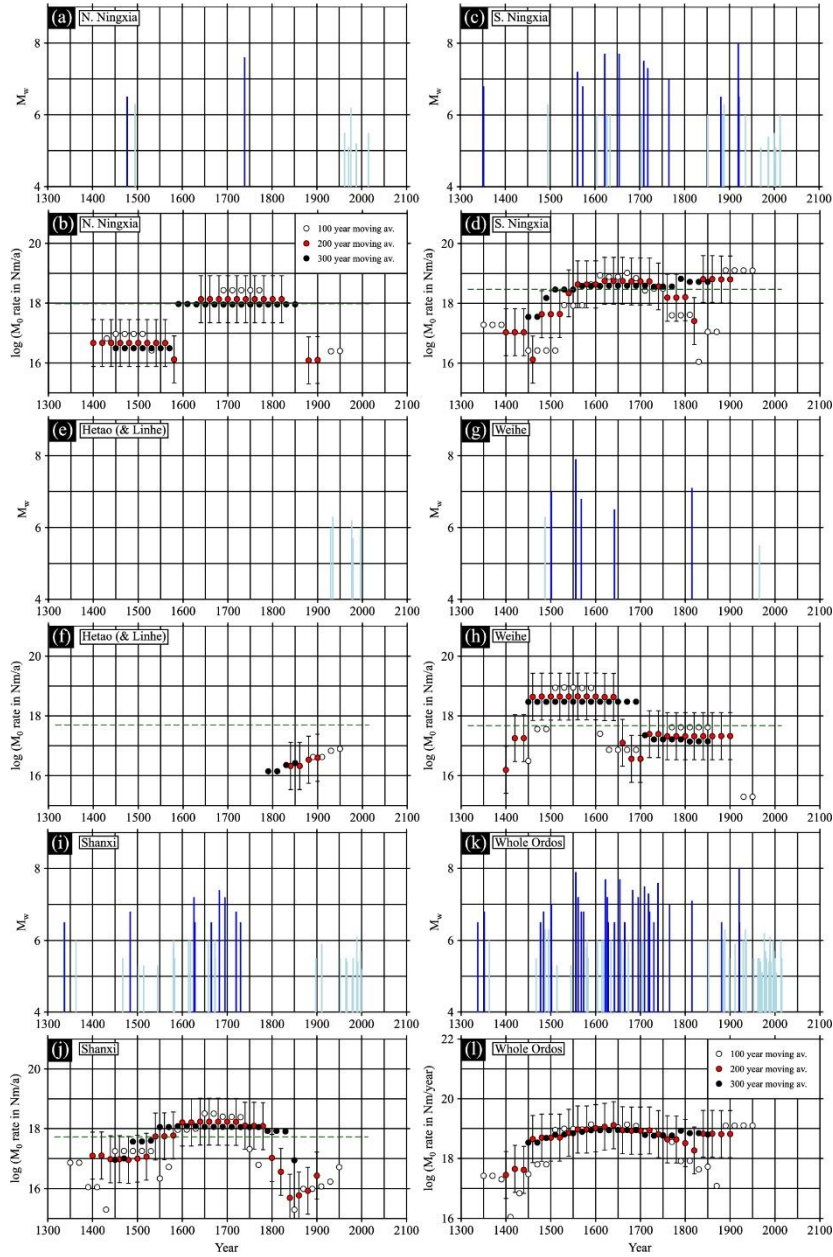


Figure 2.10 – (a) Plot of magnitude (M_w) against time for historical earthquakes with $M_w > 5$ in northern Ningxia (China) over the last 700 yr. Earthquakes with $M_w \geq 6.0$ are shown in darker blue. (b) Moving averages of the log of the seismic moment-rate (in Nm a^{-1}) for the last 700 yr, calculated every 20 yr. White dots show 100 yr moving average; red dots show 200 yr moving average; black dots show 300 yr moving average. Error bars, based on the assumption that values of M_w are known to the nearest ± 0.3 magnitude units, are shown for the 200 yr moving average. Dashed green line shows the log of the geodetic moment-rate, extrapolated over the period from 1315 to 2015. (c) and (d) Equivalent plots for Southern Ningxia. (e) and (f) Equivalent plots for the Hetao and Linhe Grabens. (g) and (h) Equivalent plots for the Weihe Graben. (i) and (j) Equivalent plots for the Shanxi Grabens. (k) and (l) Equivalent plots for all margins of the Ordos Plateau. Modified from [Middleton et al. \(2018\)](#).

Even for the seismic moment-rate, several formulations were successively proposed. A few years later, [Molnar \(1979\)](#) proposed the following methodology to take into account the seismic moment released by earthquakes with a seismic moment $M_{seis} < M_{seis(max)}$:

$$M_{seis}^{\cdot} = \frac{A}{1-B} M_{seis(max)}^{1-B} \quad (2.27)$$

with

$$A = 10^{(a + \frac{bd}{c})} \quad (2.28)$$

$$B = \frac{b}{c}$$

where

- the coefficients a and b represent the measure of the annual level of seismicity and the ratio between the number of small and large earthquakes, respectively, of the [Gutenberg and Richter \(1956\)](#) recurrence relation ([Fig. 2.11](#); see [Par. 2.2.2](#)):

$$\log N_M = a - bM \quad (2.29)$$

and are strictly related to magnitude values of the instrumental catalog;

- c and d are the coefficients of the moment magnitude (M) – seismic scalar moment (M_{seis}) relation, according to [Hanks and Kanamori \(1979\)](#):

$$\log M_{seis} = cM + d \quad (2.30)$$

- $M_{seis(max)}$ is the maximum seismic moment for the study area.

The seismic moment-rate can be calculated also by adopting a truncated cumulative Gutenberg–Richter distribution ([Hyndman and Weichert, 1983](#)), which is obtained by integrating the cumulative truncated Gutenberg-Richter distribution up to a maximum magnitude value ([Fig. 2.11](#)):

$$M_{seis} = \varphi \frac{b}{(c-b)} 10^{[(c-b)M_{max} + a + d]} \quad (2.31)$$

where

- M_{max} is the magnitude of the largest earthquake that could occur within the investigated seismogenic source zone, and its value has been estimated on the basis of available historical and instrumental seismic catalogs (for more details see [Par. 2.2.1](#));
- φ is an asymmetric correction for the stochastic magnitude - moment relation. Taking into account an average error of 0.2 on magnitudes, its value is equals to 1.27 ([Hyndman and Weichert, 1983](#));
- a and b are the coefficients of [eq. \(2.29\)](#);
- c and d are the coefficients of [eq. \(2.30\)](#);
- N_M is the cumulative annual number of earthquakes with magnitude equal to or greater than a specific magnitude value M for each seismogenic source zone.

In this thesis, the used instrumental catalogs refer to different scales, which should ideally be converted into moment magnitude (M_w) before computing eq. (2.29).

Another formulation of the truncated Gutenberg-Richter distribution can be found in [Mazzotti and Adams \(2005\)](#):

$$N(m) = N_0 \exp(-\beta m) \{1 - \exp[-\beta(M_{max} - m)]\}, \quad m < M_{max} \quad (2.32)$$

$$N(m) = 0, \quad m \geq M_{max}$$

where

- $N(m)$ is the cumulative number of earthquake of magnitude m and larger;
- M_{max} is the maximum magnitude assumed for the given source zone.

The intercept a and the slope b of the density recurrence function of eq. (2.32) are calculated as follows:

$$a = \log_{10} N_0 \quad (2.33)$$

$$b = \frac{\beta}{\ln 10}$$

This thesis mainly focused on seismic moment-rate estimations from the truncated Gutenberg-Richter distribution (eqs. 2.31-2.32). However, in order to test sensitivity on achieved results, additional computations by taking into account the Kostrov summation approach and using a catalog including all earthquakes with magnitude values equal or greater than 4.5 reported in the instrumental and the historical ones have been performed.

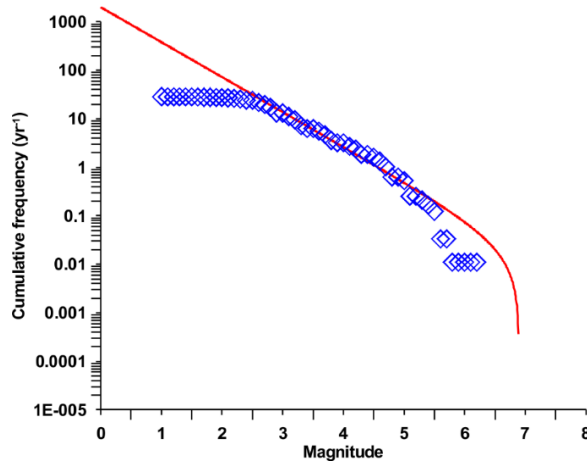


Figure 2.11 - Examples of cumulative frequency–magnitude distributions (blue diamonds) of earthquakes. The red line represents the truncated Gutenberg–Richter function. Modified from [Palano et al. \(2018\)](#).

2.2.1 Maximum Magnitude Estimation.

The maximum magnitude value (M_{max}) is defined as the upper limit of earthquake magnitude for a given region and is synonymous with the magnitude of the largest possible earthquake (Kijko and Singh, 2011). It assumes a well-defined cut-off magnitude at a maximum magnitude value, so that, by definition, no earthquakes are to be expected with magnitude exceeding M_{max} . It is very important to point out that the estimation of this parameter has a strong impact on the evaluation of the seismic moment-rate according to Hyndmann and Weichert (1983) formulation, reported in eq. (2.19). Just think that an increase of 1 magnitude unit leads to an increase of the seismic moment-rate by a factor of about 5.4 (Mazzotti et al., 2011).

Different procedures with the aim of estimate the maximum magnitude value for a region are available in literature. For example, a first simple method to estimate the maximum magnitude value can be adding 0.5 to the largest earthquake in the historical catalog of the investigated region (Kijko and Graham, 1998). However, this method may be very limited if a significant historical record for that area is not available. A second method can be found in scaling relations between the length of the fault and the maximum earthquake (Wells and Coppersmith, 1994; Leonard, 2010):

$$M_{max} = x + y \cdot \log_{10}(SRL) \quad (2.34)$$

where

- x and y are the regression coefficients;
- SRL (km) is the surface rupture length of the fault (Fig. 2.12).

Unfortunately, this second method has limitations too. Unlike the previous one, it can be applied where there are no historical data, but several problems come with deciding on whether, and how, to divide the fault up into segments. A third method for estimate the maximum magnitude value is using statistical approaches. For instance, the tool developed by Kijko and Singh (2011) uses twelve different statistical procedures. Unlike the previous two methods, this toolbox provides reliable results even under several data restrictions (magnitude of completeness and temporal length of the catalogs, magnitude distribution and uncertainties, number of earthquakes, etc.).

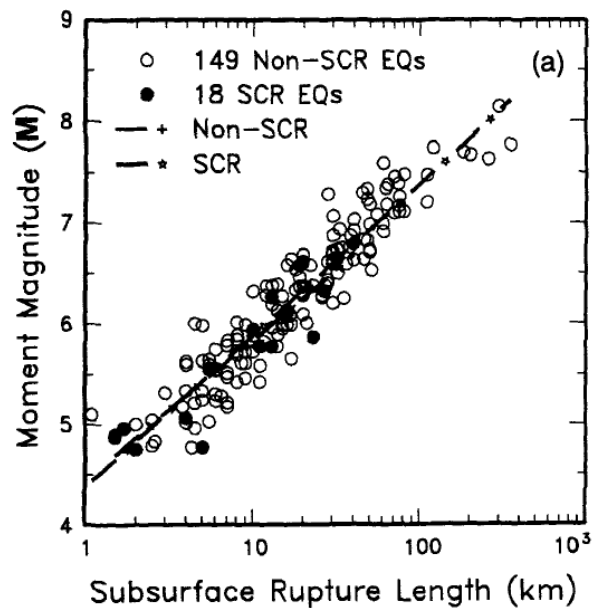


Figure 2.12 – Regression of surface rupture length on magnitude (M). Modified from Wells and Coppersmith (1994).

2.2.2 Gutenberg-Richter parameters and magnitude of completeness.

The magnitude–frequency recurrence relationship by Gutenberg and Richter describes the seismic activity within a certain seismic source. The coefficients a - and b -value characterize the seismicity within the source. The a -value, the so called “productivity”, indicates the seismic-rate of the investigated region, that depends on the size of the area, the length of the observation period, the largest seismic magnitude (Han et al., 2015). On the other side, the b -value provides the rate of fall in the frequency of events with low to large magnitude earthquakes ratio, regardless of population size. The latter parameter value typically lies between 0.6 and 1.5, with a global mean of ~ 1.0 (Frohlich and Davis, 1993). Its value has served as a kind of tectonic parameter: range values of 1.0-1.8, 0.7-1.0, 0.4-0.7 can be associated to oceanic ridge, interplate and intraplate seismicity, respectively (El-Isa and Eaton, 2014; Scholz, 2015). The b -value depends on different factors, such as material heterogeneity (Mogi, 1962) or applied shear stress (Scholz, 1968). Low values, that is a high proportion of major earthquakes, are inferred to indicate areas of crustal homogeneity and high stress, whereas, high values indicate crustal heterogeneity and low stress (Mogi, 1962; Mori and Abercrombie, 1997), and that a smaller fraction of the total earthquakes occurs at higher magnitudes (Han et al., 2015).

Several statistical techniques could be used to estimate these key parameters, and consequently, the best magnitude of completeness value: the Maximum Likelihood Estimation (MLE; Weichert, 1980; Han et al., 2015), the Least Square Regression (LSR; Han et al., 2015) and the Robust Fitting Method (RFM; Han et al., 2015). In the MLE method, the previously mentioned parameters are estimated as follows:

$$b = \frac{1}{\ln(10) \cdot (\mu_M - M_{thresh})} \quad (2.35)$$

$$a = \log_{10} \left(\frac{M}{\Delta T} \right) + b \cdot M_{thresh}$$

where

- M are the magnitudes of the analysed dataset;
- μ_M is the sampling average of the magnitudes;
- M_{thresh} is the threshold magnitude which usually corresponds to the magnitude of completeness (M_c) of the catalog, i.e., the value below which the number of detected earthquakes is considered incomplete (Rydelek and Sacks, 1989; Wiemer and Wyss 2000; Han et al., 2015);
- ΔT (yr) is the temporal window covered by the catalog.

Of course, each of the aforesaid methods has some limitations and they sometimes provide different results, even if for large data sets they usually give closer results. The MLE method is widely used but it puts more weight on smaller magnitudes, and its sensitivity to the completeness magnitude value, M_c , is very wide. Consequently, the *b-value* estimated with MLE may have a great deviation from the real value when M_c is not determined accurately. On the other hand, the sensitivity of MLE to the occurrence of events with large magnitude is accurate, since large events gain far smaller weight in the *b-value* calculation. Therefore, the *b-value* as a function of time from MLE could be reputed as an earthquake precursor (Han et al., 2015).

Regarding the LSR method, it works well under some circumstance, such as estimating the probability of the largest magnitude of earthquakes, but it shows significant bias under relatively common conditions. In fact, because of the LSR is affected greatly by the outliers, the fitting line always has a great deviation from the real linearity relation and so it may not provide reliable results.

Finally, the using of the RFM method comes from the necessity to minimize the influence of the outliers with LSR method. In fact, in RFM method the weight given to each data point depends on how far the point is from the linear fitted line. Points near the line get full weight, whereas points far from the line get reduced weight. As a result, RFM can not only provide a stable and reliable *b-value* without the strict requirement for the best magnitude of completeness value like MLE method, but also it has a good sensitivity to the occurrence of earthquakes with large magnitudes, such that it can be considered an earthquake precursor (Han et al., 2015).

2.3 Seismic Coupling Coefficient (SCC).

Ideally, the geodetically measured moment-rate of a crustal volume affected by seismogenic faults is balanced by the one seismically released in a time interval equals to the seismic cycle of the volume. Such a simple comparison is based on the following formulation provided by Kostrov (1974):

$$2 \mu V \dot{\epsilon}_{ij} = \left(\frac{1}{T} \right) \sum_{n=1}^m M_n \quad (2.36)$$

The formulation in eq. (2.36) linearly links the moment-rate geodetically measured (on the left; Fig. 2.13) to the one seismically measured (on the right; Fig. 2.1).

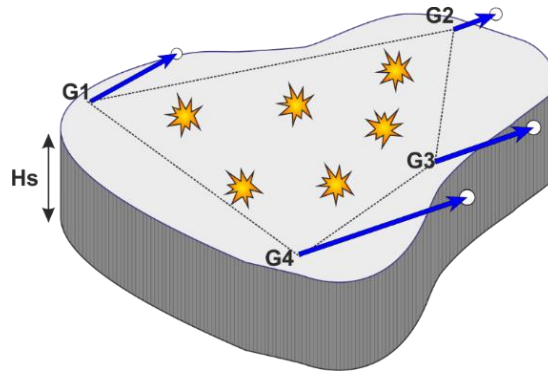


Figure 2.13 – The geodetic moment defined as the product between the shear modulus, μ , the deforming volume, V , and the strain measured at the surface, ϵ_{ij} (Kostrov, 1974).

Considering that the geodetic moment-rate is a measure of both elastic and anelastic loading rates, while the seismic moment-rate is a measure of the elastic unloading rate, the simple seismic versus geodetic moment-rates ratio, expressed as a percentage, has a theoretical range of 0-100% (Palano et al., 2018; Sparacino et al., 2020; Palano et al., 2020; Sawires et al., 2021; Sparacino et al., 2022). The SCC can be written as follows:

$$SCC = \frac{M_{seis}}{M_{geod}} \cdot 100 \quad (2.37)$$

A low SCC indicates an apparent seismic moment deficit, which suggests either a proportion of aseismic deformation (i.e., ongoing unloading by creep and other plastic process) or accumulating strain not released by seismicity (i.e., elastic storage). The more SCC value is close to 100%, the more the larger part of the deformation is released by brittle deformation, i.e., through earthquakes. SSC values greater than 100 can be attributed to additional factors. They are related to available historical and instrumental seismic information (e.g., completeness and temporal length of the catalogs, magnitude distribution and uncertainties, seismic cycle, etc.), as well as the reliability of the geodetic data (time span inadequate to sample both the seismic and the aseismic spectrum, velocity uncertainties, density of stations, long-term deformation transient, etc.), which may strongly affect the moment-rates estimations.

Seismic and geodetic moment-rates comparison appears very useful for understanding fault behavior (seismic vs aseismic), as well as to highlight regions showing gaps in seismic cycle, with obvious implications on seismic hazard assessment of regions subjected to relevant tectonic deformation (essentially for time-dependent seismic hazard assessments). Despite the variety of methods, the outcomes typically fall into one of the following categories (Fig. 2.14):

- 1) agreement, within the data uncertainties, between geodetic and seismic moment-rates;
- 2) geodetic moment-rates significantly larger than seismic ones; this is the most common case.

It is well known that geodetically observed strains include both elastic and anelastic

components, and it is difficult to differentiate these two contributions without a priori knowledge of the rheology of the crust investigated (applied geophysics methods may be useful). Because only the elastic strain is responsible for earthquakes, the comparison between geodetic and seismic strain-rates may not be balanced in regions cut by creeping faults or where significant amounts of deformation take place plastically (aseismic crustal deformation). Alternatively, the excess of the geodetic strain-rate can be released through large impending earthquakes. So, apparent discrepancies between moment-rates may occur where the seismic catalogue is incomplete, as in the case where the seismic cycle of the investigated region is longer than the duration of the observation period (under-sampling of the short earthquake catalog);

- 3) seismic moment-rates larger than geodetic ones. This case is rare but possible: seismically estimated strain is larger than geodetically measured shortly after a major earthquake if the time covered by the geodetic data is shorter than the seismic cycle. Moreover, the available geodetic velocities would be related or to a low number of GPS stations or to a set of GPS stations with a short observation time therefore leading to a not well-constrained estimation of the geodetic strain-rate, resulting in the above mentioned discrepancy.

Thus, constraining the mismatch between the geodetic and the seismic strain-rates requires a high level of accuracy and spatially (as well as temporally) dense and extensive geodetic observations, coupled with the most complete possible seismic-event catalog covering a long time interval.

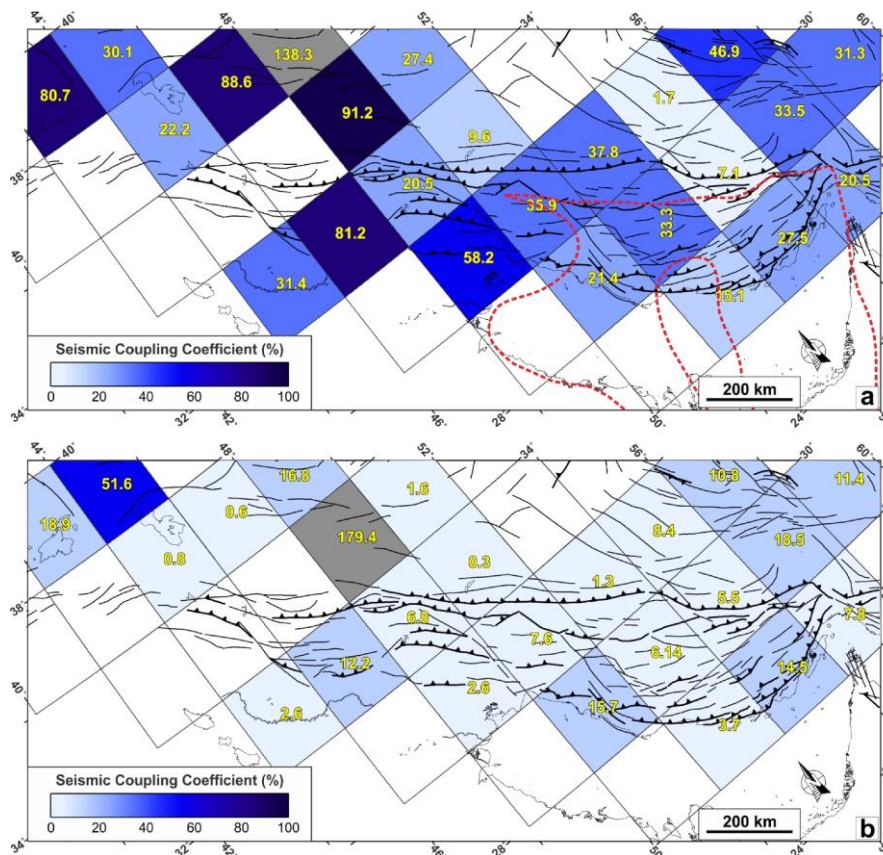


Figure 2.14 – Estimated SCC for the Zagros Fold-and-Thrust collisional belt. (a) SCC from seismic moment-rates derived by the truncated Gutenberg–Richter distribution. (b) SCC from seismic moment-rates derived by the cumulative [Kostrov \(1974\)](#) summation method. Modified from [Palano et al. \(2018\)](#).

3 – A workflow to estimate SCC

In this chapter, the code written in MATLAB program language (<https://it.mathworks.com>) to calculate the ratio between seismic and geodetic moment-rate will be explained.

Suppose that you want to analyse the SCC of a specific region. The aim of the code consists in the creation of a workflow to:

1. acquire and process available seismic data from catalogs and geodetic strain-rates;
2. compute the geodetic moment-rate;
3. compute the seismic moment-rate;
4. compute the SCC.

A lot of work is usually required to the computation of seismic and geodetic moment-rates because of the different formats of input data and the needing of several iterative steps aimed at the determination of some parameters as the seismogenic thickness and the maximum magnitude. To speed up the entire process, a *Matlab*-based workflow has been developed. The main aims of this workflow can be summarized as:

- having a unique user-friendly and flexible program (to do all the work);
- reducing the active iteration of the user to speed up the process;
- having the possibility to test several configuration of the parameters;
- having the possibility to perform only a specific part of the workflow, without necessarily running all the code.

The consequent utilities will be:

- changing input catalogs and tolerance parameters;
- changing grid dimension and position;
- changing of top and bottom cut-off depths (to take into accounts possible problems related to human-induced earthquakes, e.g. explosion quarry, or to regions with active phenomena, e.g. where seismicity is related to deep process as an active subduction, or to the automated registration process of earthquakes, e.g. events with depth equals to 0, etc.);
- testing several regression methods for the best magnitude of completeness value.

First, the single codes have been developed. In a second step, the assemblage between them has been done (Fig. 3.1). In the following paragraphs, the input files necessary to the workflow will be described, followed by the most important single codes. A summary scheme of the workflow is showed in Fig. 3.2.

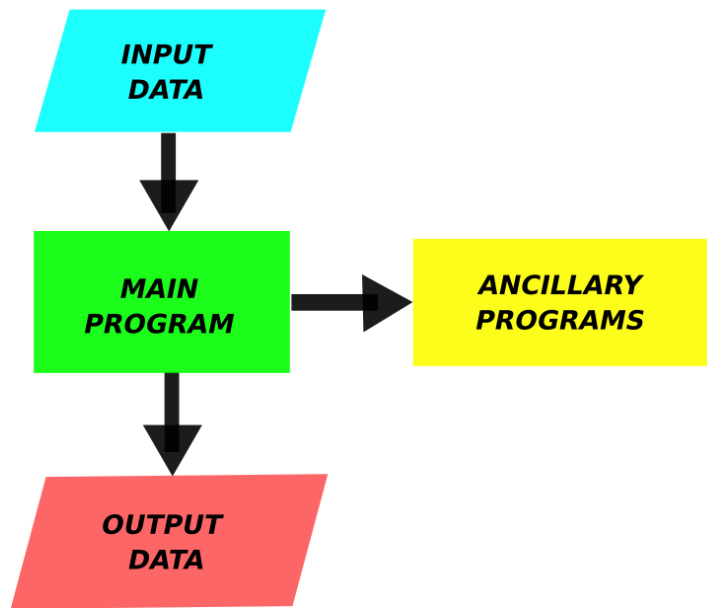


Figure 3.1 – The core of the workflow. The input data: seismic catalogs, geodetic strain-rates. The main program: a MATLAB program language (<https://it.mathworks.com>) code, which is used by the user to control everything. Ancillary programs: several codes able to do something. Output data: several output results.

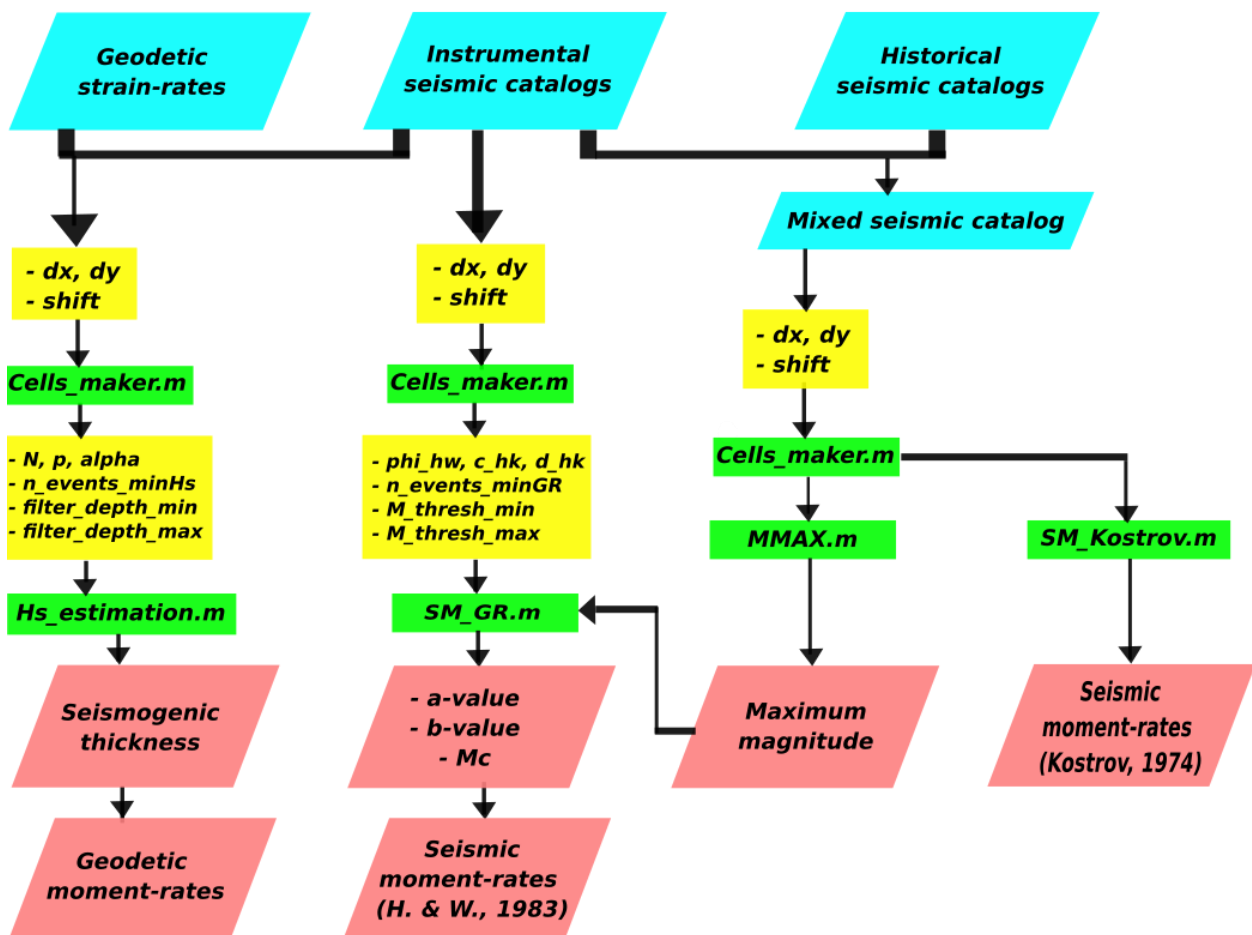
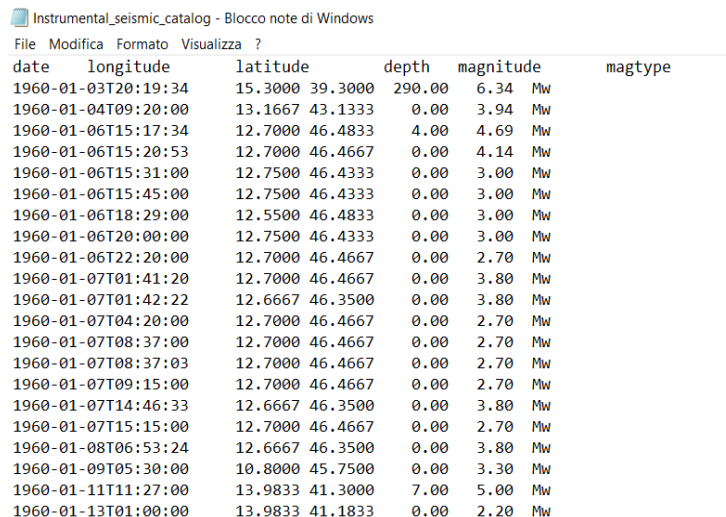


Figure 3.2 – A summary of the workflow. Input data, main parameters, programs, output data are reported in cyan blue, yellow, green and red, respectively.

3.1 Input and output files.

The seismic catalogs (the instrumental and the historical one) files must be structured with a header line as shown in Fig. 3.3. The file, formatted as in ZMAP software (Wiemer, 2001), consists of six columns (date and time of the event, longitude, latitude, depth, magnitude and magnitude type) and each header space must correspond to a tab. The date and time of the event must be written “YYYY-MM-DDThh:mm:ss”, where “YYYY-MM-DD” stands for the year, month and the day, respectively, and “Thh:mm:ss” for time, expressed in hours, minutes and seconds, respectively, as seen from the first row. This format has been chosen so that a preliminary analysis of the catalogs can be done with ZMAP software (Wiemer, 2001). About the historical seismicity catalog, if the month, day, time or depth are missing, they will be automatically set to 01, 01, 00:00:01, respectively, with a specific subroutine called *modify_datetime.m*. This subroutine corrects the date format of historical catalog events without any available month, day or time information. In order to merge two or more different seismic catalogs (they can be instrumental or historical) and removing the duplicate events, another specific subroutine was made, called *merged_catalogs.m*. This subroutine is based on a particular ZMAP software (Wiemer, 2001) utility called “Combine catalogs”, in which there is the option “Remove duplicates” as a function of four tolerance parameters related to the time, distance, magnitude and depth of the events. With this subroutine, the best tolerance parameters values, able to stabilize the number of events of the merged catalog, are tested (until the number of the duplicate events removed is less than 0.01% of the total), and then the subroutine stopped. Therefore, this subroutine combines two or more seismic catalogs removing the duplicate events as a function of the aforesaid tolerance parameters, and, in this way, different configuration can be tested in few minutes.



date	longitude	latitude	depth	magnitude	magtype
1960-01-03T20:19:34	15.3000	39.3000	290.00	6.34	Mw
1960-01-04T09:20:00	13.1667	43.1333	0.00	3.94	Mw
1960-01-06T15:17:34	12.7000	46.4833	4.00	4.69	Mw
1960-01-06T15:20:53	12.7000	46.4667	0.00	4.14	Mw
1960-01-06T15:31:00	12.7500	46.4333	0.00	3.00	Mw
1960-01-06T15:45:00	12.7500	46.4333	0.00	3.00	Mw
1960-01-06T18:29:00	12.5500	46.4833	0.00	3.00	Mw
1960-01-06T20:00:00	12.7500	46.4333	0.00	3.00	Mw
1960-01-06T22:20:00	12.7000	46.4667	0.00	2.70	Mw
1960-01-07T01:41:20	12.7000	46.4667	0.00	3.80	Mw
1960-01-07T01:42:22	12.6667	46.3500	0.00	3.80	Mw
1960-01-07T04:20:00	12.7000	46.4667	0.00	2.70	Mw
1960-01-07T08:37:00	12.7000	46.4667	0.00	2.70	Mw
1960-01-07T08:37:03	12.7000	46.4667	0.00	2.70	Mw
1960-01-07T09:15:00	12.7000	46.4667	0.00	2.70	Mw
1960-01-07T14:46:33	12.6667	46.3500	0.00	3.80	Mw
1960-01-07T15:15:00	12.7000	46.4667	0.00	2.70	Mw
1960-01-08T06:53:24	12.6667	46.3500	0.00	3.80	Mw
1960-01-09T05:30:00	10.8000	45.7500	0.00	3.30	Mw
1960-01-11T11:27:00	13.9833	41.3000	7.00	5.00	Mw
1960-01-13T01:00:00	13.9833	41.1833	0.00	2.20	Mw

Figure 3.3 – Input seismic catalog file with ZMAP software (Wiemer, 2001) format.

At this moment, the geodetic strain-rate is calculated with three different software (Par. 2.1), and so it is an input data file for the workflow. The workflow has been optimized in order to read each of the three different input file, which must be specified at the beginning of the code through the parameter *strain_method* (see Par. 3.4). In the first case, the strain-rate is calculated with VISR

software (Shen et al., 2015). In this case, the header consists of two rows and twenty-seven columns: station, longitude, latitude, the observation and interpolation parameters, the spatial constant of smoothing (i.e., “dis.”), the weight of smoothing, the chi-square and the number of sites (Fig. 3.4).

14.500	36.000	-1.8	0.3	4.5	0.3	0.00	-6.1	19.5	1.8	37.7	7.1	19.5	-5.7	10.2	6.1	29.4	-10.0	25.7	8.0	19.5
14.500	36.250	-1.8	0.3	4.4	0.3	0.00	-6.0	9.7	2.0	18.7	7.0	9.7	-5.7	5.2	6.2	15.0	-9.8	12.4	8.0	9.7
14.750	36.250	-1.8	0.3	4.6	0.3	0.00	-5.3	9.3	2.7	17.8	6.2	9.3	-5.5	5.3	6.0	14.2	-9.8	12.0	7.4	9.3
14.500	36.500	-1.8	0.2	4.2	0.2	0.00	-4.5	3.9	5.6	7.3	4.9	3.9	-5.2	2.7	7.5	6.8	-7.1	3.7	7.3	3.9
14.500	36.750	-1.8	0.2	4.1	0.2	0.00	-4.0	2.8	6.3	4.9	4.7	2.8	-5.0	2.7	8.0	4.8	-6.7	2.8	7.3	2.8
14.750	36.750	-1.7	0.2	4.3	0.2	-0.00	-3.9	3.1	6.0	5.5	4.7	3.1	-5.2	2.8	7.7	5.1	-6.9	3.4	7.3	3.1
15.000	36.750	-1.6	0.2	4.5	0.2	-0.00	-2.9	6.6	4.5	9.4	4.3	6.6	-7.8	9.3	5.8	8.9	-9.1	9.7	7.5	6.6
12.250	37.000	-2.1	0.3	3.3	0.3	-0.00	-5.2	14.5	-87.3	22.7	63.4	14.5	-57.1	17.9	-7.1	7.1	-137.4	28.0	65.1	14.5
12.500	37.000	-2.1	0.3	3.5	0.3	-0.00	-2.5	6.8	-20.7	9.6	14.3	6.8	-16.5	9.7	-4.2	4.3	-33.0	13.0	14.4	6.8
14.000	37.000	-2.2	0.2	3.7	0.2	0.00	-1.5	3.1	8.3	4.3	4.8	3.1	-1.7	4.5	10.2	5.1	-3.6	3.7	6.9	3.1
14.250	37.000	-1.9	0.2	3.7	0.2	-0.00	-5.1	5.0	6.1	5.3	5.0	5.0	-3.5	8.4	8.2	7.2	-5.6	6.8	6.9	5.0
14.500	37.000	-1.8	0.2	3.9	0.2	-0.00	-5.8	4.4	3.6	5.3	4.3	4.4	-5.5	7.1	5.3	6.5	-7.2	6.0	6.3	4.4
14.750	37.000	-1.7	0.2	4.2	0.2	0.00	-3.7	4.9	5.6	6.8	3.0	4.9	-8.0	6.9	6.2	7.0	-8.7	6.7	7.4	4.9
15.000	37.000	-1.6	0.2	4.3	0.2	-0.00	-1.9	5.5	7.9	8.3	4.4	5.5	-10.4	7.2	8.9	7.9	-11.4	7.7	10.2	5.5
15.250	37.000	-1.3	0.2	4.4	0.2	0.00	1.4	3.9	10.0	6.3	6.6	3.9	-8.3	4.8	12.1	5.8	-10.4	5.3	11.3	4.0
12.250	37.250	-1.4	0.3	2.7	0.3	0.00	-4.6	7.9	-25.6	12.5	16.1	7.9	-14.9	9.6	-3.3	3.7	-37.2	15.3	17.0	7.9
13.500	37.250	-2.5	0.2	3.4	0.2	-0.00	5.9	3.2	7.1	3.7	10.0	3.2	6.1	5.2	16.7	5.3	-3.4	3.5	10.0	3.2
13.750	37.250	-2.5	0.2	3.5	0.2	0.00	13.9	6.4	21.7	7.7	4.5	6.4	-1.1	10.1	22.6	8.4	-2.0	9.6	12.3	6.4
14.000	37.250	-2.0	0.2	3.4	0.2	0.00	4.8	5.5	16.7	6.6	5.2	5.5	0.6	8.8	18.2	7.2	-1.0	8.4	9.6	5.5
14.250	37.250	-1.9	0.2	3.6	0.2	0.00	-3.7	4.5	5.5	5.2	7.3	4.5	0.7	7.2	10.8	6.5	-4.6	6.1	7.7	4.5
14.500	37.250	-1.8	0.2	3.9	0.2	0.00	-4.6	3.7	3.9	4.6	5.5	3.7	-0.6	5.8	7.6	5.4	-4.3	5.1	5.9	3.7
14.750	37.250	-1.7	0.2	4.0	0.2	0.00	-0.7	3.8	9.3	5.5	3.6	3.8	-4.7	5.4	10.2	5.5	-5.6	5.4	7.9	3.8
15.000	37.250	-1.4	0.2	4.0	0.2	-0.00	3.9	4.8	17.1	7.6	4.6	4.8	-10.6	5.9	17.8	7.5	-11.4	6.1	14.6	4.8
15.250	37.250	-0.9	0.2	4.1	0.2	0.00	4.7	5.1	15.5	8.6	8.6	5.1	-8.7	5.5	18.2	8.1	-11.5	6.2	14.9	5.1
13.250	37.500	-2.2	0.2	3.4	0.2	-0.00	4.6	4.3	2.3	5.1	13.1	4.3	8.0	6.8	18.5	7.3	-8.2	4.4	13.4	4.3
13.500	37.500	-2.1	0.2	3.6	0.2	0.00	7.7	4.0	4.9	5.3	11.2	4.0	6.5	6.1	16.9	6.7	-5.5	4.5	11.2	4.0
13.750	37.500	-2.0	0.2	3.6	0.2	0.00	10.4	4.2	12.3	6.1	7.2	4.2	7.1	5.8	17.4	6.4	2.0	5.4	7.7	4.2
14.000	37.500	-1.8	0.2	3.6	0.2	-0.00	5.5	4.3	10.5	6.3	6.5	4.3	10.0	5.9	16.7	5.8	3.7	6.3	6.5	4.3
14.250	37.500	-1.8	0.2	3.9	0.2	0.00	-2.4	3.7	1.2	5.1	8.6	3.7	12.4	5.3	17.1	5.0	-3.4	5.4	10.3	3.7
14.500	37.500	-1.8	0.2	4.1	0.2	0.00	-3.9	3.4	3.3	4.6	6.1	3.4	14.5	4.9	17.2	4.8	0.6	4.8	8.3	3.4
14.750	37.500	-1.6	0.2	4.3	0.2	0.00	0.4	3.5	14.4	5.3	2.8	3.5	14.6	4.8	17.3	5.0	11.7	5.0	2.8	3.5
15.000	37.500	-1.0	0.2	4.1	0.2	0.00	8.2	4.3	34.6	7.1	1.7	4.3	12.4	5.1	34.7	7.1	12.3	5.1	11.2	4.4
15.250	37.500	-0.4	0.2	3.9	0.2	0.00	12.6	4.2	29.3	7.0	0.3	4.2	9.2	4.6	29.3	7.0	9.2	4.6	10.0	4.2
15.500	37.500	-0.0	0.2	3.5	0.2	0.00	17.2	3.6	20.7	5.6	-4.0	3.6	8.3	4.4	21.9	6.2	7.1	3.6	7.4	3.6
12.750	37.750	-1.9	0.2	3.2	0.2	0.00	-0.9	5.9	11.0	8.1	11.7	5.9	16.4	8.5	25.7	8.6	1.8	8.0	12.0	5.9
13.000	37.750	-1.8	0.2	3.4	0.2	0.00	0.3	4.6	5.4	5.8	11.3	4.6	12.3	7.0	20.7	6.6	-3.0	6.2	11.8	4.6
13.250	37.750	-1.8	0.2	3.5	0.2	-0.00	2.6	3.0	2.9	4.4	10.6	3.0	0.6	4.1	12.4	4.6	-8.9	3.9	10.6	3.0

Figure 3.4 – Input geodetic file calculated with VISR software (Shen et al., 2015).

In the second case, the strain is calculated according to Wessel and Bercovici (1998). The header consists of fourteen columns: longitude, latitude, error of the maximum strain, azimuth, error of the minimum strain, azimuth, dilatation, maximum shear, azimuth, rotation, 2nd invariant, maximum error, minimum error, error of the point-force Green function.

In the third case, the strain is calculated with *surfacevel2strain.m* software (Tape et al., 2009). The header consists of fourteen columns as the previous one.

Regarding the output files, the workflow returns a summary *file.csv* (Fig. 3.5) with all estimated parameters (made up by forty-four columns), and four summary figures (Figs. 3.6 - 3.9), one for each SCC calculated with different formulations and methods. About the output parameters, the program will give out, for each cell:

- the longitude (°) and the latitude (°) of the midpoint;
- the minimum and the maximum longitude and the latitude values (°);
- the area (km²);
- the maximum strain value with the relative uncertainties;
- the number of earthquakes;
- the time interval covered by the seismic instrumental catalog (yr);
- the selected maximum magnitude value with the relative uncertainties (*MMAX.m* software, mixed seismic catalog);
- the upper cut-off magnitude for Gutenberg-Richter parameters;
- the maximum magnitude value (seismic instrumental catalog);
- the geodetic moment-rates (N m yr⁻¹);

- the seismogenic thickness (km) with the relative uncertainties (km);
- the seismic moment-rates (N m yr^{-1}) according to [Kostrov \(1974\)](#) both using the seismic mixed catalog and the instrumental one only;
- the magnitude of completeness, the Gutenberg-Richter parameters, the seismic moment-rates (N m yr^{-1}) according to [Hyndman and Weichert \(1983\)](#) and the residuals estimated with MLE, LSR and RFM statistical regression methods;
- the SCC values estimated using the seismic moment-rates according to [Kostrov \(1974\)](#) and to [Hyndman and Weichert \(1983\)](#) with MLE, LSR and RFM statistical regression methods;
- the time interval covered by the mixed seismic catalog (yr);
- the date and the time of the maximum magnitude event (mixed seismic catalog);
- the magnitude ranges between the maximum magnitude value of the cell (using seismic instrumental catalog only) and the magnitude of completeness estimated with MLE, LSR and RFM statistical regression methods, in order to evaluate the goodness of the estimated b -value.

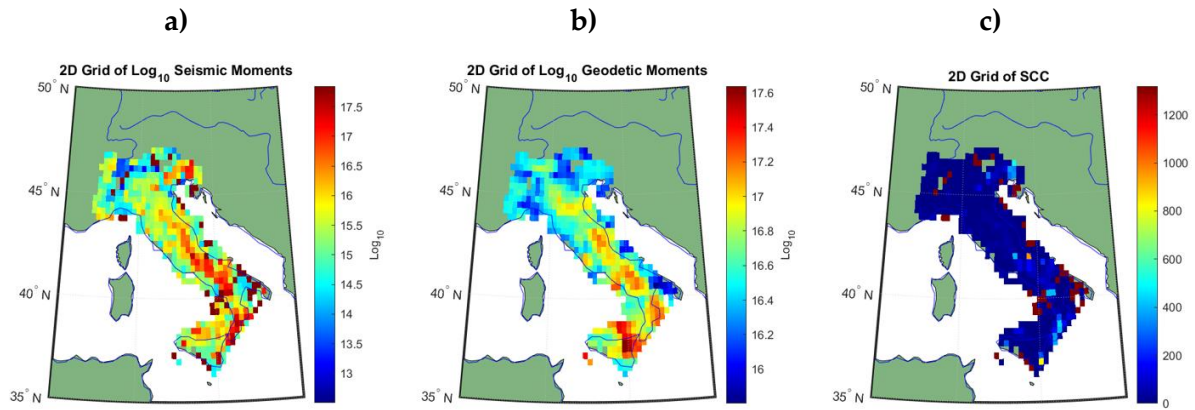


Figure 3.6 – Output figure 1 of the workflow. a) Seismic moment-rates values according to [Kostrov \(1974\)](#). b) Geodetic moment-rates according to [Savage and Simpson \(1997\)](#). c) The SCC values.

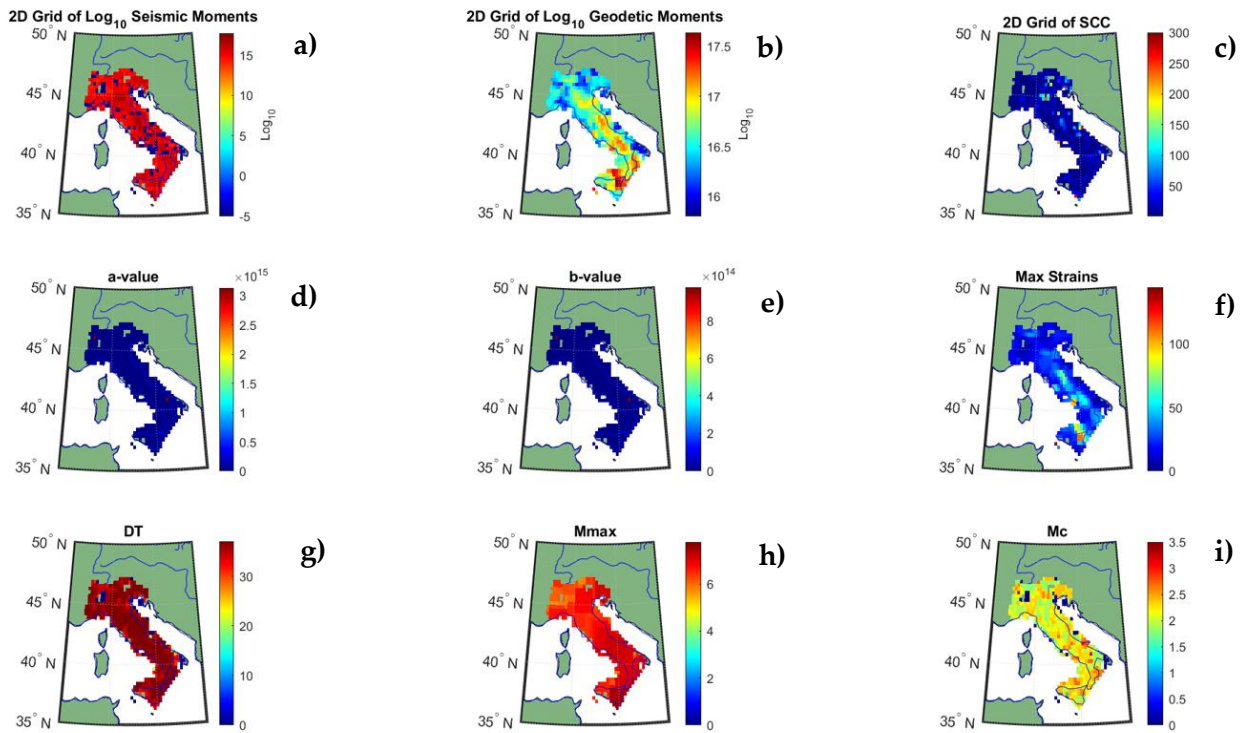


Figure 3.7 – Output figure 2 of the workflow. a) Seismic moment-rates values according to [Hyndman and Weichert \(1983\)](#). The [Gutenberg and Richter \(1956\)](#) parameters have been estimated with MLE statistical regression method. b) Geodetic moment-rates according to [Savage and Simpson \(1997\)](#). c) The SCC values. d) a -value estimated with MLE. e) b -value estimated with MLE. f) Maximum geodetic strain-rates values. g) Time interval of the seismic catalogs. h) Maximum magnitude values M_{max} distribution. i) The magnitude of completeness M_c values estimated with MLE.

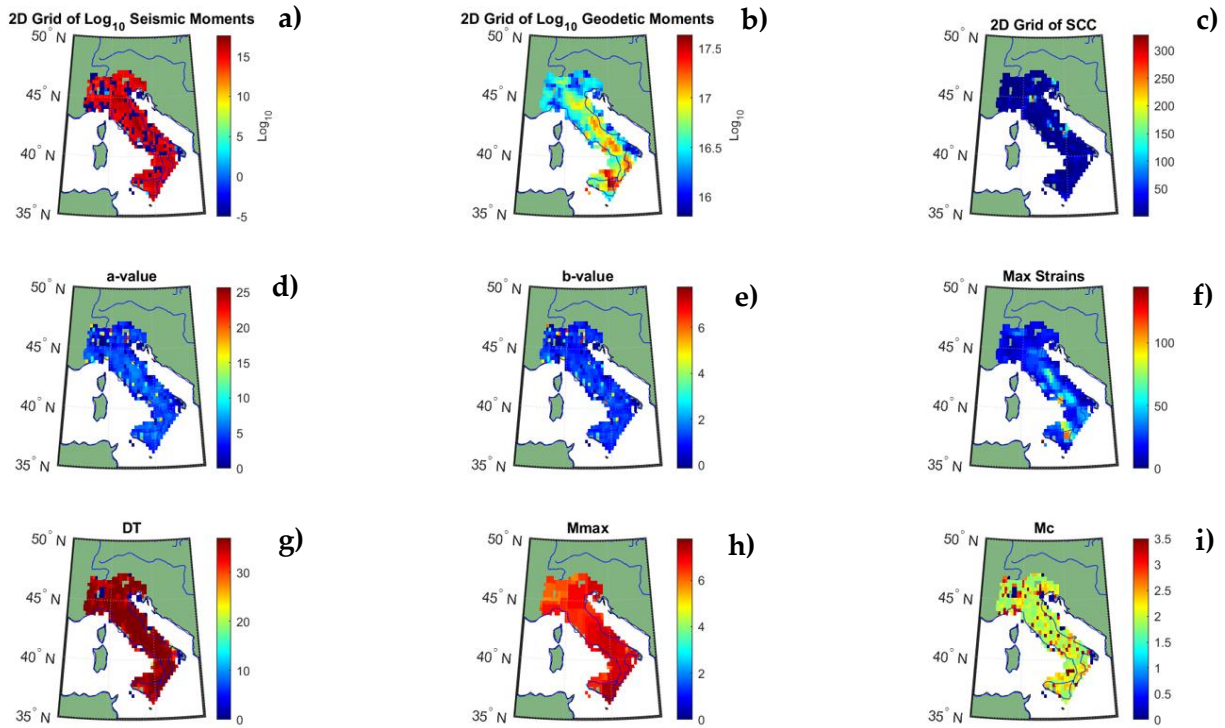


Figure 3.8 – Output figure 3 of the workflow. a) Seismic moment-rates values according to [Hyndman and Weichert \(1983\)](#). The [Gutenberg and Richter \(1956\)](#) parameters have been estimated with LSR statistical regression method. b) Geodetic moment-rates according to [Savage and Simpson \(1997\)](#). c) The SCC values. d) *a-value* estimated with LSR. e) *b-value* estimated with LSR. f) Maximum geodetic strain-rates values. g) Time interval of the seismic catalogs. h) Maximum magnitude values M_{max} distribution. i) The magnitude of completeness M_c values estimated with LSR.

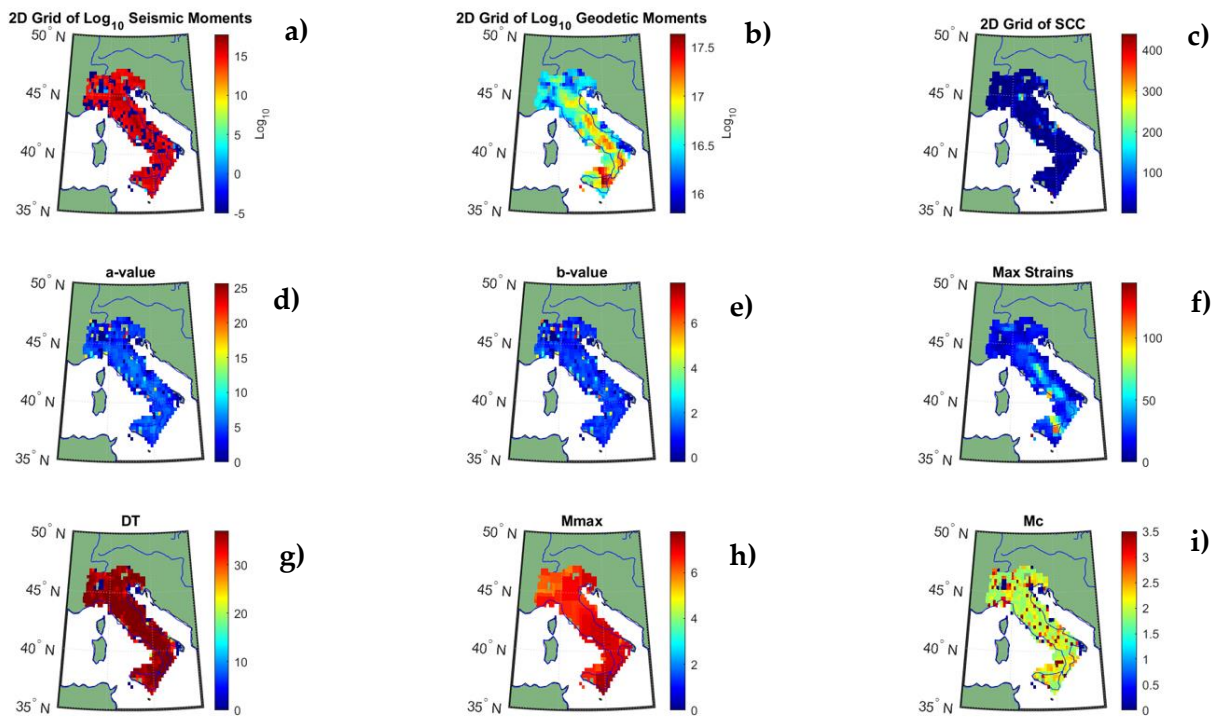


Figure 3.9 – Output figure 4 of the workflow. a) Seismic moment-rates values according to [Hyndman and Weichert \(1983\)](#). The [Gutenberg and Richter \(1956\)](#) parameters have been estimated with RFM statistical regression method. b) Geodetic moment-rates according to [Savage and Simpson \(1997\)](#). c) The SCC values. d) *a-value* estimated with RFM. e) *b-value* estimated with RFM. f) Maximum geodetic strain-rates values. g) Time interval of the seismic catalogs. h) Maximum magnitude values M_{max} distribution. i) The magnitude of completeness M_c values estimated with RFM.

3.2 *Cells_maker.m*.

Cells_maker.m, as the name suggests, “makes the cells”. Therefore, it takes the data and organizes them according to the subdivision of the investigated area into regular cells and to the different calculations that will have to be done. So, the outputs will be the several observables for each cell, which will be used in the other subsequent calculation routines for the estimation of other parameters (e.g., as the seismogenic thickness, the seismic moment-rates, etc.; Fig. 3.10).

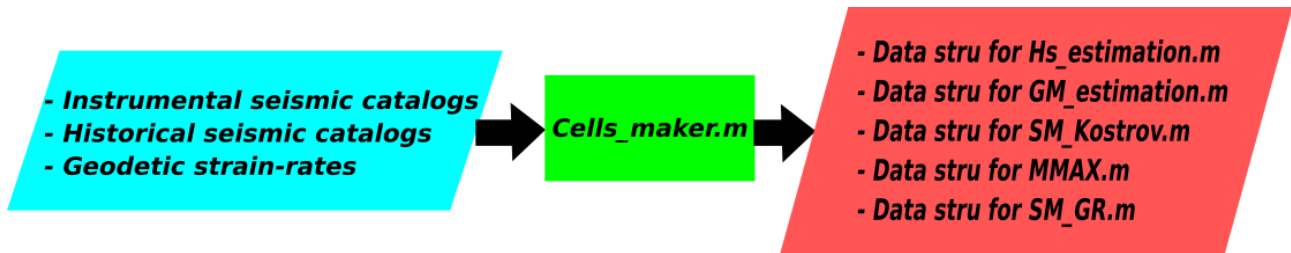


Figure 3.10 – A summary of *Cells_maker.m* program.

The definition of the grid size occurs in several levels based on what needs to be done, i.e., a denser grid will be used for the seismogenic thickness estimation, a larger one for the moment-rates and maximum magnitude estimations. Indeed, in this program several input parameters can be changed according to the user’s needs. As mentioned above, the input file is needed to be formatted as for ZMAP software (Wiemer, 2001).

Each grid is described by the following eight parameters:

- longitude distance between two midpoints;
- latitude distance between two midpoints;
- minimum longitude value, the starting longitude point of the investigated area;
- maximum longitude value, the ending longitude point of the investigated area;
- minimum latitude value, the starting latitude point of the investigated area;
- maximum latitude value, the ending latitude point of the investigated area;
- overlap along longitude directions (W-E, E-W);
- overlap along latitude directions (N-S, S-N).

The latter two parameters allow having a resulting diagonally overlap (NE-SW, SW-NE, NW-SE, SE-NW), in order to take into account any edge effect.

The versatility of the parameters allows generating different types of grid for the aforesaid different purposes. For example, the following three different types of grid will be created during each computation:

- The first grid type is set for the seismogenic thickness calculation, and it is generally the thinner one. It is shifted along longitude, latitude and diagonally with an overlap that depends on the chosen parameter value.
- The second grid type is set for the seismic and geodetic moment-rates calculation and for the Gutenberg-Richter parameters estimation. Even in this case, it is shifted along longitude, latitude and diagonally with an overlap that depends on the chosen parameter value. This dimension is generally estimated using empirical relationship that relates the length of the

fault with the maximum magnitude earthquake of the study area (Wells and Coppersmith, 1994).

- The third grid type is set for the maximum magnitude estimation (Kijko and Singh, 2011), and, like the previous ones, it is shifted along longitude, latitude and diagonally with an overlap that depends on the chosen parameter value. In general, it has an enlarged grid size respect to the previous one, in order to take into account the location uncertainties of historical earthquakes.

Summing up:

Input data/files:

- the instrumental catalog formatted as for ZMAP software (Wiemer, 2001) and the geodetic strain-rates if the code is used for the calculation of the seismogenic thickness, seismic and geodetic moment-rates, Gutenberg-Richter parameters;
- if the code is used for the maximum magnitude estimation and for the seismic moment-rate according to Kostrov (1974), the instrumental and historical catalogs (called mixed seismic catalog from here on) are used.

Output data/files:

- one data structure with all the information needed for the seismogenic thickness estimation;
- one data structure with all the information needed for the geodetic moment-rates estimation;
- one data structure with all the information needed for the seismic moment-rates estimation according to Kostrov (1974);
- one data structure with all the information needed for maximum magnitude estimation;
- one data structure with all the information needed for Gutenberg-Richter parameters and seismic moment-rate estimation;
- one file for each cell created, formatted as the catalogs, in order to be imported even from ZMAP software (Wiemer, 2001);
- an informative file for each cell. The time interval of the cell, the maximum magnitude observed, the seismic moment-rate of Kostrov normalized both for the time interval of the catalog and for the time interval of the cell (the same time interval used for and *SM_Kostrov.m*, see Par. 3.5, and *SM_GR.m*, see Par. 3.7) are reported;
- a file for each cell in which all the magnitudes of the cell are reported in ascending order. These files can be elaborated later with MMAX software (Kijko and Singh, 2011).

3.3 *Hs_estimation.m*.

This program allows to estimate the seismogenic thickness of an area previously divided into cells by the *Cells_maker.m* (Fig. 3.11) with a confidence interval obtained using the bootstrap with replacement statistical method (Chiarabba and De Gori, 2016).

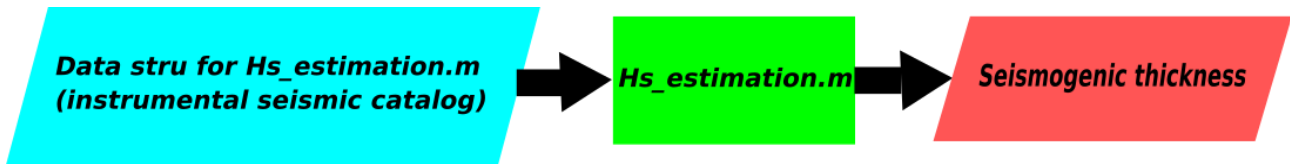


Figure 3.11 – A summary of *Hs_estimation.m* program.

This computation must be done using different mesh grids and trying different parameters configuration. Furthermore, there are several parameters to be set according to the user's needs, including:

- *N*: the number of extractions to be performed for the application of the bootstrap with replacement statistical method (e.g., 100 is set for the seismogenic thickness of Italy);
- *p*: the analysis percentile chosen. It varies between 0 and 100% (e.g., 90% is set for the seismogenic thickness of Italy);
- *alpha*: value chosen for the confidence interval. It varies between 0 and 1 (e.g., 0.9 is set for the seismogenic thickness of Italy);
- *n_events_minHs*: minimum number of earthquakes to compute *Hs_estimation.m* for a specific cell. With this parameter it is possible to set the minimum number of earthquakes falling in the cells taken into consideration for the application of the statistical method (e.g., 5 has been initially set for preliminary estimations of the seismogenic thickness of Italy, but the user can re-apply a filter to calculate it only where he wants);
- *filter_depth_min* (km): there could be several earthquakes with depth equal to zero in the catalogs, because of problems related to computational factors (if it is not possible to calculate depth, it is automatically set to zero) or due to anthropogenic factors (quarries, explosions, etc.). So, if this parameter is greater than zero, the code considers only those earthquakes that have a depth greater than or equal to *filter_depth_min*; consequently, some cells given as input may now be empty and therefore not be considered in subsequent calculations (e.g., 1 is set for the seismogenic thickness of Italy). The impact of this parameter affects only the part of the workflow in which the seismogenic thickness is estimated;
- *filter_depth_max* (km): this parameter is useful to skip those earthquakes that are related to the subduction zone, or, more simply, the user may be interested in studying only some specific interval of depth. If this parameter is greater than zero, the code considers only those earthquakes that have a depth less than or equal to *filter_depth_max*; also in this case, some cells given as input may be empty and therefore not be considered in subsequent calculations. This parameter could be useful to test different cut-off depths. The impact of this parameter affects the workflow from here on out;
- *filter_depths* (km): earthquakes with fixed depth (e.g., 5, 10, 15, 20, 33) are common on seismic catalogs. Since these events could lead to unrealistic estimation of the seismogenic thickness, the *filter_depths* parameter allows excluding all earthquakes with fixed depth.

Summing up:

Input data/files:

- the data structure coming from *Cells_maker.m* program, containing the information using the instrumental catalog;

Output:

- one file for the seismogenic thickness calculation consists of six columns (see Fig. 3.12), which shows in each row the following information for each cell: average longitude, average latitude, number of earthquakes present in the cell, average seismogenic thickness, upper extreme of the confidence interval (lower depth), lower extreme of the confidence interval (higher depth);
- one figure reporting the seismogenic thickness, the confidence level and the earthquakes distribution (see Fig. 3.13), respectively;
- one figure with the box plot of the seismogenic thickness for the grid (see Fig. 3.14).

```

6.1957800000000001e+00 4.2042339999999994e+01 5.000000000000000e+00 -9.000000000000004e+00 9.7831870078056701e+00 1.0016012912994331e+01
6.1827800000000002e+00 4.3555979999999998e+01 5.000000000000000e+00 -1.000000000000000e+01 1.000000000000000e+01 1.000000000000000e+01
6.1744090909090916e+00 4.4209354545454555e+01 1.100000000000000e+01 -1.0041599999999995e+01 1.0034806999928031e+01 1.0048303000710606e+01
6.14080071428571418e+00 4.5324707142857143e+01 1.400000000000000e+01 -1.513599999999997e+01 1.4682504507713459e+01 1.5589405492286536e+01
6.1605500000000006e+00 4.5920350000000006e+01 6.000000000000000e+00 -9.983200000000001e+00 9.9604656624541960e+00 9.9969143375458042e+00
6.4022428571428573e+00 4.3337742857142858e+01 7.000000000000000e+00 -1.000000000000000e+01 1.000000000000000e+01 1.000000000000000e+01
6.3287571428571425e+00 4.3490100000000001e+01 7.000000000000000e+00 -1.000000000000000e+01 1.000000000000000e+01 1.000000000000000e+01
6.3665000000000003e+00 4.3671160000000000e+01 5.000000000000000e+00 -1.6901000000000007e+01 1.6092789645507956e+01 1.77092115345492058e+01
6.3293285714285705e+00 4.4110714285714280e+01 7.000000000000000e+00 -1.000000000000000e+01 1.000000000000000e+01 1.000000000000000e+01
6.3131269565213927e+00 4.429410956521388e+01 2.300000000000000e+01 -1.032899999999997e+01 1.0188382286321234e+01 1.0406917713787606e+01
6.3725200000000002e+00 4.4452174999999996e+01 8.000000000000000e+00 -1.301729999999999e+01 1.2757052277487844e+01 1.3267547722121540e+01
6.36804208571428580e+00 4.4897485714285715e+01 7.000000000000000e+00 -1.000000000000000e+01 1.000000000000000e+01 1.000000000000000e+01
6.3582771428571432e+00 4.5356014285714295e+01 3.500000000000000e+01 -1.609599999999993e+01 1.5490124760714808e+01 1.6701875239285176e+01
6.3627285714285717e+00 4.5419361688311696e+01 1.540000000000000e+02 -1.517899999999998e+01 1.5039323336827120e+01 1.5318676663172877e+01
6.356743749999997e+00 4.5683581249999996e+01 1.600000000000000e+01 -1.129500000000000e+01 1.1084057438627610e+01 1.1509542561372390e+01
6.389579999999996e+00 4.6314800000000005e+01 5.000000000000000e+00 -1.079600000000003e+01 1.0619333674827400e+01 1.0972066225172600e+01
6.5400368421052625e+00 4.2935863157894730e+01 1.900000000000000e+01 -1.2707800000000002e+01 1.213820359070335e+01 1.3277396409029670e+01
6.560724999999998e+00 4.3515893749999996e+01 1.600000000000000e+01 -1.4704000000000002e+01 1.4206012818033862e+01 1.5201987181066434e+01
6.5246833333333329e+00 4.3908616666666660e+01 6.000000000000000e+01 -1.000000000000000e+01 1.000000000000000e+01 1.000000000000000e+01
6.5417914285714280e+00 4.4318025714285710e+01 3.500000000000000e+01 -1.436500000000000e+01 1.4114649070820004e+01 1.4615150929179990e+01
6.577685714285713e+00 4.4477682857142860e+01 3.500000000000000e+01 -1.697700000000001e+01 1.6652520072216041e+01 1.7221479127783962e+01
6.6117244444444436e+00 4.4734655555555536e+01 4.500000000000000e+01 -1.4569000000000001e+01 1.4376858210860105e+01 1.4761141789139897e+01
6.6113666666666671e+00 4.4910159999999998e+01 6.000000000000000e+01 -1.1925500000000001e+01 1.1781911845500431e+01 1.206098815499571e+01
6.5745980952380947e+00 4.5091131428571430e+01 1.050000000000000e+02 -1.146400000000000e+01 1.1327355076860995e+01 1.1600644923139006e+01
6.579987499999998e+00 4.5308442499999998e+01 8.000000000000000e+01 -1.324350000000001e+01 1.3049121614373009e+01 1.3437878385626993e+01
6.5980545454545450e+00 4.5452009999999994e+01 2.200000000000000e+01 -1.546430000000003e+01 1.529513041235124e+01 1.5732361587664883e+01
6.5413000000000006e+00 4.5692900000000002e+01 6.000000000000000e+01 -1.284230000000001e+01 1.1920280081345908e+01 1.21643191851854094e+01
6.5450857142857135e+00 4.6285814285714288e+01 7.000000000000000e+00 -9.980000000000003e+00 9.9492541746219086e+00 1.0012345285378011e+01
6.776755555555550e+00 4.3118900000000004e+01 9.000000000000000e+00 -1.0168000000000003e+01 1.0149574032909278e+01 1.0186425967090272e+01
6.7513000000000005e+00 4.3277050000000010e+01 1.000000000000000e+01 -1.000000000000000e+01 1.000000000000000e+01 1.000000000000000e+01
6.6934099999999995e+00 4.3538135714285708e+01 1.400000000000000e+01 -1.950400000000001e+01 1.9036769148335981e+01 1.9971230851664021e+01
6.7630857142857140e+00 4.3643757142857147e+01 7.000000000000000e+00 -1.000000000000000e+01 1.000000000000000e+01 1.000000000000000e+01
6.7809000000000002e+00 4.3897860000000001e+01 5.000000000000000e+00 -1.189699999999998e+01 1.1683654208181807e+01 1.2110345791811900e+01
6.7653647098823534e+00 4.4133411764709594e+01 1.700000000000000e+01 -2.0619600000000002e+01 1.9850701160930247e+01 2.1388498831069757e+01
6.770908487084872e+00 4.4320113414634143e+01 8.200000000000000e+01 -1.926189999999997e+01 1.8030512517054048e+01 1.8485287482345346e+01
6.739206280788178e+00 4.4502971921182272e+01 8.120000000000000e+02 -1.439040000000001e+01 1.4332774536341374e+01 1.4448025463508620e+01
6.7671053571428583e+00 4.4711563214285710e+01 2.200000000000000e+02 -1.2281000000000001e+01 1.220121541703164e+01 1.2260784858296837e+01
6.737428985072469e+00 4.4901286956521737e+01 2.070000000000000e+02 -1.1217400000000003e+01 1.1182327038249447e+01 1.1252472961750590e+01
6.7728029850746271e+00 4.5053868656716425e+01 6.700000000000000e+01 -1.0603800000000001e+01 1.0565065605289551e+01 1.0642534394730452e+01
6.7094206349206367e+00 4.5306042857142856e+01 6.300000000000000e+01 -1.614800000000003e+01 1.5852010305292286e+01 1.6443909094707721e+01
6.7337600000000011e+00 4.5469476000000007e+01 5.000000000000000e+01 -1.348849999999997e+01 1.3349567402089599e+01 1.3627432597918394e+01
6.7640615384615384e+00 4.5665938461538460e+01 1.300000000000000e+01 -1.273600000000001e+01 1.241803547678805e+01 1.3053964523212196e+01
6.7194062500000014e+00 4.5911068749999998e+01 1.600000000000000e+01 -1.645929999999999e+01 1.6175184395654636e+01 1.6743415604345362e+01

```

Figure 3.12 – Output file from *Hs_estimation.m* program.

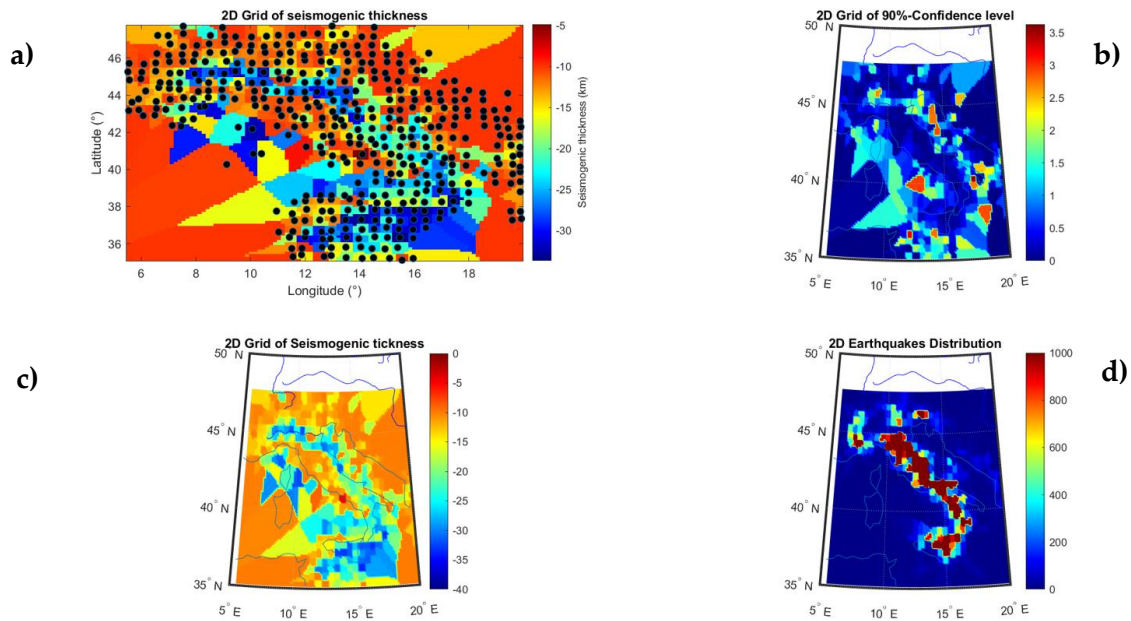


Figure 3.13 – Output figure 1 from *Hs_estimation.m* program. a) 2D colour grid of coloured cells with respect to the seismicogenic thickness with the nearest neighbour’s regression interpolation method. b) 2D colour map of coloured cells with respect to the seismicogenic thickness with the nearest neighbour’s regression interpolation method. c) 2D colour grid showing the confidence level (km) of the analysed cells with the bootstrap statistical method. d) 2D colour grid showing the number of earthquakes falling in the analysed cells with the bootstrap statistical method.

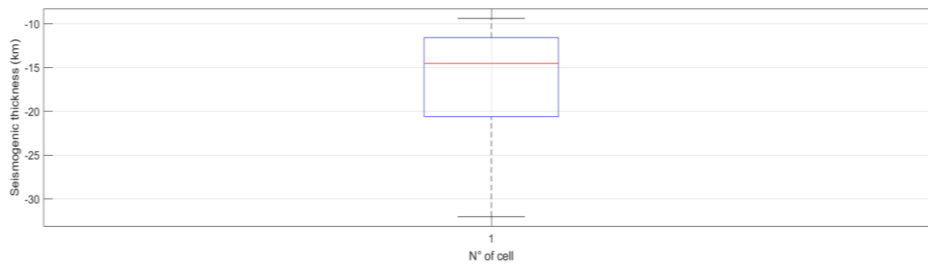


Figure 3.14 – Output figure 2 from *Hs_estimation.m* program. The box plot of the seismicogenic thickness is reported.

3.4 *GM_estimation.m*.

This program estimates the geodetic moment-rates according to [Savage and Simpson \(1997\)](#) formulation. It has been structured in order to be able to import the three different input files of the geodetic strain-rates ([Fig. 3.15](#)).



Figure 3.15 – A summary of *GM_estimation.m* program.

Also in this case there are some parameters to be set according to the user’s needs:

- *strain_method*: with this parameter the user selects the input file to be used for the geodetic moment-rate estimation. A number is associated with each method;
- μ (Pa): value chosen for the shear modulus of the crust. It usually varies between $3.0 \cdot 10^{10}$ Pa and $3.3 \cdot 10^{10}$ Pa, for depth less and greater than 20 km, respectively (e.g., $3.0 \cdot 10^{10}$ Pa is the typical value of average crustal rocks; [Turcotte and Schubert, 2002](#)).

Summing up:

Input data/files:

- the data structure coming from *Cells_maker.m* program, containing the information using the instrumental catalog;
- the data structure coming from *Hs_estimation.m* program, containing the mean value of the seismogenic thickness for each cell of the grid;
- the areas values of each cell of the grid, calculated with a specific secondary subroutine called *calculate_Areas.m*. This subroutine calculates the areas values for each cell of the grid, starting from the longitude and latitude values of the investigated region and from a reference ellipsoid;
- the maximum geodetic strain-rate value, calculated with a specific secondary subroutine called *calculate_MaxStrain.m*. This subroutine returns the maximum value of the geodetic strain-rates, starting from the output files of the three different aforesaid software used (see [Par. 3.1](#)).

Output data/files:

- the geodetic moment-rates estimation for each cell of the grid;
- one figure with the box plot of the geodetic moment-rates ([Fig. 3.16](#)).

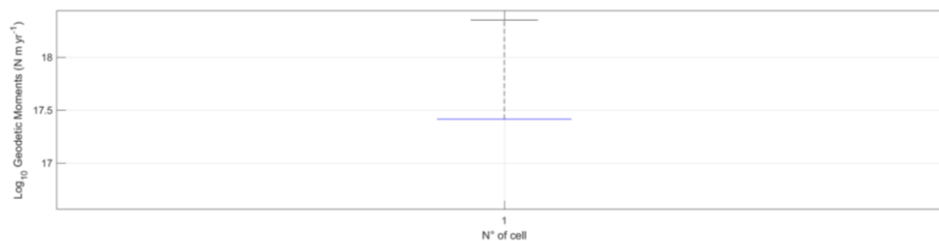


Figure 3.16 – Output figure from *GM_estimation.m* program. The box plot of the geodetic moment is reported.

3.5 *SM_Kostrov.m*.

This program has two main principal features: first of all, it estimates the annual variation of the seismic moment-rates according to [Kostrov \(1974\)](#), normalized for the time interval of the single cell, which results significant for the cells of instrumental and historical catalogs. Secondly, since, the more temporally homogeneous is the distribution of the magnitudes falling in each cell, the more the Kostrov seismic moment-rate estimation will be accurate: this program is able to perform an ancillary calculation with moving averages ([Fig. 3.17](#)). So, chosen a time interval in which each cell is subdivided (e.g., 20 years), and giving in input the geodetic moment-rate ([Par. 3.4](#)), the moving

average of the seismic moment-rate of Kostrov can be obtained at three moving time windows (e.g., 100, 200 and 300 years) in a timeline (Middleton et al., 2018), in order to study its distribution over time within each specific cell. This timeline allows also identifying periods of time (within each cell) when there is a mismatch between the seismic and the geodetic moment-rates. These values can be saved by the user. A third use of this program allows calculating the seismic moment-rate according to Kostrov (1974) using the instrumental seismic catalog only, even if it is not very significant.

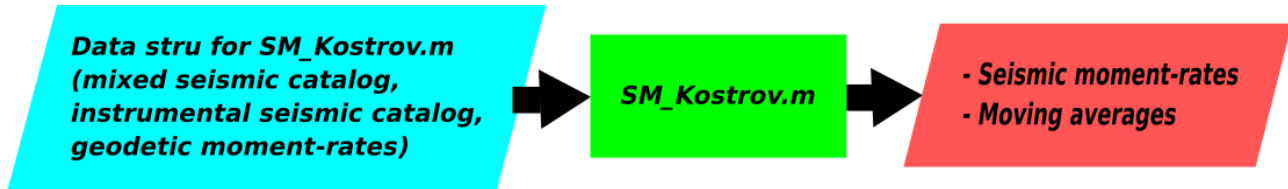


Figure 3.17 – A summary of *SM_Kostrov.m* program.

Also in this case there are several parameters to be set according to the user's needs, including:

- *plot_figureKostrov*: this parameter allows the user to choose to make the graphs relating to the Kostrov moving average. If its value is greater than 0 a folder containing as many figures as the number of the cells is created;
- *plot_figureKostrov_ins*: this parameter allows the user to choose to make the graphs relating to the Kostrov moving average using the instrumental catalog. If its value is equal to 2 a folder is created containing as many figures as the number of the cells;
- *min_mag*: cut-off magnitude value below which all instrumental earthquakes are cut to create the mixed seismic catalog;
- *delta_year*: time interval in which each cell will be subdivided for the Kostrov seismic moment-rate moving averages estimation (e.g., 20 years);
- *half_windows*: size of the analysis time windows (they all start and end at the same time);
- *starts_windows*: start of the analysis windows (e.g., 1050-50=1000; 1100-100=1000);
- *end_windows*: end of the analysis windows (e.g., 2010+50=2060; 1960+100=2060).

Summing up:

Input data/files:

- the data structure coming from *Cells_maker.m* program, containing the information using the mixed seismic catalog;
- the data structure coming from *Cells_maker.m* program, containing the information using the instrumental seismic catalog;
- the previously calculated geodetic moment-rates (Par. 3.4).

Output data/files:

- the seismic moment-rates according to Kostrov (1974) for each cell of the grid;
- a folder which contains one figure for each cell made up by two panels about the estimation of the seismic moment-rate according to Kostrov (Fig. 3.18). The first panel shows the trend of magnitudes with the time interval of a single cell. The second panel shows the moving averages of the base 10 logarithm of the Kostrov seismic moment-rate

and the base 10 logarithm of the geodetic moment-rate of each cell (Middleton et al., 2018);

- a folder like the previous one, using the instrumental seismic catalog only.

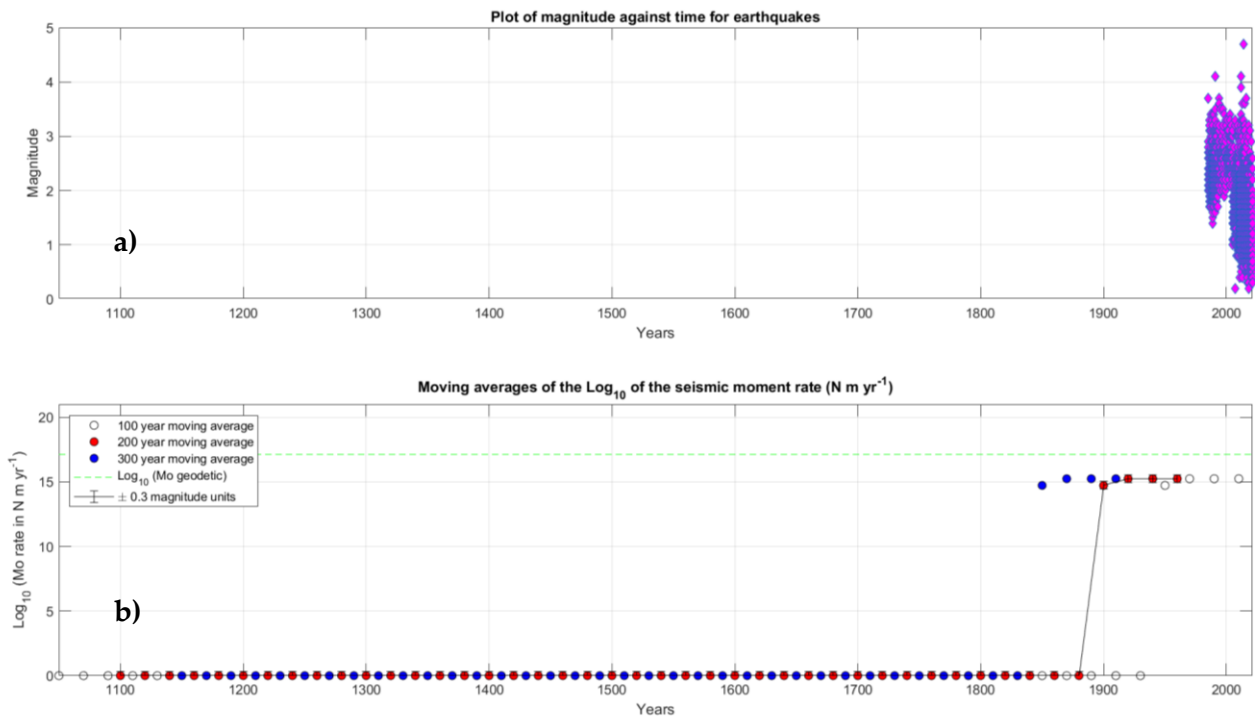


Figure 3.18 – Output figure from *SM_Kostrov.m* program for each analysed cell. a) Magnitude distribution of earthquakes with time. The earthquakes are represented with fuchsia diamonds. b) Moving averages of the seismic moment-rate according to Middleton et al. (2018). The 100, 200, 300 year moving averages are reported with white, red and blue circles, respectively. The geodetic moment-rate is represented with the green dashed line.

3.6 MMAX.m software.

The toolbox developed by Kijko and Singh (2011) has been linked to the workflow in order to estimate the maximum magnitude value for each cell of the grid starting from the seismic catalog obtained by the merging of the historical and the instrumental ones (Fig. 3.19). As has been said before, the cell's size of the grid used for this purpose has been enlarged in order to take into account the location uncertainties of the historical earthquakes (see Par. 3.2). This software, by adopting twelve different statistical procedures, provides reliable results for the investigated area, even under different data restrictions (magnitude of completeness and temporal length of the catalogs, magnitude distribution and uncertainties, number of earthquakes, etc.), and it is usually applied on regions where only a limited number of large earthquakes is available. For each cell, among the twelve estimated maximum magnitude values, the one associated with the smallest uncertainty has been chosen.

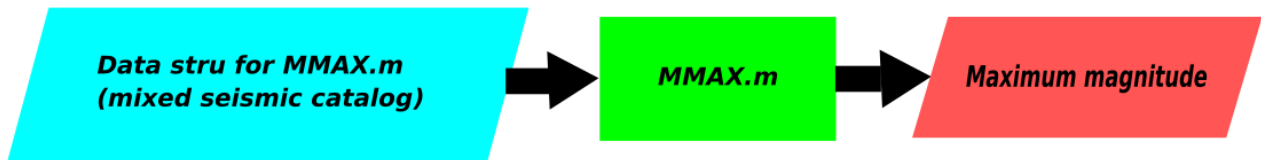


Figure 3.19 – A summary of *MMAX.m* program.

Also in this case there are several parameters to be set according to the user's needs, including:

- *n_events_minMMAX*: minimum number of earthquakes of each cell of the grid to compute *MMAX.m* software;
- *sd_mag*: average error assumed on magnitude values (e.g., 0.3 is set for Italy case study);
- *model_uncertainty_beta*: the assumed uncertainty of the model (the default value is 25%).

Summing up:

Input data/files:

- the data structure coming from *Cells_maker.m* program, containing the information using the mixed catalog.

Output data/files:

- the maximum magnitude value associated with the smallest relative uncertainty for each cell of the grid.

3.7 *SM_GR.m*.

Starting from the grid obtained with the instrumental seismic catalog only, this program estimates the Gutenberg-Richter parameters *a-value* and *b-value* using three different statistical regression methods (Maximum Likelihood Estimation, MLE, Least Square Regression, LSR, and Robust Fitting Method, RFM) and the seismic moment-rate according to [Hyndman and Weichert \(1983\)](#), whose formula is remembered ([Par. 2.2, eq. 2.17](#)):

$$M_{seis}^{\cdot} = \varphi \frac{b}{(c-b)} 10^{[(c-b)M_{max}+a+d]} \quad (3.1)$$

The input data are the following: a cell, the maximum optimal magnitude value for that cell estimated with the *MMAX* software ([Kijko and Singh, 2011](#); see [Par. 3.6](#)), and the magnitude of completeness value, suitably chosen by looking at [Fig. 3.21](#) generated with unitary value. An advanced version of this program has also been created, which automates the process of finding the best magnitude of completeness value. In particular, given in input a range of possible completeness magnitude values and a sampling step, for each of the three regression methods previously used (MLE, LSR, RFM), it looks for which completeness magnitude value among those provided in input minimize the chi-square function. This value will be identified as the best completeness magnitude value, respectively for each of the above three regression methods ([Fig. 3.20](#)).



Figure 3.20 – A summary of *SM_GR.m* program.

Also in this case there are several parameters to be set according to the user's needs and the quality of the results to be obtained, including:

- *save_cells_ins*: this parameter allows the user to choose to save the cells of the instrumental catalog (to speed up the calculation in the case of numerous tests). If it equals to 0 it does not save them, if it equals to 1 it saves them;
- *plot_figureGR*: this parameter allows the user to choose to make the graphs relating to the estimation of the Gutenberg-Richter parameters (to speed up the calculation in the case of several tests). If its value is greater than 0 a folder is created containing two figures for each cell. The two figures correspond one to the estimate of the Gutenberg-Richter parameters (six panels) and the other (six panels) to the residuals of each regression method;
- *M_{max}*: the maximum magnitude value of each cell of the grid estimated with *MMAX.m*;
- *φ*: correction factor for the asymmetry of the stochastic moment-magnitude relation. According with [Hyndman and Weichert \(1983\)](#) moment-rates formulation, this value depends on the uncertainty about the maximum magnitude value that it wants to account for. The value of this parameter was set to 1.27, assuming an uncertainty of 0.2 on all the earthquake magnitudes of the considered cell ([Mazzotti and Adams, 2005](#));
- *c*: parameter of the conversion between the magnitude and the seismic moment. Fixed according to [Hanks and Kanamori \(1979\)](#), it is used for the estimation of the seismic moment-rate according to the formulation of [Hyndman and Weichert \(1983\)](#);
- *d*: parameter of the conversion between the magnitude and the seismic moment. Fixed according to [Hanks and Kanamori \(1979\)](#), it is used for the estimation of the seismic moment-rate according to the formulation of [Hyndman and Weichert \(1983\)](#);
- *M_{thresh_min}*: lower cut-off value for magnitude of completeness to be analysed;
- *M_{thresh_max}*: upper cut-off value for magnitude of completeness to be analysed. If *M_{thresh_min}*=*M_{thresh_max}*=0, the user will iteratively select the best value of magnitude of completeness;
- *same_cut-off_mag*: upper cut-off value for magnitude to be analysed for each cell, in order to estimate *a-value* and *b-value* on middle class magnitude (small and moderate values) events only. The user can choose whether to use the same value for all the cells, or choose with an iteratively procedure a value for each cell, or import a file with cut-off values previously select for each cell;
- *bin*: binning for testing the magnitude of completeness;
- *n_events_minGR*: minimum number of earthquakes of each cell of the grid to compute *SM_GR.m*.

Summing up:

Input data/files:

- the data structure coming from *Cells_maker.m* program, containing the information using the instrumental catalog;
- the maximum magnitude value for each cell of the grid (see [Par. 3.6](#)).

Output data/files:

- *a-value*, *b-value*, magnitude of completeness for each cell of the grid (calculated with MLE, LSR and RFM statistical methods);
- the seismic moment-rate for each cell according to [Hyndmann and Weichert \(1983\)](#);
- two figures for each cell. The first figure consists of six panels about the estimation of the Gutenberg-Richter parameters ([Fig. 3.21](#)). The first panel at the top left shows a map of the investigated area with the highlighted analysed cell; the second panel at the centre left shows a longitude-latitude map of the earthquakes of the analysed cell with a depth bar; the third panel at the bottom left shows the depth distribution of the earthquakes falling in the analysed cell as a function of the magnitudes; the first panel at the top right shows the fitting between the [Gutenberg and Richter \(1956\)](#) recurrence relationship (using the three different pairs (*a*; *b*) estimated with the three different statistical methods) and the logarithm to base 10 of the number of earthquakes (the observed data, represented with the white squares); the second panel at the centre right shows the truncated Gutenberg-Richter distribution (using the three different pairs (*a*; *b*) estimated with the three different statistical methods) according to [Mazzotti and Adams \(2005\)](#); the third panel at the bottom right shows the absolute residual of the logarithm number of events according to [Han et al. \(2015\)](#) for each statistical method. The second figure, also made up of six panels, shows the predicted and the residuals of each regression method, on the left and on the right, respectively ([Fig. 3.22](#)).

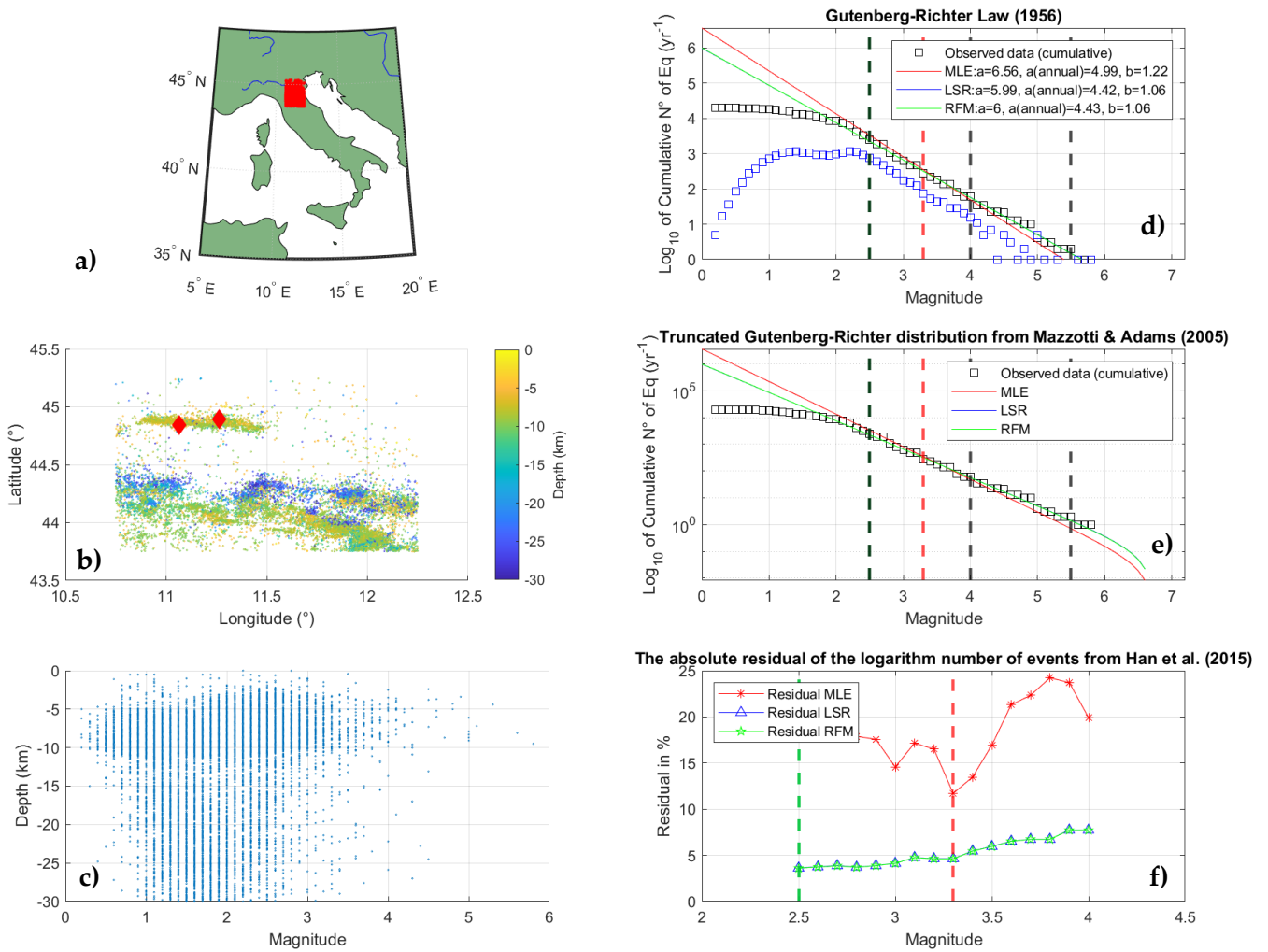


Figure 3.21 – Output figure 1 from *SM_GR.m* program. a) Map of the investigated area; in red the analysed cell is reported. b) Longitude-latitude map of the earthquakes of the analysed cell with a depth coloured bar. Events with magnitude > 5.5 are represented with red diamonds. c) Depth distribution of the earthquakes falling in the analysed cell as a function of the magnitudes. d) Fitting between the [Gutenberg and Richter \(1956\)](#) recurrence relationship obtained using different pairs of a and b parameters estimated with MLE, LSR and RFM statistical regression methods (reported with red, blue and green continuous lines, respectively) and the cumulative number of observed earthquakes (white squares with black outline). The discrete observed data are also reported with white squares with blue outline. The minimum and the maximum values of magnitude of completeness and the chosen cut-off magnitude for the analysed cell are reported with black dashed lines. The best magnitude of completeness values with MLE, LSR and RFM methods are reported with red, blue and green dashed lines, respectively. e) Fitting between the truncated Gutenberg-Richter distribution according to [Mazzotti and Adams \(2005\)](#) using different pairs of a and b parameters estimated with MLE, LSR and RFM statistical regression methods (reported with red, blue and green continuous curves, respectively) and the cumulative number of observed earthquakes (white squares with black outline). The minimum and the maximum values of magnitude of completeness and the chosen cut-off magnitude for the analysed cell are reported with black dashed lines. The best magnitude of completeness values with MLE, LSR and RFM methods are reported with red, blue and green dashed lines, respectively. f) The absolute residual of the logarithm number of events according to [Han et al. \(2015\)](#) for each statistical regression method. MLE, LSR and RFM are reported with red asterisks, blue triangles and green stars snap lines, respectively. The minimum and the maximum values of magnitude of completeness are reported with red, blue and green dashed lines, respectively.

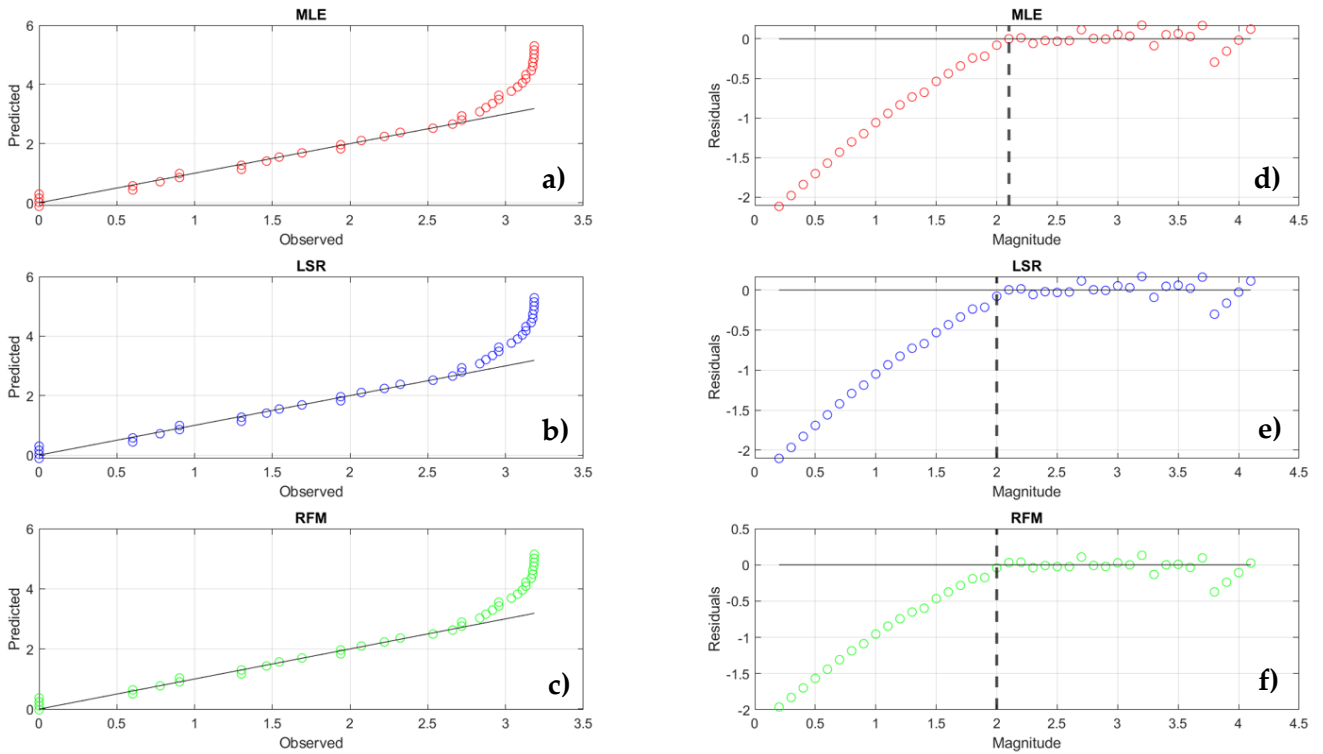


Figure 3.22 – Output figure 2 from *SM_GR.m* program for each analysed cell. a) Comparison between the observed magnitude (cumulative) and the predicted ones with MLE reported with red circles and grey continuous line, respectively. b) Comparison between the observed magnitude (cumulative) and the predicted ones with LSR reported with blue circles and grey continuous line, respectively. c) Comparison between the observed magnitude (cumulative) and the predicted ones with RFM reported with green circles and grey continuous line, respectively. d) Analysis of the residual data (i.e., the difference between the observed and predicted data) with MLE as a function of the observed data. The best value of magnitude of completeness is reported with black dashed line. e) Analysis of the residual data (i.e., the difference between the observed and predicted data) with LSR as a function of the observed data. The best value of magnitude of completeness is reported with black dashed line. f) Analysis of the residual data (i.e., the difference between the observed and predicted data) with RFM as a function of the observed data. The best value of magnitude of completeness is reported with black dashed line.

3.8 Possible improvements.

A first possible improvement of the workflow could be found in the geometry of the mesh, actually regular and rectangular, but it may not always be useful in this way. There are situations in which it may be more appropriate to have geometries of a different type, for example regular polygonal (Palano et al., 2020) or irregular shape (Sparacino et al., 2020). Secondly, the geodetic strain-rates calculation modality. As has been told above, right now the geodetic moment-rates are calculated using the output file with the geodetic strain-rates coming from three different software (see Par. 3.1) as an input data for the workflow. Therefore, this procedure must necessarily be done separately. A nice goal could be to integrate the computation of the geodetic strain-rates inside the workflow using a generic geodetic velocity solution running in MATLAB program language (<https://it.mathworks.com>). Another improvement that could be done is related to the uncertainties of most of the parameters used as input in the workflow. Now, the workflow does not take into account the uncertainties of some quantities, and another specific program, not related to the main one, has been done. Moreover, it should be remembered that as regards the seismic moment-rates,

the changing parameters are the *a-value*, *b-value* and M_{max} ; in turn, the estimations of *a-* and *b-value* depend from M_c estimation so that possible errors of its estimate would propagate into the estimations of the aforesaid parameters (*a-* and *b-value*). Currently, to get the best estimation of the Gutenberg-Richter curve, a reasonable number of earthquakes from small- to mid-size earthquakes ($M < 5$) for each investigated cell (at least 35 events) have been considered. The quality of the fit has been monitored cell by cell with the graphic outputs showed in [Figs. 3.22-3.23](#).

As regards the geodetic one, on the other hand, they are H_s , *max strain* and μ . The variation of all these six parameters affects the estimation of the uncertainty of the final SCC. Then, another useful improvement that could be done is to link the uncertainty estimation program to the workflow.

4 – The case study of Italy

In this chapter the background setting, the used seismological and geodetic data and the obtained results for Italy will be present in detail.

4.1 General background of Italy.

The Neogene-Quaternary kinematic evolution of Italy was controlled by the interactions between the relative motions of African and Eurasian plates, which are currently converging at a rate ~ 5.5 mm/yr along an \sim N-S direction (D'Agostino and Selvaggi, 2004; Palano et al., 2012), and its tectonics has been accommodated by a puzzle of tectonic units developed during the subduction and collision of the Alpine and Apennine belts (De Mets et al., 1990; Dercourt et al., 1986; Malinverno and Ryan, 1986; Doglioni et al., 1994; Patacca et al., 1990; Faccenna et al., 2001; Faccenna et al., 2014; Fig. 4.1). This framework is greatly complicated by the presence of the Adria microplate, i.e., a promontory of Africa toward Eurasia, which causes active compression all along its borders, and the growth of the broad Adria-verging outer, i.e., Dinarides and Southern Alps, and inner, i.e., Northern Apennine Arc and the Calabrian Arc, thrust systems (e.g., Gorshkov et al., 2002). Conversely, in the Southern Apennine Arc, this compression front is no longer active, at least since the Early-Middle Pleistocene. Tomographic images show that the initially continuous Apennines subduction has been segmented into different arcs, due to the nature of the subducting material (Lucente et al., 1999; Piromallo and Morelli, 2003; Margheriti et al., 2003) in agreement with geologic reconstruction (Royden et al., 1987; Govers and Wortel, 2005; Faccenna et al., 2014).

Beneath the Southern Apennine Arc, the subduction of the Ionian/Adria lithospheres ceased diachronously from north to south (Galli et al., 2008; Van Hinsbergen et al., 2009; Faccenna et al., 2014; Van Hinsbergen et al., 2014). This is shown by the frontal thrust sheet, which is sealed by early Pleistocene marine sediments in the northern sector, whereas early Pleistocene deposits are still involved in compressional deformation in the southern sector (Cinque et al., 1993), and late Middle Pleistocene ones in the Bradanic trough (Pieri et al., 1997). It is possible that the continuous and current (Anderson and Jackson, 1987; Devoti et al., 2002; Serpelloni et al., 2005) rotation of Adria microplate after the end of the slab subduction (~ 0.65 Ma ago) controlled the onset of the present extensional regime, which produced new normal faults superimposed upon inactive transpressional ones (Patacca and Scandone, 1989). At present, the convergence between Africa and Eurasia is accommodated by a complex deformation of the Alps and Apennine systems due to the fragmentation of the west-dipping slab (Royden et al., 1987). In this framework, the Padano-Adriatic margin of the Apennines (northern sector of the Northern Apennine Arc) is characterized by compressional earthquakes that are generated by the buried active frontal thrust of the Adria-verging chain, whereas the remaining sector of the Northern Apennine Arc (south to 43.3° N) and the Southern Apennine Arc are dominated by medium-strong extensional events that are mainly caused by NW-SE normal faults running along the axis of the chain (i.e., dozens of km west to the

thrust front (Anderson and Jackson, 1987; Westaway, 1992; Pondrelli et al., 2002; Hunstad et al., 2002; Chiarabba et al., 2005). Recent geodetic studies reveal that the Apennines are undergoing a NE-trending extension, with deformation rates higher in the Southern Apennines (e.g., Devoti et al., 2017).

Finally, different current of thoughts exist about what the actual processes are that take place in Calabria, which is the location of the greatest earthquakes of the entire orogeny. This is the only region where a subducting slab is well depicted by deep earthquake location along a “Benioff plane” (e.g., Amato et al., 1993; Faccenna et al., 2011; Neri et al., 2012; Presti et al., 2019) and P-wave and S-wave anomalies in tomographic images (e.g., Piromallo and Morelli, 2003; Pontevivo and Panza, 2006; Prada et al., 2020). The slab can be interpreted as Ionian oceanic lithosphere dipping ~500 km NW into the Tyrrhenian asthenosphere. Actually, no one knows whether the slab is entirely detached, or, as suggested by tomographic studies (e.g., Neri et al., 2009; Scarfi et al., 2018), whether it is still continuous only below Southern Calabria (focal mechanisms show diffused down-dip compression only at depths N150 km, meaning no active pull of the slab there; Frepoli et al., 1996; Scarfi et al., 2021). However, the Northern and Central Calabria (north of the Catanzaro Straits) could presently follow the same stress trajectories of the Southern Apennines (Galli and Scionti, 2006; Galli et al., 2006; Scudero et al., 2020), sharing the same slip-vectors of Adria vs. Europe (i.e., D’Agostino and Selvaggi, 2004). Conversely, in Southern Calabria, the NW-SE crustal extension could still be driven by the SE-retreating slab (Fig. 4.1), the bending of which is accompanied by strong earthquakes (i.e., the $M_s = 7.5$, 1905 event; Galli and Molin, 2007).

This seismotectonic picture, coupled with the historical record of seismicity, highlights that most of the potentially surface faulting earthquakes are concentrated in Central and Southern Italy, south of the above-mentioned 43°N parallel (Chiarabba et al., 2005; Fig. 4.1). Indeed, according to the CPTI04 (<http://emidius.mi.ingv.it/CPTI>), of the ninety earthquakes reported, only fifteen belong to the Alpine domain (mainly NE Alps), and only four of these with $6.5 \leq M_w \leq 6.7$. Conversely, Calabria includes eleven events with $6.5 \leq M_w \leq 7.3$, nineteen of which are scattered along the whole Apennines with $6.5 \leq M_w \leq 7.0$, while three events with $M_w > 6.5$ occurred in Sicily (Galli et al., 2008).

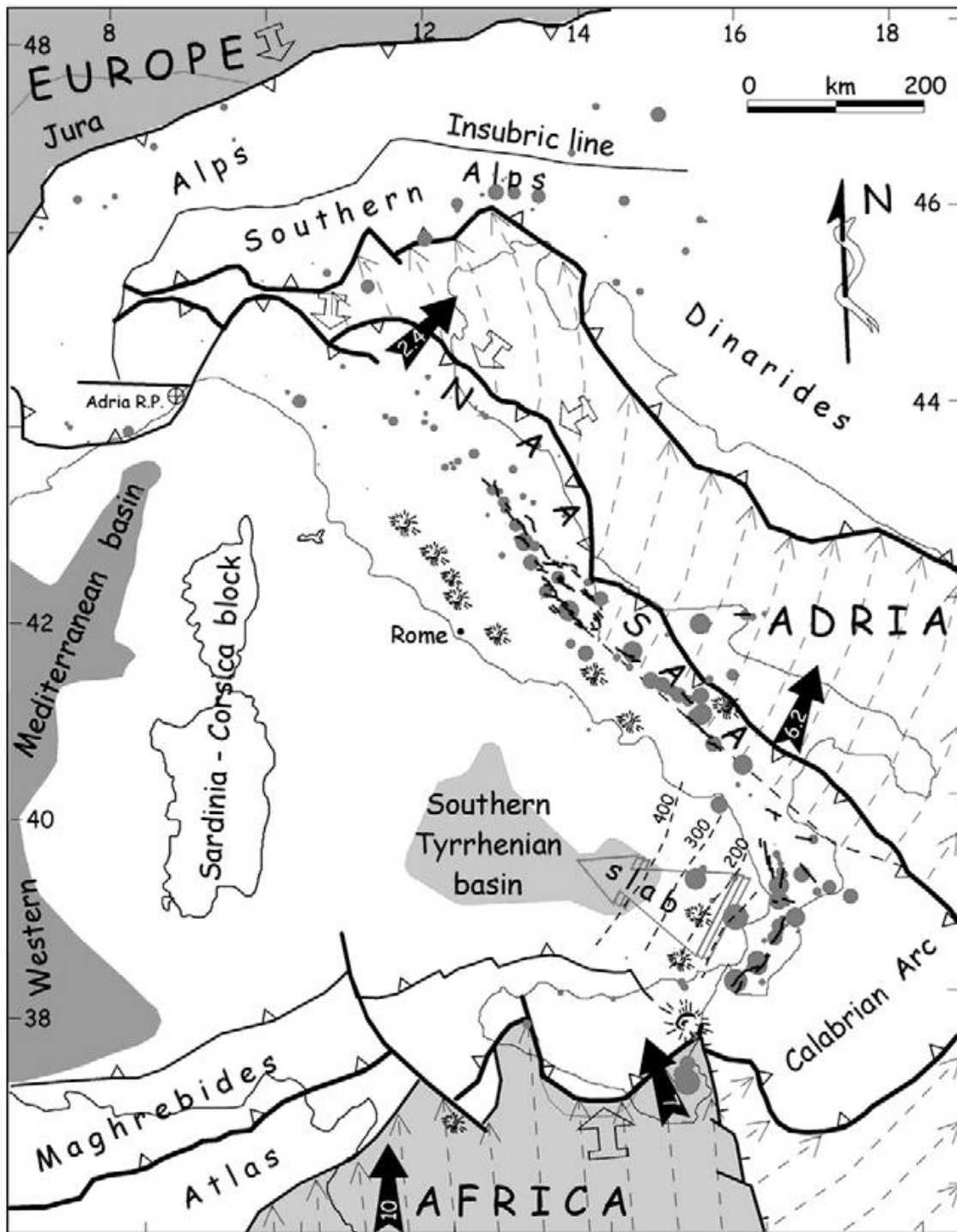


Figure 4.1 - Main structural and kinematics features of the Italian orogen, within the relative motion of the Europe, Adria and Africa plates. The thin dashed arrows roughly indicate the slip-vectors of Adria vs Europe and Africa vs Europa. Black arrows indicate VLBI and SRL velocities (mm/yr; Ward, 1994). The bold continuous line is the compressive front of the Alpine–Apennine chain (Northern and Southern Apennine Arcs, NAA and SAA, respectively). Quaternary volcanoes and isobaths (in km) of the Ionian lithospheric slab (dashed lines in southern Tyrrhenian basin) are also shown. Grey circles are the $M > 5.5$ earthquakes (only for Italy; CPTI04, <http://emidius.mi.ingv.it/CPTI>). Note that the seismicity occurs mainly along the central southern Apennines chain, and partly in eastern Sicily and south-eastern Alps. The “fragmented” line along the Apennine axis depicts the known outcropping seismogenetic faults. Modified from Galli et al. (2008).

4.2 Data.

In this paragraph, the used data for Italy case study will be described in details.

4.2.1 Seismological data.

4.2.1.1 Historical Seismicity.

Two catalogs of historical seismicity have been analysed:

- The SHARE European Earthquake Catalog (<https://www.emidius.eu/SHEEC/>), consists of two portions:
 1. The SHARE European Earthquake Catalog (SHEEC) 1000-1899, compiled under the coordination of “Istituto Nazionale di Geofisica e Vulcanologia” of Milan, building on the data contained in AHEAD (Archive of Historical Earthquake Data) and with the methodology developed in the frame of the project “Network of Research Infrastructures for European Seismology” (NERIES). This first portion is composed by 4722 earthquakes, covering the March 1000 - December 1899 time interval, and having magnitude values between 0.0 and 8.5 and focal depths ranging in the 0 - 150 km interval. All the earthquake magnitudes are referred to M_w (moment magnitude) scale.
 2. The SHARE European Earthquake Catalog (SHEEC) 1900-2006, compiled by GFZ Potsdam. This catalog represents a temporal and spatial excerpt of “The European-Mediterranean Earthquake Catalog” (EMEC) for the last millennium (Grünthal and Wahlström, 2012) with some modifications, which are described in Grünthal et al. (2013). This second portion is composed by 19126 earthquakes, covering the January 1900 - January 2006 time interval, having magnitude values between 3.5 and 8.3 and focal depths ranging in the 0 - 660 km interval. All the earthquake magnitudes are referred to M_w (moment magnitude) scale.

Merging these two portions, and extracting events only for Italian region, the final catalog covers the January 1005 - January 1984 time interval, and has magnitude values between 0.0 and 7.42 and focal depths ranging in the 0 - 71 km interval (Figs. 4.2-4.4). All the earthquake magnitudes are referred to M_w (moment magnitude) scale.

- The CFTI5Med, managed by the “Istituto Nazionale di Geofisica e Vulcanologia” (<http://storing.ingv.it/cfti/cfti5/>); from this catalog, we selected 560 earthquakes, covering the January 2 B.C. – October 1997 time interval, having magnitude values between 4.5 and 7.4 and focal depths fixed to 9.99 km (Fig. 4.3). All the earthquake magnitudes are referred to M_e (equivalent magnitude based on macroseismic observations) scale (Guidoboni et al., 2018; Guidoboni et al., 2019).

These two catalogs were merged and after several tests, the final selected historical catalog is composed by 16198 earthquakes, covering the March 1000 - January 1984 time interval, and having magnitude values between 0.0 and 8.5.

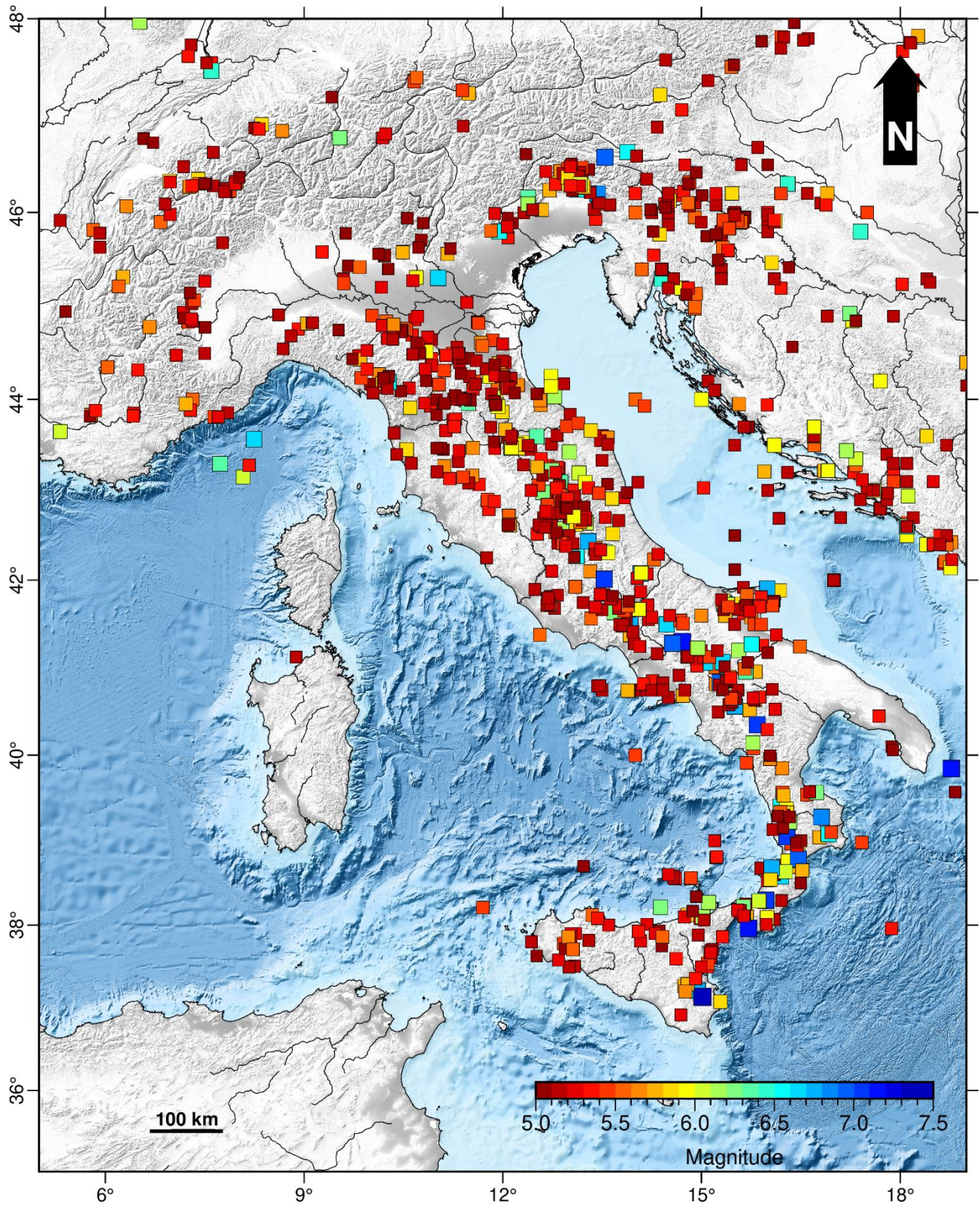


Figure 4.2 – The historical merged SHARE catalog (<https://www.emidius.eu/SHEEC/>). Historical earthquakes ($M \geq 5$) occurring during 1005 – 1984 time interval are represented with squares proportional to the magnitude.

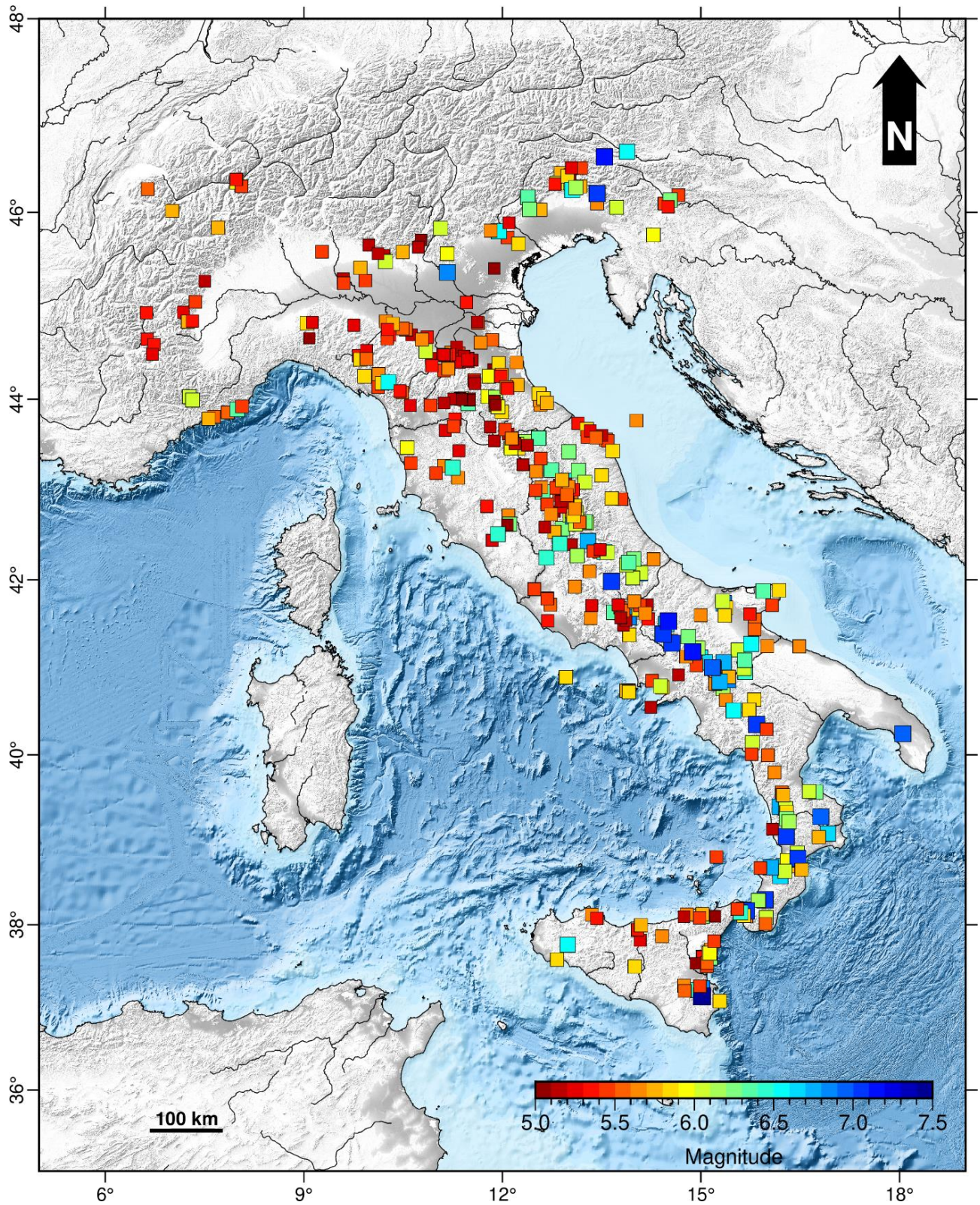


Figure 4.3 – The historical CFTI5Med catalog (<http://storing.ingv.it/cfti/cfti5/>). Historical earthquakes ($M > 5$) occurring during January 2 B.C. – October 1997 time interval are represented with squares proportional to the magnitude.

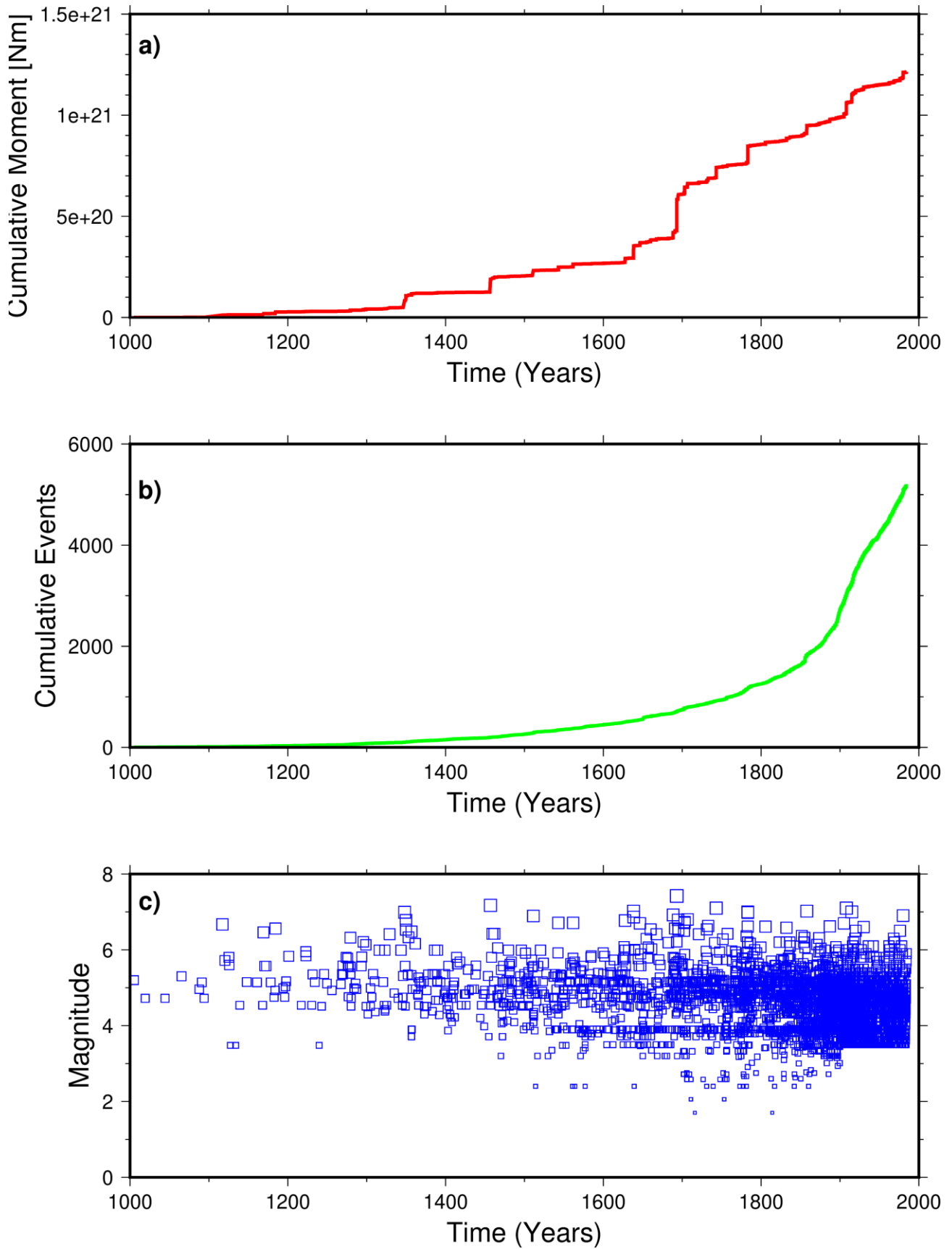


Figure 4.4 – Some plots for the historical merged SHARE catalog (<https://www.emidius.eu/SHEEC/>). a) Cumulative moment-time plot (red line). b) Cumulative events-time plot (green line). c) Magnitude-time plot (blue squares); events are represented with symbols proportional to the magnitude.

4.2.1.2 Instrumental Seismicity.

Two available catalogs of instrumental seismicity for Italy have been analysed:

- Iside, managed by the “Istituto Nazionale di Geofisica e Vulcanologia” (<http://iside.rm.ingv.it/>); from this catalog, we selected 397552 earthquakes, covering the January 1985 - January 2022 time interval, having magnitude values between 0.0 and 7.0 and focal depths ranging in the 0 - 250 km interval (Figs. 4.5-4.7). All the earthquake magnitudes are referred to M_L (local magnitude) scale.
- HORUS (HOMogenized instrUMENTal Seismic catalog), managed by the “Istituto Nazionale di Geofisica e Vulcanologia” (<http://horus.bo.ingv.it/>); from this catalog, we selected 411310 earthquakes, covering the January 1960 - January 2022 time interval, having magnitude values between 0.1 and 6.81 and focal depths ranging in the 0 - 200 km interval (Fig. 4.6). In this catalog, earthquakes magnitudes have been homogenized with conversion relationships between various types of traditional magnitudes (M_L , M_d , M_s , m_b) and moment magnitude M_w , in order to obtain a homogeneous catalog of instrumental earthquakes in terms of M_w (ISIDE Working Group, 2007; Lolli and Gasperini, 2012; Gasperini et al., 2012, 2013a, 2013b; Lolli et al., 2014, 2015, 2018; Lolli et al., 2020).

Because the results obtained using the aforesaid seismic catalogs are very similar, in this Thesis only those obtained using the Iside (<http://iside.rm.ingv.it/>) catalog will be reported.

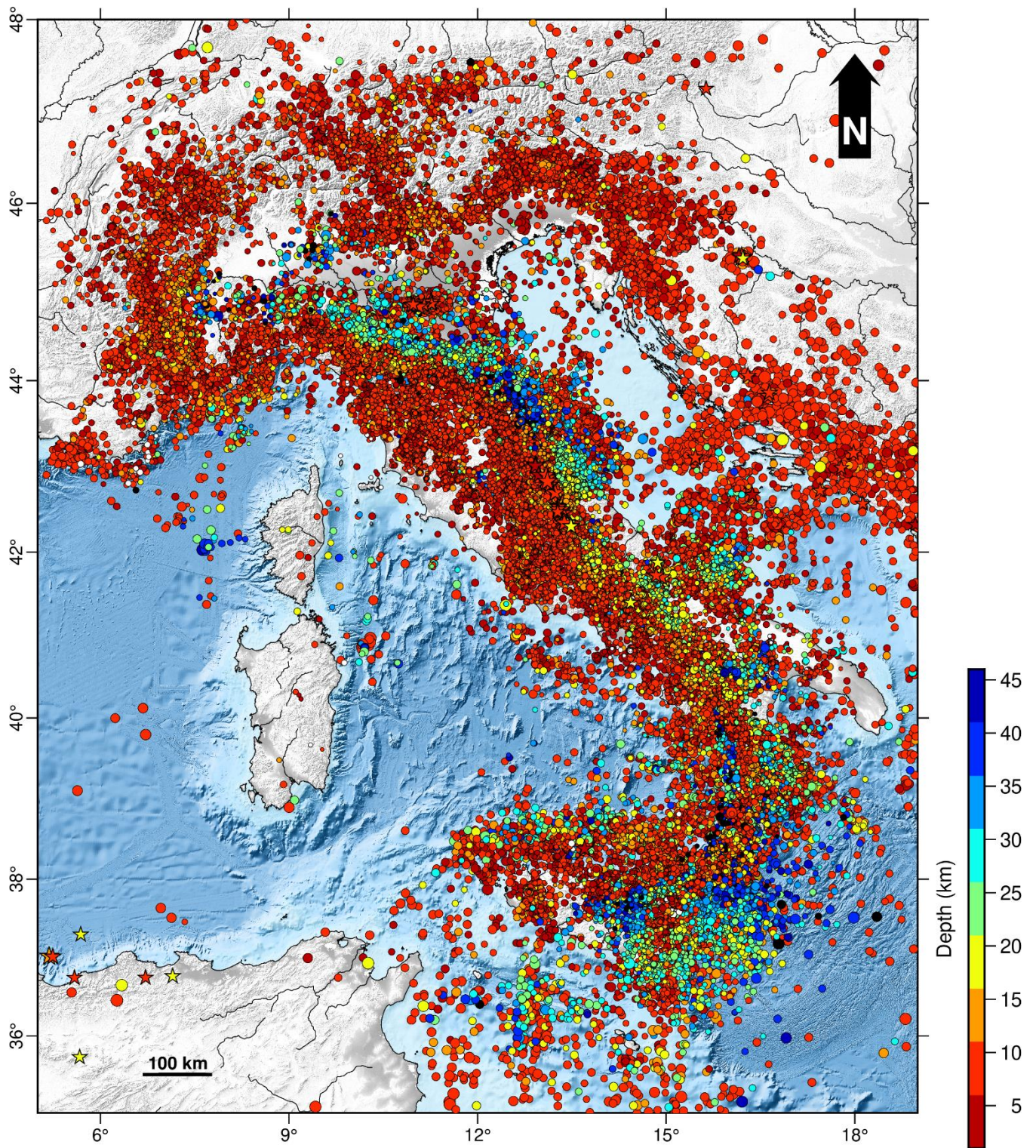


Figure 4.5 – The instrumental crustal seismicity ($M \geq 1.5$) occurring in the investigated area since 1985 (<http://iside.rm.ingv.it/>). Symbols are coloured according to focal depth (< 50 km). Events with $M < 5$ and $M \geq 5$ are represented with symbols proportional to the magnitude, circles and stars, respectively.

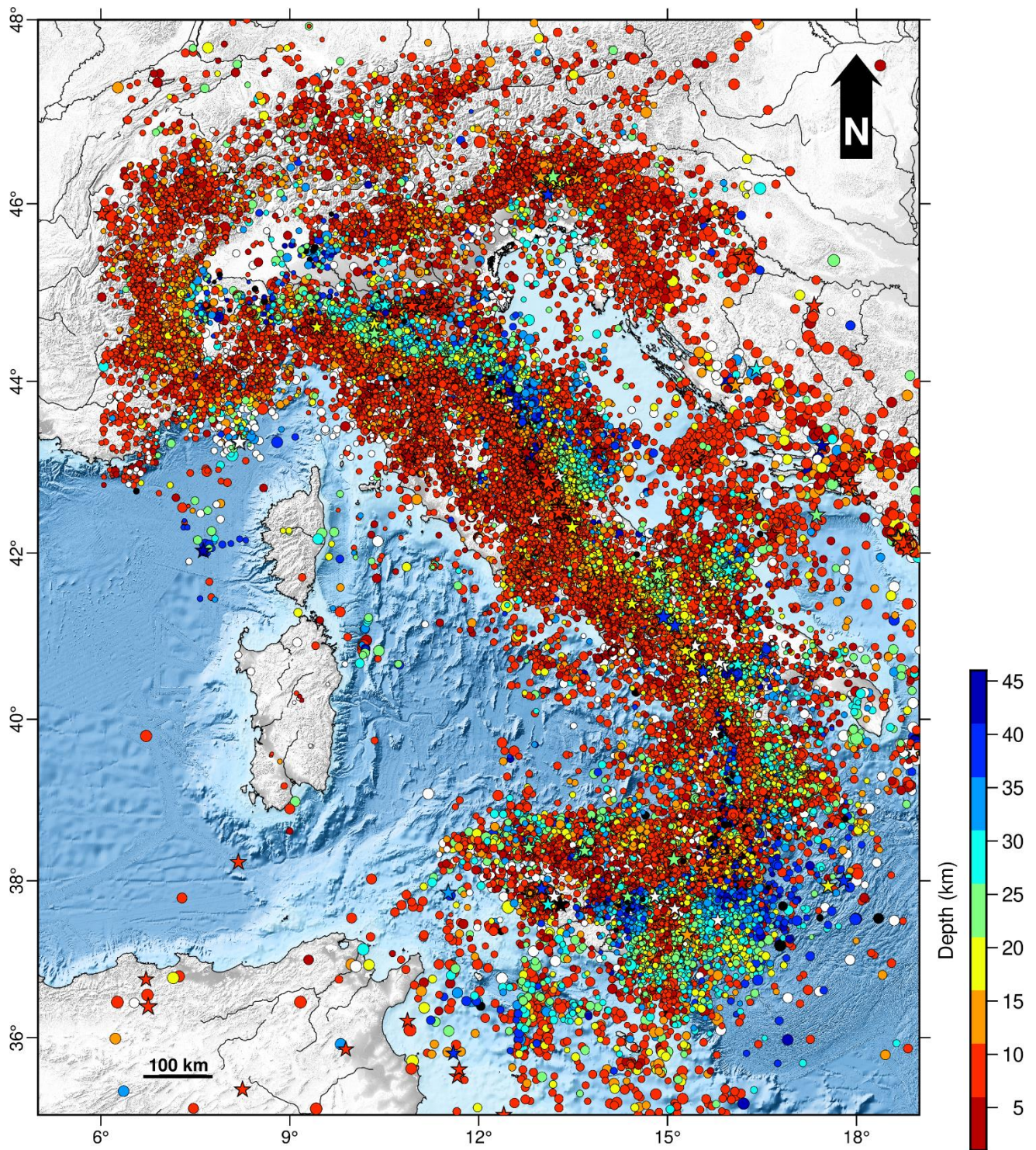


Figure 4.6 – The instrumental crustal seismicity ($M \geq 1.5$) occurring in the investigated area since 1985 (<http://horus.bo.ingv.it/>). Symbols are coloured according to focal depth (< 50 km). Events with $M < 5$ and $M \geq 5$ are represented with symbols proportional to the magnitude, circles and stars, respectively.

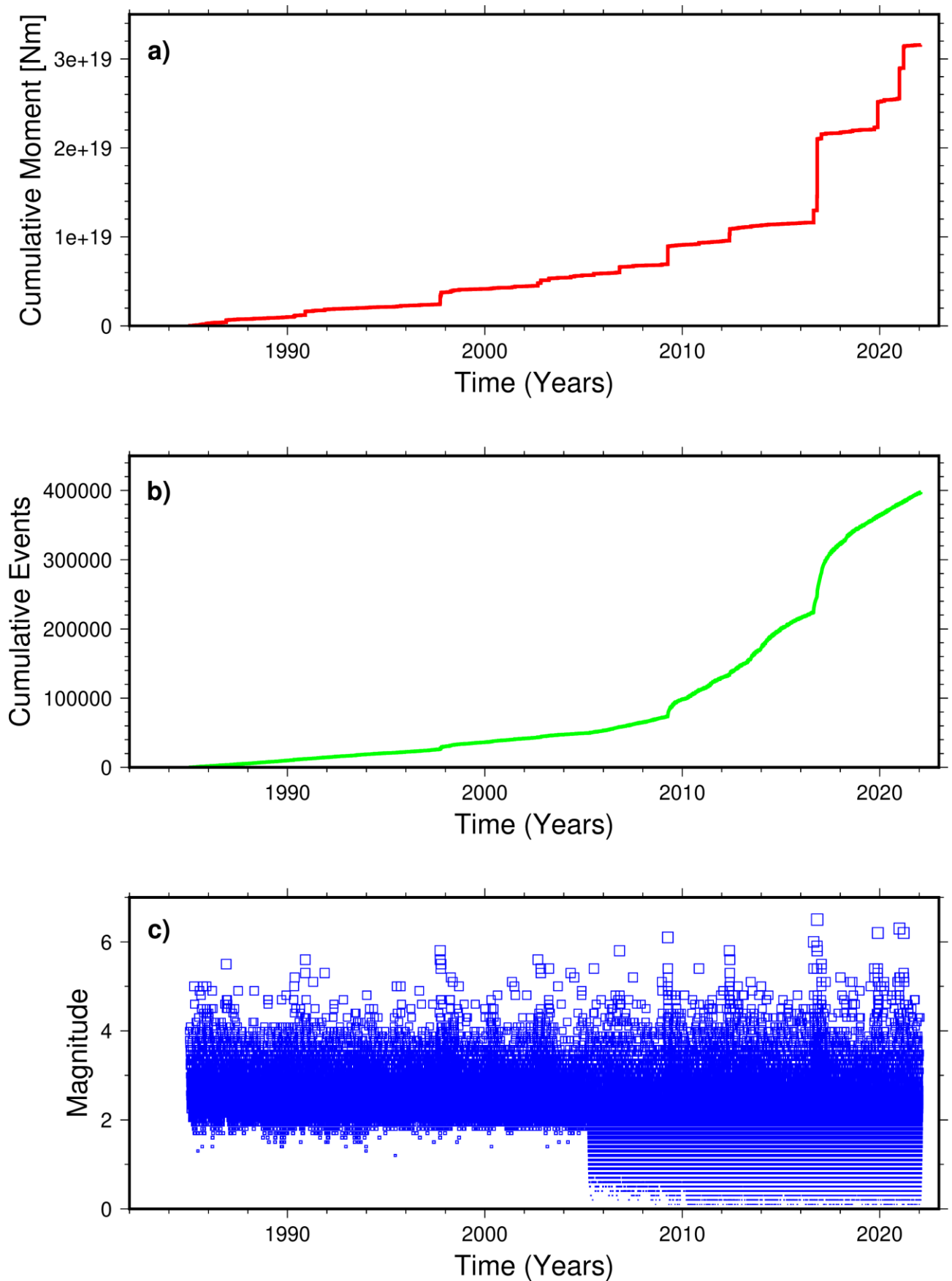


Figure 4.7 – Some plots for the instrumental catalog (<http://iside.rm.ingv.it/>). a) Cumulative moment-time plot (red line). b) Cumulative events-time plot (green line). c) Magnitude-time plot (blue squares); events are represented with symbols proportional to the magnitude.

4.2.2 GNSS data.

All the available permanent GNSS data have been collected and processed. To this aim, we collected data from the following global scale repositories (Fig. 4.8):

- SOPAC (<http://sopac-csrc.ucsd.edu/>);
- UNAVCO (<https://www.unavco.org/>);
- EUREF (<https://www.epncb.oma.be/>);

from the following national scale web-sites:

- ASI (<https://www.asi.it/tlc-e-navigazione/galileo/>);
- RING (<http://ring.gm.ingv.it/>);
- ITALPOS (<https://hxgnsmartnet.com/it-it/>);
- NETGEO (<http://www.netgeo.it/page.php?Id=63>);

and on several regional scales, i.e., continuous geodetic networks managed by local or regional institutions, collected and archived in the local database of “Osservatorio Etneo dell’Istituto Nazionale di Geofisica e Vulcanologia”.

The GNSS data have been processed using the GAMIT/GLOBK software (Herring et al., 2018; <http://www-gpsg.mit.edu>). In order to improve the crustal deformation field of the study area, the obtained solution have been merged with the available ones coming from literature, using a unique reference frame (Fig. 4.8).

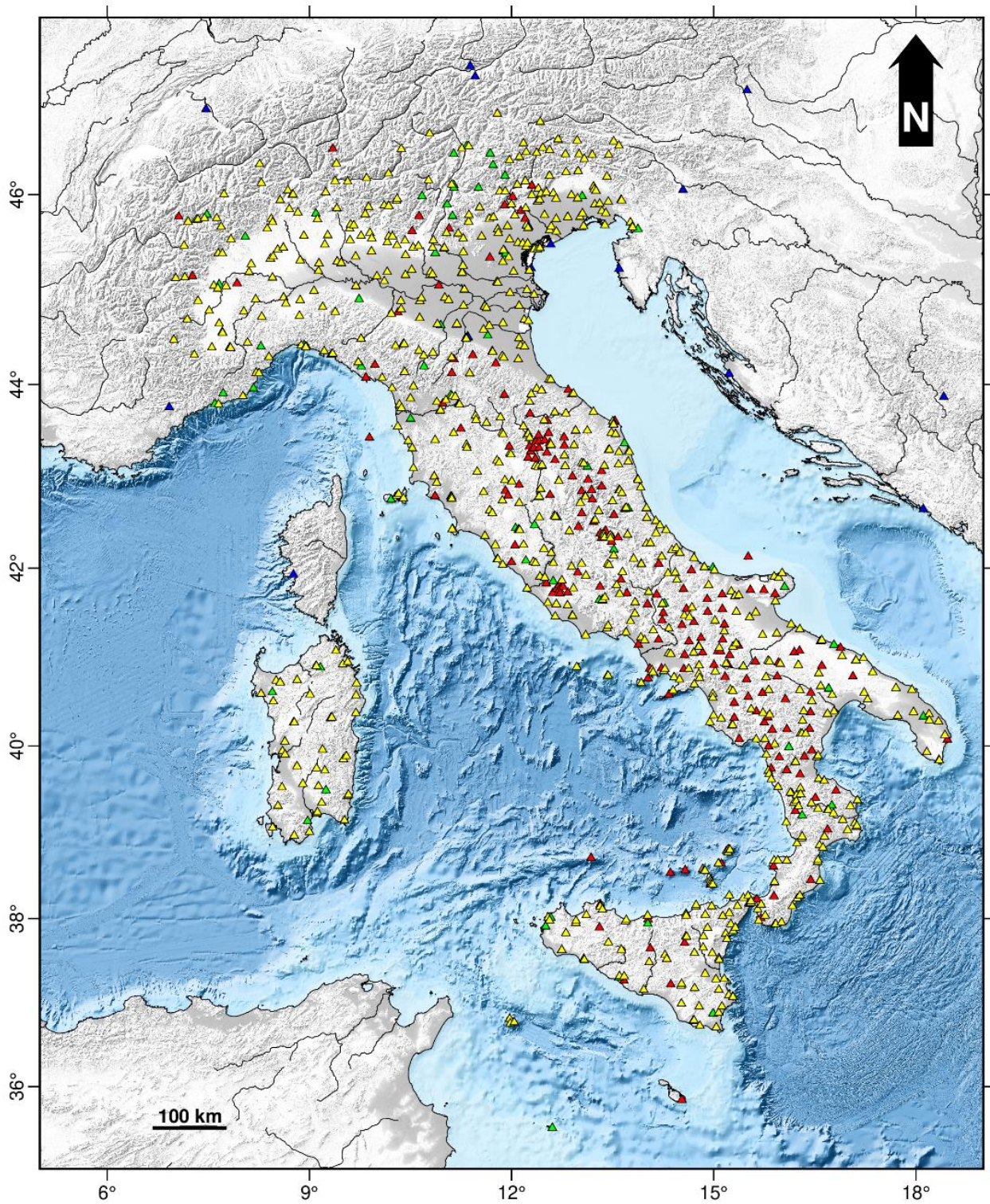


Figure 4.8 – Continuous GNSS stations for the Italian region are reported as coloured triangles. EUREF (<https://www.epncb.oma.be/>), ASI (<https://www.asi.it/>), RING (<http://ring.gm.ingv.it/>) and other networks are reported with blue, green, red and yellow, respectively.

4.2.2.1 Data processing.

As we told above, the GNSS phase observations were processed by using the GAMIT/GLOBK 10.71 software (Herring et al. 2018; <http://www-gpsg.mit.edu>; Fig. 4.8). GAMIT/GLOBK is a GNSS analysis package, designed to run under any UNIX operating system and developed at the Massachusetts Institute of Technology (MIT), the Harvard-Smithsonian Center for Astrophysics, Scripps Institution of Oceanography and Australian National University. Because of the large number of processed sites (Fig. 4.9), the GAMIT analysis was performed independently for 13 sub-networks (Fig. 4.10), each made by 65-75 stations, with each sub-network sharing a set of high-quality IGS (<https://www.igs.org>) stations, in order to improve the overall configuration of the network and to tie the regional stations to an external global reference frame, in the combination step with GLOBK.

The GNSS phase data were weighted according to an elevation-angle-dependent error model using an iterative analysis procedure whereby the elevation dependence was determined by the observed scatter of phase residuals. In this analysis, the parameters of satellites orbit were fixed to the IGS final products. IGS absolute antenna phase center models (igs08.atx and igs14_wwww.atx available at <ftp://ftp.igs.org/pub/station/general/>) for both satellite and ground-based antennas were adopted in order to improve the accuracy of vertical site position component estimations (Schmid et al., 2007). To eliminate phase biases related to drifts in the satellite and receiver clock oscillators during the processing step, first-order ionospheric delay corrections were adopted by using the ionosphere-free linear combination of GNSS phase observables (a double differencing technique). Second-order ionospheric corrections (Petrie et al., 2010) were applied by using the IONEX files (<https://cddis.nasa.gov/archive/gnss/products/ionex/>) from the Center for Orbit Determination in Europe (CODE). The tropospheric delay was modelled as a piecewise linear model and estimated using the Vienna Mapping Function 1 (VMF1) model (Boehm et al., 2006) with a 10° cut-off. The Earth Orientation Parameters (EOP) were tightly constrained to a set of a priori values obtained from IERS Bulletin B. The ocean tidal loading was corrected using the FES2004 model (Lyard et al., 2006) along with the International Earth Rotation Service (IERS) 2003 model for diurnal and semidiurnal solid Earth tides. The results of this processing step are daily estimates of loosely constrained station coordinates and other parameters, along with the associated variance-covariance matrices.

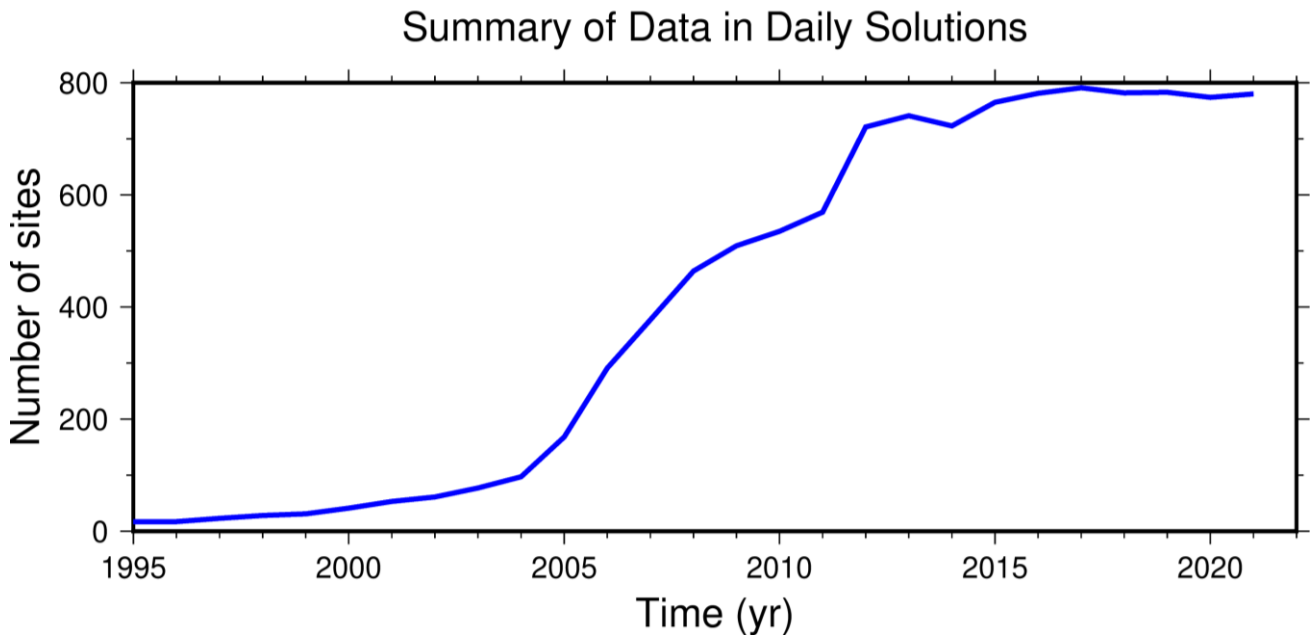


Figure 4.9 - Summary of data in daily solutions. The number of continuous GNSS sites included in each combined daily solution is shown with blue curve.

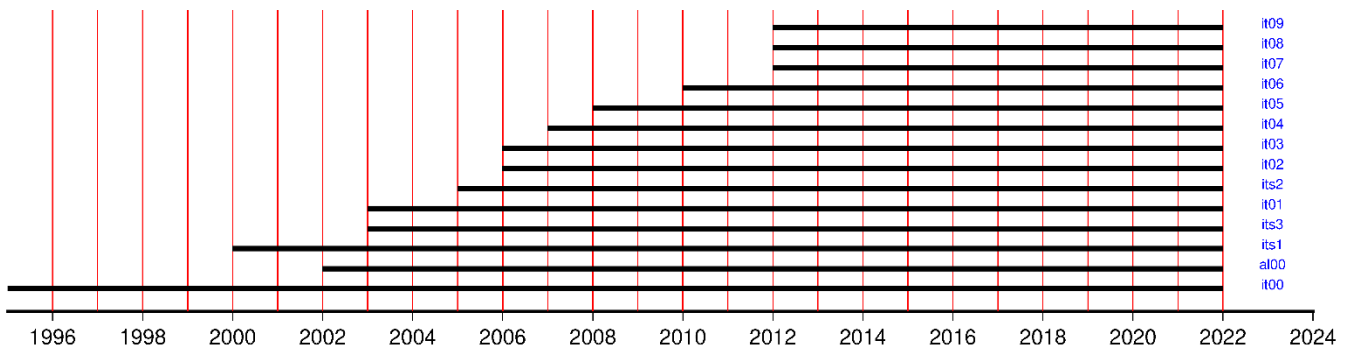


Figure 4.10 – The processed sub-networks with the relative time coverage. Each of them shares a set of high-quality IGS (<https://www.igs.org>) stations in order to improve the overall configuration of the network and to tie the regional stations to an external global reference frame.

4.2.2.2 Analysis of time series parameters.

This subparagraph describes the analysis carried out for the characterization and estimation of linear components, seasonal components and offsets of each daily series obtained.

The observed motion $\mathbf{y}(t)$ of each site in each direction can be written as

$$y(t_i) = a + b t_i + c \sin(2\pi t_i) + d \cos(2\pi t_i) + e \sin(4\pi t_i) + f \cos(4\pi t_i) + \sum_{j=1}^{n_g} g_j H(t_i - T_{g_j}) + \sum_{j=1}^{n_h} h_j H(t_i - T_{h_j}) t_i + \sum_{j=1}^{n_k} k_j \exp\left(-\frac{t_i - T_{k_j}}{\tau_j}\right) H(t_i - T_{k_j}) + v_i \quad (4.1)$$

where t_i for $i = 1 \dots N$ are the daily solutions epochs in units of years, and H is the Heaviside step function. The first two terms are the site position, a , and linear rate, b , respectively. Coefficients c and d describe the annual periodic motion, and e and f describe semi-annual motion. The next term corrects for any number (n_g) of offsets, with magnitudes \mathbf{g} and epochs \mathbf{T}_g . Post seismic motion is modelled as a rate change h_j and/or an exponential decay with magnitude k_j at selected earthquake epochs T_{h_j} and T_{k_j} . The measurement errors, \mathbf{v} , are initially assumed to be independent, identically distributed and random with $E(\mathbf{v}) = 0$.

Assuming that the offsets epochs, rate change epochs, exponential decay epochs, and exponential decay time constants are known, the model is linear with respect to the coefficient

$$\mathbf{x} = [a \ b \ c \ d \ e \ f \ \mathbf{g} \ \mathbf{h} \ \mathbf{k}]^T \quad (4.2)$$

so that

$$\mathbf{y}(t) = \mathbf{A} \mathbf{x} + \mathbf{v} \quad (4.3)$$

where \mathbf{A} is design matrix of partial derivatives. The weighted least squares solution yields the best linear unbiased estimates of the unknown parameters (Nikolaidis, 2002).

When a time series is analysed, placement of the offsets, rate changes, and decays are somewhat subjective and perhaps the most difficult part of the analysis. Non-seismic offsets can be identified by careful inspection of the data residuals, particularly where hardware changes occurred at a site. In placing co-seismic and post-seismic parameters, the proximity of the site to the rupture, quantity and quality data before and after the event, and prior knowledge of the expected signals can be considered.

4.2.2.3 Velocity field computation.

In a successive step, the GAMIT daily solutions (or SINEX files), in the form of loosely-constrained H-files, were combined with GLOBK (GLOBal Kalman filter) software package, a suite of programs whose primary purpose is to estimate a consistent set of daily coordinates (i.e., time series) for all involved sites. Each time series was analysed for linear velocities, periodic signals, and antenna jumps according to 4.1 and by using the TSVIEW software package (Herring, 2003). In this step, any position estimate with uncertainty greater than 20 mm or whose value differed by more

than 15 mm from the best-fitting linear trend was removed to obtain clean time series. To account properly for temporally correlated noise in the velocity estimation, a first-order Gauss-Markov approach ([Herring, 2003](#)) was adopted. As a final step, by using the GLORG module of GLOBK, the daily solutions and their full covariance matrices were combined to estimate a consistent set of positions and velocities in a Eurasian reference frame ([Altamimi et al., 2016](#); [Fig. 4.11](#)).

GNSS phase processing can take a considerable time and GLOBK provides a fast method for make large network solutions, combining many days to years of data together and studying alternative parameterization and reference frames for the velocities of sites. In fact, its two main uses are to generate velocity field estimates and time series in a well-defined and often different reference frames, but it can also be used to merge large networks of GNSS sites or different GNSS processing. It is also good to know that GLOBK is a smoothing Kalman filter and can incorporate random walk process noise in its estimation (method for accounting for temporally correlated noise in time series).

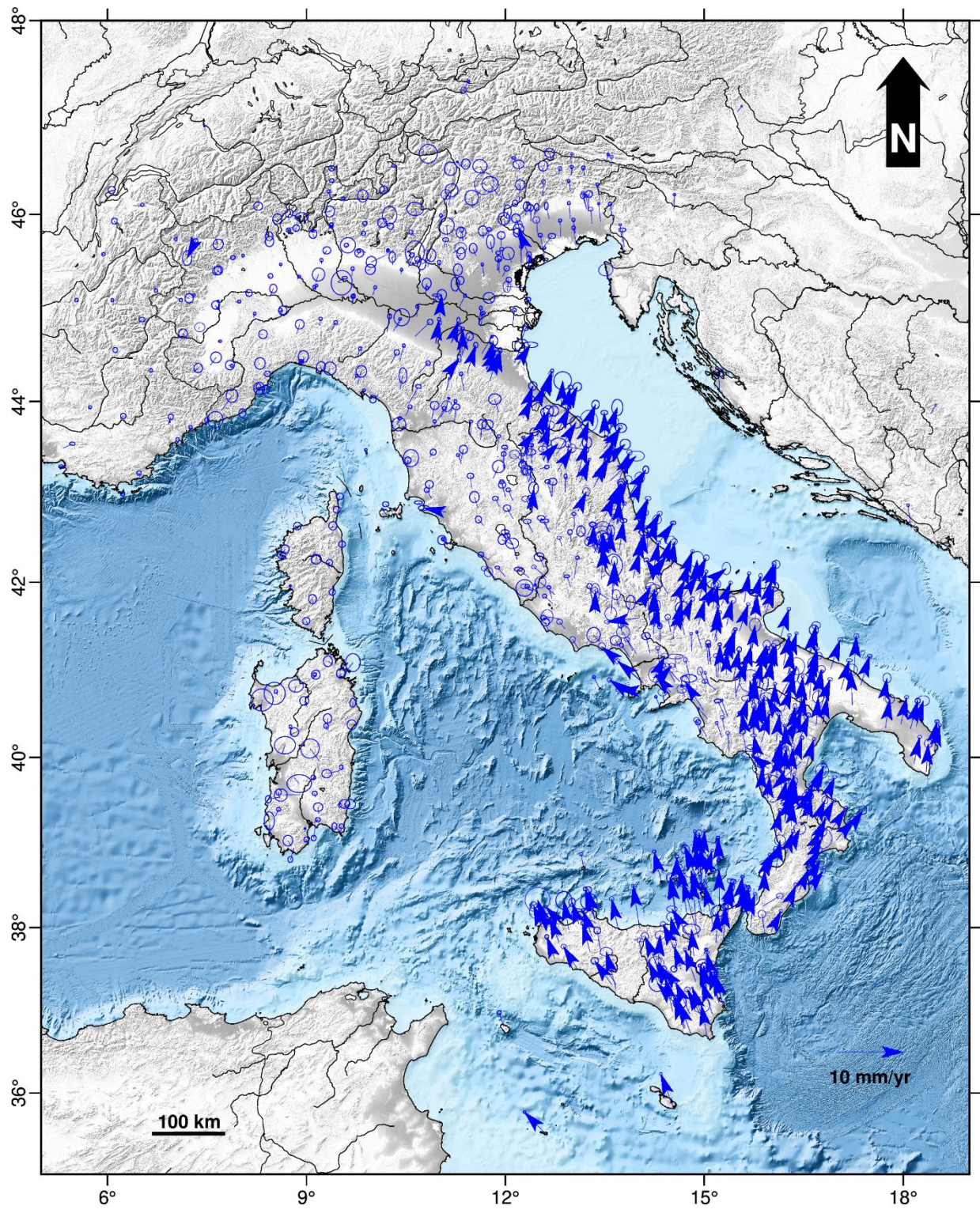


Figure 4.11 – Geodetic velocity field and 95% confidence ellipses for Italy in a fixed Eurasian plate.

4.2.2.4 Strain-rates computation.

The horizontal strain-rates were estimated using the first of the three methods presented in [Chapter 2](#). The method of [Shen et al. \(2015\)](#) allows modelling the horizontal velocity gradients on a regularly spaced $0.25^\circ \times 0.25^\circ$ grid by means of a least squares inversion ([Fig. 4.12](#)). The method takes into account optimal weighting functions of the data, allowing obtaining a finer resolution, especially on regions characterized by sparsely distributed data. In detail, the weight for each observation is given by the product of the area of the Voronoi cell occupied by the GNSS site and a Gaussian weight ($\exp(-\Delta R_{ij}^2/D_j^2)$); where R_{ij} is the distance of site i from the grid point j and D_j is a smoothing parameter determined for each evaluation site, based on the in situ data strength, so that the total weight (W) of observations on each grid point is the same.

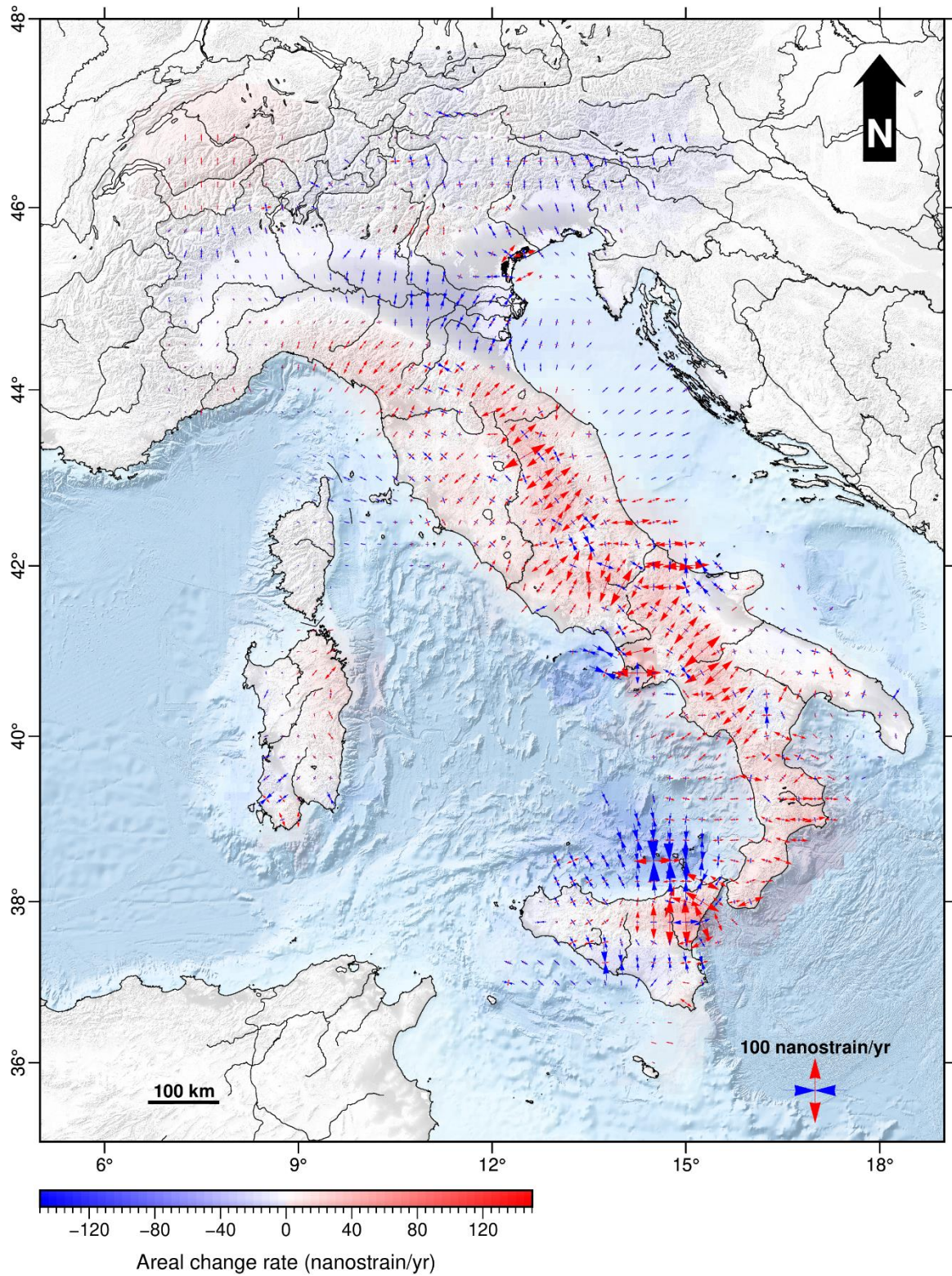


Figure 4.12 – Geodetic strain-rate field for Italy: the background colour represents the rate of areal change, while arrows represent the greatest extensional (red) and contractional (blue) horizontal strain-rates.

4.3 The application of the workflow: Results.

In this paragraph, parameters estimation and obtained results for Italy will be exposed. The used approaches and the mathematical formulation for intermediate parameters and seismic and geodetic moment-rates computation have just been discussed in [Chapter 2](#).

4.3.1 Seismic source zonation and cell size definition.

The seismic and geodetic moment-rates comparison, as well as seismic hazard, are usually calculated on seismically homogeneous source zones that are defined because of tectonic, geological and seismic considerations ([Mazzotti et al., 2011](#); [Sparacino et al., 2020](#)). Available seismic zonation for the study area (e.g., [Meletti et al., 2021](#) and references therein) consists of several small size sources along main active faults. Most of the seismic sources are not fully covered by GNSS stations, so that the strain-rates information can only be derived from the velocity interpolation. To overcome these limitations and enable a common estimation for different tectonic settings without the need for a priori tectonic information, a spatially extended parametrization for the seismic sources has been adopted. Several tests have been done in order to subdivide the study area, with different grid-knots dimension and resulting overlap. Finally, the study area has been divided into a regular grid with square cells of $1^\circ \times 1^\circ$, in which the distance between two grid-knots is 0.25° . In this way, an overlap between the cells has been created in order to remove any edge effect.

4.3.2 M_{max} estimation.

We have seen in [Chapter 2](#) that different approaches exist to estimate the M_{max} value of a given region. For Italy case study, the maximum magnitude value has been estimated using the toolbox developed by [Kijko and Singh \(2011\)](#). The mixed seismic catalog with $M \geq 5$, assuming an average error of 0.3 on magnitude values and a model uncertainty of 25%, has been used as the input file. M_{max} values have been estimated by considering the same grid-knots of the other computations, where the cell's overlap has been enlarged in order to take the location uncertainties of historical earthquakes into account. For each cell with at least 30 events, among the twelve estimated M_{max} values, the one associated with the smallest uncertainty has been chosen as the best one.

The pattern of [Fig. 4.13a](#) is characterized by values ranging from 4.3 to 7.77. The highest values (> 7.0) have been estimated for Central and Southern Italy, mainly because of the devastating M_w 7.1 1908 Messina, M_w 7.19 1456 Central-Southern Apennines, M_w 7.32 1693 Southeast Sicily earthquakes. Magnitudes values within the 6.5 - 7.0 were estimated for the upper part of Central Apennines. Values between 6.0 - 6.5 have been founded in Northern Apennines. Alps are characterized by smaller values ranging 5.0 - 5.5; the eastern Po Valley is characterized by values ranging 6.5 - 7.0, mainly because of the 1976 Friuli earthquake. The southwest part of Sicily is characterized by values ranging 6.0 - 6.5, while the central one by lower values ranging 5.0 - 5.5. South-eastern Alps are characterized by higher values, i.e. > 6.5 , than the western ones, i.e. < 5.5 . Estimated uncertainties ([Fig. 4.13b](#)) range from 0.0 to 0.95, with the largest values (~ 0.95) in Northern Alps and Central Italy.

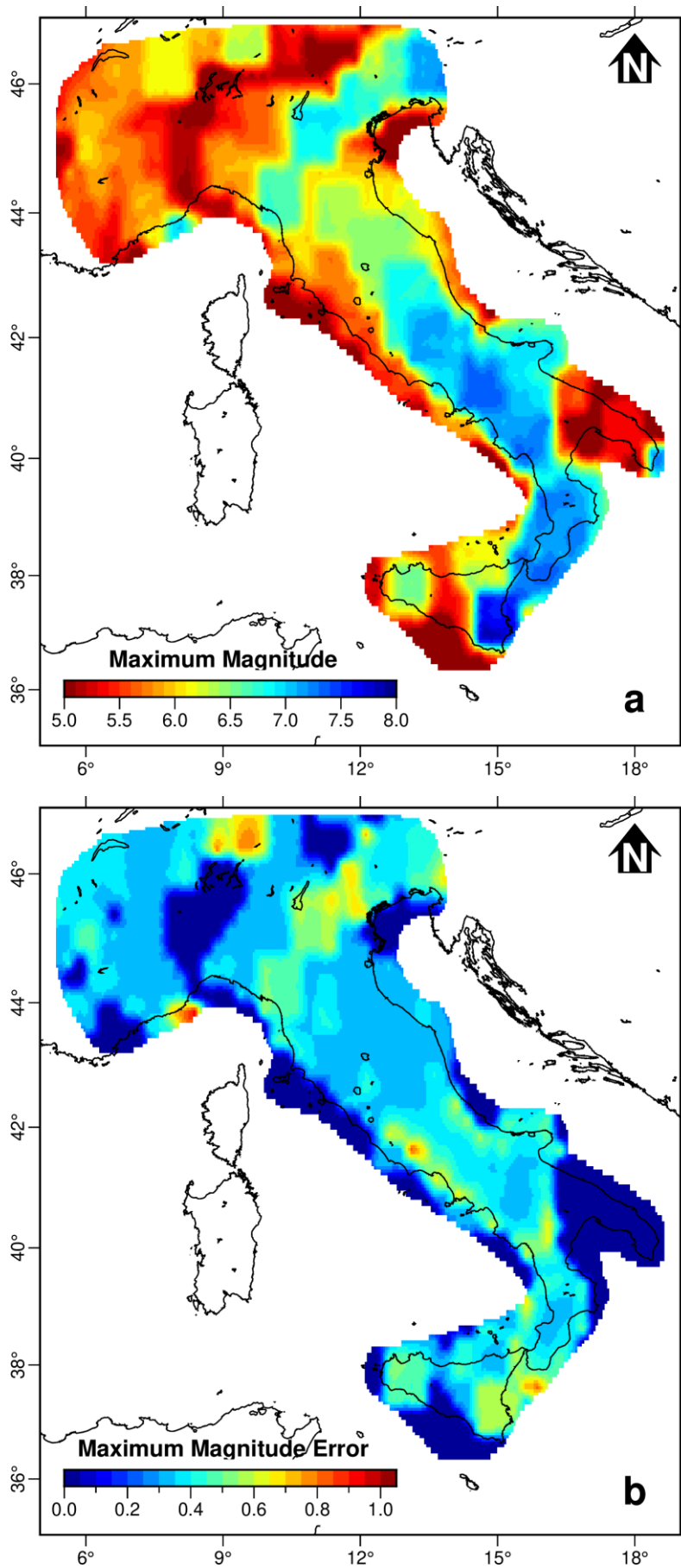


Figure 4.13 – Spatial pattern of estimated maximum magnitude (a) along with its estimated uncertainties (b) for Italy, using the kriging regression interpolation method.

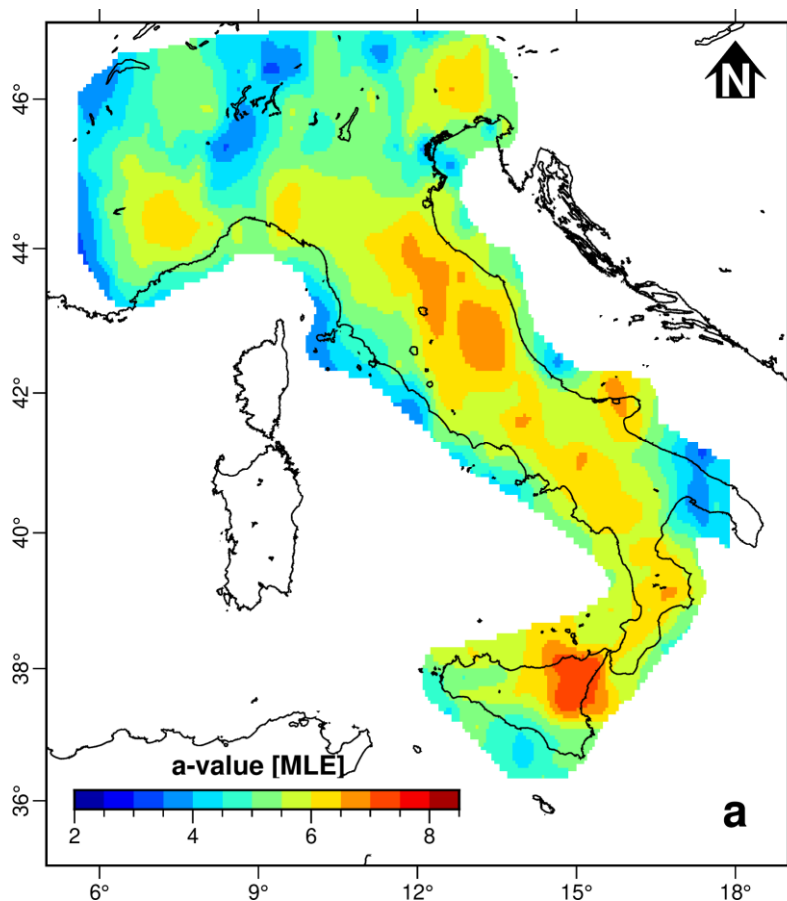
4.3.3 Coefficients of the Gutenberg-Richter recurrence relation.

As mentioned previously, the coefficients a and b of the Gutenberg-Richter recurrence relation (eq. 2.30) express the frequency vs. magnitude distribution of earthquakes over a given space-time interval.

These coefficients have been estimated within the $1^\circ \times 1^\circ$ grid. Computation has been limited to cells with at least 30 earthquakes, by using the Iside instrumental seismic catalog (<http://iside.rm.ingv.it/>) with $M_w > 2$ and the three different approaches previously exposed: the Maximum Likelihood Estimation (MLE; Weichert, 1980), the Least Square Regression (LSR; Han et al., 2015), and the Robust Fitting Method (RFM; Han et al., 2015). These three different methods have been performed in order to check the robustness of achieved results.

The a - and b -value distribution varies significantly over the area. The a -value ranges between 3.31 - 7.32 (Fig. 4.14a), 2.55 - 7.34 (Fig. 4.14b) and 2.55 - 7.27 (Fig. 4.14c), for MLE, LSR and RFM methods, respectively. Values smaller than 5.5 are distributed for the most part of Northern Italy. The higher values are distributed in Central and Southern Apennines, and in the north-eastern part of Sicily. Despite their various limitations and different statistical approaches (Par. 2.2.2), a quite similar pattern can be seen for all the methods.

The b -value ranges between 0.68 - 1.49 for MLE method (Fig. 4.15a), and between 0.56 - 1.49 both for LSR (Fig. 4.15b) and RFM (Fig. 4.15c) methods. Even for the b -values, the three methods show a general agreement. There could be seen some differences in Central Apennines, Messina Straits and southern Sicily, with MLE method showing lower values.



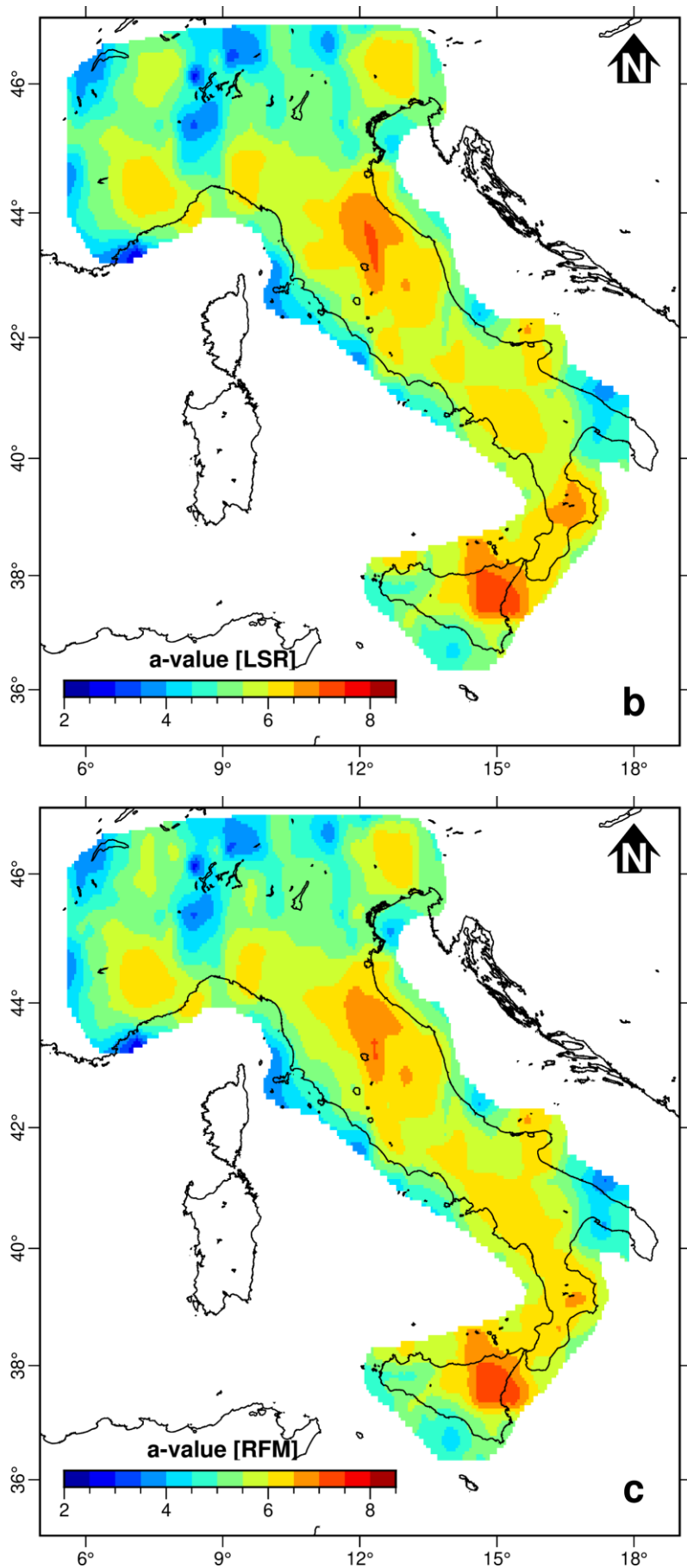
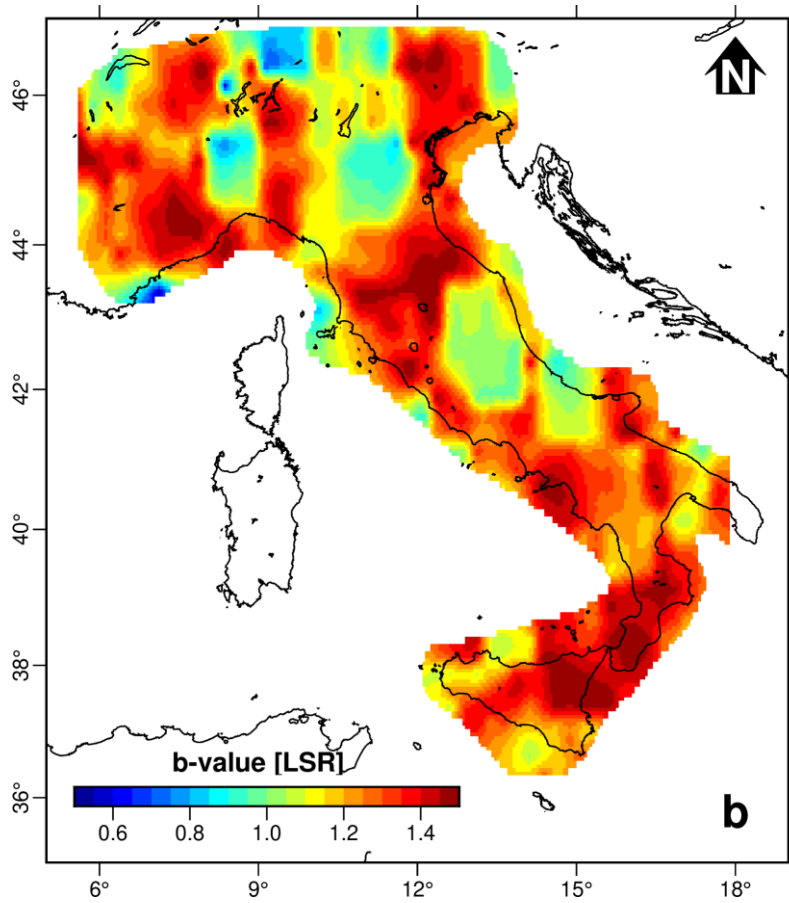
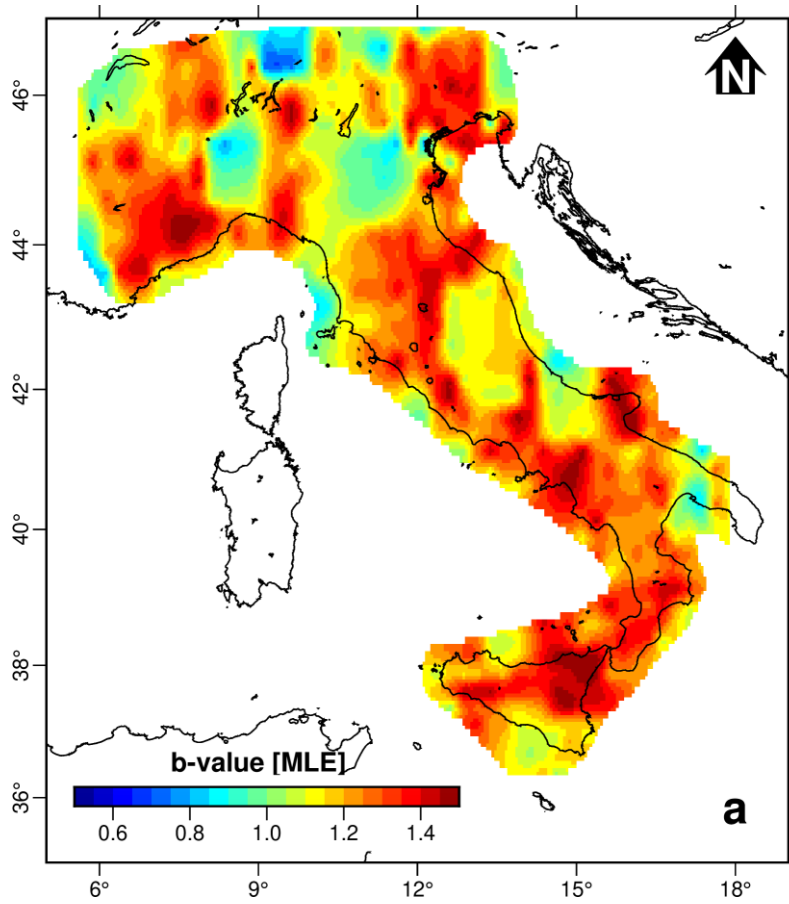


Figure 4.14 – Spatial pattern of *a*-value for Italy as estimated by the MLE (a), LSR (b) and RFM (c) statistical approaches, using the kriging regression interpolation method.



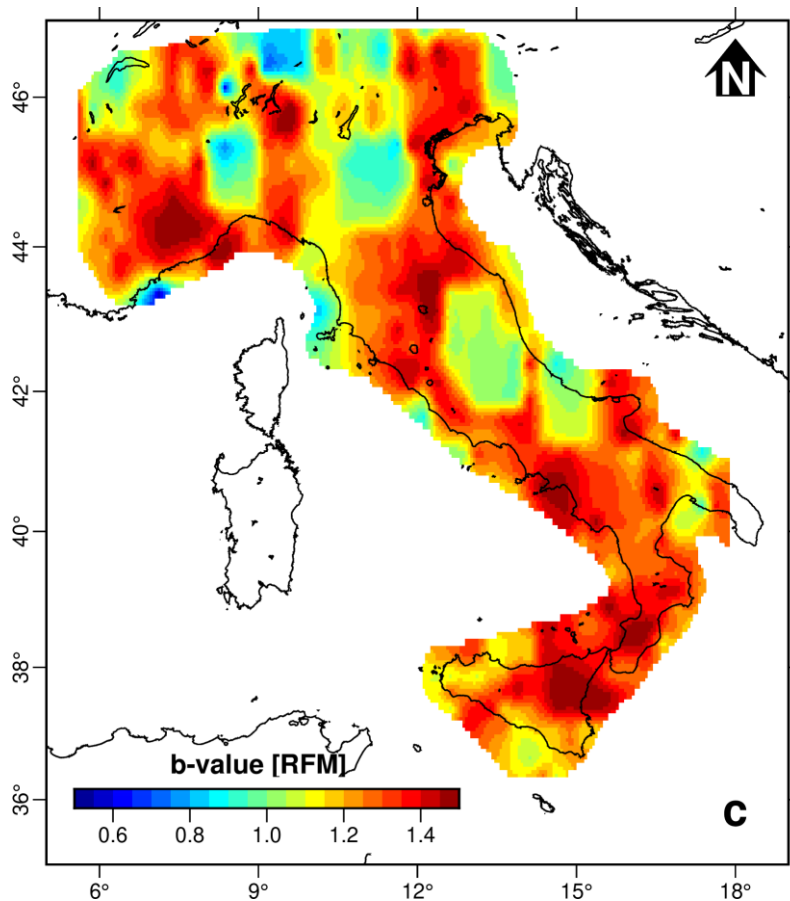


Figure 4.15 – Spatial pattern of *b-value* for Italy as estimated by the MLE (a), LSR (b) and RFM (c) statistical approaches, using the kriging regression interpolation method.

4.3.4 The seismogenic thickness.

As has been said in the previous chapters, the seismogenic thickness layer is a key parameter for seismic hazard since it helps constrain the maximum depth of faulting and the potential earthquake magnitude (Nazareth and Hauksson, 2004).

Previous studies in Italy have estimated a seismogenic thickness which varies between 10 – 20 km for Southern Italy (Jenny et al., 2004), 10 ± 2.5 km for Apennines and Calabrian Arc (Hunstad et al., 2003; D’Agostino et al., 2011; D’Agostino, 2014). For Chiarabba and De Gori (2016) the seismogenic thickness is about 12 - 14 km along the eastern Alps, 16 - 18 km in Southern Apennines and 6 - 10 km in the Northern Apennines (but they used a dataset with a time interval different from that used in this PhD Thesis).

To estimate the thickness of the seismogenic layer of Italy, the investigated region has been divided into a regular grid with square cells ($0.5^\circ \times 0.5^\circ$), with a 64% overlap and by taking into account the events of the instrumental seismic catalog with depths ranges in 1 - 30 km. Computation has been limited to cells with at least 25 earthquakes (Fig. 4.16).

The events reported in the used seismic instrumental catalog do not report hypocentral vertical errors, therefore the bootstrap statistic with replacement implemented in *Hs_estimation.m* program (Chap. 3, Par. 3.3), in order to evaluate the impact of these errors to the seismogenic thickness estimation, provides a reasonable uncertainty estimation. With this statistical method, the

depths falling within a cell are randomly sampled with replacement. Then, the 90th percentile of the new frequency distribution has been computed for each resample and the process was repeated N times, thus obtaining N estimates of the desired measures. These values define the empirical bootstrap distribution from which we compute the 90% confidence interval, that is, the range of depths that hold the parameter of interest with a frequency of 90% if the experiment is repeated.

Along the Apennines extensional belt, significant variations in seismogenic thickness are found, with the more elevated values of depths ranging between 10 and 18 km. More in details, the obtained values are the following:

- $H_s \sim 10 - 15$ km in Alps and central Apennines;
- $H_s \sim 20 - 25$ km in Northern Apennines and Southern Calabria;
- $H_s \sim 25 - 30$ km south-eastern Sicily.

In general, the obtained results are slight higher than those found in literature are.

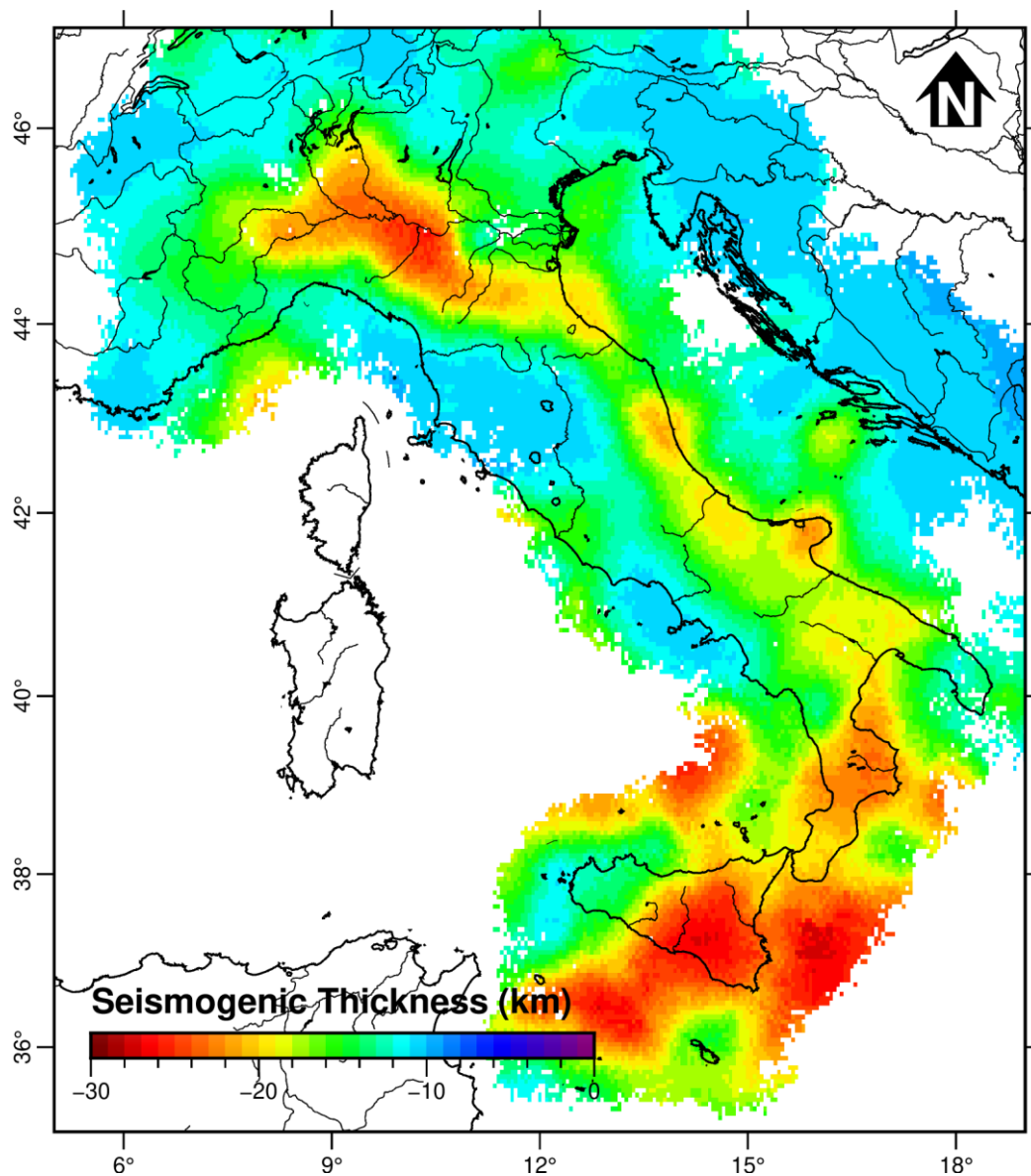


Figure 4.16 – Smoothed seismogenic thickness pattern beneath Italy using the nearest neighbour’s regression interpolation method. The layer thickness has been estimated by considering all earthquakes with focal depth lesser than 30 km and $M > 2.0$.

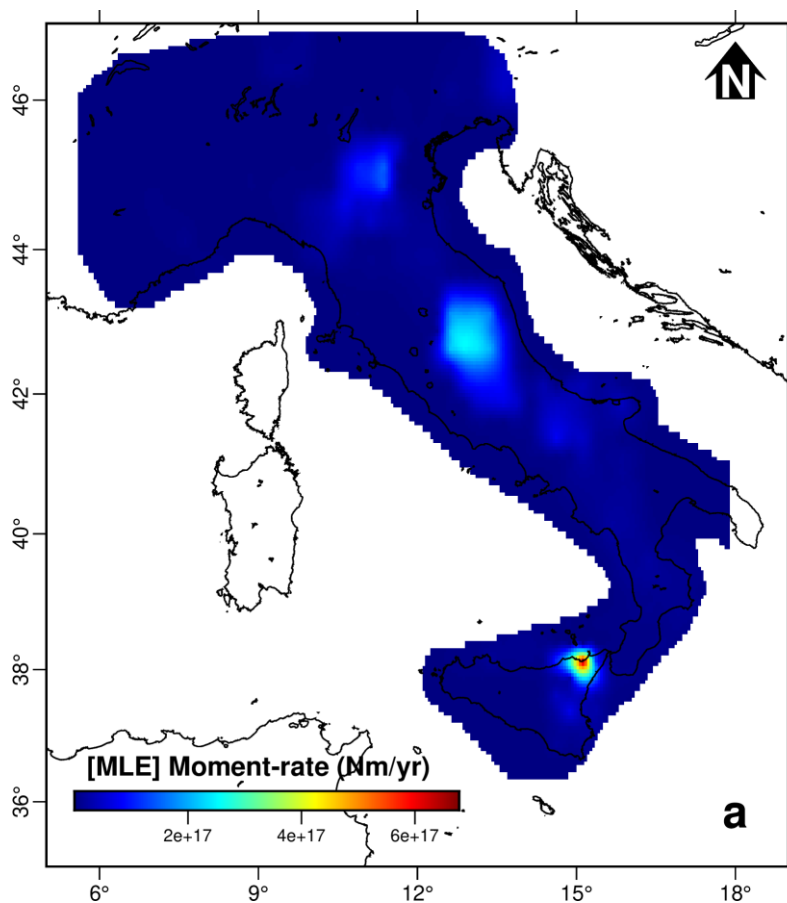
4.3.5 Seismic moment-rates.

The estimated moment-rates for Italy by considering the truncated Gutenberg-Richter distribution are reported in Fig. 17. Given the overall wide range of values, we obtained the following ranges of values (distinguished according to the statistical methods used for *a*- and *b*-value calculation):

- MLE: $7.58 \cdot 10^{13}$ - $6.80 \cdot 10^{17}$ N m yr⁻¹ (Fig. 17a);
- LSR: $7.22 \cdot 10^{13}$ - $8.02 \cdot 10^{17}$ N m yr⁻¹ (Fig. 17b);
- RFM: $7.24 \cdot 10^{13}$ - $9.41 \cdot 10^{17}$ N m yr⁻¹ (Fig. 17c).

The seismic moment-rates above are estimated according to eq. (2.32). We can see that low values are concentrated in most of the study area, especially on Alps and on Southern Apennines. The intermediate values are founded in Northern and Central Apennines, while the highest in the north-eastern part of Sicily.

The seismic moment-rates were also estimated by using the summation approach of Kostrov (1974) and achieved values range in the interval $1.46 \cdot 10^{13}$ - $3.45 \cdot 10^{17}$ N m yr⁻¹ (Fig. 18). With this method, higher values have been found, especially in Central and Southern Apennines, Messina Straits and Southern Sicily.



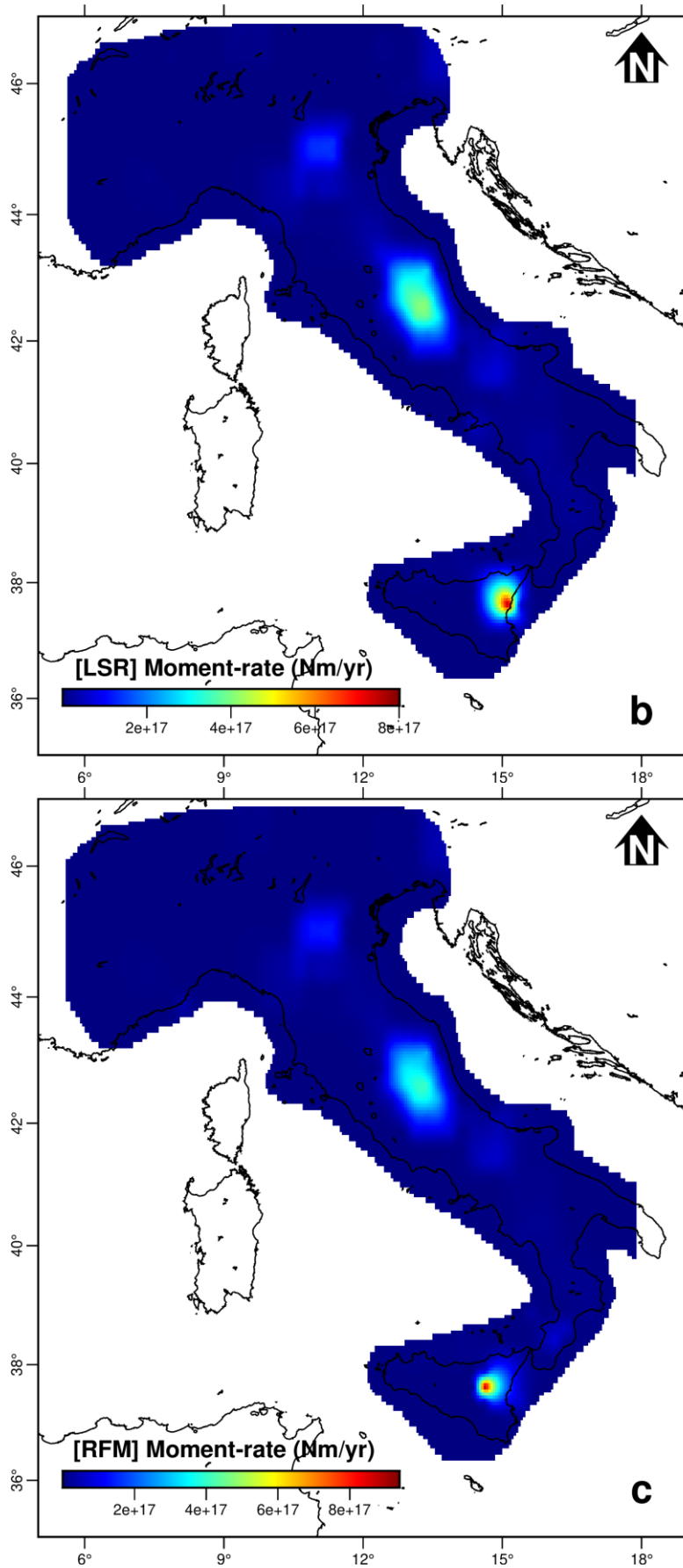


Figure 4.17 – Spatial pattern of the estimated seismic moment-rates for Italy, by considering the truncated Gutenberg-Richter distribution with MLE (a), LSR (b) and RFM (c) statistical approaches, using the kriging regression interpolation method.

The Kostrov approach reported in eq. (2.27) is influenced by the distribution of the magnitudes inside the investigated region (see [Supplementary Material](#) for more details) and it just normalizes the cumulative estimated seismic moments for the recorded events by the temporal duration of the catalog (1021 years in this case, for the merged catalog). As a result, this method is closely dependent on i) the length of the catalog, and ii) the possible lack of large earthquakes (with high recurrence rate compared to the catalog duration). Conversely, the truncated cumulative Gutenberg-Richter distribution approach according to eq. (2.32) takes into account the incompleteness of the catalog using the magnitude distribution of the events through the estimate of the *b-value*, and therefore it is insensitive to the duration of the observation period.

In general, the study area is characterized by low seismic moment-rate values, whereas cells with intermediate and high values concentrate along the Central and Southern Apennines and on the south-eastern side of Sicily. Results coming from both approaches are fairly similar for most of the investigated area, therefore providing robust estimations on upper/lower boundaries of the seismic moment-rates.

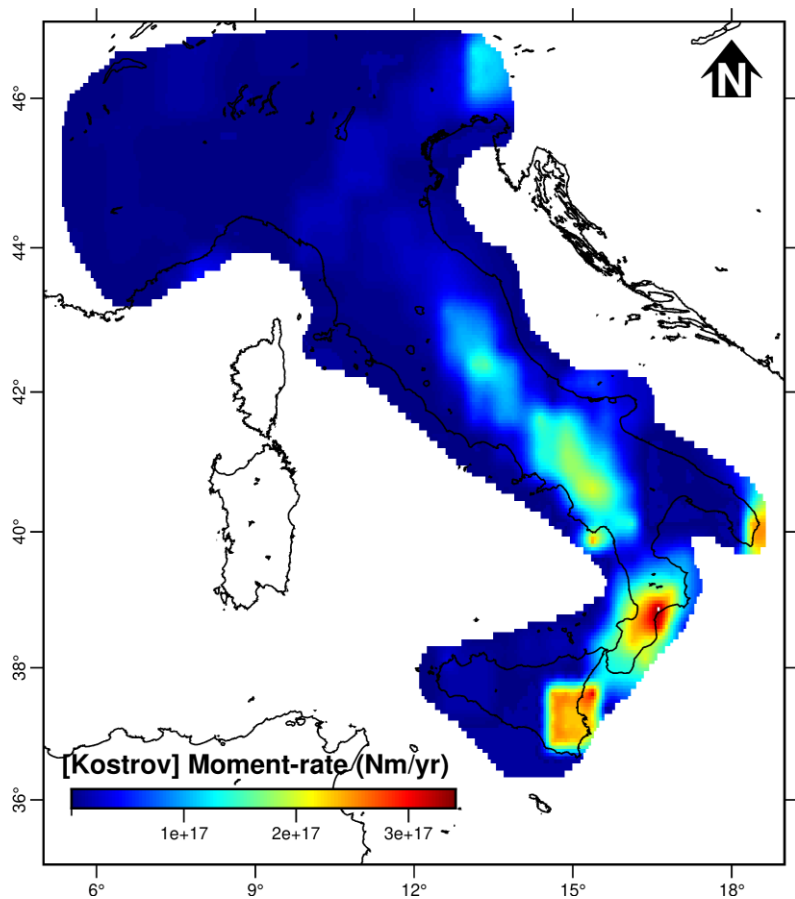


Figure 4.18 – Spatial pattern of the estimated seismic moment-rates by considering the cumulative Kostrov summation method, using the kriging regression interpolation method.

4.3.6 Geodetic strain and moment-rates.

The values of the geodetic strain and moment-rates are reported in [Fig. 19a](#) and [Fig. 19b](#), respectively.

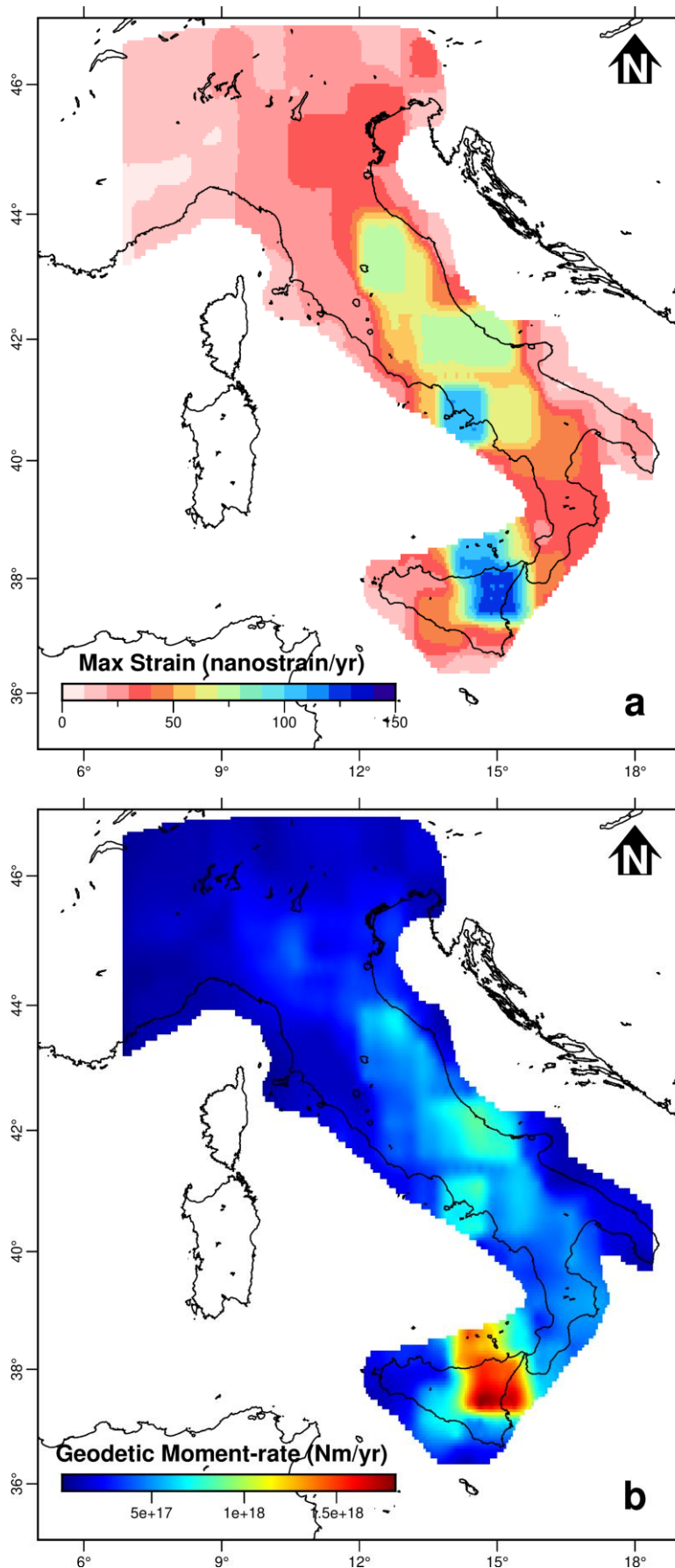


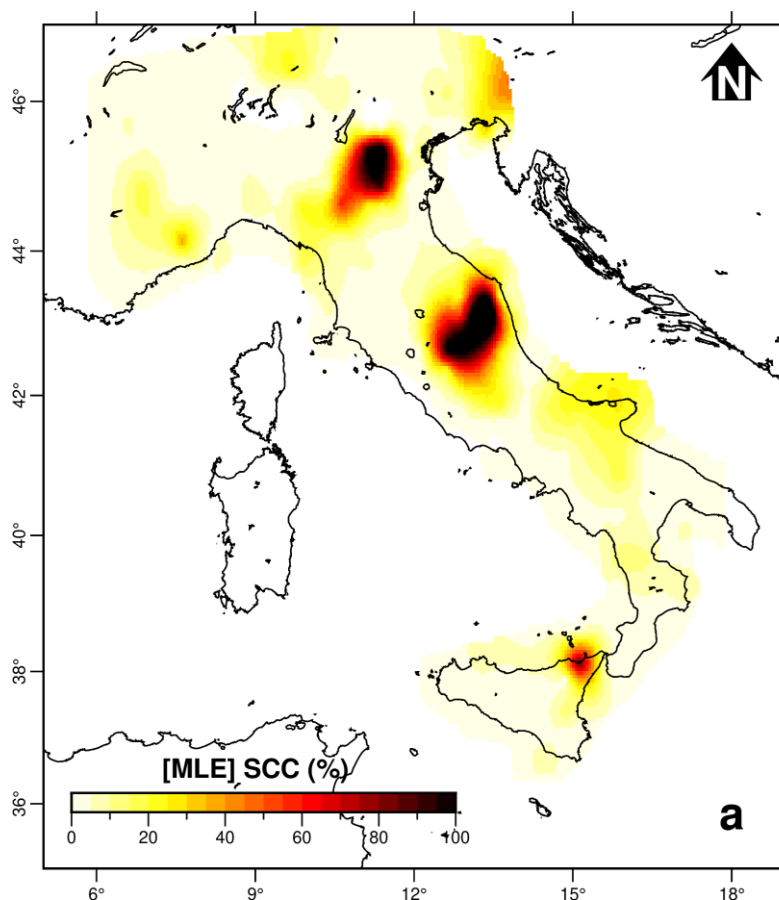
Figure 4.19 – (a) Spatial pattern of the maximum geodetic strain-rates for Italy, previously estimated with the method described in Shen et al. (2015). (b) Spatial pattern of the estimated geodetic moment-rates for Italy according with Hyndman and Weichert (1983) formulation. A kriging regression interpolation method has been adopted for both panels.

The maximum values of the geodetic strain-rates previously estimated according with [Shen et al. \(2015\)](#), range in the interval $10 - 120$ nanostrain yr^{-1} . Low values are mostly concentrated in Alps and Northern Apennines, while intermediate values are found in the rest of the study area. High values of the geodetic moment-rates have been found only in the northeastern part of Sicily.

The geodetic moment-rates values estimated according to [eq. \(2.16\)](#) are reported in [Fig. 19b](#) and range in the interval $1.62 \cdot 10^{16} - 1.82 \cdot 10^{18}$ N m yr^{-1} . Low values are mostly concentrated in Alps and Northern Apennines, while moderate values are found in the rest of the study area. The pattern of the geodetic moment-rates, like the previous one, is characterized by high values only in the north-eastern part of Sicily.

4.3.7 Seismic Coupling Coefficient (SCC).

The SCC estimations for Italy are reported in [Figs. 4.20 - 4.21](#). Most of the area is characterized by low ($< 25\%$) and intermediate ($25\% - 50\%$ interval) SCC values, while only a few cells show high ($50\% - 75\%$ interval) and very high SCC values ($> 75\%$). For SCC calculated using the seismic moment-rates estimated by considering the truncated Gutenberg-Richter distribution (MLE-SCC, LSR-SCC and RFM-SCC hereafter; [Fig. 4.20abc](#)), cells with intermediate SCC values are located in a small area of Northern Apennines (Friuli), while in Emilia and Central Apennines intermediate and high values are detected. In the rest of the area, low values predominate.



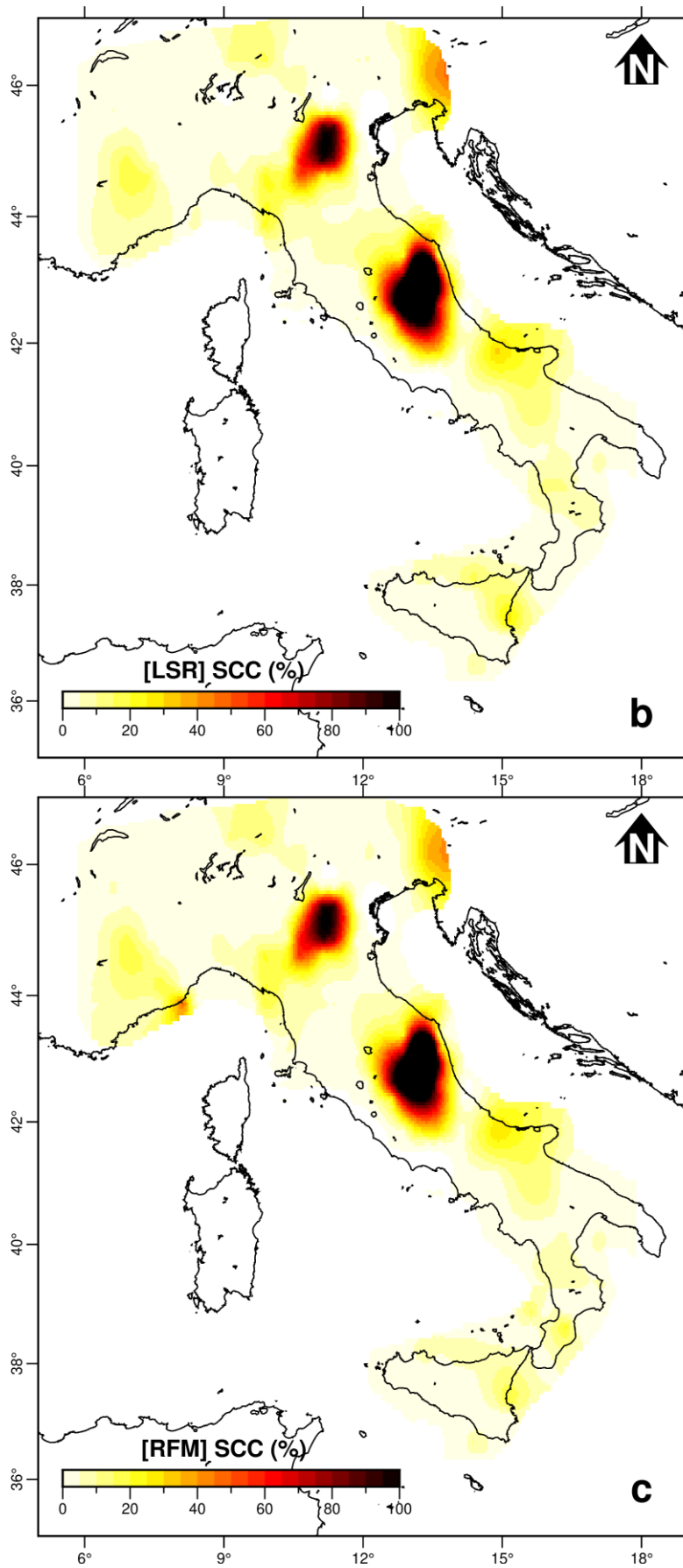


Figure 4.20 – Spatial pattern of the Seismic Coupling Coefficient (SCC) for Italy, using the seismic moment-rates estimated by considering the truncated Gutenberg-Richter distribution with MLE (a), LSR (b) and RFM (c) statistical approaches, using the kriging regression interpolation method.

Keeping in mind that the seismic moment summation method of Kostrov is strongly influenced by the catalog completeness and suffers from the possible lack of large earthquakes with high recurrence rate compared to the catalog duration (Par. 2.2), some considerations have been done. For SCC calculated using the seismic moment-rates estimated by considering Kostrov approach (K-SCC, hereafter; Fig. 4.21), cells with high SCC values are located in Southern Alps (Friuli), Southern Apennines, Calabrian Arc and Messina Straits. Intermediate SCC values are found in Central Apennines and Southern Sicily. Cells with low SCC values are located in the rest of the study area.

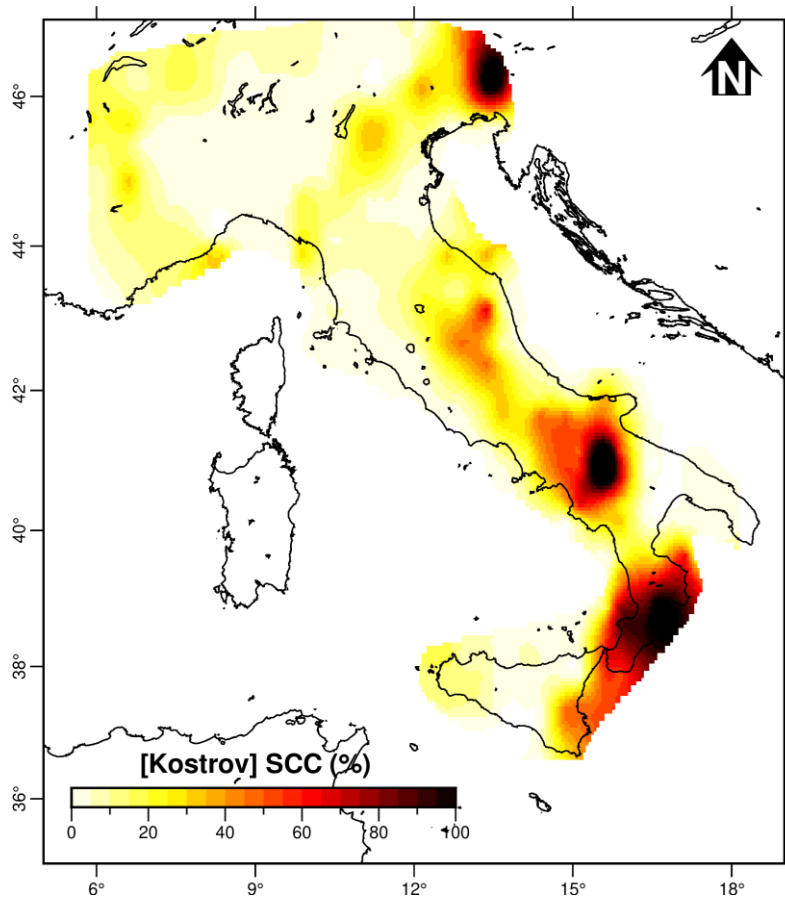


Figure 4.21 – Spatial pattern of the Seismic Coupling Coefficient (SCC) for Italy, considering the seismic moment-rates estimated with the cumulative Kostrov summation method, using the kriging regression interpolation method.

4.3.8 Discussion.

In this section, the by-products of the geodetic and seismic moment-rates computation, which are significant for characterizing the seismicity and general features of the study area will be discussed.

The updated GNSS horizontal velocity field provides very dense information on the present-day kinematics of the study area and permits to figure out some important features at regional scale (Fig. 4.11):

- the distinct patterns between the Tyrrhenian and Adriatic domains, represented, respectively, by the NW- and NE-directed velocities marking the active extension along the Apennines chain;
- the ongoing compression in NE Southern Alps and Northern Sicily;
- the extension across the North-eastern Sicily and the Sicily Channel;
- the Corsica–Sardinia block demonstrating no residual motion with respect to the Eurasian plate.

Earthquakes with extensional mechanisms mainly occur along the Apennines, while compressive mechanisms are detected near the active fronts (Pondrelli et al., 2006). The strain-rate field (Fig. 4.12) clearly depicts the extension along the Apennines and along the north-eastern part of Sicily, and the compression on Southern Alps. Overall, the strain-rate field agrees with previous GNSS estimations (Devoti et al., 2008; Devoti and Riguzzi, 2018).

A relevant by-product is the *b-value* of the Gutenberg-Richter recurrence relation (Fig. 4.15). For most of the study area, the estimated values fall in the 0.8 - 1.2 interval. Small patches with high values greater than 1.4 can be observed in Central Apennines, Calabrian Arc and south-eastern part of Sicily. A relative increase of the *b-value* may suggest a tendency to low stress accumulation. Patches characterized by values lower than 0.8 concentrate along most in the Alps and in some patches in Northern Apennines, suggesting a general tendency for a relative reduction in stress accumulation.

A continuous map of the thickness of the seismogenic layer beneath Italy region (Fig. 4.16) has been provided. Along the Apennines extensional belt, significant variations in seismogenic thickness are found, with the more elevated values of depths ranging between 10 and 30 km. The base of the seismogenic layer broadly coincides with the brittle-ductile transition where little-to-no earthquakes are commonly expected (Scholz, 1998). Theoretical crustal strength envelopes based on power law rheology suggest that the brittle-ductile transition depth should correlate with strain-rate and anti-correlate with heat flow (Sibson, 1984). In other words, thinner brittle crust should be weaker and may be expected to deform more rapidly and thus has a higher strain-rate. In addition, thinner seismogenic layers generally imply higher surface heat flow and hotter geothermal gradients (Sparacino et al., 2022). Moreover, several studies have shown a correlation between the seismogenic thickness and the heat flow (Chiarabba and De Gori, 2016). It is known that the transition from brittle faulting to plastic flow in the continental crust depends on several factors, such as temperature, rock composition and strain-rate. In particular, Chiarabba and De Gori (2016) found that the temperature plays a fundamental role for the determination of the seismogenic thickness of Italy, which follows the pattern of the heat flow, with the highest values and shallowest cut-offs in the Quaternary magmatic areas along the Tyrrhenian side. It reflects therefore the maturity of lithospheric delamination, which account for fault segmentation, controlling the lateral extent of faults and the potential earthquake magnitudes, in this case in Italy. In general, the calculated seismogenic thickness can be used to infer the maximum potential magnitude of expected earthquakes and the potential moment release, and also to constrain the locking depth of a fault. This information is important because it is required to model the deformation on a fault system, and to include geodetic data in seismic hazard models (Chiarabba and De Gori, 2016).

Another relevant by-product is the spatial pattern of M_{max} over the study area (Fig. 4.13a). The results obtained outline a band of increasing values along the Central Apennines with a peak in the southern part of Sicily, and they agree with those obtained by [Petricca et al. \(2022\)](#). Overall, although our estimations come from purely seismicity-based approaches ([Kijko and Singh, 2011](#)), results provide a realistic picture of the upper magnitude limits of large earthquakes that can strike the investigated region.

Several factors related to the deficiency in available geodetic (short time span, velocity uncertainties, density of stations, long-term deformation transient, etc.) and seismic (completeness and temporal length of catalogs, magnitude distribution and uncertainties, seismic cycle, etc.) data may affect the moment-rates estimation ([Palano et al., 2018](#); [Sparacino et al., 2020](#); [Sparacino et al., 2022](#)). Regarding the geodetic data, station density is close to the average value of western and central Europe ([Masson et al., 2019](#); [Sparacino et al., 2020](#)). Time series of the used GNSS dataset generally do not include large earthquakes that could significantly contribute with co-seismic and post-seismic displacements to the estimated geodetic velocities. Therefore, the estimated regional velocity and the related strain-rate field are statistically significant in most of the study area.

Other major factors influencing the geodetic moment-rate estimations are the seismogenic thickness and the crustal rigidity modulus. Geodetic moment-rate estimations can be influenced also by the orientations of active faults within the investigated crustal volume ([Carafa et al., 2017](#)). This imply an increase of 15% of the geodetic moment-rate estimations for the regions where the dominant faulting style is normal or reverse, which on turn led to a decrease of the estimated SCC values. According to [Carafa et al. \(2017\)](#), geodetic moment-rate estimations have been rescaled by using the value of 2.31 instead of 2 in (eq. 2.17); results show a further decrease of the SCC values without however changing the general pattern, therefore it was discarded. Although all these tests highlighted that the assumptions of different parameters led to different geodetic moment-rate estimations, the range of all these estimations is narrow and the pattern of SCC over the whole region is not particularly influenced. The values of geodetic moment-rates shown above (Fig. 4.19b) can be considered as a realistic estimation for the Italy case study.

For what concern the seismic data, both the duration and completeness of the seismic catalog govern their adequacy to estimate seismic moment-rates over a given region ([Ward, 1998](#)). A seismic catalog with a short duration (~ 100 - 300 years) could be insufficient to capture the seismic cycle of a given region. To acquire valid seismic moment-rates from seismic catalogs, the average earthquake recurrence interval should be shorter than the catalog duration ([Ward, 1998](#); [Pancha et al., 2006](#); [Mazzotti et al., 2011](#); [Palano et al., 2018](#)). Regarding Italy study area, the mixed catalog spans a duration of ~ 1017 years with ~ 53% of the computational cells above a duration greater than 400 years. As previously highlighted, a duration of 400 years can be considered the minimal temporal length to reasonably capture the statistical long-term behaviour of seismicity over the study area considering previous studies ([Hunstad, 2003](#); [D'Agostino, 2014](#)). [Ward \(1998\)](#) deduced that seismic catalogs spanning a 150 - 300 years time interval would not reflect the long-term situation of the investigated region. Moreover, he found that these time spans would be fine for regions deforming at rates of about 100 nanostrain/year. Therefore, the estimated seismic moment-rates (Figs. 4.17 - 4.18) can be considered reliable for most of the study area.

4.3.9 Conclusive remarks.

The kinematics and tectonics for the Italy region have been reviewed in order to acquire an improved estimation of the SCC by merging and analysing seismic and geodetic datasets. To quantify the SCC, by-products, such as the seismogenic thickness, the expected maximum magnitude and the Gutenberg-Richter parameters, have been estimated. Considering the K-SCC values and keeping in mind the general limitations of the method, the following observations could be found:

- Regions with very high to high SCC are located in a small area of Northern Apennines, Friuli, Central and Southern Apennines, Calabria, Messina Straits and Southern Sicily. These regions, characterized by active faults, show a full seismic deformation (Fig. 4.21). These SCC values mirror the strong events happened in the past in these areas.
- Regions with intermediate SCC are located in the most of the analysed area. For these regions, the intermediate SCC could be partially attributed to the aseismic components of deformation and to catalog incompleteness. Moreover, the temporal distribution of the past large earthquakes also indicates a high possibility of impending earthquakes in these areas.
- In general, regions with low SCC (widely distributed along the study area) and absence of large earthquakes are identified as potential seismic gaps. Can we define as such the areas of Italy that we have obtained? Lowest deformation and seismicity rates are found for central and western Sicily even from Jenny et al. (2006). Conversely, D'Agostino (2014) found complete seismic release in the Apennines. The answer can be found in the seismic catalogs used for the computation of the moment-rate. A seismic catalog with few or without small events can generate high seismic moment-rate and, consequently, high SCC.
- Finally, we can say that the K-SCC works better over large areas (Fig. 4.21). In particular, it estimates high SCC values for most of the regions characterized by the occurrence of large earthquakes in the last century (e.g. the M_w 6.5 1976 in Friuli, the M_w 6.9 1980 in Irpinia, the M_w 5.7 2002 in Molise, and the M_w 6.1 2009 in L'Aquila, the M_w 6.0 - 5.9 - 6.5 2016 and $M_w > 5$ 2017 seismic sequence in Amatrice-Visso-Norcia, Central Italy). Moreover, such an approach highlights low SCC values for regions as the Emilia one, recently stroked by a seismic sequence (M_w 5.9) in 2012. Conversely, the same regions show high SCC values, when the truncated cumulative Gutenberg-Richter distribution is adopted (Fig. 4.20abc). This feature suggests that the historical catalog for the Emilia region would be too short to estimate adequately the local long-term seismic moment release. This inference is supported by the occurrence of few destroying earthquakes in the last 1000 years, as for instance the 1570 Ferrara earthquake (Guidoboni et al., 2011). Moreover, the historical catalog of the last 1000 years for Central and Southern Italy appears adequate for SCC estimations. The fact that the SCC estimations coming from the truncated cumulative Gutenberg-Richter distribution differ on some regions of Italy from the ones coming from the Kostrov method, would be related to a possible inadequacy of the chosen grid size. Estimations adopting different grid size will be carried out in future studies.

5 – Other Applications of the Method

In this chapter, some examples of application of the method will be exposed in order to highlight differences in the procedures, limitations and benefits. The SCC calculation method has been also applied in four areas of the Mediterranean regions, i.e., Ibero-Maghrebian region (Sparacino et al., 2020), Sicily Channel (Palano et al., 2020), Aegean-Anatolian region (Sparacino et al., 2022) and Egypt (Sawires et al., 2021), with the same mathematical formulations but with some computational differences (Fig. 5.1). A major difference is given by the adopted computational geometry. In the Ibero-Maghrebian region and in Egypt we adopted irregular grids, according to the local seismogenic zonation. For the Sicily Channel analysis, we used a polygon with vertices defined by the GPS stations at the borders of the region. For the Aegean-Anatolian region, we adopted a regular squared grid as previously done (Chapter 4) for Italy.

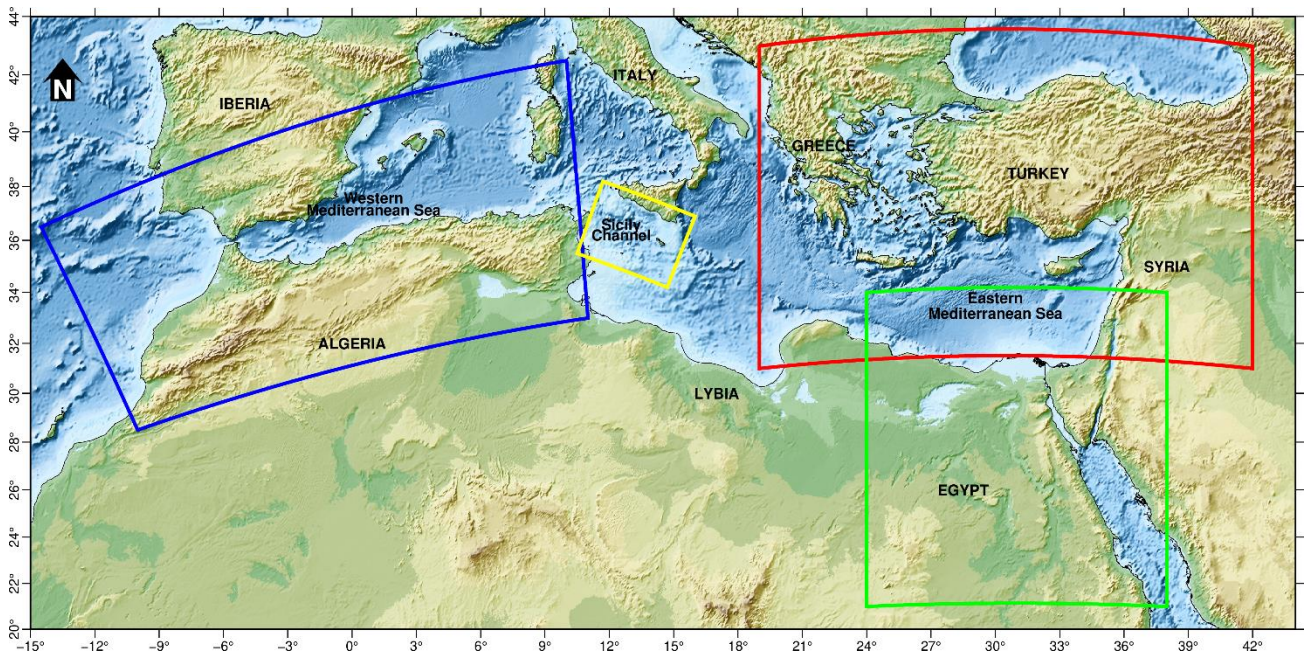


Figure 5.1 - Simplified map of the studied Mediterranean areas. From W to E, the Ibero-Maghrebian region, the Sicily Channel, the Aegean-Anatolian region and Egypt are reported with blue, yellow, red and green boxes, respectively.

5.1 The Ibero-Maghrebian region.

The tectonic setting of the South-eastern Iberia-Maghreb region (western Mediterranean border; Fig. 5.2) results from the Cenozoic orogenic evolution within the complex framework of the Eurasia-Nubia plate convergence (e.g., Michard et al., 2002; Platt et al., 2003). The present-day plate tectonic setting was reached in the earliest Miocene, with the welding of the Iberian Peninsula to the Eurasia plate. At that time, the main plate boundary between Africa and Eurasia in the Western Mediterranean region developed along the transpressive fault zone connecting the Açores triple junction to the Rif and Tell Atlas through the Gibraltar Orogenic Arc (e.g., McKenzie, 1970; Andrieux

et al., 1971). In Southern Iberia, the Betics show a mainly North-North-West (NNW) direction of tectonic transport, turning around the Gibraltar Strait to a prevailing South-West (SW)-directed thrusting along the Rif while an overall South-South-East (SSE)-directed tectonic transport dominated the Tell Atlas fold-thrust belt. The inner side of the Gibraltar Orogenic Arc is occupied by the Alboran basin (Fig. 5.2), a back-arc basin formed mainly during the early Miocene (e.g., Comas et al., 1999).

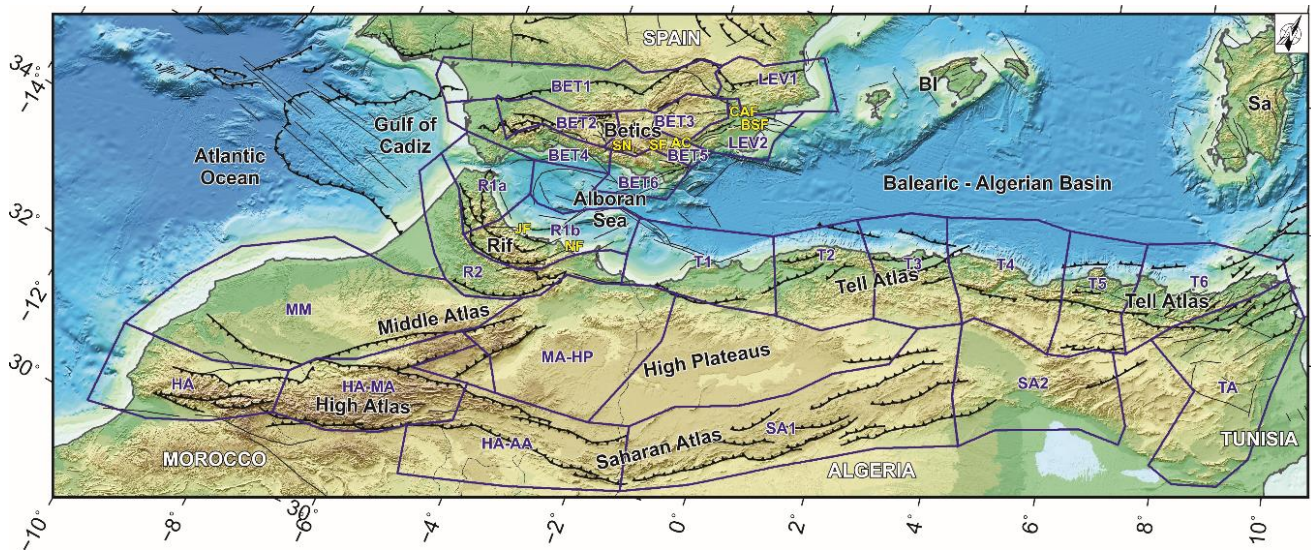


Figure 5.2 - Simplified tectonic map of North-western Africa and South-eastern Iberia. Mapped faults are re-drawn. Seismic source zones (Betics seismic source zones: BET1, BET2, BET3, BET4, BET5, BET6; Atlas seismogenic sources: HA, HA-AA, HA-MA, SA1, SA2; TA represents High, Middle, Saharan, and Tunisian Atlas, as well as the north-eastern part of the Anti-Atlas; Levante seismogenic regions: LEV1, LEV2; Moroccan Meseta-High Plateaus seismic source zones: MA-HP, MM; Rif seismogenic sources; R1a, R1b, R2; Tell seismogenic source zones: T1, T2, T3, T4, T5, T6) analysed are also reported as blue solid polygons. The map is plotted in an oblique Mercator projection. Modified from Sparacino et al. (2020).

A number of on- and off-shore active fault systems dissect the study area and are responsible for a large amount of the current seismic release of the region. Among them, the Trans Alboran shear zone (a major NE-SW trending left-lateral strike-slip system) cuts the Alboran basin, and branches into the Eastern Betics shear zone and into the Nekor/Al-Hoceima seismic zone, northward and southward, respectively (e.g., Bourgois et al., 1992; Masana et al., 2004; Garcia et al., 2006). In addition, the Trans Alboran shear zone is westward connected to southern Spanish off-shore by the right-lateral Yusuf fault (Ballesteros et al., 2008). In western Algeria, active faulting occurs within the Tell Atlas, along NE-SW-trending, right-stepping en-echelon reverse faults (Meghraoui et al., 1986). In eastern Algeria, active reverse faulting occurs in a broader area (Meghraoui and Pondrelli, 2012; Bahrouni et al., 2013; Rabaute and Chamot-Rooke, 2014) and is coupled with right-lateral strike slip faulting on EW-trending faults (Maouche et al., 2013). Active faulting is recognized along the Aurès Mountains and the southern Atlas region (Ben Hassen et al., 2014).

Southern Iberia and Maghreb regions have been subject by the occurrence of large earthquakes (with estimated magnitude $M \geq 6.5$) in the last centuries (www.emidius.eu/SHEEC/; Peláez et al., 2007; Hamdache et al., 2010). Global Navigation Satellite System (GNSS)-based measurements show that active deformation involves both Southern Iberia and Maghreb regions

with rates up to 6 mm/year (e.g., [Palano et al., 2015](#); [Bougrine et al., 2019](#)). Such a GNSS-based active deformation has been interpreted in terms of elastic block modeling (e.g., [Bougrine et al., 2019](#); [Koulali et al., 2011](#)). However, the detection of a significant aseismic deformation component on the Betic–Rif system (~75%; see [Stich et al. \(2007\)](#) for details) highlights that the comparison of seismic and geodetic deformation-rates would not be balanced across the region. Results achieved in this study support the inference on the aseismic deformation behaviour for most of the Betics and Rif regions, revealing a fully seismic deformation along most of the Tell Atlas.

5.1.1 Seismological Data.

To estimate the seismic moment-rates pattern over the study area, four available catalogs of historical seismicity have been used:

- the SHARE European Earthquake Catalog (<https://www.emidius.eu/SHEEC/>);
- a catalog of main Moroccan earthquakes from 1045 to 2005 ([Peláez et al., 2007](#));
- a catalog of main earthquakes for northern Algeria from AD 856 to 2008 ([Hamdache et al., 2010](#));
- a catalog for the Iberian Peninsula, from 880 BC to 1900 ([Martínez Solares et al., 2002](#)).

Historical earthquakes are largely concentrated along the Azores-Gibraltar fault zone, along the Betic-Rif system, and along the Tell Atlas fold-thrust belt ([Fig. 5.3a](#)). In detail, the strongest historical earthquakes ($M \geq 7.0$) are mainly concentrated on the Azores-Gibraltar fault system (AD 1309, 1356, 1761, and 1755 events) and along the Tell Atlas fold-thrust belt (AD 856, 1365, 1716, 1722, 1790, 1832, 1867, and 1891 events).

Concerning the instrumental seismicity occurring in the study area, we collected a catalog from the International Seismological Centre (www.isc.ac.uk/) by considering all earthquakes with $M \geq 1.0$ and depth ≤ 300 km. The distribution of instrumental seismicity as well as the main seismotectonic features are concentrated across the Nubia-Eurasia plate boundary ([Fig. 5.3b-c](#)).

The used seismic catalog covers 1000 years and its completeness varies considerably throughout the period of time studied and throughout the study region.

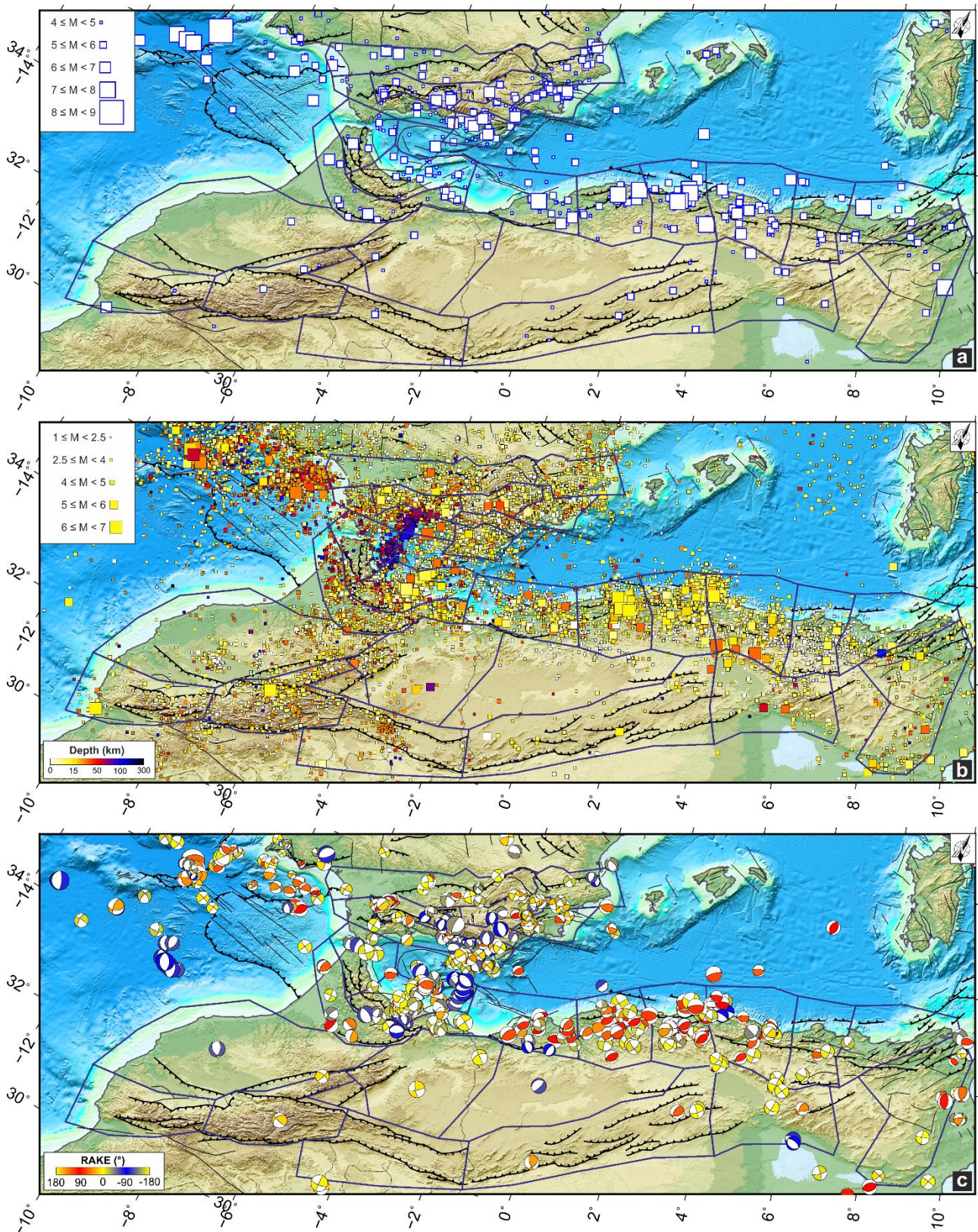


Figure 5.3 - (a) Historical earthquakes (blue squares; $M \geq 4.0$) occurring during AD 856-1950. (b) Instrumental crustal seismicity ($M \geq 1.0$) occurring in the investigated area since 1910. Symbols are colored according to focal depth. (c) Lower hemisphere, equal area projection for fault plane solutions (with $M \geq 3$) compiled from the investigated area; fault plane solutions are colored according to rake: red indicates pure thrust faulting, blue is pure normal faulting, and yellow is strike-slip faulting. Modified from Sparacino et al. (2020).

5.1.2 Geodetic Data.

To estimate the pattern of geodetic moment-rates for the study area, an extensive GNSS dataset which, covering 20 years of observations (from 1999.00 up to 2019.00), includes more than 300 continuous GNSS sites have been used:

- EUREF Permanent GNSS Network (www.epncb.oma.be);
- Crustal Dynamics Data Information System (<https://cddis.nasa.gov/>);
- UNAVCO (www.unavco.org);
- local and regional networks ([Palano et al., 2015](#)).

Time series of this GNSS dataset cover different time spans, ranging from 3.5 to 20 years with an average duration of 8.7 years. We also included 25 episodic GNSS sites located in Morocco with measurements carried out during the 1999.80 - 2006.71 time interval ([Koulali et al., 2011](#)). The GNSS phase observations were processed by using the GAMIT/GLOBK 10.7 software ([Herring et al., 2017](#)) following the strategy described in [Palano \(2015\)](#). As a final processing step, a consistent set of positions and velocities in the International Terrestrial Reference Frame ITRF2014 reference frame ([Altamimi et al., 2016](#)) has been computed.

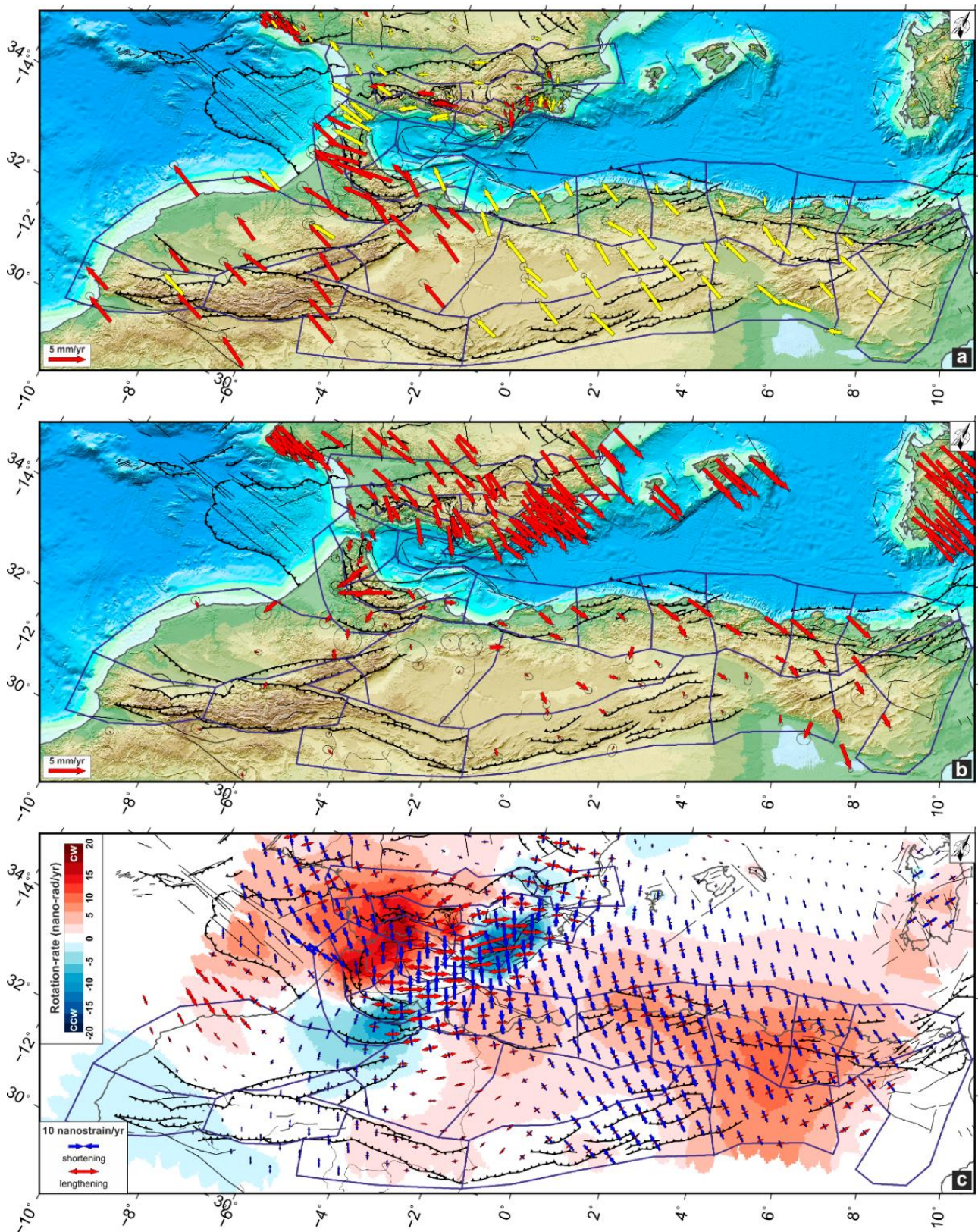


Figure 5.4 - Global Navigation Satellite System (GNSS) velocities and 95% confidence ellipses in a fixed (a) Eurasian and (b) Nubia reference frame. Continuous and episodic GNSS stations are reported as yellow and red arrows, respectively. (c) Geodetic strain-rate field: red and blue arrows represent the greatest extensional (ϵ_{Hmax}) and contractional (ϵ_{Hmin}) horizontal strain-rates, respectively; the colours in the background show the rotation strain-rate (which describes the rotations with respect to a downward positive vertical axis with clockwise (cw) positive and counter clockwise (ccw) negative, as in normal geological conventions). The map is plotted in an oblique Mercator projection. Modified from Sparacino et al. (2020).

5.1.3 SCC Results and conclusive remarks.

The study area has been divided into twenty-five crustal seismogenic source zones (Fig. 5.3) by taking into account the seismic zonation available in recent literature (Peláez et al., 2018; CNIG, 2013), which have been defined on the basis of the latest tectonic, geological, and seismological considerations. Some of these zones are well-defined on the basis of constraints coming from the analysis of the earthquake catalog (stationarity of the completeness periods, evaluation of the mean activity rate) and from a set of geological and seismotectonic considerations, such as style, geometry, and distribution of fault systems (with direct evidence of Holocene activity) and their relation to the local stress and deformation regimes. Other zones, although defined on similar seismotectonic or geological information, are lacking a clear correspondence between the contemporary seismic activity and the Holocene tectonic activity.

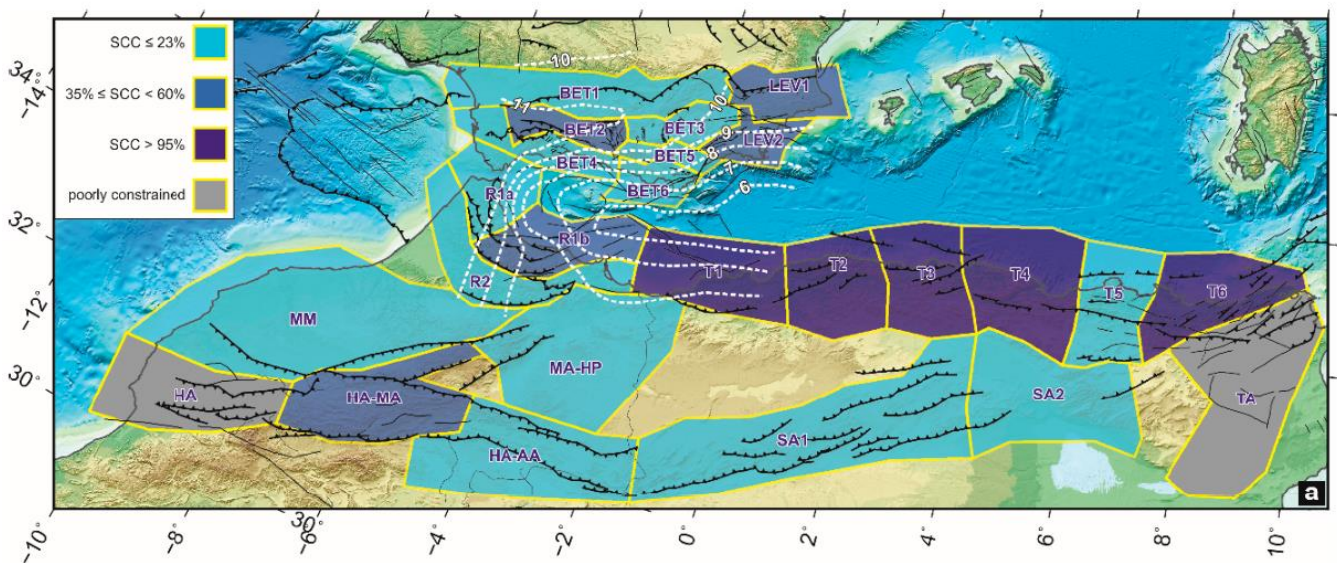


Figure 5.5 - (a) Seismic coupling coefficient (SCC), expressed as a percentage of the seismic/geodetic moment-rate ratio as computed in this study. As discussed in the main text, three principal ranges of SCC values have been identified: low (less than 23%), intermediate (between 35% and 60%) and high (more than 95%). In grey are reported the SSZ excluded from the comparison, i.e., HA and TA. The white dashed line represents the depth (in km) of the brittle-ductile transition. Modified from Sparacino et al. (2020).

Based on the achieved SCC values, we considered three principal ranges of values: less than 23%, between 35% and 60%, and more than 95% (Fig. 5.5).

A large sector of the study area, comprising Betics (BET1, BET3, BET4, BET5, BET6), Rif (R1a, R2), High, Middle, and Saharan Atlas (MM, MA-HP, HA-AA, SA1, SA2), and one region in the Tell Atlas (T5), is characterized by SCC values lower than 23%. This result is highly consistent with previous estimations computed for the Betics and Rif areas (Stich et al., 2007) which highlighted how only about 24% of crustal deformation is released seismically. A number of indicators such as surface heat flow, seismic tomography and local rheological models provided evidence of a weak crustal rheology; therefore, supporting the inference on the aseismic behaviour of some sectors of the region.

In detail, surface heat flow measurements available for the area show high values (100-120 mW m⁻²; Torné et al., 2000; Polyak et al., 1996) along the eastern sector of the Alboran basin and moderate

values (60-75 mW m⁻²) along the Betics (Fernández et al., 1998) and Rif (Rimi et al., 1998) regions. In the central and southern Gulf of Cadiz, the surface heat flow is characterized by values close to 40-50 mW m⁻² (Mahsas et al., 2008), assuming typical values for stable continental/oceanic lithosphere (Pollack and Chapman, 1977). Local seismic tomographies have inferred a low-velocity zone at 18-km depth beneath the central Betics, indicating variations in lithology and/or in the rigidity of the lower crust rocks (e.g., Serrano et al., 2002). Local rheological models (e.g., Fernández-Ibáñez and Soto, 2008) highlighted how the crustal yield strength as well as the inferred depth of the brittle-ductile transition follow the curved shape of the Gibraltar arc with maximum depths of 12-9 km, whereas in the Rif and the Betics, such a transition became shallower eastward (~6-5 km depth). All these geological and geophysical evidences support the inference on the aseismic behaviour, at least of the Betics and Rif regions.

Intermediate SCC values (between 35% and 60%) have been observed for HA-MA, R1b, LEV1, LEV2 and BET2 seismogenic source zones; therefore, suggesting how these regions account only for a moderate seismic fraction of the total deformation-rate budget. Some of these regions are characterized by well-known active faults which frequently generate moderate earthquakes such as LEV2 and R1b. On these zones, a significant contribution to the measured crustal deformation can be attributed to aseismic post-seismic mechanisms such as afterslip and/or viscoelastic relaxation, as for instance documented for earthquakes striking the R1b source zone in the last decades (González et al., 2009).

The higher SCC values (> 95%) have been observed along the Tell Atlas zones (T1, T2, T3, T4, T6), suggesting how the measured crustal deformation over these zones is mostly released through earthquakes. All these source zones are characterized by SCC values larger than 100%. These values are not surprising, since, along the Tell Atlas zones, the crustal shortening of ~5 mm/year related to the Nubia-Eurasia oblique convergence is largely adsorbed on off-shore reverse structures bordering the North African margin (Palano et al., 2015; Bougrine et al., 2019). Therefore, a relevant portion of the long-term elastic strain accumulation is not captured by the on-shore GNSS stations. In addition, a number of moderate to large earthquakes have epicenters concentrated off-shore (not sampled by GNSS stations), such as the 1790 Oran ($M \sim 7$) (Yelles Chauche, 2017), the 1856 Djijelli M_w 7.2 (Roger and Hébert, 2008), and the 2003 Boumerdes M_w 6.8 (Hamdache et al., 2004) earthquakes. Therefore, their released seismic energy corresponds to strain with no full counterpart on the on-shore surface. Both these features lead to an underestimation of geodetic strain-rate. As above mentioned, the geodetic moment-rate estimations are affected by the assumed computational parameters; even if increasing the seismogenic thickness value up to 25 km and/or computational parameters (grid size and weighting threshold) for strain-rates estimation, the SCC values for Tell Atlas zones remain confined to values larger than 100%. All these considerations, coupled with the occurrence of large destructive events ($M > 7$) both in historical and instrumental periods, add realistic constraints on the seismic behaviour of the region. In such a context, the low SCC value inferred for T5 source zone (~20%) appears puzzling. The seismic moment-rate is based on a maximum magnitude M_{max} of 5.8, about 1 order of magnitude unit lesser than the values estimated for the other Tell Atlas source zones. It must be noted that an increase of 1 magnitude unit leads to an increase by a factor of ~5.4 of the moment-rate, therefore leading to a SCC value close to 100%. These considerations, while on

one hand suggest that the low SCC value inferred for T5 source zone could be poorly representative of its seismic behaviour, on the other suggest that the possibility of forthcoming earthquakes in the region may increase. Since in this region the occurrence of a moderate earthquake (1985 Constantine M_w 5.8 event) is documented in the available seismic catalogs, it appears to be a potential seismic gap like other well studied regions of the world (e.g., Rong et al., 2003; Gupta and Gahalaut, 2014).

5.2 The Sicily Channel.

The Sicily Channel is part of the Pelagian block (Burollet et al., 1978; Ben-Avraham and Grasso, 1991; Lentini et al., 2006), a 25-30 km thick continental crustal portion of the Nubian continental margin, which extends from the Sahel region of Tunisia to eastern Sicily, and is separated from the Ionian basin by a regional tectonic boundary named the Hyblean-Maltese Escarpment fault system (Fig. 5.6).

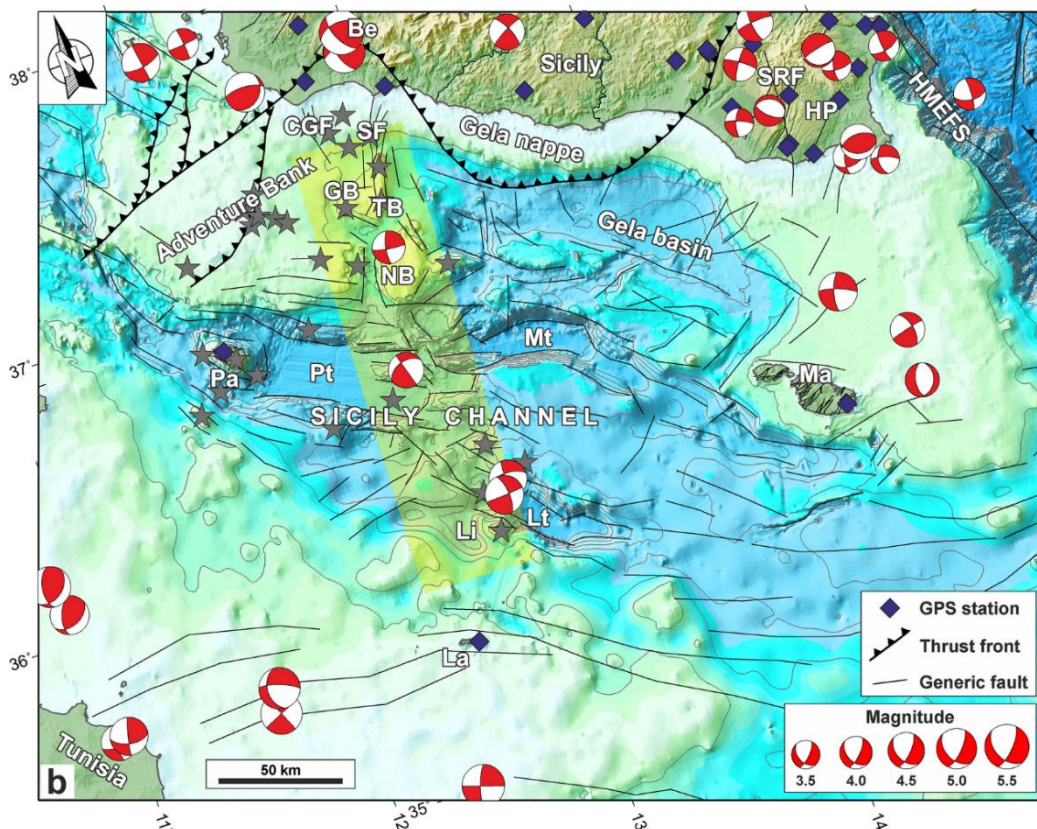


Figure 5.6 - Simplified tectonic map of the Sicily Channel and surrounding areas (the map is plotted in an oblique Mercator projection). Modified from Palano et al. (2020).

The tectonic configuration of the Pelagian block includes a series of mostly WNW-ESE trending structural highs and basins, bordered by variously oriented faults of Neogene-Quaternary age.

Evolution of the Pelagian block has been strongly influenced by the complex Nubia-Eurasia plate interaction, with considerable changes in structural styles, convergence attitude and deformation rates since the Late Cretaceous (DeMets et al., 2015). Starting from the Late Miocene and mostly during the Early Pliocene, a lithospheric-scale continental rifting occurred in the central

part of the Pelagian block (Torelli et al., 1995), with a subsequent phase (Late Pliocene-Pleistocene) characterized by a magma-assisted extension (Civile et al., 2010). This rifting process led to the development of NW-SE-trending tectonic depressions (e.g., Pantelleria, Linosa and Malta troughs), bordered by crustal normal faults with variable throws (Boccaletti et al., 1987; Fig. 5.6). A broad N-S-oriented belt, defined on the basis of tectonic bathymetric, volcanic and magnetic lineaments and extending from Lampedusa Island to the Graham Bank (Lodolo et al., 2012; Cello, 1987; Argnani, 1990; Fig. 5.6), separates the rift system in two sectors: the Pantelleria trough to the west, and the Malta and Linosa troughs to the east (Fig. 5.6). Along this deformation belt, the magmatic activity started in the Nameless Bank in the Late Miocene and continued to the present-day close to Pantelleria and to the south-eastern wedge of the Graham Bank (Cavallaro and Coltelli, 2019; Beccaluva et al., 1981) and is characterized by a wide spectrum of volcanic rocks with tholeiitic, alkaline and peralkaline affinities (Peccerillo, 2005).

Previous studies have also highlighted that instrumental seismicity mainly concentrates along the N-S-oriented belt and is characterized by moderate levels of seismic energy release (magnitude up to 4.7), with predominance of earthquakes at 10-20 km of depth, and occasionally deeper events (Calò and Parisi, 2014; Spampinato et al., 2017). Nevertheless, the occurrence of large earthquakes ($M > 7$) during historical times on nearby regions (e.g., the 856 M 7, Hamdache et al., 2010; the 1693 M 7.5, Guidoboni et al., 2007; and the 1935 M 7.1, Suleiman et al., 2004, earthquakes striking the Tunisia, the Hyblean Plateau and the off-shore of NW Libya, respectively) would suggest, for Sicily Channel sector, a greater seismic hazard than that currently expected (Panzera et al., 2015).

5.2.1 Seismological Data.

We collected a catalog of instrumental seismicity taking into account all data records reported in online bulletins (<http://www.isc.ac.uk/iscbulletin/search/catalogue/>; <http://iside.rm.ingv.it>). For the study area (Fig. 5.5), we selected 1780 earthquakes covering the time interval 1966-2018, with magnitude between 1.5 and 5.5. Hypocentres collected from ISC bulletin span the 1966-1984 time interval. For the earthquakes of this period (~3% of the whole collected dataset), the bulletin does not provide uncertainties of location parameters, except for a few records, for which the mean error on horizontal coordinates is ~12 km. Records coming from the other bulletin (<http://iside.rm.ingv.it>) cover the period 1985-2018, and refer to earthquakes mainly acquired by the seismic network managed by Istituto Nazionale di Geofisica e Vulcanologia (INGV). Uncertainties of the hypocenter locations are, on average, 3, 6 and 2 km for longitude, latitude and depth coordinates, respectively. Nevertheless, numerous locations are reported with fixed focal depth, so they may suffer from greater uncertainties. Available historical seismic catalogs report, for the area in Fig. 5.7, the occurrence of large earthquakes ($M \geq 6.5$) since 1125 (<https://www.emidius.eu/SHEEC/>). The accuracy of these catalogs is not uniform and the epicentral location of some historical earthquakes may result uncertain, mainly due to the presence of wide sea areas and the sparsely populated region. This is the case of several earthquakes, which are clustered closely to the main towns and villages, clearly reflecting the distribution of populated areas along

the southern Sicilian coastal area and Pantelleria island where the shocks could be felt (Spampinato et al., 2017). The seismic catalog was complete for magnitudes greater than 2.8 since 1968.

The seismic moment-rate estimate for the study area is $6.58 \cdot 10^{15}$ Nm/year. Considering that seismic moment-rate estimates are commonly affected by the completeness and the temporal length of seismic catalogs, we performed some tests to assess the robustness of our estimates (see Supplementary Material for more details).

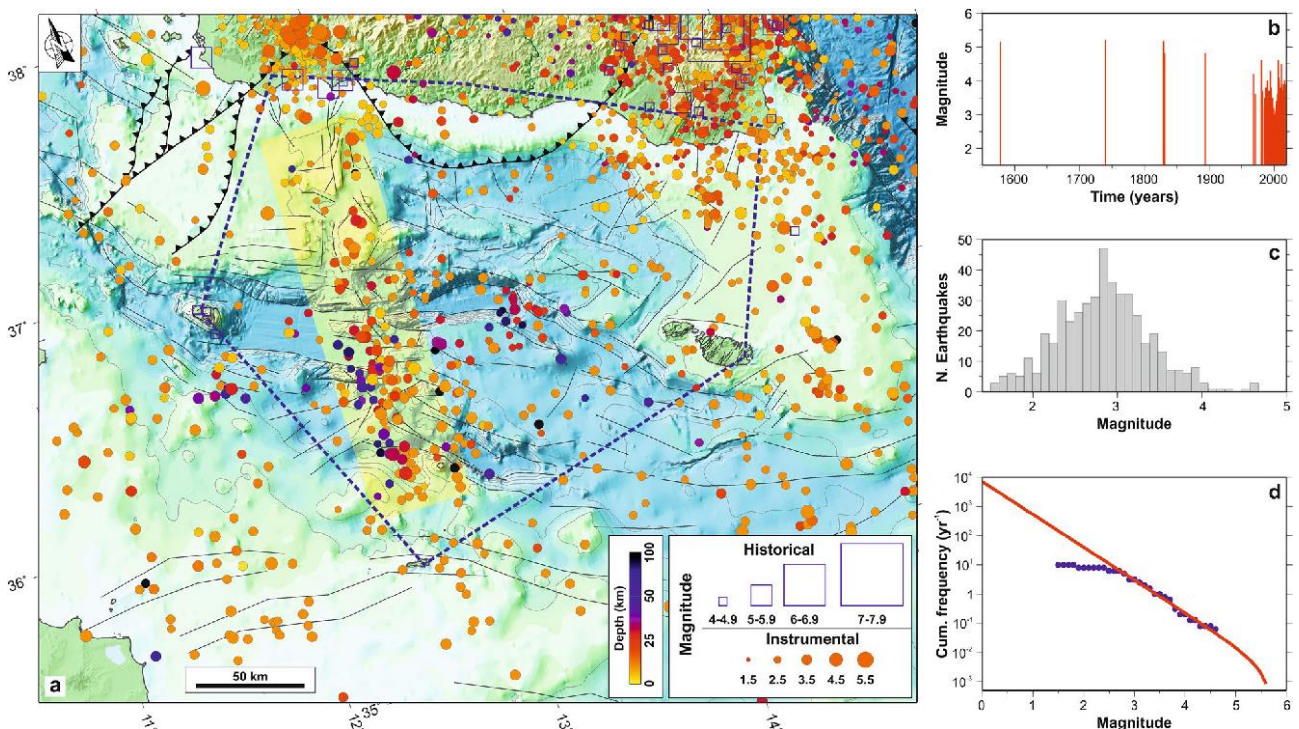


Figure 5.7 - (a) Instrumental (circle) and historical (square) seismicity of northern Sicily Channel. The instrumental seismicity covers the 1966-2018 interval and has been collected from various sources (<http://www.isc.ac.uk/iscbulletin/search/catalogue/>; <http://inside.rm.ingv.it>). The yellow strip represents the N-S tectonic belt. The blue polygon defines the study area; inside this area, the historical seismicity covers the 1578-1965 time interval (<https://www.emidius.eu/SHEEC/>). (b) Temporal trend of historical and instrumental seismicity for the study area (blue polygon in panel a). (c) Magnitude range histogram for instrumental seismicity striking the study area. (d) Cumulative frequency-magnitude distributions (blue points) of earthquakes for the study area. The red line represents the truncated Gutenberg-Richter formulation (Hyndman and Weichert, 1983). Maps compiled using the Generic Mapping Tool, version 5 (Wessel et al., 2013); image editing using Inkscape, version 1 (<https://inkscape.org>). Modified from Palano et al. (2020).

5.2.2 Geodetic Data.

GPS observations acquired in the 2001.0 - 2018.0 time-interval from continuous stations located around the Sicily Channel and southern Sicily have been analysed to describe the current crustal deformation in the study area. Estimated GPS velocities, referred to a Nubia-fixed reference frame (Palano et al., 2015), and associated uncertainties (at 95% level of confidence) are reported in Fig. 5.8. Within this frame, the station LAMP (Lampedusa, Fig. 5.8) shows a residual velocity of ~ 1 mm/year towards SSE, evidencing a small deviation from Nubia. Stations on the Hyblean-Malta block are moving toward ENE with rates of ~ 2.3 mm/year, while stations in Pantelleria (PZIN) and along the SW Sicilian on-shore move eastward, with rates ranging between ~ 3.8 and 2.1 mm/year,

respectively. The strain-rate field also suggests that the western sector of our study area (Fig. 5.7a) is dominated by a prevailing contractional field, with ϵ_{hmin} axes having a WNW-ESE orientation between Pantelleria and SW Sicily, and a NW-SE attitude between Pantelleria and Lampedusa. Conversely, the eastern sector is characterized by a strike-slip deformation field, with ϵ_{Hmax} and ϵ_{hmin} axes aligned to the NE-SW and to the NW-SE direction, respectively (Fig. 5.8). Assuming a value of 13 km (Panzer et al., 2015) as average seismogenic thickness H_s , we estimated a geodetic moment-rate of $7.24 \cdot 10^{17}$ Nm/year for the investigated area. We performed some tests to assess the robustness of this estimate calculating additional strain-rate fields by simply varying the size of the computational grid (see Supplementary Material for more details).

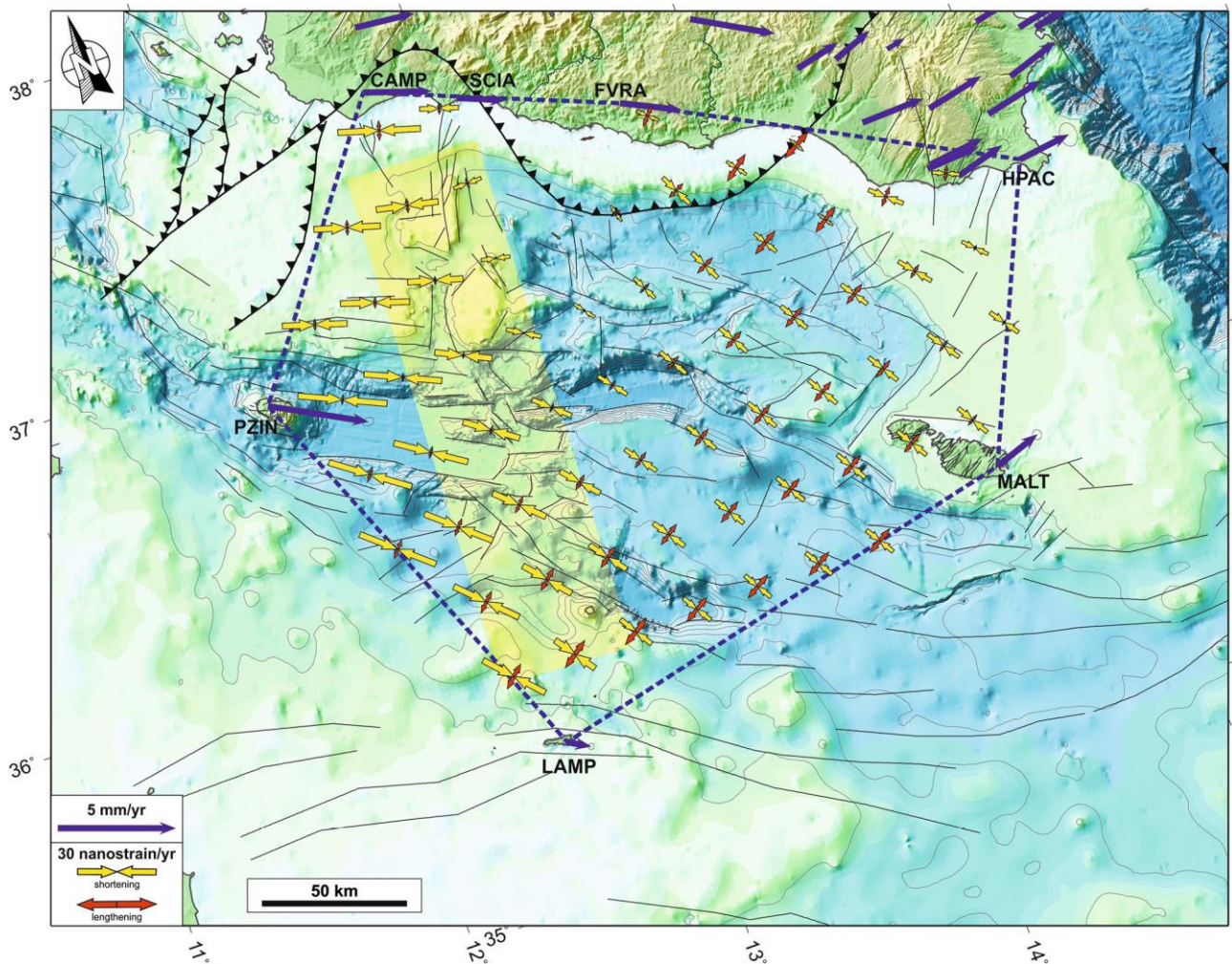


Figure 5.8 - Estimated GPS velocities and associated uncertainties (at the 95% level of confidence) are reported as blue arrows. Velocities refer to a Nubian-fixed reference frame (Palano et al., 2015). The geodetic horizontal strain-rate field (red and yellow arrows indicate the greatest extensional and contractional strain-rates, respectively) as estimated for the area defined by the blue polygon is also reported. Maps compiled using the Generic Mapping Tool, version 5 (Wessel et al., 2013); image editing using Inkscape, version 1 (<https://inkscape.org>). Modified from Palano et al. (2020).

5.2.3 SCC Results and conclusive remarks.

Estimates of seismological and geodetic moment-rates, $6.58 \cdot 10^{15}$ Nm/year and $7.24 \cdot 10^{17}$ Nm/year, respectively, highlight that seismicity accounts only for $\sim 0.9\%$ of crustal deformation.

Such a deficit would suggest either a proportion of aseismic deformation (i.e., ongoing unloading by creep and other plastic process) or accumulating strain not released by seismicity (i.e. elastic storage). Moreover, in a region affected by active faulting capable of generating earthquakes with large magnitudes ($M > 7$), we need to re-evaluate the conditions for a reliable seismic hazard assessment to address the following questions: (i) is the lack of large earthquakes related to a longer return period than the observation time-span? (ii) will the excess of deformation be released through major impending earthquakes?

The integrated analysis of available morpho-bathymetric data and seismic reflection profiles allows identifying main tectonic features whose location, geometry and inferred kinematics are in good agreement with observed recent seismicity and geodetic data. Basin depocenters mark first order structural boundaries between different morphostructural domains. However, seismic reflection data suggest that these structural depressions are not tectonically active, since recent sediment filling the basin depocenter does not show evidence of incipient deformations, while horizontally onlapping the acoustic basement. The infill of the basins could be subdivided into two different seismo-stratigraphic units, the lower showing evidence of past deformations. Consequently, the unconformity separating the lower, deformed, and the upper undeformed units, although not precisely stratigraphically correlated, represents the end of tectonic activity responsible for the opening of the deep depressions. Seismic reflection profiles show evidences of active deformation only along a N-S trending corridor (i.e. the Lampedusa-Sciacca shear zone - LSSZ), where a diffuse and complex pattern of transtensional and transpressional deformation is presently affecting the sedimentary sequence up to the seafloor. These evidences suggest that seismic deformation occurs mainly along very narrow active tectonic areas, which are able to account for only ~ 0.9% of the total deformation budget measured geodetically.

Based on the geodetic, seismological and seismic reflection data analysed in this study and those coming from literature (gravity maps, heat-flow and crustal thickness) allow us to consider a ductile rheology of the crust beneath the investigated area, where the anomalous thermal state and the low thickness of the crust would significantly inhibit frictional sliding in favour of creeping and aseismic deformation. In such a scenario, the detected seismic deformation budget requires an aseismical restoration. This implies a thorough re-evaluation of the seismic hazards in this region, where only a small portion of the inferred deformation would be compensated by minor to moderate future earthquakes.

5.3 The Aegean-Anatolian Region.

The Aegean and Anatolian microplates are affected by the highest deformation rates of the Mediterranean (Fig. 5.9), with complex tectonics leading to many large magnitude earthquakes in the past. The seismic and the associated tsunami hazard are the highest in Europe. Despite the copious datasets and different parameterization and/or assumptions, the aforementioned studies only identified a few regions where the estimated geodetic/tectonic moment-rate is released purely by seismic activity, such as the Cephalonia Transform Fault (central Ionian Sea) and the westernmost branch of the North Anatolian fault, in the North Aegean Trough. Furthermore, the remaining part

of central and northern Greece is believed to deform in aseismic mode (Rontogianni, 2010; Chousianitis et al., 2015). The behaviour of the Hellenic subduction zone is widely debated with contrasting results, ranging from fully coupled (Ganas and Parsons, 2009) to various degrees of uncoupled deformation (e.g. Papazachos and Kiratzi, 1996; Scholz and Campos, 2012; Apel, 2011; Vernant et al., 2014 and references therein). In Anatolia, the first estimation of seismic coupling (Ward, 1998) concluded that the observed deformation is largely aseismic. Since then, no other estimations have been performed, despite its high seismic hazard (e.g. Bohnhoff et al., 2016 and references therein).

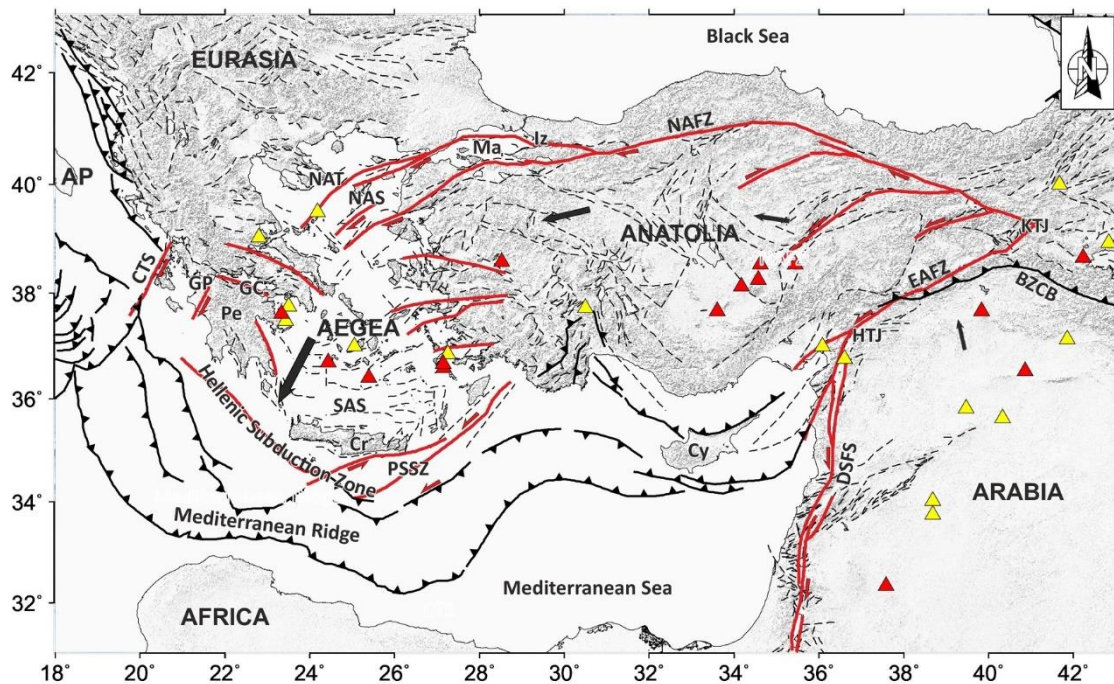


Figure 5.9 - Tectonic setting of the Aegean-Anatolia region. Major faults and thrusts are reported in red and black, respectively, while minor tectonic lineaments are reported as dashed black lines. The black arrows represent the GNSS motion across the Anatolian and Aegean blocks. Holocene and Pleistocene volcanoes are reported as yellow and red triangles, respectively. Abbreviations are: Ma, Marmara Sea; NAT, North Aegean Trough; CTS, Cefalonia transform fault; GP, Gulf of Patras; GC, Gulf of Corinth; Pe, Peloponnese; NAS, North Aegean Sea; SAS, South Aegean Sea; Cr, Crete, PSSZ, Pliny-Strabo shear zone; Cy, Cyprus; NAFZ, North Anatolian fault zone; EAFZ, East Anatolian fault Zone; KTJ, Karliova triple junction; HTJ, Hatay triple junction; DSFS, Dead Sea fault system; BZCB, Bitlis-Zagros collisional belt; Ap, Apulia. Modified from Sparacino et al. (2022).

5.3.1 Seismological Data.

The occurrence of several large earthquakes in the Aegean-Anatolian region is well documented in remarkably complete historical records and written sources (Bohnhoff et al., 2016). By taking into account both the SHEEC and SHARE-CET catalogs (<https://www.emidius.eu/SHEEC>; Stucchi et al., 2013; Grünthal et al., 2013; Papadopoulos, 2011), we compiled a catalog of 678 historical earthquakes (HE, hereinafter) occurring in the investigated area during the 1003 - 1903 period and with estimated moment magnitude $M_w \geq 5$. Historical seismicity is widespread over the whole investigated area (Fig. 5.10), with the strongest earthquakes ($M \geq 7$) mainly concentrated along the western and eastern sectors of NAFZ, the EAFZ and along the Hellenic Trench. The largest

earthquake occurred in on August 8, 1303 (M_w 8.26, [Stucchi et al., 2013](#)), with the estimated epicenter located to the east of Crete.

We also compiled a catalog of instrumental seismicity (IE, hereinafter) by merging the records reported in the following online catalogs:

- National catalog for Greece managed by the “Institute of Geodynamics-National Observatory of Athens” (<http://www.gein.noa.gr/en/seismicity/earthquake-catalogs>);
- National catalog for Turkey managed by the “Kandilli Observatory and Earthquake Research Institute of Bogazici University” (<http://www.koeri.boun.edu.tr/sismo/2/earthquake-catalog>);
- ISC catalog (<http://www.isc.ac.uk>);
- ISC-GEM catalog (<http://www.isc.ac.uk/iscgem/index.php>);

The resulting catalog has a time span from August 1903 to December 2020 for a total amount of 864298 events, with ranges in magnitude and depth from 1.5 to 7.8 and from 0 to 50 km, respectively. The largest earthquakes reported in the catalog ([Fig. 5.10](#)) occurred along the central (i.e., the 1944 M_w 7.6 Ulumescit event and the 1943 M_w 7.5 Comert-Ilgaz one) and eastern sectors of NAFZ (i.e., the 1939 M_w 7.8 Erzincan event), and in the southern Aegean region (i.e. the 1956 M_w 7.7 Amorgos event). The magnitude of completeness for the instrumental catalog, as computed in this study, ranges between 2.5 - 3.6 values.

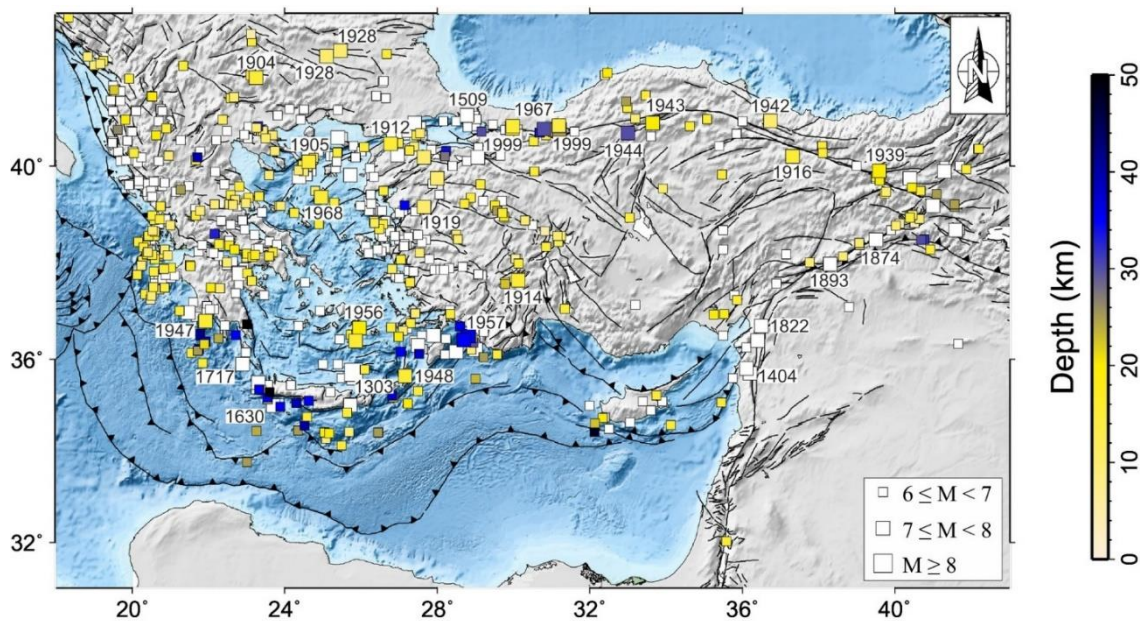


Figure 5.10 - Strong historical (1003 - 1903) and instrumental (August 1903 - December 2020) earthquakes ($M \geq 7$) in the Aegean-Anatolian region. Modified from [Sparacino et al. \(2022\)](#).

5.3.2 Geodetic Data.

We analysed an extensive GNSS dataset by collecting raw observations from SOPAC (<ftp://garner.ucsd.edu/pub>), EUREF (<https://www.epncb.oma.be>), NOAA (<ftp://alt.ngs.noaa.gov/cors>) and UNAVCO (<ftp://data-out.unavco.org>). The GNSS phase observations were processed by using the GAMIT/GLOBK 10.7 software ([Herring et al., 2018](#)) following the approach described in [Palano et al. \(2020\)](#) in order to estimate a consistent set of

positions and velocities in a fixed Eurasian reference frame (Palano et al., 2017). To improve the spatial density of the geodetic velocity field over the study area, we integrated our solutions with those reported in recent literature (Nocquet, 2012; Tatar et al., 2012; Aktüg et al., 2013; Tiryakioğlu et al., 2013; Vernant et al., 2014; Chousianitis et al., 2015; Metois et al., 2015; England et al., 2016; D'Agostino et al., 2020) by solving for Helmert transformation parameters that minimize the differences between velocities at common sites (e.g. Herring et al., 2018). We removed all sites having a formal error greater than 1.5 mm/year (e.g. 3 times larger the average error of the whole dataset) in their velocity; all the removed sites correspond to literature solutions and account for less than 5% of the whole dataset. The final velocity field is reported in Fig. 5.11a. We estimated the horizontal strain-rates using the method of Shen et al. (2015), which allows us to model the horizontal velocity gradients on a regularly spaced grid by means of a least squares inversion. To estimate strain-rates along the Hellenic and the Cyprian subduction zones, we defined a composite velocity field given by our final velocity field and by the one, computed on a $0.5^\circ \times 0.5^\circ$ grid, from the expected motion of the Nubian plate with respect to the Eurasian one. The subduction interface by Basili et al. (2013) is used to define the northern boundary of the Nubian velocity field. Our final strain-rate field is reported in Fig. 5.11b.

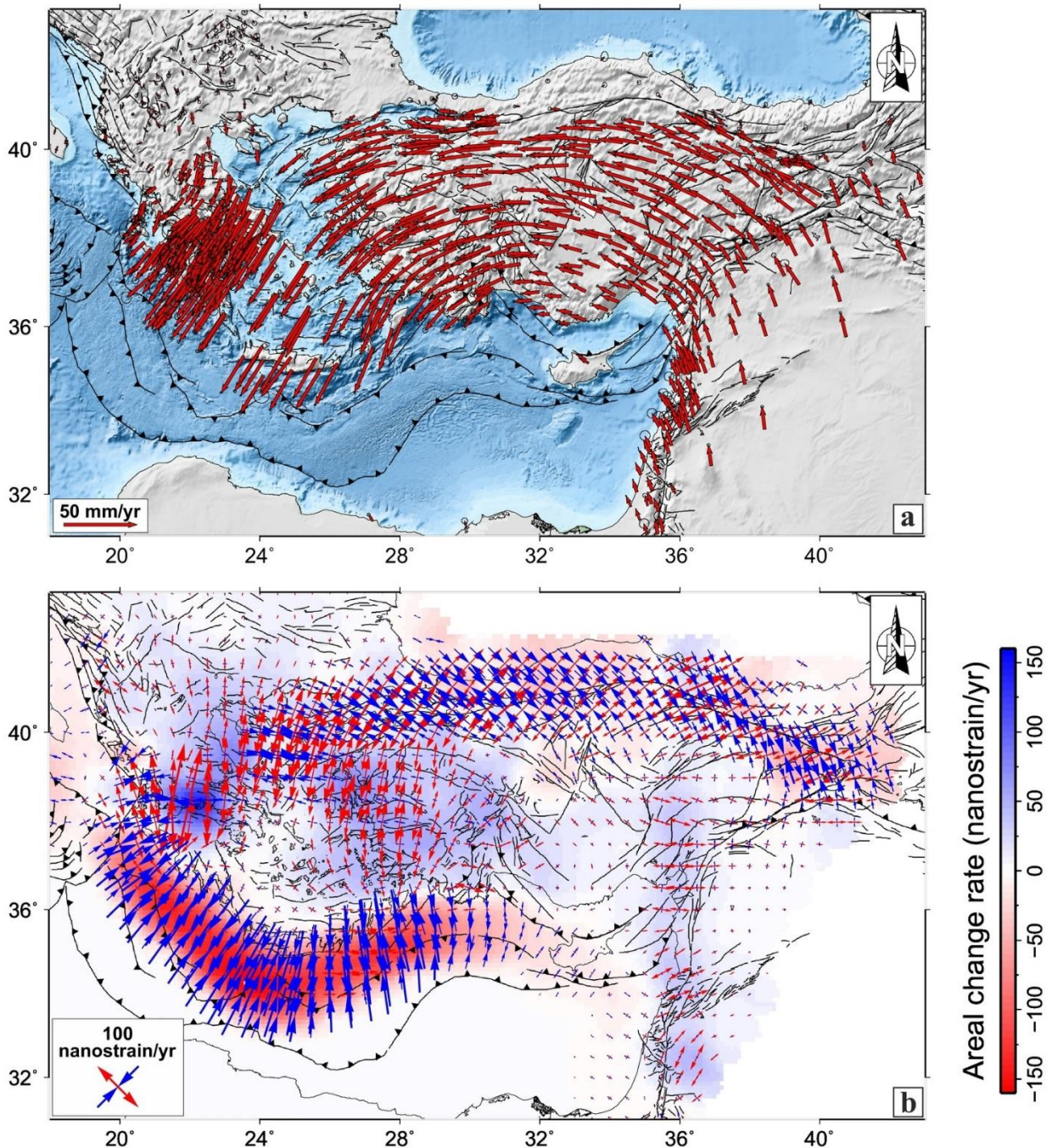


Figure 5.11 – (a) GNSS velocities and 95% confidence ellipses in a fixed Eurasian plate. (b) Geodetic strain-rate field: the background colour represents the rate of areal change, while arrows represent the greatest extensional (red) and contractional (blue) horizontal strain-rates. Modified from Sparacino et al. (2022).

5.3.3 SCC Results and conclusive remarks.

SCC estimation for the Aegean-Anatolian area is reported in Fig. 5.12. Most of the area is characterized by low (< 35%) and intermediate (35% - 70% interval) SCC values, while only a few cells show values larger than 70% (with some cells exceeding 100%). Cells with high SCC values are located along a N-S-oriented boundary between western and central Anatolia, in the south-eastern Peloponnese, along the eastern sector of the Hellenic volcanic arc, and at the NAZF and EAZF

junction (Karlioiva triple junction); active faults in these regions are therefore fully coupled. Cells with intermediate SCC values are located in northern Albania, western Greece (CTF, Peloponnese and Gulf of Corinth), along the western sector of the Hellenic volcanic arc, south-western of Crete, and western and south-eastern Turkey, suggesting an intermediate coupling for major tectonic elements, such as EAFZ, western NAFZ (i.e. the fault segment close to Izmut area) and CTF and most of southern PSSZ. Low SCC values have been estimated for most of central and eastern Turkey, the off-shore surrounding Cyprus, northern and central Greece and along most of the Hellenic subduction zone, pointing toward an aseismic behaviour of active faults. Achieved results for the Aegean region generally agree with most of the previous findings (Ward, 1998; Jackson and McKenzie, 1988; Vernant et al., 2014; Jenny et al., 2004; Rontogianni, 2010; Chousianitis et al., 2015). Regarding Anatolia, our SCC estimates differ from the one performed by Ward (1998), pointing to a higher degree of coupling, especially on the western and central sectors of the region.

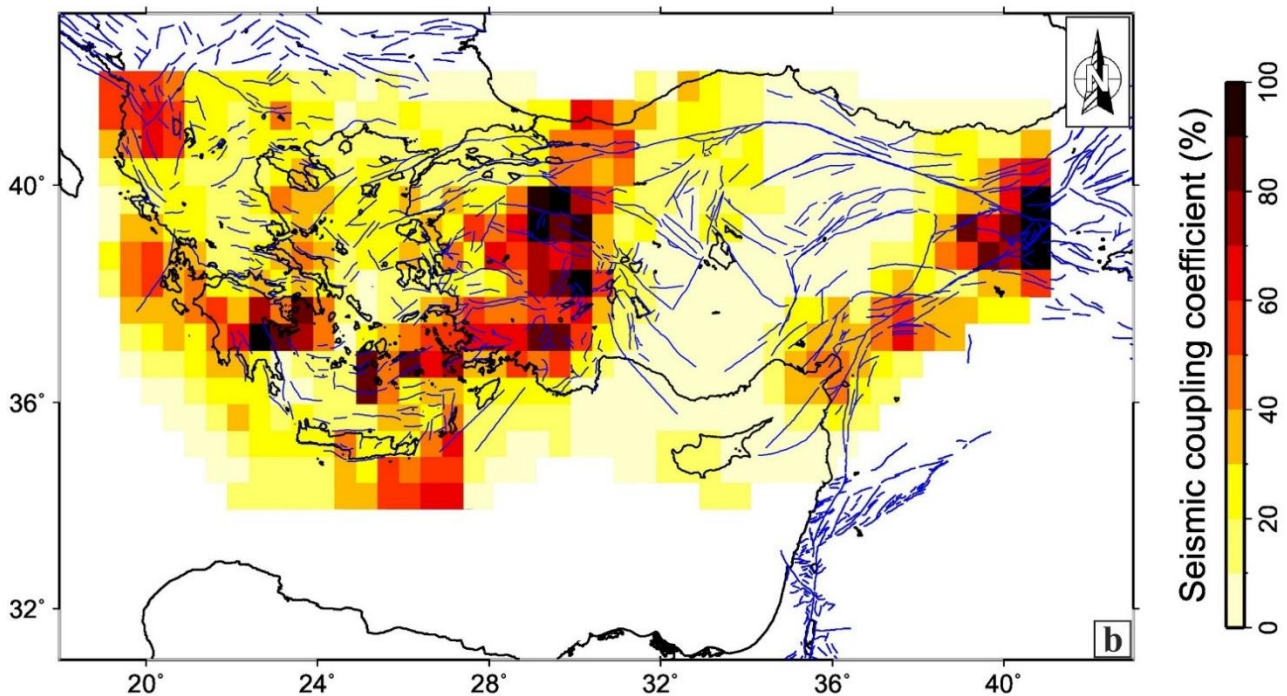


Figure 5.12 – Spatial pattern of the seismic coefficient coupling (SCC). Modified from Sparacino et al. (2022).

5.4 Egypt.

An updated earthquake catalog, focal mechanism solutions coming from previous publications, and novel strain-rate field data were used to study the spatial patterns of seismic and geodetic moment-rates of the Egypt.

The primary tectonic features of the surrounding plate boundaries of Egypt were studied and discussed by several researchers (Ben-Menahem et al., 1976; Ben-Avraham et al., 1987; WCC-Woodward Clyde Consultants, 1985; Kebeasy, 1990; DeMets et al., 2010). The Nubian-Eurasian plate margin in the north, and the Gulf of Suez-Red Sea plate margin, and the Gulf of Aqaba-Dead Sea Transform Fault system in the east represent the three main tectonic features in the vicinity of Egypt

(Fig. 5.13). On one hand, based on the analysis of fault systems, oceanic spreading, and earthquake slip vectors, the global kinematic models by DeMets et al. (2010) show that across a wide zone in the Mediterranean Sea, both the Nubian and Eurasian plates are converging. The Nubian plate is moving in a northerly direction relative to the Eurasian plate at a rate of about 10 mm/year (DeMets et al., 2010). This form of closeness is translated in the form of the Cyprian and the Hellenic Arcs along the Eastern Mediterranean region (Fig. 5.13). On the other hand, the Arabian plate is continuing to rotate away, in a north-eastward divergent movement, from the Nubian plate along the Gulf of Suez-Red Sea Rift (Hempton, 1987; Bosworth and McClay, 2001; Schlumberger, 1984) (Fig. 5.13). This rift is considered one of the premier examples of the creation of a new ocean and ongoing rifting. This rift system may extend further towards the north beneath the Suez Canal area, but the alluvial Nile deposits (Freund et al., 1970) probably mask this possible extension. Finally, the differential motion between the Nubian and the Arabian plates (about 15 mm/year) is thought to be taken up by the Gulf of Aqaba-Dead Sea Transform Fault System (Salamon et al., 2003). This is a seismically active 1100 km long left-lateral strike-slip transform boundary (Fig. 5.13) that connects the northern Mediterranean triple junction in the north to the Red Sea spreading center in the south (Bartov et al., 1980). Geological evidence suggests that a pure strike-slip motion with slip rates between 5 and 10 mm/year occurs along this transform fault (Joffe and Garfunkel, 1987; Sneh, 1996; Marco et al., 1997). This left-lateral sense of motion was recognized by the minor pull-apart in young sediments, cut and offset of man-made structures, and drainage lines (Garfunkel et al., 1981; Zilberman et al., 2000; Amit et al., 1999; Klinger et al., 2000; Gomez et al., 2003; Sawires et al., 2017).

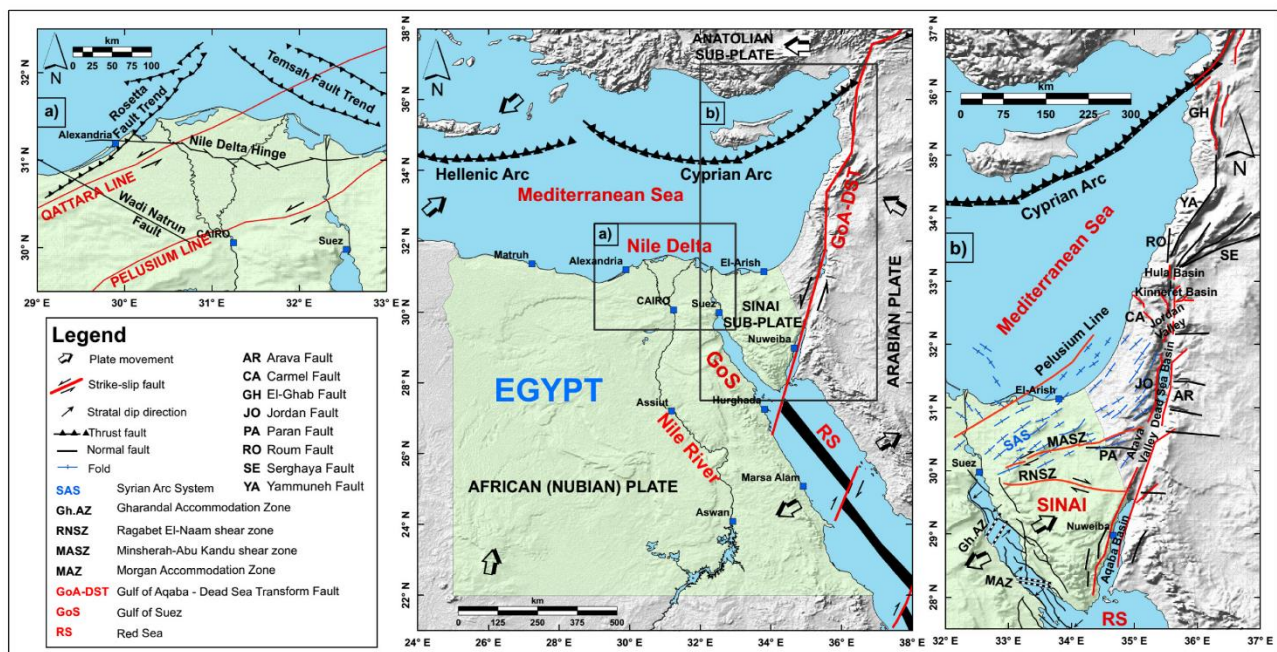


Figure 5.13 – Compiled global tectonic sketch for Egypt and its surrounding regions, the Nile Delta region, the Sinai Peninsula and the Dead Sea regions. Abbreviations for the geographic features, faults, and shear zones are included in the legend. Modified from Sawires et al. (2021).

5.4.1 Seismological Data.

As a first step towards the delimitation of areal seismic sources and the estimation of relevant seismicity parameters, an earthquake catalog was compiled from the beginning taking into account previous catalogs. A spatial region extending from 24 to 38 E longitudes and from 21 to 34 N latitudes was considered, within the period starting from 2200 B.C. until 2020. In the compilation, all shallow earthquakes ($H_s < 35$ km) above magnitude 3.0 on any magnitude scale were gathered. Several catalogs, bulletins, and publications were inspected and gathered to compile the dataset.

- The Poissonian earthquake catalog by [Sawires et al. \(2016\)](#) for Egypt was considered as a priority since they considered both historical and instrumental earthquakes, covering large spatial (the whole territory of Egypt) and temporal extension (2200 B.C.-2014). The final number of earthquakes gathered from this catalog was 22054 events.
- The local instrumental earthquake catalog of the Egyptian National Seismic Network was published by [Abd El-Aal et al. \(2020\)](#). They considered the time period from 1997 to 2019. A number of 1543 earthquakes from this reference (including magnitudes equal to or greater than 3.0) was also included in our catalog.
- An additional number of earthquakes (4885 events) were collected from the Israel National Seismic Network (FDSN; <https://www.fdsn.org/networks/detail/IS/>) in addition to other related publications ([Deif et al., 2017](#)).
- The instrumental earthquake catalog developed by [Deif et al. \(2017\)](#) for the Arabian Peninsula was also considered, especially for the Red Sea region. Their catalog covers the period between 1900 and 2015, and 974 earthquakes from it were considered to be included in our database.
- Besides these local bulletins and catalogs (for Egypt, Israel, and the Arabian Peninsula), data from regional and international bulletins were also gathered. Within the period from 2014 until the present, a number of 393, 12, and 73 earthquakes in this region have been collected from the International Seismological Centre (ISC; <http://www.isc.ac.uk/iscbulletin/search/>), the ISC-EHB bulletin (<http://www.isc.ac.uk/isc-ehb/>), and the National Earthquake Information Center, United States Geological Survey (USGS; <https://earthquake.usgs.gov/earthquakes/search/>), respectively.

These data were merging in a catalog of 29934 events; after duplicated events have been removed following several procedures, a final catalog with 3419 earthquakes was obtained covering the geographic region between 21° and 34° N latitudes, and between 24° and 38° E longitudes, and within the period from 2200 B.C. to 2020, including both historical and instrumental earthquakes ([Figs. 5.14-5.15](#), respectively).

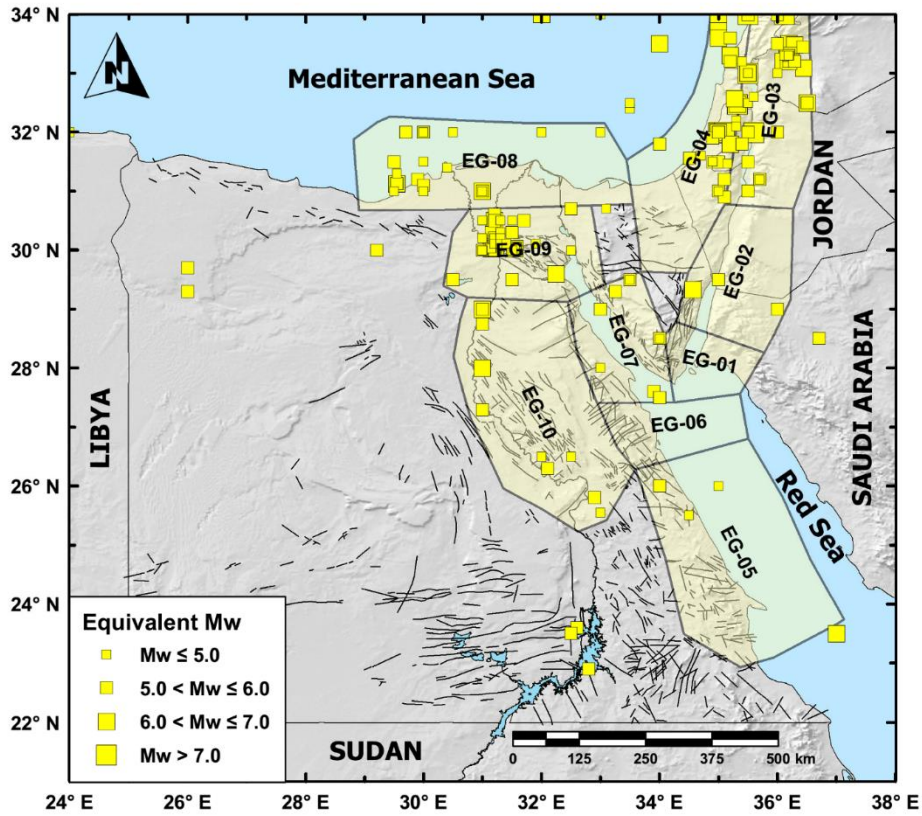


Figure 5.14 - Historical earthquakes (2200 B.C.-1899 A.D.) of Egypt and its surroundings (after Sawires et al., 2016; EGSA, 1981). Black lines refer to EGSA (1981). In Sawires et al. (2021), polygons labelled from EG-01 to EG-10 refer to the delimited seismic sources. Modified from Sawires et al. (2021).

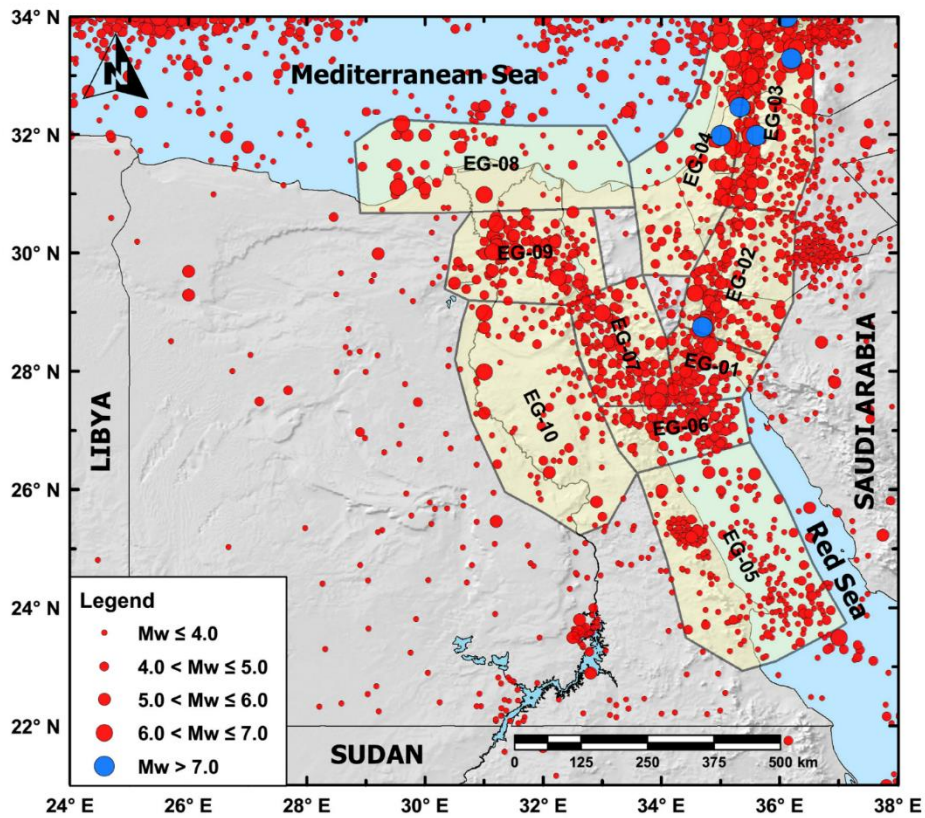


Figure 5.15 - Spatial distribution of declustered instrumental seismicity (1900-2020). Modified from Sawires et al. (2021).

5.4.2 Geodetic Data.

A recent update of geodetic velocities and horizontal strain-rates for Egypt has been published by [Rashwan et al. \(2021\)](#), therefore in the following, we refer to these results. The geodetic velocity field has been derived from a set of episodic and continuous GNSS observations collected during the 1995-2005 and 2000-2018 time spans, respectively. GNSS stations prevailing cover the eastern sector of Egypt, allowing measurement of the crustal deformation related to the most relevant tectonic elements of the region. In particular, in [Rashwan et al. \(2021\)](#), it is evidenced that (i) the north-western coastal area and central Egypt show a pattern in agreement with the rigid motion of the Nubian Plate; (ii) the stations located along the western side of the Red Sea show a northward motion of ~ 1 mm/year; (iii) the stations located on the north-eastern Sinai Peninsula show an NNW motion with rates larger than 1.6 mm/year; and (iv) the stations on the Nile Delta show a complex pattern, both on the horizontal and vertical components, reflecting the general subsidence of the area.

[Rashwan et al. \(2021\)](#) also estimated the horizontal strain-rate field over a regular $0.5^\circ \times 0.5^\circ$ grid. Considering such a horizontal strain-rate field ([Fig. 5.16](#)), values up to ~ 25 nstrain/year can be observed along the Gulf of Aqaba-Dead Sea Transform Fault with extension along with the WSW-ENE orientation, passing to SW-NE attitudes along the Red Sea basin. Along the region between the Nile Valley and the Red Sea, the strain field shows a NNE-SSW attitude with rates progressively decreasing westward. The Gulf of Suez shows values ranging from ~ 20 nstrain/year (southward) to ~ 8 nstrain/year (northward), while on the northern sector of the Nile, the shortening strain axes show an E-W orientation with values up to ~ 8 nstrain/year.

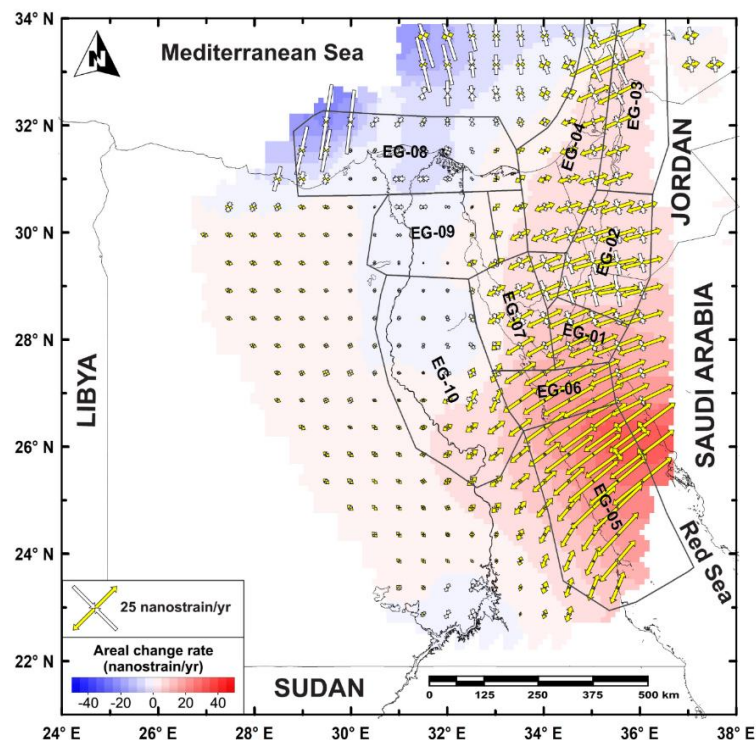


Figure 5.16 - Geodetic strain-rate field (after [Rashwan et al., 2021](#)) overlain by the defined seismic sources. Colour scale range (from blue to red) in the background of the plot shows the areal change in the strain-rate field, while the arrows refer to the maximum extensional (in red) and maximum contractional (in blue) horizontal strain-rates. Modified from [Sawires et al. \(2021\)](#).

5.4.3 SCC Results and conclusive remarks.

The obtained seismic-geodetic moment-rates ratios (SCC%) are depicted in Fig. 5.17. Based on the estimated SCC results, we could consider three principal ratio ranges in the current study. Four delimited seismic sources are characterized by lower SCC values (less than 20%). They are the EG-05, EG-06, EG-08, and EG-10 seismic sources. They cover the seismicity along the central Red Sea region, the triple junction between the Gulf of Suez, Gulf of Aqaba, and the Red Sea, the northern Nile Delta block, and the central part of the Nile Valley, respectively (Fig. 5.17). Such a result suggests that in these sectors, deformation occurs prevalingly in an aseismic mode. As mentioned above, moment-rates estimations for EG-08 and EG-10 must be considered with caution, being the computed strain-rates not homogeneously distributed within the seismic zones. Since the moment-rates estimations have been performed by taking into account the largest strain-rate values for both zones, we performed an additional computation by considering the average strain-rate value. Achieved results do not significantly alter the previous considerations, being the new SCC values increasing of a factor of 1.3 and 2.2 for the EG-08 and EG-10 zones, respectively.

Another ratio range is observed for the sources EG-01, EG-04, EG-07, and EG-09 (Fig. 5.17), characterized by moderate SCC values (between 20% and 60%). They defined the seismic activity along the southern Gulf of Aqaba, north-eastern Sinai and eastern Mediterranean coast, the southern and central parts of the Gulf of Suez, and the Cairo-Suez district and northern Gulf of Suez, respectively (Fig. 5.17). Therefore, these moderate SCC values are suggesting that these areas account for only an intermediate seismic fraction from the total budget of the deformation rate. Some of these seismic regions are characterized by well-known active faults that frequently generate moderate seismic activity such as in the Cairo-Suez district, the southern and central half-grabens of the Gulf of Suez.

Finally, the highest SCC values (actually $> 100\%$, labelled as $> 60\%$ in Fig. 5.17) have been reached in the current study for the EG-02 and EG-03 seismic sources. Both zones are located along the GoA-DST, which extends in the NE-SW direction. Such results suggest that the crustal deformation is mostly released through seismic activity. As mentioned above, strain-rate estimation for EG-03 concentrated only on the western side of the source, while no estimations are available for the eastern side. The high SCC value in this source points to an underestimation of the geodetic rates or an overestimation of the seismic ones, as discussed previously. The high seismic rate is well constrained because of the long-time interval covered by the catalog as well as the occurrence of some $M \geq 6.0$ earthquakes (since 590 A.D.). Moreover, an underestimation of geodetic rates could be possible because of the existence of very few stations within the seismic zone, which therefore would not be enough to properly constrain the deformation pattern of active faults. Regarding the EG-02 source, seismic moment-rate, as explained previously, was computed from individually recorded earthquakes in the last 50 years. This implies that the obtained result must be also considered with care.

To conclude, the obtained results provide the basis of the evaluation of the completeness periods of the earthquake catalog, guide the spatial delimitation, definition, and characterization of the potential seismic active sources for future seismotectonics and probabilistic seismic hazard

assessment studies, and motivation for the integration of geodetic data with the seismic data for seismic hazard studies.

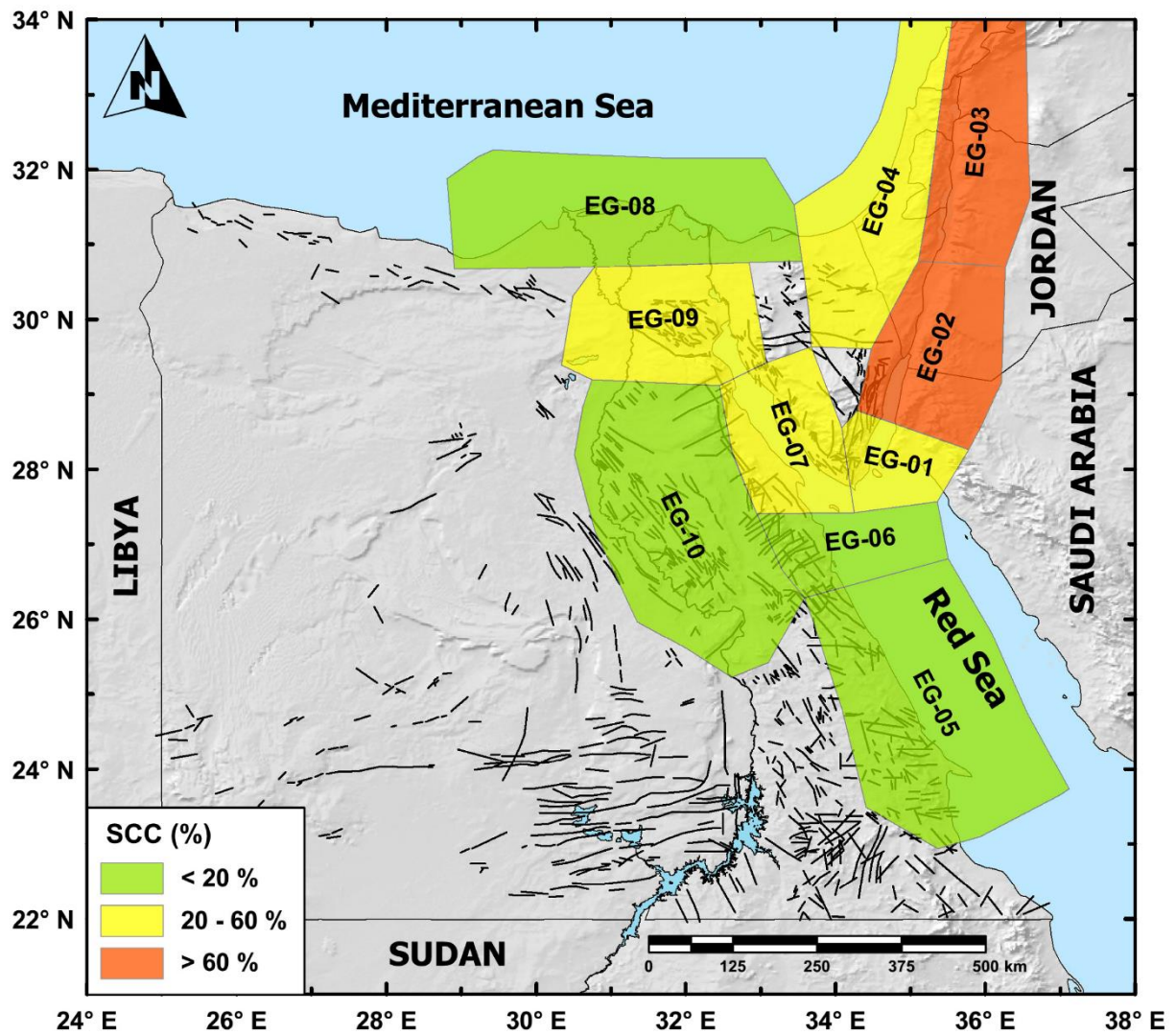


Figure 5.17 - Seismic coupling coefficient (SCC) is depicted as a percentage of the seismic-geodetic moment-rate ratio. Modified from Sawires et al. (2021).

6 – General Discussion

In this chapter the general problems and limitations related to the method will be discussed in details.

6.1 General estimation problems.

The method has been applied in different areas and the majority of the critical issues are related to the estimated parameters necessary for the application of the formulas for seismic and geodetic moment-rates computation ([Chap. 2](#)). Moreover, it should be remembered that as regards the seismic moment, the parameters that vary are the following:

- *a-value*;
- *b-value*;
- the maximum magnitude value, M_{max} .

As regards the geodetic moment they are:

- the seismogenic thickness, H_s ;
- the maximum strain value;
- the shear modulus, μ .

Keeping in mind that the variation of all these six parameters affects the estimate of the final SCC, it follows that the statistical methods used for calculating them are of key importance.

Being aware that on the one hand, the earthquake occurrences and statistics may not be steady state over the whole timescales of the used seismic catalog and that on the other hand, the truncated Gutenberg-Richter distribution allows taking into account the probable incompleteness of the catalog, the obtained results must be compared with available and independent geological and geophysical observations.

The geometry of the used grid for moment-rate calculation plays a significant role. For example, for Italy case study another criticality is due to its geographic conformation. The regular grid used for the moment-rates calculation can be too small to contain the main fault systems, especially in Southern Apennines and this aspect could have affected the final MLE-LSR and RFM-SCC values ([Chap. 4](#)). The source zones used by [Jenny et al. \(2006\)](#) for Southern Italy, with irregular shape, are based on tectonic interpretation and they could be more suitable for Italy. So, if on one hand the aseptic spirit workflow ([Chap. 3](#)) simplifies a part of the work, on the other must be keeping in mind that for some areas a regular geometry may strongly limit the subdivision of the analysed study area into sources with specific seismotectonic characteristics. This problem could be solved improving the workflow with a variable geometry.

In [Table 6.1](#) a summary of the adopted and estimated parameters are reported for all the investigated zones.

	Ibero-Maghrebian Region (Sparacino et al., 2020)	Italy	Sicily Channel (Palano et al., 2020)	Aegean-Anatolian Region (Sparacino et al., 2022)	Egypt (Sawires et al., 2021)
Grid geometry	irregular shapes	regular squared	polygon	regular squared	irregular shapes
H_s (km)	15, 18, 20 see Table 2 (Sparacino et al., 2020)	10 - 30 see Par 4.3.4	9 - 13	30, 35, 40 see Supplementary Material (Sparacino et al., 2022)	18 - 27 see Table 3 (Sawires et al., 2021)
μ (N m ⁻²)	$3 \cdot 10^{10}$	$3 \cdot 10^{10}$	$3 \cdot 10^{10}$	$3 \cdot 10^{10}$	$3 \cdot 10^{10}$
Strain grid (°)	0.5 x 0.5	0.25 x 0.25	0.25 x 0.25	0.5 x 0.5	0.5 x 0.5
c	1.5	1.5	1.5	1.5	1.5
d	9.05	9.1	9.1	9.1	9.1
M_{max}	see Table 1 (Sparacino et al., 2020)	3.7 - 7.3	5.7	6.0 - 8.5	5.40 - 7.85
A (m ²)	see Table 2 (Sparacino et al., 2020)	different for each cell	$4.1 \cdot 10^{10}$	Not listed online	see Table 3 (Sawires et al., 2021)
a -value	see Table 1 (Sparacino et al., 2020)	2.54 - 7.87 (MLE) 0.30 - 7.91 (LSR) 0.30 - 7.94 (RFM)	3.85	4.67 - 7.85 (MLE) 3.28 - 7.98 (RFM)	Not listed online
b -value	see Table 1 (Sparacino et al., 2020)	0.35 - 1.80 (MLE) 0.50 - 1.90 (LSR) 0.46 - 1.90 (RFM)	1.12	0.66 - 1.37 (MLE) 0.50 - 1.26 (RFM)	see Table 2 (Sawires et al., 2021)
M_{seis} (Nm yr ⁻¹)	see Table 1 (Sparacino et al., 2020)	$7.58 \cdot 10^{13}$ - $6.80 \cdot 10^{17}$ (MLE) $7.22 \cdot 10^{13}$ - $8.02 \cdot 10^{17}$ (LSR) $7.23 \cdot 10^{13}$ - $9.41 \cdot 10^{17}$ (RFM)	$6.58 \cdot 10^{15}$	$8.2 \cdot 10^{15}$ - $9.8 \cdot 10^{18}$ (MLE) $5.3 \cdot 10^{15}$ - $8.6 \cdot 10^{18}$ (Kos)	$2.1 \cdot 10^{16}$ - $213 \cdot 10^{16}$ see Table 2 (Sawires et al., 2021)
M_{geod} (Nm yr ⁻¹)	see Table 2 (Sparacino et al., 2020)	$1.62 \cdot 10^{16}$ - $1.82 \cdot 10^{18}$	$7.24 \cdot 10^{17}$	$5.8 \cdot 10^{17}$ - $1.5 \cdot 10^{19}$	$26.4 \cdot 10^{16}$ - $493 \cdot 10^{16}$ see Table 3 (Sawires et al., 2021)
M_c	not listed online	1.7 - 2.9	2.8	2.5 - 3.6 (MLE)	see Table 1 (Sawires et al., 2021)
Historical catalog (yr)	AD 856 - 1950	1005 - 1984	1578 - 1965	1003 - 1903	2200 BC - 1899 AD
Instrumental catalog (yr)	1951 - 2019	1985 - 2022	1966 - 2018	1903 - 2020	1900 - 2020
GNSS time (yr)	1999 - 2019	1995 - 2022	1995 - 2020	1999 - 2020	1995 - 2018

Table 6.1 – Summary of adopted (M_{max} , H_s , A , μ , c , d) and estimated (a , b , M_c , M_{seis} , M_{geod}) parameter values. Seismic and geodetic time interval datasets are also reported.

6.2 General uncertainties and limits.

Geodetic and seismic moment-rates estimates are affected by some physical uncertainties. It is clear that several factors control the obtained results, and it may be useful to have a priori knowledge of the investigated zone. Nevertheless, there are some key points that must be kept in mind when we apply the shown methodology. Summing up, the principal additional critical factors that may affect seismic and geodetic moment-rates estimations are the following.

1) Availability of historical and instrumental information.

Seismic moment-rate estimates are commonly affected by the completeness (i.e. all the earthquakes above a given magnitude should be fully reported) and by the temporal length of the seismic catalogs (considering that a relatively short time-interval of 100-300 years may not be representative of typical seismic cycles in a given region, and so it could be poorly adequate in capturing the seismic cycle of a particular area and therefore it could underestimate the seismic moment-rate). To be considered robust, seismic moment-rate estimates performed using data from seismic catalogs require shorter average earthquake recurrence intervals than the catalog duration. On the other hand, instrumental 50-100 year-long catalogs are the most common source of data used worldwide in probabilistic seismic hazard analysis, under the assumption that such a time span would be adequate to derive earthquake return periods over timescales of 500-5000 years. Summing up, the critical points are the following:

- magnitude and uncertainties distribution;
- seismic cycle of the investigated region;
- maximum magnitude estimation (it could be untrue if the seismic cycle is too short).

2) Truthfulness of geodetic data.

Moreover, factors such as GNSS stations density, network geometry and smoothing parameters chosen for strain-rate estimates also affect the resulting geodetic moment-rates. A dense geodetic dataset is strictly required. It must include continuous GNSS stations with at least 3 years of observations. Episodic measurements can be also considered (more than 5 years of observations, with more than 7 measurements; the pattern must be congruent with the nearest sites). The geodetic strain-rates should be derived by using different approaches. For instance, geodetic measurements should sample a large spatial scale:

- so that they are not affected by local strain accumulation on individual faults;

and a long enough time-interval:

- so that measurement uncertainties have a minimal effect on geodetic velocity field estimations (if they are too average the geodetic strain-rate will be underestimated);
- and adequately sample both seismic and aseismic spectrum, as well as long-term deformation transients.

Other critical factors could be due to:

- the interpolation method chosen for the geodetic strain calculation;
- many earthquakes have off-shore epicentres and consequently they will not be sampled from GNSS stations. Their seismic energy released would correspond to a strain in depth without any correspondence at the surface; this would cause another underestimation of the geodetic strain;

- the chosen crustal rigidity modulus strongly affects the geodetic moment estimation;
- a robust estimation of the seismogenic thickness (as well as its variation over the investigated area) is strictly required. It needs an instrumental catalog with well constrained focal parameters;
- geodetic moment-rate estimations can be influenced also by the orientations of active faults within the investigated crustal volume (Carafa et al., 2017). This implies an increase of 15% of the moment-rate estimations for the regions where the dominant faulting style is normal or reverse, which on turn led to a decrease of the estimated SCC values.

Moreover, is preferable that GNSS dataset does not include large earthquakes, since these could significantly contribute with co-seismic and post-seismic displacements to the estimated geodetic velocities.

The ratio between seismic and geodetic moment-rate (expressed as a percentages) has been defined as the Seismic Coupling Coefficient (SCC). Such a ratio theoretically ranges between 0 and 100%. Closer percentages to 100% reflect that a large amount of the deformation budget is released by earthquakes. In such cases, large earthquakes are the common behaviour of faulting and the time-span after the past large event became an important indication of how temporally close the next one could be. Conversely, a low ratio indicates an apparent seismic moment deficit, suggesting either accumulating strain not released by seismicity (i.e., elastic storage) or a significant proportion of aseismic deformation (i.e. ongoing unloading by creep and other plastic process). Anyway, it is possible that the SCC exceeds the 100% value when seismic moment-rate values are greater than the geodetic ones, and this case is usually observed in areas where the seismic catalogs cover a relatively short time and contain one or more large earthquakes.

As has been said before, the completeness period of the used seismic catalog, as well as its temporal span, govern the adequacy of catalogs and so they may affect the seismic moment-rate estimations for a studied region (Ward, 1998). In other words, to estimate reliable seismic moment-rates, the average earthquake recurrence interval should be shorter than the duration of the catalog. In other words, a seismic catalog with a short duration (~100 - 300 years) could be little adequate to capture the seismic cycle of a given region; indeed, seismic moment-rates estimated from seismic catalogs require that the average earthquake recurrence interval should be shorter than the catalog duration (Ward, 1998; Pancha et al., 2006; Mazzotti et al., 2011; Palano et al., 2018). This means that the used seismic catalog would be long enough to capture a complete earthquake cycle for an individual seismogenic fault or alternatively, to provide a statistical sample of all phases of the seismic cycle, including of course earthquakes, for a region containing multiple seismogenic faults. Moreover, 50 - 100 year-long instrumental catalogs are the most common source of data used to derive earthquake statistics worldwide, under the assumption that such a time span is adequate to derive earthquake return periods over timescales of 500 - 5000 years, typically used in probabilistic seismic hazard analysis. About the used methods seen for the seismic moment-rate estimation, the Kostrov approach suffers from the possible lack of both large earthquakes (with high recurrence rate compared to the catalog duration) and undetected small magnitude events. The use of a statistical

method such as the cumulative truncated Gutenberg-Richter earthquake distribution allows taking into account the probable incompleteness of the existing catalog.

The mismatch between geodetic and seismic time periods it's a fact. As we have said before, the geodetic measurements should sample a time interval long enough to minimize the effect of velocity uncertainties and adequately sample both seismic and aseismic spectrum, as well as long term deformation transients. On the other hand, the seismic moment must reflect the seismic cycle of all the faults that fall in the investigated region and therefore this aspect requires long observation times. If short observation times are used, what you get are really small values. Therefore, the effect of the mismatch between geodetic and seismic time periods could reflect in an underestimation of the moments. For example, slowly straining regions require a proportionally longer period of observation (Ward, 1998). So, a region-specific analysis of the local seismicity and tectonics is necessary in order to establish the correct time periods needed for moment-rates estimation.

6.3 Efficiency of the method.

Despite the problems and the limits, we could say that the seismic and geodetic moment-rate balance have a strong scientific and socio-economic impact since it provides significant insights into the potential seismic hazard of tectonically active regions, essentially for time-dependent seismic hazard assessments. In addition, it improves the knowledge about the elastic and anelastic behaviour of each analysed area, which could be integrated with other geophysical methods (tomography, etc.) for a more robust analysis. As has been said, valuable examples come from several tectonic regions worldwide (Masson et al., 2019; Palano et al., 2018; Mazzotti et al., 2011; Pancha et al., 2006; Bos and Spakman, 2005; Rontogianni, 2010; Chousianitis et al., 2015; Jenny et al., 2006; Palano et al., 2011; D'Agostino, 2014; Bilham and Ambraseys, 2005; Bungum et al., 2017; Stevens and Avouac, 2017; Déprez et al., 2013) and from this PhD Thesis, providing an improved picture of the seismic hazard of the whole Mediterranean area. Despite the different approaches adopted by these authors and in this PhD Thesis, all the obtained estimations have enabled achieving valuable results that document cases with a good agreement between seismic and geodetic moment-rates and also cases where geodetic moment-rates are significantly larger than the seismic ones. However, uncertainties related to the physical significance of the deformation-rates mismatch over varying spatial and temporal scales are currently poorly understood. The continuous growth in continuous seismic and GNSS networks is allowing the acquisition of spatially extensive datasets at an increasing number of tectonic areas worldwide, therefore leading to an improved comprehension of such a physical significance. Moreover, considering that the exposed method and the developed workflow can be improved in future studies, this PhD Thesis may open the doors to the fundamental understanding of earthquake prediction.

Supplementary Material

S1 - The summation method.

In this section the summation method ([Kostrov, 1974](#)) for calculating seismic moment-rate and its problems will be analysed more in details.

It is known that the more temporally homogeneous is the distribution of the magnitudes falling in the analysed region, the more the Kostrov seismic moment estimation is accurate, because its formulation is directly proportional to the number of the events falling in the analysed region and inversely proportional to the time window of the analysed region.

Italy has been divided with a regular square grid ([Chap. 4](#)). Following the wake of [Middleton et al. \(2018\)](#), inside the workflow ([Chap. 3](#)) there is a code in which, chosen a time interval in which each cell is subdivided (for example 20 years, but if the time window and the number of the events are not related, this value could be not representative for the analysed region), and giving in input the geodetic moment, the moving average of the seismic moment of Kostrov can be obtained at three several time windows (100, 200 and 300 years) in a timeline, in order to study its distribution over time within each specific cell. This timeline allows us also to identify periods of time (within each cell) when there is a mismatch between the seismic moment-rate and the present-day geodetic moment-rate.

In the following, a cell in Northern, Central, Southern Italy, i.e. Calabria and Sicily, has been selected ([Chap. 4](#)). For a better understanding of the location of the cell, the relative Gutenberg-Richter figures are shown at the top.

In the panels a) of [Figs. S1-S4](#) it could be seen that when the magnitude distribution is homogeneous, the moving average of the seismic moment-rate is well estimated; conversely, when the distribution is sporadic or absent, the moving average is null. It is clear that the Kostrov approach reported is strongly affected by the distribution of the magnitudes inside the investigated region. The second information that these plots give us is the immediate identification of the periods of time in which the geodetic moment-rate is higher or lesser than the seismic one.

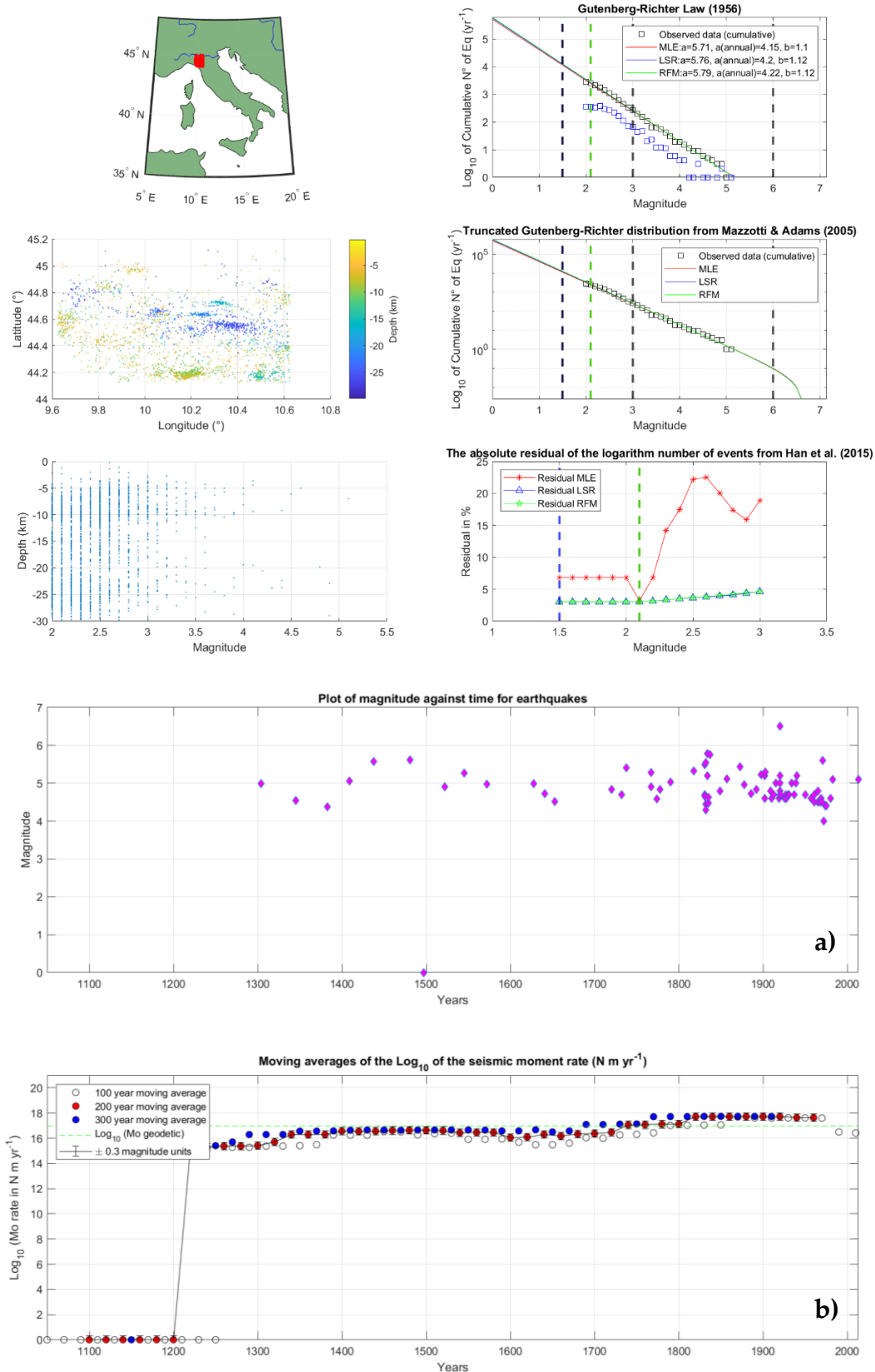


Figure S1 - Selected cell of Northern Italy (longitude: 9.65 - 10.65; latitude: 44.1 - 45.1). a) Magnitude distribution of earthquakes with time. The earthquakes are represented with fuchsia diamonds. b) Moving averages of the log of the seismic moment-rate (in Nm yr^{-1}), calculated every 20 year. The 100, 200, 300 year moving averages are reported with white, red and blue circles, respectively. Error bars, based on the assumption that values of M_w are known to the nearest ± 0.3 magnitude units, are shown for the 200 year moving average. Dashed green line shows the log of the geodetic moment-rate, extrapolated over the period from 1995 to 2022.

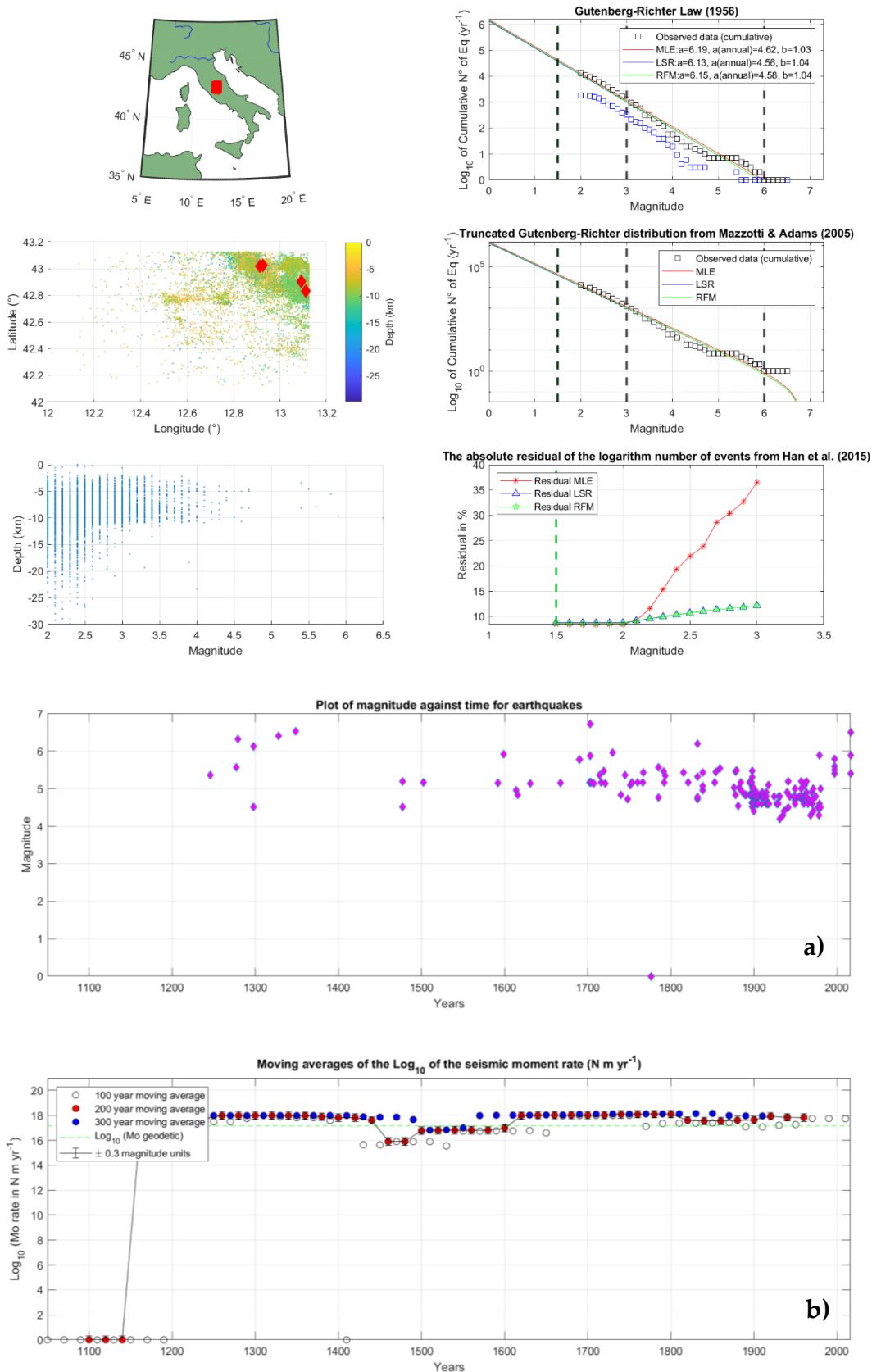


Figure S2 - Selected cell of Central Italy (longitude: 12.15 - 13.15; latitude: 42.15 - 43.15). a) Magnitude distribution of earthquakes with time. The earthquakes are represented with fuchsia diamonds. b) Moving averages of the log of the seismic moment-rate (in Nm yr^{-1}), calculated every 20 year. The 100, 200, 300 year moving averages are reported with white, red and blue circles, respectively. Error bars, based on the assumption that values of M_w are known to the nearest ± 0.3 magnitude units, are shown for the 200 year moving average. Dashed green line shows the log of the geodetic moment-rate, extrapolated over the period from 1995 to 2022.

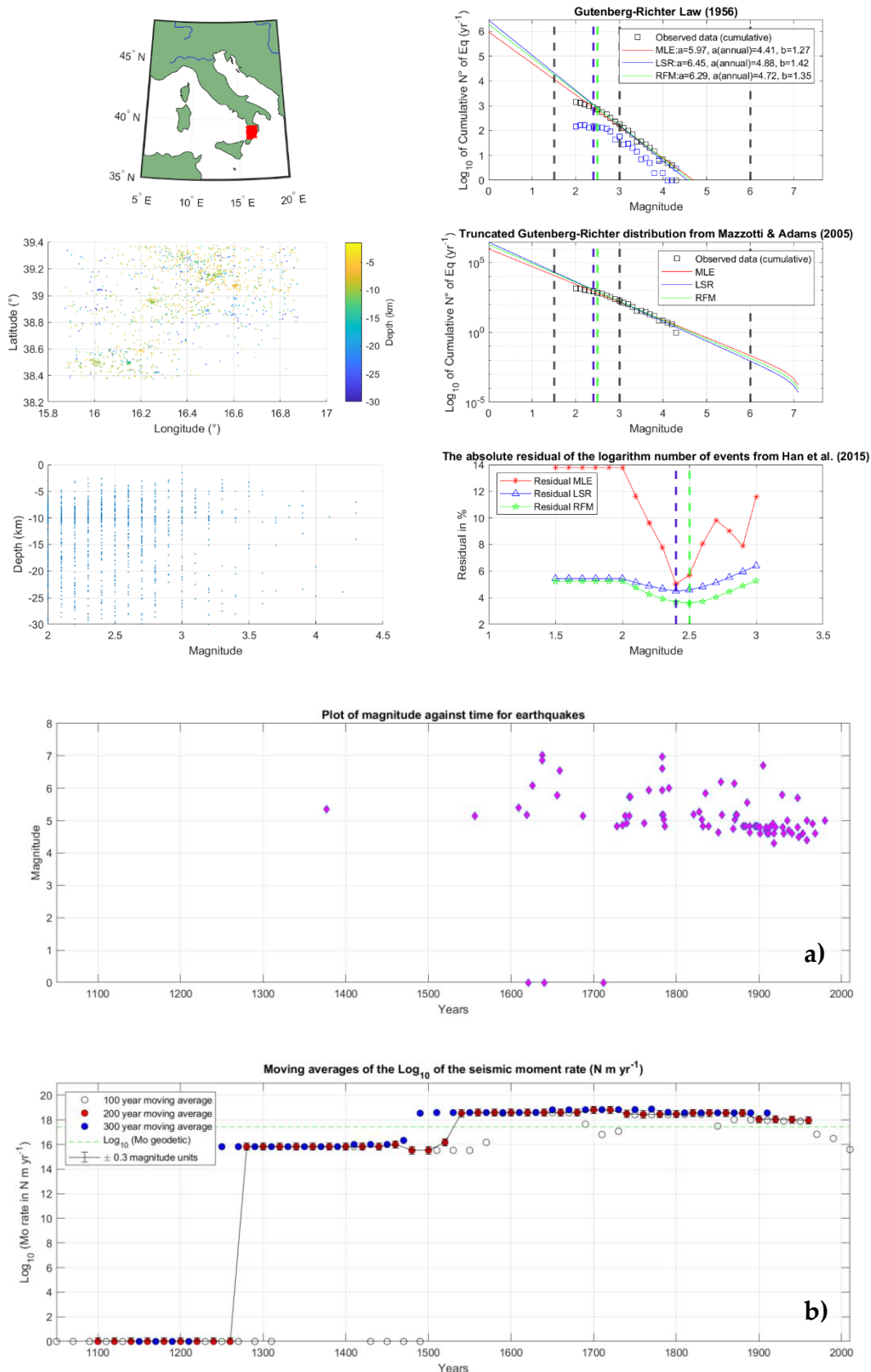


Figure S3 - Selected cell of Southern Italy, Calabria (longitude: 15.85 - 16.85; latitude: 38.35 - 39.35). a) Magnitude distribution of earthquakes with time. The earthquakes are represented with fuchsia diamonds. b) Moving averages of the log of the seismic moment-rate (in Nm yr^{-1}), calculated every 20 year. The 100, 200, 300 year moving averages are reported with white, red and blue circles, respectively. Error bars, based on the assumption that values of M_w are known to the nearest ± 0.3 magnitude units, are shown for the 200 year moving average. Dashed green line shows the log of the geodetic moment-rate, extrapolated over the period from 1995 to 2022.

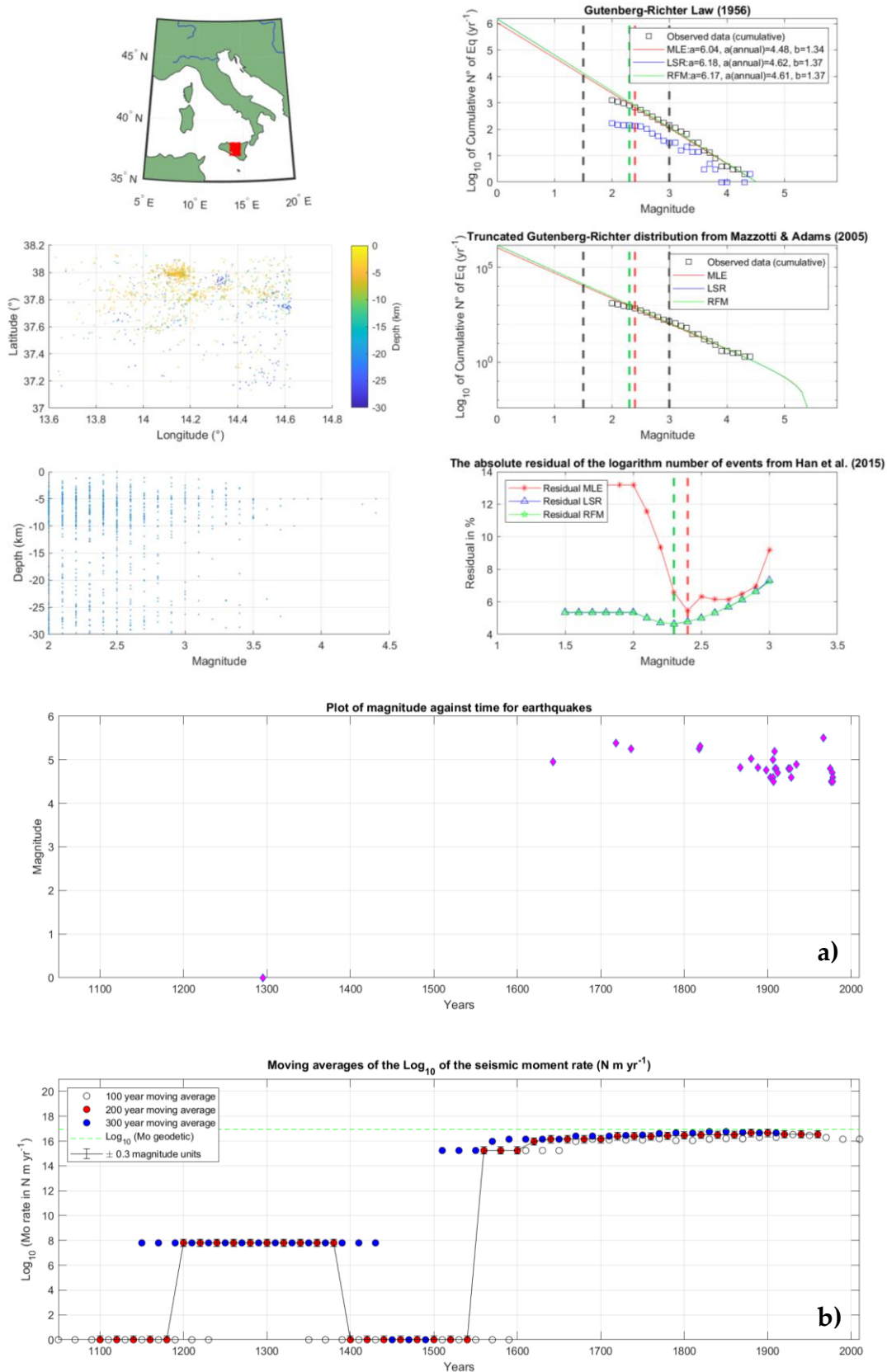


Figure S4 - Selected cell of Southern Italy, Sicily (longitude: 13.65 - 14.65; latitude: 37.15 - 38.15). a) Magnitude distribution of earthquakes with time. The earthquakes are represented with fuchsia diamonds. b) Moving averages of the log of the seismic moment-rate (in Nm yr^{-1}), calculated every 20 year. The 100, 200, 300 year moving averages are reported with white, red and blue circles, respectively. Error bars, based on the assumption that values of M_w are known to the nearest ± 0.3 magnitude units, are shown for the 200 year moving average. Dashed green line shows the log of the geodetic moment-rate, extrapolated over the period from 1995 to 2022.

S2 - Moment-rates tests for Sicily Channel.

Regarding the seismic moment-rate, our seismic catalog is temporally short with respect to the estimated return period for a wide area encompassing the investigated one, so it might not be complete. To test this eventuality, as a and b parameters are well constrained, we did some additional tests by simply varying M_x in the 4.6 - 7.5 interval, where the lower value is the maximum magnitude reported in our instrumental catalog, and the greater one represents the largest magnitude reported in the historical catalog for the surrounding regions. Results of this test (Fig. S5b) highlight that the seismic moment-rate increases according to the increase of M_x . Estimated values range in the interval $2.51 \cdot 10^{15} - 3.18 \cdot 10^{16}$ Nm/year. Even considering the largest value, again the difference between the seismic moment-rate and the geodetic one remains large (seismicity accounts only for 4.4% of the geodetic deformation).

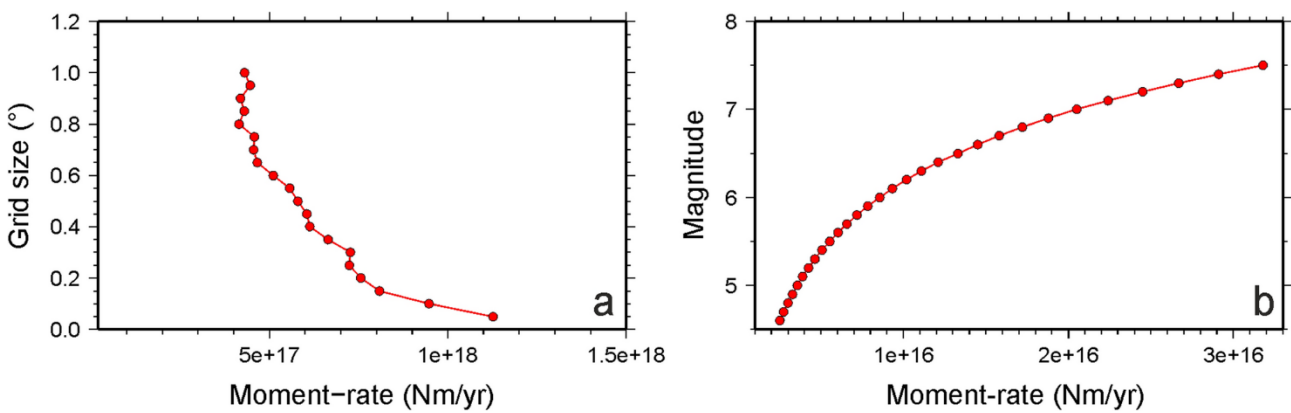


Figure S5 - a) Variation of geodetic moment-rate with respect to the size of the computational grid. b) Variation of seismic moment-rate with respect to increasing M_x values. Maps compiled using the Generic Mapping Tool, version 5 (<https://www.generic-mapping-tools.org>).

In order to assess the robustness of our moment-rate estimations we performed some additional computations of the strain-rate field by simply varying the size of the computational grid (from 0.05° to 1.0° ; see Fig. S6).

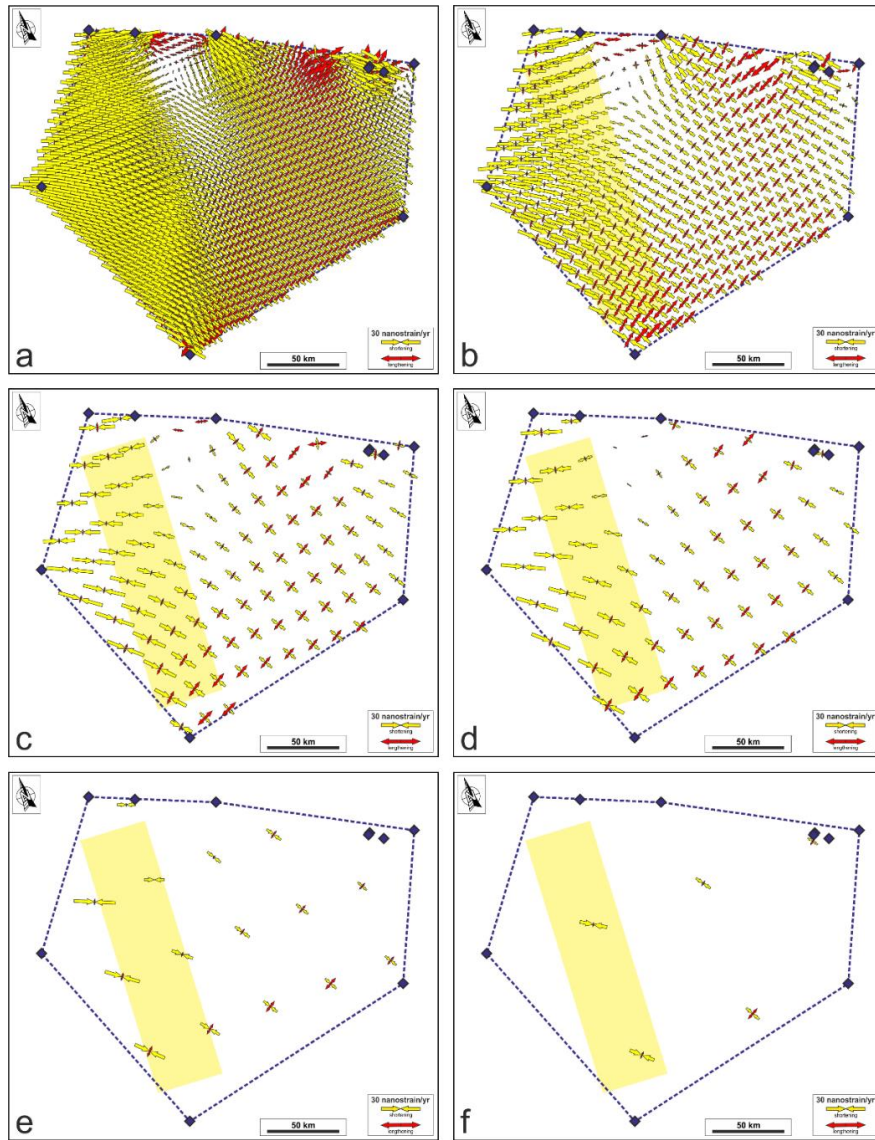


Figure S6 - Examples of strain-rate fields computed by using different grid size: a) $0.05^\circ \times 0.05^\circ$, b) $0.10^\circ \times 0.10^\circ$, c) $0.20^\circ \times 0.20^\circ$, d) $0.25^\circ \times 0.25^\circ$, e) $0.50^\circ \times 0.50^\circ$, f) $1.0^\circ \times 1.0^\circ$. The yellow strip represents the N-S-oriented tectonic belt. The blue polygon defines the study area. The blue diamonds represent the continuous GPS stations. Maps compiled using the Generic Mapping Tool, version 5 (<https://www.generic-mapping-tools.org>); image editing using Inkscape, version 1 (<https://inkscape.org>).

Results highlight that, as the grid size increases, the smoothing pattern and the number of local artefacts decrease (Fig. S6). Moreover, moment-rates estimates in the interval $1.13 \cdot 10^{18} - 4.31 \cdot 10^{17}$ Nm/year decrease as the computational grid size increases (Fig. S5a), its estimation being related to the largest value of strain-rate in the investigated region. However, even considering the smallest value, the difference between geodetic and seismic moment-rates remains too large, as seismicity accounts only for 1.4% of the geodetic deformation. We performed additional estimations varying the seismogenic thickness H_s in the 9-13 km interval. Results of this last test (Fig. S7) highlight that the geodetic moment-rate decreases according to the decrease of H_s . Estimated values range in the interval $2.98 \cdot 10^{17} - 1.13 \cdot 10^{18}$ Nm/year. Considering again the smallest value, seismic deformation accounts only for $\sim 2\%$ of the geodetic one.

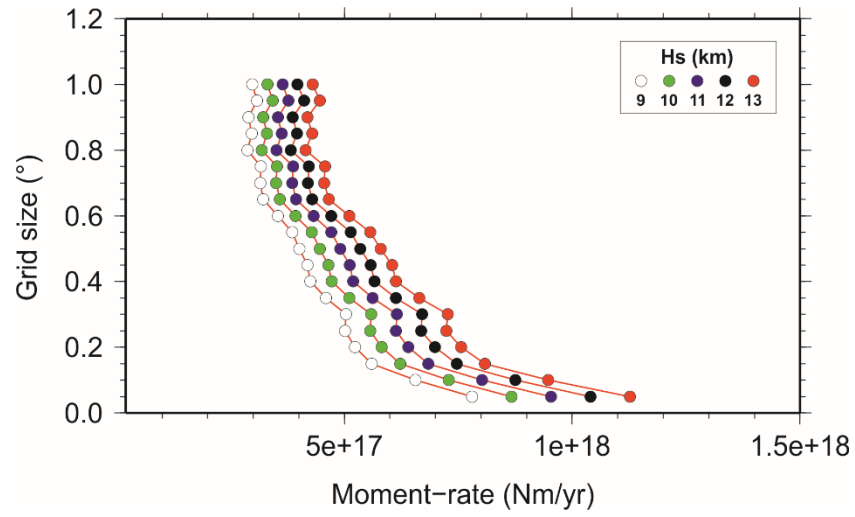


Figure S7 - Variation of geodetic moment-rate with respect to the size of the computational grid and the seismogenic thickness H_s . Maps compiled using the Generic Mapping Tool, version 5 (<https://www.generic-mapping-tools.org>).

References

- Abd El-Aal, A.E.-A.K., AbdelHafiez, H.E., Saadalla, H., & Soliman, M.S. (2020). A homogenous moment magnitude and local magnitude scaling relation for earthquakes in Egypt. *NRIAG J. Astron. Geophys.*, 9, 532–538. <https://doi.org/10.1080/20909977.2020.1794445>.
- Agenzia Spaziale Italiana (ASI). Available online: <https://www.asi.it/tlc-e-navigazione/galileo/> (accessed on 29 July 2022).
- Allmendinger, R.W., Reilinger, R., & Loveless, J. (2007). Strain and rotation rate from GPS in Tibet, Anatolia, and the Altiplano. *Tectonics*, 26(3). <https://doi.org/10.1029/2006TC002030>.
- Altamimi, Z., Rebischung, P., Métivier, L., & Collilieux, X. (2016). ITRF2014: A new release of the International Terrestrial Reference Frame modeling nonlinear station motions. *Journal of Geophysical Research: Solid Earth*, 121(8), 6109-6131. <https://doi.org/10.1002/2016JB013098>.
- Amato, A., Alessandrini, B., Cimini, G.B., Frepoli, A., & Selvaggi, G. (1993). Active and remnant subducted slabs beneath Italy: evidence from seismic tomography and seismicity. *Ann. Geofis.*, 36, 201–214.
- Amit, R., Zilberman, E., Porat, N., & Enzel, Y. (1999). Relief Inversion in the Avrona Playa as Evidence of Large-Magnitude Historical Earthquakes, Southern Arava Valley, Dead Sea Rift. *Quat. Res.*, 52, 76-91. <https://doi.org/10.1006/qres.1999.2050>.
- Anderson, J.G. (1979). Estimating the seismicity from geological structure for seismic-risk studies. *Bulletin of the Seismological Society of America*, 69(1), 135-158. <https://doi.org/10.1785/BSSA0690010135>.
- Anderson, H., & Jackson, J. (1987). Active tectonics of the Adriatic region. *Geophys. J. R. Astr. Soc.*, 91(3), 937–983. <https://doi.org/10.1111/j.1365-246X.1987.tb01675.x>.
- Andrieux, J., Fontbote, J.M., & Mattauer, M. (1971). Sur un modèle explicatif de l'arc de Gibraltar. *Earth Planet. Sci. Lett.*, 12, 191-198. [https://doi.org/10.1016/0012-821X\(71\)90077-X](https://doi.org/10.1016/0012-821X(71)90077-X).
- Aki, K. (1966). Generation and propagation of G waves from the Niigata earthquake of June 14, 1964. Part 2. Estimation of earthquake moment, released energy and stress-strain drop from G wave spectrum. *Bull. Earth. Res. Ins.*, 44(1), 73-88. <http://doi:10.15083/0000033586>.

- Aktüğ, B., Parmaksız, E., Kurt, M., Lenk, O., Kılıçoğlu, A., Gürdal, M.A., & Ozdemir, S. (2013). Deformation of Central Anatolia: GPS implications. *J. Geodyn.*, 67, 78-96. <https://doi.org/10.1016/j.jog.2012.05.008>.
- Apel, E.W. (2011). Shells on a Sphere: Tectonic Plate Motion and Plate Boundary Deformation. PhD. Dissertation. University of California, Berkeley, USA. <https://escholarship.org/uc/item/7xm5z7bb>.
- Argnani, A. (1990). The strait of Sicily rift zone: foreland deformation related to the evolution of a back-arc basin. *J. Geodyn.*, 12, 311-331. [https://doi.org/10.1016/0264-3707\(90\)90028-S](https://doi.org/10.1016/0264-3707(90)90028-S).
- Bahrouni, N., Bouaziz, S., Soumaya, A., Ben Ayed, N., & Attafi, K. (2013). Active deformation analysis and evaluation of earthquake hazard in Gafsa region (Southern Atlas of Tunisia). *Geophys. Res. Abstr.*, 15, EGU2013-EGU1009.
- Ballesteros, M., Rivera, J., Muñoz, A., Muñoz-Martín, A., Acosta, J., Carbó, A., & Uchupi, E. (2008). Alboran basin, Southern Spain. Part II: Neogene tectonic implications for the orogenic float model. *Mar. Petrol. Geol.*, 25, 75-101. <https://doi.org/10.1016/j.marpetgeo.2007.05.004>.
- Bartov, Y., Steinitz, G., Eyal, M., & Eyal, Y. (1980). Sinistral movement along the Gulf of Aqaba-Its age and relation to the opening of the Red Sea. *Nature*, 285, 220-222. <https://doi.org/10.1038/285220a0>.
- Basili, R., Tiberti, M.M., Kastelic, V., Romano, F., Piatanesi, A., Selva, J., & Lorito, S. (2013). Integrating geologic fault data into tsunami hazard studies. *Nat. Hazards Earth Syst. Sci.*, 13(4), 1025-1050. <https://doi.org/10.5194/nhess-13-1025-2013>.
- Beccaluva, L., Colantoni, P., Di Girolamo, P., & Savelli, C. (1981). Upper Miocene submarine volcanism in the Strait of Sicily (Banco Senza Nome). *Bull. Volcanol.*, 44, 573-581. <https://doi.org/10.1007/BF02600587>.
- Ben-Avraham, Z., Nur, A., & Giuseppe, C. (1987). Active transcurrent fault system along the North African passive margin. *Tectonophysics*, 141, 249-260. [https://doi.org/10.1016/0040-1951\(87\)90189-2](https://doi.org/10.1016/0040-1951(87)90189-2).
- Ben-Avraham, Z., & Grasso, M. (1991). Crustal structure variations and transcurrent faulting at the eastern and western margins of the eastern Mediterranean. *Tectonophysics*, 196(3-4), 269-277. [https://doi.org/10.1016/0040-1951\(91\)90326-N](https://doi.org/10.1016/0040-1951(91)90326-N).

- Ben Hassen, M., Deffontaines, B., & Turki, M.M. (2014). Recent tectonic activity of the Gafsa fault through morphometric analysis: Southern Atlas of Tunisia. *Quat. Int.*, 338, 99-112. <https://doi.org/10.1016/j.quaint.2014.05.009>.
- Ben-Menahem, A., Nur, A., & Vered, M. (1976). Tectonics, seismicity and structure of the Afro-Eurasian junction—The breaking of an incoherent plate. *Phys. Earth Planet. Inter.*, 12, 1-50. [https://doi.org/10.1016/0031-9201\(76\)90005-4](https://doi.org/10.1016/0031-9201(76)90005-4).
- Bilham, R., & Ambraseys, N. (2005). Apparent Himalayan slip deficit from the summation of seismic moments for Himalayan earthquakes, 1500-2000. *Current Science*, 88 (10), 1658-1663. <http://www.jstor.org/stable/24110492>.
- Boccaletti, M., Cello, G., & Tortorici, L. (1987). Transtensional tectonics in the Sicily channel. *J. Struct. Geol.*, 9(7), 869-876. [https://doi.org/10.1016/0191-8141\(87\)90087-3](https://doi.org/10.1016/0191-8141(87)90087-3).
- Boehm, J., Werl, B., & Schuh, H. (2006). Troposphere mapping functions for GPS and very long baseline interferometry from European centre for medium range weather forecasts operational analysis data. *J. Geophys. Res.*, 111, B02406. <https://doi.org/10.1029/2005JB003629>.
- Bohnhoff, M., Martínez-Garzón, P., Bulut, F., Stierle, E., & Ben-Zion, Y. (2016). Maximum earthquake magnitudes along different sections of the North Anatolian fault zone. *Tectonophysics*, 674, 147-165. <https://doi.org/10.1016/j.tecto.2016.02.028>.
- Bos, A.G., & Spakman, W. (2005). Kinematics of the southwestern U.S. deformation zone inferred from GPS motion data. *J. Geophys. Res.*, 110, B08405. <https://doi:10.1029/2003JB002742>.
- Bosworth, W., & McClay, K. (2001). Structural and stratigraphic evolution of the Gulf of Suez Rift, Egypt: A synthesis. In Peri-Tethys Memoir 6: Peri-Tethyan Rift/Wrench Basins and Passive Margins, Ziegler, P.A., Cavazza, W., Robertson, A.H.F., Crasquin-Soleau, S., Eds.; French National Museum of Natural History: Paris, France; pp. 567–606. ISBN 2-85653-528-3.
- Bougrine, A., Yelles-Chaouche, A.K., & Calais, E. (2019). Active deformation in Algeria from Continuous GPS measurements. *Geophys. J. Int.*, 217, 572-588. <https://doi.org/10.1093/gji/ggz035>.
- Bourgois, J.A., Mauffret, A., Ammar, N.A., & Demnati, N.A. (1992). Multichannel seismic data imaging of inversion tectonics of the Alboran Ridge (western Mediterranean Sea). *Geo Mar. Lett.*, 12, 117-122. <https://doi.org/10.1007/BF02084921>.
- Bungum, H., Lindholm, C.D., & Mahajan, A.K. (2017). Earthquake recurrence in NW and central Himalaya. *J. Asian Earth Sci.*, 138, 25-37. <http://doi:10.1016/j.jseas.2017.01.034>.

- Burollet, P.F., Mugniot, J.M., & Sweeney, P. (1978). The geology of the Pelagian block: the margins and basins of southern Tunisia and Tripolitania. In *The Ocean Basins and Margins. The Western Mediterranean* (eds Nairn, A.E.M. et al.) 331–359 (Plenum, New York). https://doi.org/10.1007/978-1-4684-3039-4_6.
- Calò, M., & Parisi, L. (2014). Evidences of a lithospheric fault zone in the Sicily Channel continental rift (southern Italy) from instrumental seismicity data. *Geophys. J. Int.*, 199, 219-225. <https://doi.org/10.1093/gji/ggu249>.
- Carafa, M.M., Valensise, G., & Bird, P. (2017). Assessing the seismic coupling of shallow continental faults and its impact on seismic hazard estimates: a case-study from Italy. *Geophysical Journal International*, 209(1), 32-47. <https://doi.org/10.1093/gji/ggx002>.
- Cardozo, N., & Allmendinger, R.W. (2009). SSPX: A program to compute strain from displacement/velocity data. *Computers & Geosciences*, 35(6), 1343-1357. <https://doi.org/10.1016/j.cageo.2008.05.008>.
- Cavallaro, D., & Coltelli, M. (2019). The Graham volcanic field offshore southwestern Sicily (Italy) revealed by high-resolution seafloor mapping and ROV images. *Front. Earth Sci.*, 7, 1. <https://doi.org/10.3389/feart.2019.00311>.
- Cello, G. (1987). Structure and deformation processes in the Strait of Sicily “rift zone”. *Tectonophysics*, 141, 237-247. [https://doi.org/10.1016/0040-1951\(87\)90188-0](https://doi.org/10.1016/0040-1951(87)90188-0).
- Chiarabba, C., & De Gori, P. (2016). The seismogenic thickness in Italy: constraints on potential magnitude and seismic hazard. *Terra Nova*, 28(6), 402-408. <https://doi.org/10.1111/ter.12233>.
- Chiarabba, C., Jovane, L., & DiStefano, R. (2005). A new view of Italian seismicity using 20 years of instrumental recordings. *Tectonophysics*, 395(3-4), 251-268. <https://doi.org/10.1016/j.tecto.2004.09.013>.
- Chousianitis, K., Ganas, A., & Evangelidis, C.P. (2015). Strain and rotation rate patterns of mainland Greece from continuous GPS data and comparison between seismic and geodetic moment release. *J. Geophys. Res.*, 120, 3909-3931. <https://doi:10.1002/2014JB011762>.
- Cinque, A., Patacca, E., Scandone, P., & Tozzi, M. (1993). Quaternary kinematic evolution of the Southern Apennines. Relationships between surface geological features and deep lithospheric structures. *Annals of Geophysics*, 36(2), 249–260.

- Civile, D., Lodolo, E., Accettella, D., Geletti, R., Ben-Avraham, Z., Deponte, M., Facchin, L., Ramella, R., & Romeo, R. (2010). The Pantelleria graben (Sicily Channel, central Mediterranean): an example of intraplate 'passive' rift. *Tectonophysics*, 490, 173-183. <https://doi.org/10.1016/j.tecto.2010.05.008>.
- CNIG (2013). Update of Seismic Hazard Maps of Spain; Centro Nacional de Información Geográfica: Madrid, Spain.
- Comas, M.C., Platt, J.P., Soto, J.I., & Watts, A.B. (1999). The origin and tectonic history of the Alboran Basin: Insights from Leg 161 results. In Proceedings of the Ocean Drilling Program; Scientific Results; Zahn, R., Comas, M.C., Klaus, A., Eds.; Ocean Drilling Program: College Station, TX, USA; Volume 161, pp. 555-580.
- Crustal Dynamics Data Information System (CDDIS). NASA's Archive of Space Geodesy Data. Available online: <https://cddis.nasa.gov/> (accessed on 09 August 2022).
- Crustal Dynamics Data Information System (CDDIS). The IONEX files. Available at: <https://cddis.nasa.gov/archive/gnss/products/ionex/> (accessed on 09 August 2022).
- CPTI Working Group, 2004. Catalogo Parametrico dei Terremoti Italiani, version 2004 (CPTI04). INGV, Bologna. <http://emidius.mi.ingv.it/CPTI> (accessed on 29 July 2022).
- D'Agostino, N., & Selvaggi, G. (2004). Crustal motion along the Eurasia-Nubia plate boundary in the Calabrian Arc and Sicily and active extension in the Messina Straits from GPS measurements. *Journal of Geophysical Research: Solid Earth*, 109(B11402). <https://doi.org/10.1029/2004JB002998>.
- D'Agostino, N., D'Anastasio, E., Gervasi, A., Guerra, I., Nedimović, M.R., Seeber, L., & Steckler, M. (2011). Forearc extension and slow rollback of the Calabrian Arc from GPS measurements. *Geophysical Research Letters*, 38(17). <https://doi.org/10.1029/2011GL048270>.
- D'Agostino, N. (2014). Complete seismic release of tectonic strain and earthquake recurrence in the Apennines (Italy). *Geophys. Res. Lett.*, 41, 1155-1162. <https://doi.org/10.1002/2014GL059230>.
- D'Agostino, N., Metois, M., Koci, R., Duni, L., Kuka, N., Ganas, A., Georgiev, I., Jouanne, F., Kaludjerovic, N., & Kandic, R. (2020). Active crustal deformation and rotations in the southwestern Balkans from continuous GPS measurements. *Earth Planet. Sci. Lett.*, 539, 116246. <https://doi.org/10.1016/j.epsl.2020.116246>.

- Deif, A., Al-Shijbi, Y., El-Hussain, I., Ezzelarab, M., & Mohamed, A.M.E. (2017). Compiling an earthquake catalogue for the Arabian Plate, Western Asia. *J. Asian Earth Sci.*, 147, 345-357. <https://doi.org/10.1016/j.jseaes.2017.07.033>.
- DeMets, C., Gordon, R.G., Argus, D.F., & Stein, S. (1990). Current plate motions. *Geophysical Journal International*, 101(2), 425-478. <https://doi.org/10.1111/j.1365-246X.1990.tb06579.x>.
- DeMets, C., Gordon, R.G., & Argus, D.F. (2010). Geologically current plate motions. *Geophys. J. Int.*, 181(1), 1-80. <https://doi.org/10.1111/j.1365-246X.2009.04491.x>.
- DeMets, C., Iaffaldano, G., & Merkuriev, S. (2015). High-resolution neogene and quaternary estimates of Nubia–Eurasia–North America Plate motion. *Geophys. J. Int.*, 203, 416-427. <https://doi.org/10.1093/gji/ggv277>.
- Déprez, A., Doubre, C., Masson, F., & Ulrich, P. (2013). Seismic and aseismic deformation along the East African Rift System from a reanalysis of the GPS velocity field of Africa. *Geophys. J. Int.*, 193, 1353-1369. <http://doi:10.1093/gji/ggt085>.
- Dercourt, J., Zonenshain, L.P., Ricou, L.E., Kazmin, V.G., Le Pichon, X., Knippe, A.L., Grandjacquet, C., Sbotshikov, I.M., Geysant, J., Lepvrier, C., Pechersky, D.H., Boulin, J., Sibouet, J.C., Savostin, L.A., Sorokhtin, O., Westphal, M., Bazhenov, M.L., Lauer, J.P., & Biju-Duval, J. (1986). Geological evolution of the Tethys belt from the Atlantic to the Pamirs since the Lias. *Tectonophysics*, 123(1-4), 241-315. [https://doi.org/10.1016/0040-1951\(86\)90199-X](https://doi.org/10.1016/0040-1951(86)90199-X).
- Devoti, R., Ferraro, C., Guegen, E., Lanotte, R., Luceri, V., Nardi, A., Pacione, R., Rutigliano, P., Sciarretta, C., & Vespe, F. (2002). Geodetic control on recent tectonic movements in the central Mediterranean area. *Tectonophysics*, 346(3-4), 151–167. [https://doi.org/10.1016/S0040-1951\(01\)00277-3](https://doi.org/10.1016/S0040-1951(01)00277-3).
- Devoti, R., Riguzzi, F., Cuffaro, M., & Doglioni, C. (2008) New GPS constraints on the kinematics of the Apennine subduction. *Earth and Planetary Science Letters*, 273(1-2), 163-174. <https://doi.org/10.1016/j.epsl.2008.06.031>.
- Devoti, R., & Riguzzi, F. (2018). The velocity field of the Italian area. *Rendiconti Lincei. Scienze Fisiche e Naturali*, 29(1), 51-58. <https://doi.org/10.1007/s12210-017-0651-x>.
- Doglioni, C., Mongelli, F., & Pieri, P. (1994). The Puglia uplift (SEItaly): an anomaly in the foreland of the Apenninic subduction due to the buckling of a thick continental lithosphere. *Tectonics*, 13(5), 1309-1321. <https://doi.org/10.1029/94TC01501>.

- EGSA Egyptian Geological Survey Authority (1981). Geological Map of Egypt; Egyptian Geological Survey: Cairo, Egypt.
- El-Fiky, G.S., Kato, T., & Fujii, Y. (1997). Distribution of vertical crustal movement rates in the Tohoku district, Japan, predicted by least-squares collocation. *Journal of Geodesy*, 71(7), 432-442. <https://doi.org/10.1007/s001900050111>.
- El-Isa, Z.H., & Eaton, D.W. (2014). Spatiotemporal variations in the b-value of earthquake magnitude–frequency distributions: Classification and causes. *Tectonophysics*, 615, 1-11. <https://doi.org/10.1016/j.tecto.2013.12.001>.
- England, P., Houseman, G., & Nocquet, J.M. (2016). Constraints from GPS measurements on the dynamics of deformation in Anatolia and the Aegean. *J. Geophys. Res.: Solid Earth*, 121(12), 8888-8916. <https://doi.org/10.1002/2016JB013382>.
- EUREF. Permanent GNSS Network. Available online: www.epncb.oma.be (accessed on 09 August 2022).
- Faccenna, C., Becker, T.W., Lucente, F.P., Jolivet, L., & Rossetti, F. (2001). History of subduction and back arc extension in the Central Mediterranean. *Geophysical Journal International*, 145(3), 809-820. <https://doi.org/10.1046/j.0956-540x.2001.01435.x>.
- Faccenna, C., Molin, P., Orecchio, B., Olivetti, V., Bellier, O., Funiciello, F., Minelli, L., Piromallo, C., & Billi, A. (2011). Topography of the Calabria subduction zone (southern Italy): Clues for the origin of Mt. Etna. *Tectonics*, 30(1). <https://doi.org/10.1029/2010TC002694>.
- Faccenna, C., Becker, T.W., Auer, L., Billi, A., Boschi, L., Brun, J.P., Capitanio, F.A., Funiciello, F., Horvath, F., Jolivet, L., Piromallo, C., Royden, L., Rossetti, F., & Serpelloni, E. (2014). Mantle dynamics in the Mediterranean. *Reviews of Geophysics*, 52, 283-332, <https://doi.org/10.1002/2013RG000444>.
- Farolfi, G., & Del Ventisette, C. (2017). Strain rates in the Alpine Mediterranean region: Insights from advanced techniques of data processing. *GPS solutions*, 21(3), 1027-1036. <https://doi.org/10.1007/s10291-016-0588-z>.
- Fernández, M., Marzán, I., Correia, A., & Ramalho, E. (1998). Heat flow, heat production, and lithospheric thermal regime in the Iberian Peninsula. *Tectonophysics*, 291, 29-53. [https://doi.org/10.1016/S0040-1951\(98\)00029-8](https://doi.org/10.1016/S0040-1951(98)00029-8).
- Fernández-Ibáñez, F., & Soto, J.I. (2008). Crustal rheology and seismicity in the Gibraltar Arc (western Mediterranean). *Tectonics*, 27(2). <https://doi.org/10.1029/2007TC002192>.

- Ferranti, L., Palano, M., Cannavò, F., Mazzella, M.E., Oldow, J.S., Gueguen, E., Mattia, M., & Monaco, C. (2014). Rates of geodetic deformation across active faults in southern Italy. *Tectonophysics*, 621, 101-122. <https://doi.org/10.1016/j.tecto.2014.02.007>.
- Frank, F.C. (1966). Deduction of Earth strains from survey data. *Bull. Seismol. Soc. Am.*, 56, 35-42. <https://doi.org/10.1785/BSSA0560010035>.
- Frepoli, A., Selvaggi, G., Chiarabba, C., & Amato, A. (1996). State of stress in the Southern Tyrrhenian subduction zone from fault-plane solutions. *Geophysical Journal International*, 125(3), 879-891. <https://doi.org/10.1111/j.1365-246X.1996.tb06031.x>.
- Frohlich, C., & Davis, S.D. (1993). Teleseismic b values; or, much ado about 1.0. *J. Geophys. Res.: Solid Earth*, 98 (B1), 631-644. <https://doi.org/10.1029/92JB01891>.
- Galli, P., & Scionti, V. (2006). Two unknown M>6 historical earthquakes revealed by palaeoseismological and archival researches in eastern Calabria (southern Italy). Seismotectonic implications. *Terra Nova*, 18(1), 44-49. <https://doi.org/10.1111/j.1365-3121.2005.00658.x>.
- Galli, P., Ruga, A., Scionti, V., & Spadea, R. (2006). Archaeoseismic evidence for a Late Roman earthquake in the Crotona area (Ionian Calabria, southern Italy): Seismotectonic implications. *Journal of Seismology*, 10(4), 443-458. <https://doi.org/10.1007/s10950-006-9030-2>.
- Galli, P., & Molin, D. (2007). Il terremoto del 1905 in Calabria; revisione del quadro macrosismico ed ipotesi sismogenetiche. In *Extended Abstracts of the 26° GNGTS National Congress, Rome 13–15 November 2007*, pp. 259–260.
- Galli, P., Galadini, F., & Pantosti, D. (2008). Twenty years of paleoseismology in Italy. *Earth-Science Reviews*, 88(1-2), 89-117. <https://doi.org/10.1016/j.earscirev.2008.01.001>.
- Ganas, A., & Parsons, T. (2009). Three-dimensional model of Hellenic Arc deformation and origin of the Cretan uplift. *J. Geophys. Res.: Solid Earth*, 114 (B6). <https://doi.org/10.1029/2008JB005599>.
- Garfunkel, Z., Zak, I., & Freund, R. (1981). Active faulting in the dead sea rift. *Tectonophysics*, 80, 1–26. [https://doi.org/10.1016/0040-1951\(81\)90139-6](https://doi.org/10.1016/0040-1951(81)90139-6).
- Gasperini, P., Lolli, B., Vannucci, G., & Boschi, E. (2012). A comparison of moment magnitude estimates for the European–Mediterranean and Italian region. *Geophysical Journal International*, 190, 1733-1745. <https://doi.org/10.1111/j.1365-246X.2012.05575.x>.

- Gasperini, P., Lolli, B., & Vannucci, G. (2013a). Empirical Calibration of Local Magnitude Data Sets Versus Moment Magnitude in Italy. *Bull. Seism. Soc. Am.*, 103, 2227-2246. <https://doi.org/10.1785/0120120356>.
- Gasperini, P., Lolli, B., & Vannucci, G. (2013b). Body-Wave Magnitude m_b Is a Good Proxy of Moment Magnitude M_w for Small Earthquakes ($m_b < 4.5-5.0$). *Seismological Research Letters*, 84(6), 932-937. <https://doi.org/10.1785/0220130105>.
- Gomez, F., Meghraoui, M., Darkal, A.N., Hijazi, F., Mouty, M., Suleiman, Y., Sbeinati, R., Darawcheh, R., Al-Ghazzi, R., & Barazangi, M. (2003). Holocene faulting and earthquake recurrence along the Serghaya branch of the Dead Sea fault system in Syria and Lebanon. *Geophys. J. Int.*, 153, 658-674. <https://doi.org/10.1046/j.1365-246X.2003.01933.x>.
- González, P.J., Palano, M., & Fernández, J. (2009). Study of the present-day tectonics and seismogenetic sources of the Al-Hoceima region (Morocco) using GPS and MTINSAR. In Proceedings of the Fringe 2009 Workshop, Frascati, Italy, 30 November-4 December; Volume 30.
- Gorshkov, A.I., Panza, G.F., Soloviev, A.A., & Aoudia, A. (2002). Morphostructural zonation and preliminary recognition of seismogenic nodes around the adria margin in peninsular Italy and Sicily. *Journal of Seismology and Earthquake Engineering*, 4(1), 1-24.
- Govers, R., & Wortel, M.J.R. (2005). Lithosphere tearing at STEP faults: Response to edges of subduction zones. *Earth and Planetary Science Letters*, 236(1-2), 505-523. <https://doi.org/10.1016/j.epsl.2005.03.022>.
- Gracia, E., Pallas, R., Soto, J.I., Comas, M.C., Moreno, X., Masana, E., Santanach, P., Diez, S., Garcia, M., & Dañobeitia, J. (2006). Active faulting offshore SE Spain, (Alboran Sea): Implications for earthquake hazard assessment in the southern Iberian Margin. *Earth Planet. Sci. Lett.*, 241, 734-749. <https://doi.org/10.1016/j.epsl.2005.11.009>.
- Grünthal, G., & Wahlström, R. (2012). The European-Mediterranean Earthquake Catalogue (EMEC) for the last millennium. *Journal of Seismology*, 16, 535-570. <https://doi.org/10.1007/s10950-012-9302-y>.
- Grünthal, G., Wahlström, R., & Stromeier, D. (2013). The SHARE European Earthquake Catalogue (SHEEC) for the time period 1900-2006 and its comparison to the European-Mediterranean Earthquake Catalogue (EMEC). *Journal of Seismology*, 17(4), 1339-1344. <https://doi.org/10.1007/s10950-013-9379-y>.

- Guidoboni, E., Ferrari, G., Mariotti, D., Comastri, A., Tarabusi, G., & Valensise, G. (2007). Catalogue of Strong Earthquakes in Italy (461 BC-1997) and Mediterranean Area (760 BC-1500). INGV-SGA, <http://storing.ingv.it/cfti4 med/>.
- Guidoboni, E. (2011). *Terremoti a Ferrara e nel suo territorio: un rischio sottovalutato*. Ferrara, voci di una città. Fondazione Cassa di Risparmio di Ferrara. Retrieved July 2021.
- Guidoboni, E., Ferrari, G., Mariotti, D., Comastri, A., Tarabusi, G., Sgattoni, G., & Valensise, G. (2018). CFTI5Med, Catalogo dei Forti Terremoti in Italia (461 a.C.-1997) e nell'area Mediterranea (760 a.C.-1500). Istituto Nazionale di Geofisica e Vulcanologia (INGV). <https://doi.org/10.6092/ingv.it-cfti5>.
- Guidoboni, E., Ferrari, G., Tarabusi, G., Sgattoni, G., Comastri, A., Mariotti, D., Ciuccarelli, C., Bianchi, M.G., & Valensise, G. (2019). CFTI5Med, the new release of the catalogue of strong earthquakes in Italy and in the Mediterranean area. *Scientific Data*, 6, 80. <https://doi.org/10.1038/s41597-019-0091-9>.
- Gupta, H., & Gahalaut, V.K. (2014). Seismotectonics and large earthquake generation in the Himalayan region. *Gondwana Res.*, 25, 204-213. <https://doi.org/10.1016/j.gr.2012.11.006>.
- Gutenberg, B., & Richter, C.F. (1956). Earthquake magnitude, intensity, energy, and acceleration: (Second paper). *Bull. Seismol. Soc. Am.*, 46 (2), 105-145. <https://doi.org/10.1785/BSSA0460020105>.
- Haines, A.J., & Holt, W.E. (1993). A procedure for obtaining the complete horizontal motions within zones of distributed deformation from the inversion of strain rate data. *Journal of Geophysical Research: Solid Earth*, 98(B7), 12057-12082. <https://doi.org/10.1029/93JB00892>.
- Hamdache, M., Peláez, J.A., & Yelles Chauche, A.K. (2004). The Algiers, Algeria earthquake (Mw 6.8) of 21 May 2003: Preliminary report. *Seismol. Res. Lett.*, 75, 360-367. <https://doi.org/10.1785/gssrl.75.3.360>.
- Hamdache, M., Peláez, J.A., Talbi, A., & López Casado, C. (2010). A unified catalog of main earthquakes for northern Algeria from a.d. 856 to 2008. *Seismol. Res. Lett.*, 81, 732-739. <https://doi.org/10.1785/gssrl.81.5.732>.
- Han, Q., Wang, L., Xu, J., Carpinteri, A., & Lacidogna, G. (2015). A robust method to estimate the b-value of the magnitude–frequency distribution of earthquakes. *Chaos, Solitons & Fractals*, 81, 103-110. <https://doi.org/10.1016/j.chaos.2015.09.004>.

- Hanks, T.C., & Kanamori, H. (1979). A moment magnitude scale. *J. Geophys. Res.*, 84, 2348–2350. <https://doi.org/10.1029/JB084iB05p02348>.
- Hempton, M.R. (1987). Constraints on Arabian Plate motion and extensional history of the Red Sea. *Tectonics*, 6, 687-705. <https://doi.org/10.1029/TC006i006p00687>.
- Herring, T. (2003). MATLAB Tools for viewing GPS velocities and time series. *GPS solutions*, 7(3), 194-199. <https://doi.org/10.1007/s10291-003-0068-0>.
- Herring, T.A., King, R.W., Floyd, M.A., & McClusky, S.C. (2018). Introduction to GAMIT/GLOBK, Release 10.7. Massachusetts Institute of Technology: Cambridge, UK. Available online: <http://www-gpsg.mit.edu> (accessed on 27 July 2022).
- HORUS (HOMogenized instrUMENTal Seismic catalogue), <http://horus.bo.ingv.it/> (accessed on 01 August 2022).
- Hunstad, I., Selvaggi, G., D’Agostino, N., England, P., Clarke, P., & Pierozzi, M. (2003). Geodetic strain in peninsular Italy between 1875 and 2001. *Geophysical Research Letters*, 30(4), 1828. <https://doi.org/10.1029/2002GL016447>.
- Hyndman, R.D., & Weichert, D.H. (1983). Seismicity and rates of relative plate motion on the plate boundaries of western North America. *Geophys. J. R. Astron. Soc.*, 72, 59-82. <https://doi:10.1111/j.1365-246X.1983.tb02804.x>.
- IGS International GNSS Service. Available online: <https://www.igs.org> (accessed on 10 August 2022).
- Inkscape, version 1. Available online: <https://inkscape.org> (accessed on 09 August 2022).
- Institute of Geodynamics – National Observatory of Athens. Available online: <http://www.gein.noa.gr/en/seismicity/earthquake-catalogs> (accessed on 10 August 2022).
- International GNSS Service. IGS absolute antenna phase center models. Available online: <ftp://ftp.igs.org/pub/station/general/> (accessed on 10 August 2022).
- International Seismological Centre. Available online: <http://www.isc.ac.uk/> (accessed on 09 August 2022).
- International Seismological Centre. ISC-EHB bulletin. Available online: <http://www.isc.ac.uk/isc-ehb/> (accessed on 09 August 2022).

- International Seismological Centre. ISC-GEM Earthquake Catalogue. Available online: <http://www.isc.ac.uk/iscgem/index.php> (accessed on 10 August 2022).
- ISIDe. Available online: <http://iside.rm.ingv.it/> (accessed on 01 August 2022).
- ISIDe Working Group (2007). Italian Seismological Instrumental and Parametric Database (ISIDe). Istituto Nazionale di Geofisica e Vulcanologia (INGV). Available online: <https://doi.org/10.13127/ISIDE> (accessed on 29 July 2022).
- ITALPOS. Available online: <https://hxgnsmartnet.com/it-it> (accessed on 29 July 2022).
- Jackson, J., & McKenzie, D. (1988). The relationship between plate motions and seismic moment tensors, and the rates of active deformation in the Mediterranean and Middle East. *Geophys. J. Int.*, 93(1), 45-73. <https://doi.org/10.1111/j.1365-246X.1988.tb01387.x>.
- Jenny, S., Goes, S., Giardini, D., & Kahle, H.G. (2004). Earthquake recurrence parameters from seismic and geodetic strain rates in the eastern Mediterranean. *Geophys. J. Int.*, 157(3), 1331-1347. <https://doi.org/10.1111/j.1365-246X.2004.02261.x>.
- Jenny, S., Goes, S., Giardini, D., & Kahle, H.G. (2006). Seismic potential of southern Italy. *Tectonophysics*, 415, 81-101. <https://doi:10.1016/j.tecto.2005.12.003>.
- Joffe, S., & Garfunkel, Z. (1987). Plate kinematics of the circum Red Sea-A re-evaluation. *Tectonophysics*, 141, 5-22. [https://doi.org/10.1016/0040-1951\(87\)90171-5](https://doi.org/10.1016/0040-1951(87)90171-5).
- Kandilli Observatory and Earthquake Research Institute (KOERI) of Bogazici University. Available online: <http://www.koeri.boun.edu.tr/sismo/2/earthquake-catalog> (accessed on 10 August 2022).
- Kebeasy, R. (1990). Seismicity. In *The Geology of Egypt*; A.A. Balkema: Rotterdam, The Netherlands; pp. 51-59.
- Kijko, A., & Graham, G. (1998). Parametric-historic procedure for probabilistic seismic hazard analysis part I: estimation of maximum regional magnitude m_{max} . *Pure Appl. Geophys.*, 152(3), 413-442. <https://doi.org/10.1007/s000240050161>.
- Kijko, A., & Singh, M. (2011). Statistical tools for maximum possible earthquake magnitude estimation. *Acta Geophys.*, 59, 674-700. <https://doi:10.2478/s11600-011-0012-6>.

- Klinger, Y., Avouac, J.P., Abou Karaki, N., Dorbath, L., Bourles, D., & Reyss, J.L. (2000). Slip rate on the Dead Sea transform fault in northern Arava valley (Jordan). *Geophys. J. Int.*, 142, 755-768. <https://doi.org/10.1046/j.1365-246x.2000.00165.x>.
- Kostrov, V. (1974). Seismic moment and energy of earthquakes, and seismic Row of rock. *Izv. Acad. Sci. USSR Phys. Solid Earth*, 1, 23-44.
- Koulali, A., Ouazar, D., Tahayt, A., King, R.W., Vernant, P., Reilinger, R.E., McClusky, S., Mourabit, T., Davila, J.M., & Amraoui, N. (2011). New GPS constrains on active deformation along the Africa-Iberia plate boundary. *Earth Planet. Sci. Lett.*, 308, 211-217. <https://doi.org/10.1016/j.epsl.2011.05.048>.
- Lentini, F., Carbone, S., Guarnieri, P., Dilek, Y., & Pavlides, S. (2006). Collisional and postcollisional tectonics of the Apenninic-Maghrebian orogen (southern Italy). *Spec. Pap. Geol. Soc. Am.*, 409, 57. [https://doi.org/10.1130/2006.2409\(04\)](https://doi.org/10.1130/2006.2409(04)).
- Leonard, M. (2010). Earthquake fault scaling: Self-consistent relating of rupture length, width, average displacement, and moment release. *Bulletin of the Seismological Society of America*, 100(5A), 1971-1988. <https://doi.org/10.1785/0120090189>.
- Lodolo, E., Civile, D., Zanolta, C., & Geletti, R. (2012). Magnetic signature of the Sicily channel volcanism. *Mar. Geophys. Res.*, 33(1), 33-44. <https://doi.org/10.1007/s11001-011-9144-y>.
- Lolli, B., & Gasperini, P. (2012). A comparison among general orthogonal regression methods applied to earthquake magnitude conversions. *Geophysical Journal International*, 190(2), 1135-1151. <https://doi.org/10.1111/j.1365-246X.2012.05530.x>.
- Lolli, B., Gasperini, P., & Vannucci, G. (2014). Empirical conversion between teleseismic magnitudes (mb and Ms) and moment magnitude (Mw) at the Global, Euro-Mediterranean and Italian scale. *Geophysical Journal International*, 199(2), 805-828. <https://doi.org/10.1093/gji/ggu264>.
- Lolli, B., Gasperini, P., Mele, F.M., & Vannucci, G. (2015). Recalibration of the Distance Correction Term for Local Magnitude (ML) Computations in Italy. *Seismological Research Letters*, 86(5), 1383-1392. <https://doi.org/10.1785/0220150020>.
- Lolli, B., Gasperini, P., & Rebez, A. (2018). Homogenization in terms of Mw of local magnitudes of Italian earthquakes occurred before 1981. *Bull. Seism. Soc. Am.*, 108(1), 481-492. <https://doi.org/10.1785/0120170114>.

- Lolli, B., Randazzo, D., Vannucci, G., & Gasperini, P. (2020). The Homogenized Instrumental Seismic Catalog (HORUS) of Italy from 1960 to Present. *Seismological Research Letters*, 91(6), 3208-3222. <https://doi.org/10.1785/0220200148>.
- Lucente, F.P., Chiarabba, C., Cimini, G.B., & Giardini, D. (1999). Tomographic constraints on the geodynamic evolution of the Italian region. *Journal of Geophysical Research: Solid Earth*, 104(B9), 20307-20327. <https://doi.org/10.1029/1999JB900147>.
- Lyard, F., Lefevre, F., Letellier, T., & Francis, O. (2006). Modelling the global ocean tides: Modern insights from fes2004. *Ocean Dyn.*, 56, 394–415. <https://doi.org/10.1007/s10236-006-0086-x>.
- Mahsas, A., Lammali, K., Yelles, K., Calais, E., Freed, A., & Briole, P. (2008). Shallow afterslip following the 2003 May 21, Mw = 6.9 Boumerdes earthquake, Algeria. *Geophys. J. Int.*, 172, 155-166. <https://doi.org/10.1111/j.1365-246X.2007.03594.x>.
- Malinverno, A., & Ryan, W.B.F. (1986). Extension in the Tyrrhenian Sea and shortening in the Apennines as result of arc migration driven by sinking of the lithosphere. *Tectonics*, 5(2), 227–245. <https://doi.org/10.1029/TC005i002p00227>.
- Maouche, S., Abtout, A., Merabet, N.E., Aïfa, T., Lamali, A., Bouyahiaoui, B., & Ayache, M. (2013). Tectonic and Hydrothermal Activities in Debagh, Guelma Basin (Algeria). *J. Geophys. Res.*, 409475, <https://doi.org/10.1155/2013/409475>.
- Marco, S., Agnon, A., Ellenblum, R., Eidelman, A., Basson, U., & Boas, A. (1997). 817-Year-old walls offset sinistrally 2.1 m by the Dead Sea transform, Israel. *J. Geodyn.*, 24, 11-20. [https://doi.org/10.1016/S0264-3707\(96\)00041-5](https://doi.org/10.1016/S0264-3707(96)00041-5).
- Margheriti, L., Lucente, F.P., & Pondrelli, S. (2003). SKS splitting measurements in the Apenninic-Tyrrhenian domain (Italy) and their relation with lithospheric subduction and mantle convection. *Journal of Geophysical Research: Solid Earth*, 108(B4), 2218. <https://doi.org/10.1029/2002JB001793>.
- Martínez Solares, J.M., & Mezcuca, J. (2002). Seismic Catalog of the Iberian Peninsula (880 BC-1900); IGN: Madrid, Spain; (In Spanish).
- Masana, E., Martínez-Díaz, J.J., Hernández-Enrile, J.L., & Santanach, P. (2004). The Alhama de Murcia fault (SE Spain), a seismogenic fault in a diffuse plate boundary: Seismotectonic implications for the Ibero-Magrebian region. *J. Geophys. Res.*, 109. <https://doi.org/10.1029/2002JB002359>.

- Masson, F., Chéry, J., Hatzfeld, D., Martinod, J., Vernant, P., Tavakoli, F., & Ghafory-Ashtiani, M. (2005). Seismic versus aseismic deformation in Iran inferred from earthquakes and geodetic data. *Geophys. J. Int.*, 160, 217-226. <https://doi:10.1111/j.1365-246X.2004.02465.x>.
- Masson, C., Mazzotti, S., Vernant, P., & Doerflinger, E. (2019). Extracting small deformation beyond individual station precision from dense Global Navigation Satellite System (GNSS) networks in France and western Europe. *Solid Earth*, 10(6), 1905-1920. <https://doi.org/10.5194/se-10-1905-2019>.
- MATLAB software. Available online: <https://it.mathworks.com> (accessed on 29 July 2022).
- Mazzotti, S., & Adams, J. (2005). Rates and uncertainties on seismic moment and deformation in eastern Canada. *Journal of Geophysical Research: Solid Earth*, 110(B9). <https://doi:10.1029/2004JB003510>.
- Mazzotti, S., Leonard, L.J., Cassidy, J.F., Rogers, G.C., & Halchuk, S. (2011). Seismic hazard in western Canada from GPS strain rates versus earthquake catalog. *J. Geophys. Res.*, 116, B12310. <https://doi:10.1029/2011JB008213>.
- McKenzie, D.P. (1970). Plate tectonics of the Mediterranean region. *Nature*, 226, 239-243. <https://doi.org/10.1038/226239a0>.
- Meghraoui, M., Cisternas, A., & Philip, H. (1986). Seismotectonics of the lower Chelif basin: Structural background of the El Asnam (Algeria) earthquake. *Tectonics*, 5, 809-836. <https://doi.org/10.1029/TC005i006p00809>.
- Meghraoui, M., & Pondrelli, S. (2012). Active faulting and transpression tectonics along the plate boundary in North Africa. *Ann. Geophys.*, 55. <https://doi.org/10.4401/ag-4970>.
- Menke, W. (1989). *Geophysical Data Analysis: Discrete Inverse Theory*. Rev. Ed., Academic Press, 289 pp.
- Metois, M., D'Agostino, N., Avallone, A., Chamot-Rooke, N., Rabaute, A., Duni, L., Kuka, N., Koci, R., & Georgiev, I. (2015). Insights on continental collisional processes from GPS data: Dynamics of the peri-Adriatic belts. *J. Geophys. Res.: Solid Earth*, 120(12), 8701-8719. <https://doi.org/10.1002/2015JB012023>.
- Michard, A., Chalouan, A., Feinberg, H., Goffé, B., & Montigny, R. (2002). How does the Alpine belt end between Spain and Morocco? *Bull. Soc. Géol. France*, 173, 3-15. <https://doi.org/10.2113/173.1.3>.

- Middleton, T.A., Parsons, B., & Walker, R.T. (2018). Comparison of seismic and geodetic strain rates at the margins of the Ordos Plateau, northern China. *Geophysical Journal International*, 212(2), 988-1009. <https://doi.org/10.1093/gji/ggx446>.
- Miller, C.K., & Furlong, K.P. (1988). Thermal-mechanical controls on seismicity depth distributions in the San Andreas fault zone. *Geophys. Res. Lett.*, 15, 1429-1432. <https://doi.org/10.1029/GL015i012p01429>.
- Mogi, K. (1962). Study shocks caused by the fracture of heterogeneous materials and its relations to earthquake phenomena. *Bulletin of Earthquake Research Institute, University of Tokyo*, 40, 123-173.
- Molnar, P. (1979). Earthquake recurrence intervals and plate tectonics. *Bulletin of the Seismological Society of America*, 69(1), 115-133. <https://doi.org/10.1785/BSSA0690010115>.
- Molnar, P. (1992). Fault mechanics and transport properties of rocks: a festschrift in honor of W.F. Brace, ch. 18, *Fault Mechanics and Transport Properties of Rocks*, eds. B. Evans and T. Wong, San Diego, Acad. Press.
- Mori, J., & Abercrombie, R.E. (1997). Depth dependence of earthquake frequency-magnitude distributions in California: implications for rupture initiation. *J. Geophys. Res.: Solid Earth*, 102(B7), 15081-15090. <https://doi.org/10.1029/97JB01356>.
- Nazareth, J.J., & Hauksson, E. (2004). The seismogenic thickness of the southern California crust. *Bulletin of the Seismological Society of America*, 94(3), 940-960. <https://doi.org/10.1785/0120020129>.
- Neri, G., Orecchio, B., Totaro, C., Falcone, G., & Presti, D. (2009). Subduction beneath southern Italy close the ending: Results from seismic tomography. *Seismological Research Letters*, 80(1), 63-70. <https://doi.org/10.1785/gssrl.80.1.63>.
- Neri, G., Marotta, A.M., Orecchio, B., Presti, D., Totaro, C., Barzaghi, R., & Borghi, A. (2012). How lithospheric subduction changes along the Calabrian Arc in southern Italy: geophysical evidences. *International Journal of Earth Sciences*, 101(7), 1949-1969. <https://doi.org/10.1007/s00531-012-0762-7>.
- NETGEO. Available online: <http://www.netgeo.it/page.php?Id=63> (accessed on 29 July 2022).
- Nikolaidis, R. (2002). Observation of Geodetic and seismic deformation with the Global Positioning System. Doctoral Dissertation PhD Thesis, Scripps Inst. Of Oceanogr, La Jolla, San Diego: University of California, 249.

- National Geodetic Survey (NGS). Available online: <http://geodesy.noaa.gov> (accessed on 10 August 2022).
- Nocquet, J.M. (2012). Present-day kinematics of the Mediterranean: a comprehensive overview of GPS results. *Tectonophysics*, 579, 220–242. <https://doi.org/10.1016/j.tecto.2012.03.037>.
- Palano, M., Cannavò, F., Ferranti, L., Mattia, M., & Mazzella, M.E. (2011). Strain and stress fields in the Southern Apennines (Italy) constrained by geodetic, seismological and borehole data. *Geophys. J. Int.*, 187, 1270-1282. <https://doi:10.1111/j.1365-246X.2011.05234.x>.
- Palano, M., González, P.J., & Fernández, J. (2015). The diffuse plate boundary of Nubia and Iberia in the Western Mediterranean: Crustal deformation evidence for viscous coupling and fragmented lithosphere. *Earth Planet. Sci. Lett.*, 430, 439-447. <https://doi.org/10.1016/j.epsl.2015.08.040>.
- Palano, M., Piromallo, C., & Chiarabba, C. (2017). Surface imprint of toroidal flow at retreating slab edges: the first geodetic evidence in the Calabrian subduction system. *Geophys. Res. Lett.*, 44(2), 845-853. <https://doi.org/10.1002/2016GL071452>.
- Palano, M., Imprescia, P., Agnon, A., & Gresta, S. (2018). An improved evaluation of the seismic/geodetic deformation-rate ratio for the Zagros Fold-and-Thrust collisional belt. *Geophys. J. Int.*, 213, 194-209. <https://doi:10.1093/gji/ggx524>.
- Palano, M., Ursino, A., Spampinato, S., Sparacino, F., Polonia, A., & Gasperini, L. (2020). Crustal deformation, active tectonics and seismic potential in the Sicily Channel (Central Mediterranean), along the Nubia-Eurasia plate boundary. *Scientific Reports*, 10, 21238. <https://doi.org/10.1038/s41598-020-78063-1>.
- Pancha, A., Anderson, J.G., & Kreemer, C. (2006). Comparison of seismic and geodetic scalar moment rates across the Basin and Range Province. *Bull. Seismol. Soc. Am.*, 96, 11-32. <https://doi:10.1785/0120040166>.
- Panzerà, F., D'Amico, S., Lombardo, G., Galea, P., & Akinci, A. (2015). Overview of the seismic hazard in the Sicily channel archipelagos. In Establishment of an Integrated Italy-Malta Crossborder System of Civil Protection: Geophysical Aspects (eds Panzerà, F. & Lombardo, G.) 31-45 (Aracne, Rome).
- Papadopoulos, G.A. (2011). A Seismic History of Crete: The Hellenic Arc and Trench. Athens.

- Papazachos, C.B., & Kiratzi, A.A. (1996). A detailed study of the active crustal deformation in the Aegean and surrounding area. *Tectonophysics*, 253 (1-2), 129–153. [https://doi.org/10.1016/0040-1951\(95\)00047-X](https://doi.org/10.1016/0040-1951(95)00047-X).
- Patacca, E., & Scandone, P. (1989). Post-Tortonian mountain building in the Apennines: the role of the passive sinking of a relic lithospheric slab. In: Boriani, A., Bonafede, M., Piccardo, G.B., Vai, G.B. (Eds.), *The Lithosphere in Italy: Advance in Earth Science Research*. Accademia Nazionale dei Lincei, Rome, pp. 157–176. <http://hdl.handle.net/11568/172693>.
- Patacca, E., Sartori, R., & Scandone, P. (1990). Tyrrhenian basin and Apenninic arcs: kinematic relations since late Tortonian times. *Mem. Soc. Geol. Ital.*, 45, 425-451.
- Peccerillo, A. (2005). The Sicily Province. In *Plio-quadernary volcanism in Italy* (ed. Peccerillo, A.) 215-255 (Springer-Verlag, Berlin).
- Peláez, J.A., Chourak, M., Tadili, B.A., Aït Brahim, L., Hamdache, M., López Casado, C., & Martínez Solares, J.M. (2007). A catalog of main Moroccan earthquakes from 1045 to 2005. *Seismol. Res. Lett.*, 78, 614-621. <https://doi.org/10.1785/gssrl.78.6.614>.
- Peláez, J.A., Henares, J., Hamdache, M., & Sanz de Galdeano, C. (2018). An updated seismic model for northwestern Africa. In *Proceedings of the 16th European Conference on Earthquake Engineering*, Thessaloniki, Greece, 18-21 June.
- Petricca, P., Carminati, E., & Doglioni, C. (2022). Estimation of the maximum earthquakes magnitude based on potential brittle volume and strain rate: The Italy test case. *Tectonophysics*, 229405. <https://doi.org/10.1016/j.tecto.2022.229405>.
- Petrie, E.J., King, M.A., Moore, P., & Lavallée, D.A. (2010). Higher-order ionospheric effects on the GPS reference frame and velocities. *J. Geophys. Res.*, 115(B3), B03417. <https://doi.org/10.1029/2009JB006677>.
- Pieri, P., Vitale, G., Benedice, P., Dogliosi, C., Gallicchio, S., Giano, S., Loizzo, R., Moretti, M., Prosser, G., Sabato, L., Schiattarella, M., Tramutoli, M., & Tropeano, M. (1997). Tettonica quaternaria nell'area bradano-ionica. *Il Quaternario*, 10(2), 535–542.
- Piromallo, C., & Morelli, A. (2003). P wave tomography of the mantle under the Alpine-Mediterranean area. *Journal of Geophysical Research: Solid Earth*, 108(B2). <https://doi:10.1029/2002JB001757>.

- Platt, J.P., Whitehouse, M.J., Kelley, S.P., Carter, A., & Hollick, L. (2003). Simultaneous extensional exhumation across the Alboran Basin: Implications for the causes of late orogenic extension. *Geology*, 31, 251-254. [https://doi.org/10.1130/0091-7613\(2003\)031<0251:SEEATA>2.0.CO;2](https://doi.org/10.1130/0091-7613(2003)031<0251:SEEATA>2.0.CO;2).
- Pollack, H.N., & Chapman, D.S. (1977). On the regional variation of heat flow, geotherms, and lithospheric thickness. *Tectonophysics*, 38, 279-296. [https://doi.org/10.1016/0040-1951\(77\)90215-3](https://doi.org/10.1016/0040-1951(77)90215-3).
- Polyak, B.G., Fernández, M., Khutorskoy, M.D., Soto, J.I., Basov, I.A., Comas, M.C., Khain, V.Y., Alonso, B., Agapova, G.V., Mazurova, I.S., Negredo, A., Tochitsky, V.O., de la Linde, J., Bogdanov, N.A., & Banda, E. (1996). Heat flow in the Alboran Sea, western Mediterranean. *Tectonophysics*, 263, 191-218. [https://doi.org/10.1016/0040-1951\(95\)00178-6](https://doi.org/10.1016/0040-1951(95)00178-6).
- Pondrelli, S., Morelli, A., Ekström, G., Mazza, S., Boschi, E., & Dziewonski, A.M. (2002). European-Mediterranean regional centroid-moment tensors: 1997-2000. *Physics of the Earth and Planetary Interiors*, 130(1-2), 71-101. [https://doi.org/10.1016/S0031-9201\(01\)00312-0](https://doi.org/10.1016/S0031-9201(01)00312-0).
- Pondrelli, S., Salimbeni, S., Ekström, G., Morelli, A., Gasperini, P., & Vannucci, G. (2006). The Italian CMT dataset from 1977 to the present. *Physics of the Earth and Planetary Interiors*, 159(3-4), 286-303. <https://doi.org/10.1016/j.pepi.2006.07.008>.
- Pontevivo, A., & Panza, G.F. (2006). The lithosphere-asthenosphere system in the Calabrian Arc and surrounding seas-Southern Italy. *Pure and Applied Geophysics*, 163(8), 1617-1659. <https://doi.org/10.1007/s00024-006-0093-3>.
- Prada, M., Ranero, C.R., Sallarès, V., Grevemeyer, I., de Franco, R., Gervasi, A., & Zitellini, N. (2020). The structure of Mediterranean arcs: New insights from the Calabrian Arc subduction system. *Earth and Planetary Science Letters*, 548, 116480. <https://doi.org/10.1016/j.epsl.2020.116480>.
- Prescott, W.H., & Savage, J.C. (1976). Strain accumulation on the San Andreas fault near Palmdale, California. *Journal of Geophysical Research*, 81(26), 4901-4908. <https://doi.org/10.1029/JB081i026p04901>.
- Presti, D., Totaro, C., Neri, G., & Orecchio, B. (2019). New earthquake data in the Calabrian subduction zone, Italy, suggest revision of the presumed dynamics in the upper part of the subducting slab. *Seismological Research Letters*, 90(5), 1994-2004. <https://doi.org/10.1785/0220190024>.

- Rabaute, A., & Chamot-Rooke, N. (2014). Active Tectonics of the Africa-Eurasia Boundary from Algiers to Calabria. Map at 1:500,000 Scale; Geosubsight, Paris, France; ISBN 978-2-9548197-0-9.
- Rashwan, M., Sawires, R., Radwan, A.M., Sparacino, F., Peláez, J.A., & Palano, M. (2021). Crustal Strain and Stress Fields in Egypt from Geodetic and Seismological Data. *Remote Sens.*, 13, 1398. <https://doi.org/10.3390/rs13071398>.
- Reid, H.F. (1910). The mechanism of the earthquake, The California Earthquake of April 18, 1906, Report of the State Earthquake Investigation Commission, 2, Washington D.C.: Carnegie Institution.
- Rete Integrata Nazionale GNSS (RING). Available online: <http://ring.gm.ingv.it/> (accessed on 29 July 2022).
- Rimi, A., Chalouan, A., & Bahi, L. (1998). Heat flow in the westernmost part of the alpine mediterranean system (The Rif, Morocco). *Tectonophysics*, 285, 135-146. [https://doi.org/10.1016/S0040-1951\(97\)00185-6](https://doi.org/10.1016/S0040-1951(97)00185-6).
- Roger, J., & Hébert, H. (2008). The 1856 Djijelli (Algeria) earthquake and tsunami: Source parameters and implications for tsunami hazard in the Balearic Islands. *Nat. Hazards Earth Syst. Sci.*, 8, 721-731. <https://doi.org/10.5194/nhess-8-721-2008>.
- Rong, Y., Jackson, D.D., & Kagan, Y.Y. (2003). Seismic gaps and earthquakes. *J. Geophys. Res.*, 108, 2471. <https://doi.org/10.1029/2002JB002334>.
- Rontogianni, S. (2010). Comparison of geodetic and seismic strain rates in Greece by using a uniform processing approach to campaign GPS measurements over the interval 1994–2000. *J. Geodyn.*, 50, 381-399. <https://doi.org/10.1016/j.jog.2010.04.008>.
- Royden, L., Patacca, E., & Scandone, P. (1987). Segmentation and configuration of subducted lithosphere in Italy: An important control on thrust-belt and foredeep-basin evolution. *Geology*, 15(8), 714-717. [https://doi.org/10.1130/0091-7613\(1987\)15<714:SACOSL>2.0.CO;2](https://doi.org/10.1130/0091-7613(1987)15<714:SACOSL>2.0.CO;2).
- Rydelek, P.A., & Sacks, I.S. (1989). Testing the completeness of earthquake catalogues and the hypothesis of self-similarity. *Nature*, 337(6204), 251-253. <https://doi.org/10.1038/337251a0>.
- Salamon, A., Hofstetter, A., Garfunkel, Z., & Ron, H. (2003). Seismotectonics of the Sinai subplate-The eastern Mediterranean region. *Geophys. J. Int.*, 155, 149-173. <https://doi.org/10.1046/j.1365-246X.2003.02017.x>.

- Savage, J.C., & Burford, R.O. (1973). Geodetic determination of relative plate motion in central California. *Journal of Geophysical Research*, 78(5), 832-845. <https://doi.org/10.1029/JB078i005p00832>.
- Savage, J.C. (1983). Strain accumulation in western United States. *Annual Review of Earth and Planetary Sciences*, 11, 11-43.
- Savage, J.C. (1990). Equivalent strike-slip earthquake cycles in half-space and lithosphere-asthenosphere earth models. *Journal of Geophysical Research: Solid Earth*, 95(B4), 4873-4879. <https://doi.org/10.1029/JB095iB04p04873>.
- Savage, J.C., Lisowski, M., & Prescott, W.H. (1990). An apparent shear zone trending north-northwest across the Mojave Desert into Owens Valley, eastern California. *Geophysical Research Letters*, 17(12), 2113-2116. <https://doi.org/10.1029/GL017i012p02113>.
- Savage, J.C., & Simpson, R.W. (1997). Surface strain accumulation and the seismic moment tensor. *Bull. Seismol. Soc. Am.*, 87(5), 1345-1353. <https://doi.org/10.1785/BSSA0870051345>.
- Sawires, R., Peláez, J.A., Fat-helbary, R.E., & Ibrahim, H.A. (2016). An earthquake catalogue (2200 B.C. to 2013) for seismotectonic and Seismic Hazard Assessment Studies in Egypt. In *Earthquakes and Their Impact on Society*; D'Amico, S., Ed.; Springer International Publishing: Cham, Switzerland; pp. 97-136. ISBN 9783319217536.
- Sawires, R., Peláez, J.A., Fat-Helbary, R.E., Panzera, F., Ibrahim, H.A., & Hamdache, M. (2017). Probabilistic Seismic Hazard Deaggregation for Selected Egyptian Cities. *Pure Appl. Geophys.*, 174, 1581-1600. <https://doi.org/10.1007/s00024-017-1490-5>.
- Sawires, R., Peláez, J.A., Sparacino, F., Radwan, A.M., Rashwan, M., & Palano, M. (2021). Seismic and Geodetic Crustal Moment Rates Comparison: New Insights on the Seismic Hazard of Egypt. *Applied Sciences*, 11, 7836. <https://doi.org/10.3390/app11177836>.
- Scarfi, L., Barberi, G., Barreca, G., Cannavò, F., Koulakov, I., & Patanè, D. (2018). Slab narrowing in the Central Mediterranean: The Calabro-Ionian subduction zone as imaged by high resolution seismic tomography. *Scientific reports*, 8(1), 1-12. <https://doi.org/10.1038/s41598-018-23543-8>.
- Scarfi, L., Langer, H., Messina, A., & Musumeci, C. (2021). Tectonic regimes inferred from clustering of focal mechanisms and their distribution in space: application to the Central Mediterranean Area. *Journal of Geophysical Research: Solid Earth*, 126(1), e2020JB020519. <https://doi.org/10.1029/2020JB020519>.
- Schlumberger (1984). *Geology of Egypt*. In Well Evaluation Conference; Schlumberger: Cairo, Egypt.

- Schmid, R., Steigenberger, P., Gendt, G., Ge, M., & Rothacher, M. (2007). Generation of a consistent absolute phase-center correction model for GPS receiver and satellite antennas. *J. Geodesy*, 81, 781-798. <https://doi.org/10.1007/s00190-007-0148-y>.
- Scholz, C.H. (1968). Experimental study of the fracturing process in brittle rock. *J. Geophys. Res.*, 73(4), 1447-1454. <https://doi.org/10.1029/JB073i004p01447>.
- Scholz, C.H. (1990). *The mechanics of earthquakes and faulting*. Cambridge University Press.
- Scholz, C.H. (1998). A further note on earthquake size distributions. *Bull. Seismol. Soc. Am.*, 88(5), 1325-1326. <https://doi.org/10.1785/BSSA0880051325>.
- Scholz, C.H., & Campos, J. (2012). The seismic coupling of subduction zones revisited. *J. Geophys. Res.: Solid Earth*, 117 (B5). <https://doi.org/10.1029/2011JB009003>.
- Scholz, C.H. (2015). On the stress dependence of the earthquake b value. *Geophysical Research Letters*, 42(5), 1399-1402. <https://doi.org/10.1002/2014GL062863>.
- Scudero, S., De Guidi, G., Caputo, R., & Perdicaro, V. (2020). A semi-quantitative method to combine tectonic stress indicators: example from the Southern Calabrian Arc (Italy). *Bulletin of the Geological Society of Greece*, 56(1), 280-316. <https://doi.org/10.12681/bgsg.23485>.
- Serpelloni, E., Anzidei, M., Baldi, P., Casula, G., & Galvani, A. (2005). Crustal velocity and strain-rate fields in Italy and surrounding regions: new results from the analysis of permanent and non-permanent GPS networks. *Geophysical Journal International*, 161(3), 861-880. <https://doi.org/10.1111/j.1365-246X.2005.02618.x>.
- Serrano, I., Zhao, D.P., & Morales, J. (2002). 3-D crustal structure of the extensional Granada Basin in the convergent boundary between the Eurasian and African plates. *Tectonophysics*, 344, 61-79. [https://doi.org/10.1016/S0040-1951\(01\)00201-3](https://doi.org/10.1016/S0040-1951(01)00201-3).
- Shen, Z.K., Jackson, D.D., & Ge, B.X. (1996). Crustal deformation across and beyond the Los Angeles basin from geodetic measurements. *Journal of Geophysical Research: Solid Earth*, 101(B12), 27957-27980. <https://doi.org/10.1029/96JB02544>.
- Shen, Z.K., Wang, M., Zeng, Y., & Wang, F. (2015). Optimal interpolation of spatially discretized geodetic data. *Bulletin of the Seismological Society of America*, 105(4), 2117-2127. <https://doi.org/10.1785/0120140247>.
- Sibson, R.H. (1984). Roughness at the base of the seismogenic zone: contributing factors. *J. Geophys. Res.: Solid Earth*, 89(B7), 5791-5799. <https://doi.org/10.1029/JB089iB07p05791>.

- Smith-Konter, B.R., Sandwell, D.T., & Shearer, P. (2011). Locking depths estimated from geodesy and seismology along the San Andreas Fault System: implications for seismic moment release. *J. Geophys. Res.*, 116, B06401. <https://doi.org/10.1029/2010JB008117>.
- Sneh, A. (1996). The Dead Sea Rift: Lateral displacement and downfaulting phases. *Tectonophysics*, 263, 277-292. [https://doi.org/10.1016/S0040-1951\(96\)00028-5](https://doi.org/10.1016/S0040-1951(96)00028-5).
- Spampinato, S., Ursino, A., Barbano, M.S., Pirrotta, C., Rapisarda, S., Larocca, G., & Platania, P.R. (2017). A reappraisal of seismicity and eruptions of Pantelleria Island and the Sicily Channel (Italy). *Pure and Applied Geophysics*, 174(7), 2475-2493. <https://doi.org/10.1007/s00024-017-1550-x>.
- Sparacino, F., Palano, M., Peláez, J.A., & Fernández, J. (2020). Geodetic Deformation versus Seismic Crustal Moment-Rates: Insights from the Ibero-Maghrebian Region. *Remote Sensing*, 12(6), 952. <https://doi.org/10.3390/rs12060952>.
- Sparacino, F., Galuzzi, B.G., Palano, M., Segou, M., & Chiarabba, C. (2022). Seismic coupling for the Aegean-Anatolian region. *Earth-Science Reviews*, 228, 103993. <https://doi.org/10.1016/j.earscirev.2022.103993>.
- Stein, R.S. (2008). Appendix D: earthquake Rate Model 2 of the 2007 Working Group for California Earthquake Probabilities, Magnitude Area Relationships. U.S. Geol. Surv. Open File Rep., 2007, 1437D, 1-16.
- Stevens, V.L., & Avouac, J.P. (2017). Millenary Mw > 9.0 earthquakes required by geodetic strain in the Himalaya. *Geophys. Res. Lett.*, 43, 1118-1123. <http://doi.org/10.1002/2015GL067336>.
- Stich, D., Martín, J.B., & Morales, J. (2007). Deformación sísmica y asísmica en la zona Béticas-Rif-Alborán. *Rev. Soc. Geol. Esp.*, 20, 311-319.
- Stucchi, M., Rovida, A., Capera, A.G., Alexandre, P., Camelbeeck, T., Demircioglu, M.B., Gasperini, P., Kouskouna, V., Musson, R.M.W., Radulian, M., Sesetyan, K., Vilanova, S., Baumont, D., Bungum, H., Fah, D., Lenhardt, W., Makropoulos, K., Martinez Solares, J.M., Scotti, O., Zivcic, M., Albini, P., Batllo, J., Papaioannou, C., Tatevossian, R., Locati, M., Meletti, C., Viganò, D., & Giardini, D. (2013). The SHARE European earthquake catalogue (SHEEC) 1000-1899. *J. Seismol.*, 17 (2), 523-544. <https://doi.org/10.1007/s10950-012-9335-2>.
- Suleiman, A.S., Albini, P., & Migliavacca, P. (2004). A short introduction to historical earthquakes in Libya. *Ann. Geophys.*, 47, 545-554.

- Tape, C., Musé, P., Simons, M., Dong, D., & Webb, F. (2009). Multiscale estimation of GPS velocity fields. *Geophysical Journal International*, 179(2), 945-971. <https://doi.org/10.1111/j.1365-246X.2009.04337.x>.
- Tatar, O., Poyraz, F., Gürsoy, H., Cakir, Z., Ergintav, S., Akpınar, Z., Koçbulut, F., Sezen, F., Türk, T., Hastaoglu, K.O., Polat, A., Levent Mesci, B., Gürsoy, O., Ayazlı, E., Çakmak, R., Belgen, A., & Yavasoglu, H. (2012). Crustal deformation and kinematics of the Eastern part of the North Anatolian Fault Zone (Turkey) from GPS measurements. *Tectonophysics*, 518, 55-62. <https://doi.org/10.1016/j.tecto.2011.11.010>.
- Thatcher, W. (1983). Nonlinear strain buildup and the earthquake cycle on the San Andreas fault. *Journal of Geophysical Research: Solid Earth*, 88(B7), 5893-5902. <https://doi.org/10.1029/JB088iB07p05893>.
- Thatcher, W. (1986). The crustal deformation cycle at convergent plate margins. *R. Soc. New Zealand Bull.*, 24, 317-332.
- The CFTI5MED Catalogo dei forti terremoti in Italia 461 A.C. – 1997 e nell'area mediterranea 760 A.C. – 1500. <http://storing.ingv.it/cfti/cfti5/> (accessed on 29 July 2022).
- The Israel National Seismic Network (FDSN). Available online: <https://www.fdsn.org/networks/detail/IS/> (accessed on 10 August 2022).
- The National Earthquake Information Center, United States Geological Survey (USGS). Available online: <https://earthquake.usgs.gov/earthquakes/search/> (accessed on 10 August 2022).
- The Scripps Orbit and Permanent Array Center (SOPAC). Available online: <http://sopac-csrc.ucsd.edu/> (accessed on 29 July 2022).
- The SHARE European Earthquake Catalogue. Available online: <https://www.emidius.eu/SHEEC> (accessed on 29 July 2022).
- Tiryakioğlu, I., Floyd, M., Erdogan, S., Güllal, E., Ergintav, S., McClusky, S., & Reilinger, R. (2013). GPS constraints on active deformation in the Isparta Angle region of SW Turkey. *Geophys. J. Int.*, 195(3), 1455-1463. <https://doi.org/10.1093/gji/ggt323>.
- Torelli, L., Grasso, M., Mazzoldi, G., Peis, D., & Gori, D. (1995). Cretaceous to Neogene structural evolution of the Lampedusa shelf (Pelagian Sea, Central Mediterranean). *Terra Nova*, 7(2), 200-212. <https://doi.org/10.1111/j.1365-3121.1995.tb00689.x>.

- Torné, M., Fernández, M., Comas, M.C., & Soto, J.I. (2000). Lithospheric structure beneath the Alboran Basin: Results from 3D gravity modeling and tectonic relevance. *J. Geophys. Res.*, 105, 3209-3228. <https://doi.org/10.1029/1999JB900281>.
- Tse, S.T., & Rice, J.R. (1986). Crustal earthquake instability in relation to the depth variation of frictional slip properties. *Journal of Geophysical Research: Solid Earth*, 91(B9), 9452-9472. <https://doi.org/10.1029/JB091iB09p09452>.
- Turcotte, D.L., & Schubert, G. (2002). *Geodynamics*. Cambridge University Press.
- UNAVCO. Available online: www.unavco.org (accessed on 09 August 2022).
- Van Hinsbergen, D.J., Edwards, M.A., & Govers, R. (2009). Geodynamics of collision and collapse at the Africa–Arabia–Eurasia subduction zone—an introduction. *Geological Society, London, Special Publications*, 311(1), 1-7. <https://doi.org/10.1144/SP311.1>.
- Van Hinsbergen, D.J., Vissers, R.L., & Spakman, W. (2014). Origin and consequences of western Mediterranean subduction, rollback, and slab segmentation. *Tectonics*, 33(4), 393-419. <https://doi.org/10.1002/2013TC003349>.
- Vernant, P., Reilinger, R., & McClusky, S. (2014). Geodetic evidence for low coupling on the Hellenic subduction plate interface. *Earth Planet. Sci. Lett.*, 385, 122-129. <https://doi.org/10.1016/j.epsl.2013.10.018>.
- Ward, S.N. (1994). A Multidisciplinary approach to seismic hazard in Southern California. *Bull. seism. Soc. Am.*, 84(5), 1293–1309. <https://doi.org/10.1785/BSSA0840051293>.
- Ward, S.N. (1998). On the consistency of earthquake moment release and space geodetic strain rates: Europe. *Geophysical Journal International*, 135(3), 1011-1018. <https://doi.org/10.1046/j.1365-246X.1998.t01-2-00658.x>.
- Ward, S.N. (1998). On the consistency of earthquake moment rates, geological fault data, and space geodetic strain: the United States. *Geophysical Journal International*, 134(1), 172-186. <https://doi.org/10.1046/j.1365-246x.1998.00556.x>.
- WCC-Woodward Clyde Consultants (1985). *Earthquake Activity and Stability Evaluation for the Aswan High Dam; Submitted to Aswan High Dam Authority; Ministry of Irrigation: Aswan, Egypt*.

- Weichert, D.H. (1980). Estimation of the earthquake recurrence parameters for unequal observation periods for different magnitudes. *Bull. Seismol. Soc. Am.*, 70, 1337-1346. <https://doi.org/10.1785/BSSA0700041337>.
- Wells, D.L., & Coppersmith, K.J. (1994). New empirical relationship among magnitude, rupture length, rupture width, rupture area, and surface displacement. *Bull. Seismol. Soc. Am.*, 84(4), 974-1002. <https://doi.org/10.1785/BSSA0840040974>.
- Wessel, P., & Bercovici, D. (1998). Interpolation with splines in tension: A Green's function approach. *Mathematical Geology*, 30, 77-93. <https://doi.org/10.1023/A:1021713421882>.
- Wessel, P., Smith, W.H.F., Scharroo, R., Luis, J.F., & Wobbe, F. (2013). Generic mapping tools: improved version released. *EOS Trans. AGU* 94, 409-410. <https://doi.org/10.1002/2013EO450001>.
- Westaway, R. (1992). Seismic moment summation for historical earthquakes in Italy: tectonic implications. *Journal of Geophysical Research: Solid Earth*, 97(B11), 15437-15464. <https://doi.org/10.1029/92JB00946>.
- Wiemer, S. (2001). A software package to analyze seismicity: ZMAP. *Seismological Research Letters*, 72(3), pp. 373-382. <https://doi.org/10.1785/gssrl.72.3.373>.
- Wiemer, S., & Wyss, M. (2000). Minimum magnitude of completeness in earthquake catalogs: examples from Alaska, the western United States, and Japan. *Bull. Seism. Soc. Am.*, 90(4), 859-869. <https://doi.org/10.1785/0119990114>.
- Williams, C.F. (1996). Temperature and the seismic/aseismic transition: observations from the 1992 Landers earthquake. *Geophys. Res Lett.*, 23, 2029-2032. <https://doi.org/10.1029/96GL02066>.
- Working Group on California Earthquake Probabilities (1995). Seismic hazards in southern California: probable earthquakes, 1994 to 2024. *Bulletin of the Seismological Society of America*, 85(2), 379-439. <https://doi.org/10.1785/BSSA0850020379>.
- Yelles Chauche, A.K., Kherroubi, A., & Beldjoudi, H. (2017). The large Algerian earthquakes (267 A.D.-2017). *Física de la Tierra*, 29, 159-182. <https://doi.org/10.5209/FITE.57617>.
- Zilberman, E., Amit, R., Heimann, A., & Porat, N. (2000). Changes in Holocene Paleoseismic activity in the Hula pull-apart basin, Dead Sea Rift, northern Israel. *Tectonophysics*, 321, 237-252. [https://doi.org/10.1016/S0040-1951\(00\)00035-4](https://doi.org/10.1016/S0040-1951(00)00035-4).

Acknowledgements

I would like to thank one by one the many people who helped to make this work possible, one way or another.

For the realization of this PhD Thesis I would like first of all to thank my Co-Supervisor, Dr. Mimmo Palano, with whom I shared this academic research path. Dr. Mimmo Palano was a fundamental reference for my scientific maturation, being also my scientific referent, since I conducted this course of study in parallel with my work as a research fellow at the National Institute of Geophysics and Volcanology (INGV) in Catania since December 2018.

A heartfelt thanks goes to my Supervisors: Professor Stefano Gresta and Professor Maria Serafina Barbano. I thank Prof. Gresta, who followed my PhD Thesis until his well-deserved retirement (December 2020), for what he transmitted to me with his undisputed sympathy, talent and availability. I infinitely thank Prof. Barbano, who subsequently guided me to the completion of this path with her always ready availability, kindness and professionalism.

A heartfelt thanks goes to my Supervisor for the period abroad (unfortunately held remotely due to the pandemic), Professor Amotz Agnon, to his research group, and to the entire Institute, *The Hebrew University of Jerusalem, Institute of Earth Sciences*, who welcomed me as a presence, with great interest and spirit of collaboration. I hope these relationships can continue into the future.

A heartfelt thanks goes to the PhD Coordinator, Professor Agata Di Stefano, always kind, helpful, and ready to intervene at any time of need in this path so important and equally full of difficulties. With her undisputed professionalism, sympathy and charisma she has always been careful, punctual and present.

A heartfelt thanks go to my University colleagues: I really hope that these relationships of friendship and collaboration that the University has allowed me to establish can continue in the future, and to the whole Department of Biological, Geological and Environmental Sciences of the University of Catania. A heartfelt thanks go to my INGV (Rome and Catania sections) colleagues too, in particular to Dr. Giuseppe Pezzo and Dr. Francesca Di Luccio, for supporting me during these three years of work carried out in parallel with my PhD. A special thank go to my colleague (University of Milano Bicocca) and long-time friend, Dr. Bruno G. Galuzzi, for supporting me both with his undisputed talent and precious friendship: I strongly believe in our continued cooperation and friendship.

And finally the last heartfelt thanks, but for this no less important, go to my friends, to my family, my parents Carmelo and Anna, my sister and my brother, who encouraged me first to begin and later to complete my doctorate, and to my dear partner Mario, who always believes in me, sharing in my struggles and successes.